GA Technologies

GA-A15999
UC-77

FINAL REPORT ON THE PEACH BOTTOM TEST ELEMENT PROGRAM

by
J. J. SAURWEIN, J. F. HOLZGRAF, C. M. MILLER,
B. F. MYERS, and C. F. WALLROTH

Prepared under
Contract DE-AT03-76ET35300
for the San Francisco Operations Office
Department of Energy

DATE PUBLISHED: NOVEMBER 1982

DISCLAIMER

DO NOT MICROFILM
COVER

DISCLAIMER

Printed in the United States of America
Available from
National Technical Information Service
U.S. Department of Commerce
5285 Port Royal Road
Springfield, Virginia 22161
NTIS Price Code: Printed Copy A-14; Microfiche A-01

GA Technologies

GA-A--15999

DE83 009706

GA-A15999
UC-77

FINAL REPORT ON THE PEACH BOTTOM TEST ELEMENT PROGRAM

by
J. J. SAURWEIN, J. F. HOLZGRAF, C. M. MILLER,
B. F. MYERS, and C. F. WALLROTH*

Prepared under
Contract DE-AT03-76ET35300
for the San Francisco Operations Office
Department of Energy

*Present address: Drägerwerk, AG, Lübeck, Federal Republic of Germany

GA PROJECT 6400
DATE PUBLISHED: NOVEMBER 1982

DISCLAIMER

ABSTRACT

Thirty-three test elements were irradiated in the Peach Bottom high-temperature gas-cooled reactor (HTGR) as part of the testing program for advanced HTGRs. Extensive postirradiation examinations and evaluations of 21 of these irradiation experiments were performed.

The test element irradiations were simulated using HTGR design codes and data. Calculated fuel burnups, power profiles, fast neutron fluences, and temperatures were verified via destructive burnup measurements, gamma scanning, and in-pile thermocouple readings corrected for decalibration effects. Analytical techniques were developed to improve the quality of temperature predictions through feedback of nuclear measurements into thermal calculations.

Dimensional measurements, pressure burst tests, diametral compression tests, ring-cutting tests, strip-cutting tests, and four-point bend tests were performed to measure residual stress, strain, and strength distributions in H-327 graphite structures irradiated in the test elements. Results were compared with unirradiated control specimens to estimate irradiation-induced changes in material properties. Experimental results were compared with design code predictions when available.

Detailed examination of fuel rods and loose fuel particles irradiated in the test elements added significantly to the data bases for outer pyrolytic carbon structural stability, fission product attack on SiC coatings, kernel migration, fission product release, and fuel rod performance. Extensive dimensional measurements on Peach Bottom test element fuel rods established a large body of irradiation strain data suitable for use in verifying fuel rod strain models.

Diffusion samples irradiated in several of the test elements were analyzed, providing important information on the diffusion of metallic fission products in H-327 graphite.

CONTENTS

FIGURES

FIGURES (Continued)

FIGURES (Continued)

FIGURES (Continued)

FIGURES (Continued)

FIGURES (Continued)

FIGURES (Continued)

FIGURES (continued)

TABLES

TABLES (Continued)

TABLES (Continued)

TABLES (Continued)

1. INTRODUCTION

The Peach Bottom Atomic Power Station, Unit No. 1, was the first high-temperature gas-cooled reactor (HTGR) in the United States. Power operation began in January 1967 and commercial operation on June 1, 1967. The plant was operated through October 31, 1974, when it was shut down for decommissioning. In addition to producing commercial power [over 1.2 million MW(e)-hr for the Philadelphia Electric Company grid], this prototype nuclear power station was used as a test facility for HTGR fuels and materials.

Thirty-three test elements were installed and irradiated in the Peach Bottom HTGR as part of the testing program for advanced HTGRs. Extensive postirradiation examinations (PIEs) and evaluations of 21 of these irradiation experiments were performed. Participants in the Peach Bottom test element program included GA Technologies Inc. (GA), Oak Ridge National Laboratory (ORNL), the United States Department of Energy (DOE, formerly ERDA and AEC), Kernforschungsanlage Jülich GmbH (KFA), Hochtemperatur Brennelement Gesellschaft (HOBEG, formerly NUKEM), the United Kingdom Atomic Energy Authority (UKAEA), and the Electric Power Research Institute (EPRI). Table 1-1 provides an overview of the program.*

The Peach Bottom test elements encompassed several fuel concepts and fuel element designs. These are described in Section 2. Through control of core location, irradiation time, fuel loadings, and test element design, the desired irradiation conditions were obtained for each experiment. Variation of these parameters permitted fuel and graphite performance to be observed over a wide range of irradiation conditions. The test elements experienced fast neutron fluences up to 4.2×10^{25} n/m^2 $[(E > 29\ fJ)_{HTGR}]$ and time-averaged fuel temperatures as high as 1640°C.

*Tables and figures appear at the end of each section.

Maximum fuel burnups were 60% and 3.1% for fissile and fertile fuel, respectively.

The test element irradiations were simulated using HTGR design codes and data (Section 3). Calculated burnups, power profiles, fast neutron fluences, and temperatures were verified via destructive burnup measurements, gamma scanning, and in-pile thermocouple readings corrected for decalibration effects (Sections 4 and 5). Analytical techniques were developed to improve the quality of temperature predictions through feedback of nuclear measurements into thermal calculations. Extensive data on irradiation-induced strain in fuel rods and H-327 graphite structures (Section 6), residual stress and strength distributions in irradiated H-327 graphite structures (Section 7), fuel performance (Section 8), and the transport of metallic fission products in H-327 graphite (Section 9) were obtained from postirradiation examinations of the test elements.

One of the test elements for which temperature predictions were improved through feedback of nuclear measurements into thermal calculations was FTE-18. Irradiation temperatures based on gamma spectrometric measurements performed by KFA are included as an appendix to this report to satisfy a GA commitment under PWS-FD-14 of the Umbrella Agreement between the United States and the Federal Republic of Germany (FRG).

Because of the massive scale of the Peach Bottom test element program, this document cannot address all aspects of the program, nor can it present data in as much detail as might be desired for certain purposes. Therefore, reports containing detailed data for specific test elements have been referenced. Table 1-1 provides a directory of the documentation for the Peach Bottom test element program.

REFERENCES

1-1. Wallroth, C. F., et al., "Postirradiation Examination of Peach Bottom Fuel Test Element FTE-3," USAEC Report GA-A13004, August 15, 1974.

1-2. Wallroth, C. F., et al., "Postirradiation Examination of Peach Bottom Fuel Test Element FTE-4," ERDA Report GA-A13452, July 1977.

1-3. Wallroth, C. F., J. F. Holzgraf, and D. D. Jensen, "Postirradiation Examination and Evaluation of Peach Bottom Fuel Test Element FTE-6," ERDA Report GA-A13943, September 1977.

1-4. Holzgraf, J. F., et al., "Postirradiation Examination and Evaluation of Peach Bottom Fuel Test Elements FTE-14 and FTE-15," DOE Report GA-A13944, February 1979.

1-5. Wallroth, C. F., et al., "Postirradiation Examination and Evaluation of Peach Bottom Molded Fuel Test Element FTE-18," Report GA-A13699, June 1, 1976.

1-6. Tiegs, T. N., and E. L. Long, Jr., "Postirradiation Examination of Recycle Test Elements from the Peach Bottom Reactor," DOE Report ORNL-5422, Oak Ridge National Laboratory, December 1978.

1-7. Saurwein, J. J., et al., "Thermal, Nuclear, and Fission Product Evaluation of Fuel Pin Test Elements FPTE-1 and FPTE-3," Report GA-A13849, December 1980.

1-8. Miller, C. M., et al., "Postirradiation Examination and Evaluation of Peach Bottom Fuel Test Element FTE-13," GA Technologies, to be published.

TABLE 1-1
SUMMARY OF PEACH BOTTOM TEST ELEMENT PROGRAM

Element I.D.	Sponsored By	Irradiation Time (EFPD)	Maximum Test Conditions				Fuel Particles		Objectives	PIE	Documentation (Ref.)
			Temp. (C°)	Burnup Fissile (%)	Burnup Fertile (%)	Fast Fluence ($\times 10^{25}$ n/m^2)	Fissile	Fertile			
FTE-1	GA	252.4	1316	20	0.2	1.2	$(Th,U)C_2$ BISO $(Th,U)C_2$ TRISO UC_2 BISO	ThC_2 BISO ThC_2 TRISO	Evaluate large HTGR fuel particles under representative conditions. Conduct controlled experiments on thermal stability, diffusion fission product release, etc., as functions of temperature and fast fluence.	Yes	
FTE-2	GA	385.4	1212	28	0.4	1.8	$(Th,U)C_2$ BISO $(Th,U)C_2$ TRISO UC_2 BISO	ThC_2 BISO ThC_2 TRISO	↓	Yes	
FTE-5	GA	897.3	1379	56	2.3	3.8	UC_2 BISO $(Th,U)C_2$ BISO UC_2 TRISO $(Th,U)C_2$ TRISO	ThC_2 BISO ThC_2 TRISO	Evaluate large HTGR fuel rods under representative HTGR conditions. Conduct controlled experiments on fuel thermal stability as function of temperature and fast fluence.	Yes	
FTE-3	GA	133.0	1167	10	<0.1	0.6	$(ThU)C_2$ TRISO UC_2 TRISO UO_2 TRISO	ThC_2 TRISO ThC_2 BISO ThO_2 BISO	↓	Yes	1-1
FTE-4	AEC	448.8	1261	36	0.7	2.0	UC_2 TRISO UO_2 TRISO $(Th,U)C_2$ TRISO	ThC_2 BISO ThO_2 BISO ThC_2 TRISO		Yes	1-2
FTE-6	AEC	644.9	1409	46	1.6	2.9	UC_2 TRISO UO_2 TRISO $(Th,U)C_2$ TRISO	ThC_2 BISO ThO_2 BISO ThC_2 TRISO	↓	Yes	1-3

TABLE 1-1 (Continued)

Element I.D.	Sponsored By	Irradiation Time (EFPD)	Maximum Test Conditions				Fuel Particles		Objectives	PIE	Documentation (Ref.)
			Temp. (C°)	Burnup Fissile (%)	Burnup Fertile (%)	Fast Fluence (x 10^{25} n/m^2)	Fissile	Fertile			
FTE-14	AEC	315.8	1574	25	0.4	1.5	UO_2 TRISO UC_2 TRISO $(Th,U)O_2$ TRISO	ThO_2 TRISO ThC_2 BISO ThO_2 BISO ThC_2 TRISO	Evaluate large HTGR fuel rods under representative HTGR conditions. Conduct controlled experiments on fuel thermal stability as function of temperature and fast fluence.	Yes	1-4
FTE-15	AEC	511.9	1624	38	1.0	2.0	UO_2 TRISO UC_2 TRISO $(Th,U)O_2$ TRISO	ThO_2 TRISO ThC_2 BISO ThO_2 BISO ThC_2 TRISO	↓	Yes	1-4
FTE-18	GA/NUKEM	511.9	1487	39	1.3	3.4	$(Th,U)O_2$ BISO	None	Evaluate irradiation performance of fuel bodies molded from fuel particles to form single monolithic structures.	Yes	1-5
FBTE-1	GA	897.3	1352	54	2.3	3.7	$(Th,U)C_2$ BISO	ThC_2 BISO	Demonstrate performance of HTGR fuel on large scale. Determine in-pile fission gas release of various fuels under representative HTGR conditions. Evaluate performance of unbounded fuel particle beds.	No	
FBTE-2	GA	897.3	1366	54	3.1	3.7	UC_2 BISO	ThC_2 BISO		No	
FBTE-3	GA	897.3	1326	58	2.8	3.7	UC_2 TRISO	ThC_2 BISO		No	
FBTE-4	GA	252.4	1219	17	0.2	1.1	$(Th,U)C_2$ TRISO	ThC_2 TRISO		No	
FBTE-5	GA	897.3	NA	57	2.4	4.1	$(Th,U)C_2$ BISO $(Th,U)C_2$ TRISO UC_2 BISO	ThC_2 BISO ThC_2 TRISO	↓	No	

TABLE 1-1 (Continued)

Element I.D.	Sponsored By	Irradiation Time (EFPD)	Maximum Test Conditions				Fuel Particles		Objectives	PIE	Documentation (Ref.)
			Temp. (C°)	Burnup Fissile (%)	Burnup Fertile (%)	Fast Fluence (x 10^{25} n/m^2)	Fissile	Fertile			
FBTE-6	GA	252.4	NA	20	0.2	1.2	$(Th,U)C_2$ BISO	ThC_2 BISO		No	
FTE-7	GA	644.9	1481	47	1.2	2.7	UO_2 TRISO	ThO_2 BISO	Demonstrate performance of HTGR fuel on large scale. Determine in-pile fission gas release of various fuels under representative HTGR conditions.	No	
FTE-8	GA	644.9	1283	49	1.8	2.6	UC_2 TRISO	ThC_2 BISO	↓	No	
FTE-9	GA	644.9	1257	45	1.4	2.8	$(Th,U)C_2$ TRISO	ThC_2 BISO	↓	No	
FTE-12	GA	644.9	1311	46	1.2	2.8	$(Th,U)O_2$ BISO	ThO_2 BISO	↓	No	
RTE-1 (FTE-11)	AEC	644.9	1640	50	1.8	3.0	UO_2 TRISO $(Th,U)O_2$ BISO UC_2 BISO UC_2 TRISO UO_2 BISO	ThO_2 BISO ThC_2 BISO ThC_2 TRISO	Provide irradiated fuel for HTGR fuel reprocessing demonstrations at ORNL. Test various oxide fuels produced with the sol-gel process under HTGR conditions.	Yes	1-6
RTE-2	AEC	701.2	1392	46	1.7	3.1	UC_2 TRISO UC_2 BISO $(Th,U)O_2$ BISO	ThC_2 BISO	↓		
RTE-4	AEC	385.4	1327	32	0.6	1.9	UC_2 TRISO UC_2 BISO $(Th,U)O_2$ BISO	ThC_2 BISO	↓	Yes	1-6
RTE-5	AEC	897.3	1393	59	2.7	4.1	UO_2 BISO $(Th,U)O_2$ BISO UC_2 BISO UC_2 TRISO	ThC_2 BISO ThC_2 TRISO ThO_2 BISO	↓	Yes	1-6

TABLE 1-1 (Continued)

Element I.D.	Sponsored By	Irradiation Time (EFPD)	Maximum Test Conditions				Fuel Particles		Objectives	PIE	Documentation (Ref.)
			Temp. (C°)	Burnup Fissile (%)	Burnup Fertile (%)	Fast Fluence (x 10^{25} n/m^2)	Fissile	Fertile			
RTE-6	AEC	897.3	1378	60	3.1	4.2	UO_2 BISO UC_2 TRISO $(Th,U)O_2$ BISO UC_2 BISO	ThO_2 BISO ThC_2 BISO	Provide irradiated fuel for HTGR fuel reprocessing demonstrations at ORNL. Test various oxide fuels under HTGR conditions.	Yes	1-6
RTE-7	AEC	252.4	1299	20	0.2	1.2	$(Th,U)O_2$ BISO UC_2 TRISO UO_2 BISO UC_2 BISO	ThC_2 BISO ThO_2 BISO ThC_2 TRISO	↓	Yes	1-6
RTE-8	AEC	897.3	1413	60	3.1	4.2	UC_2 TRISO $(Th,U)O_2$ BISO UC_2 BISO	ThC_2 BISO ThC_2 TRISO	↓	Yes	1-6
PTE-2	GA/AEC	404.4	1182	~18	~0.3	1.9	$(Th,U)C_2$ TRISO	ThC_2 TRISO	Proof-test Fort St. Vrain (FSV) fuel particles and H-327 graphite under representative HTGR conditions.	Yes	
FTE-10	GA	644.9	1320	47	1.7	2.8	$(Th,U)C_2$ TRISO	ThC_2 TRISO	Proof-test FSV fuel particles and rods under representative HTGR conditions.	No	
FTE-16	GA	511.9	1397	40	1.0	2.3	$(Th,U)C_2$ TRISO	ThC_2 TRISO	↓	Yes	
FTE-17	GA	511.9	1107	42	1.1	2.3	$(Th,U)C_2$ TRISO	ThC_2 TRISO	↓	No	

TABLE 1-1 (Continued)

Element I.D.	Sponsored By	Irradiation Time (EFPD)	Maximum Test Conditions				Fuel Particles		Objectives	PIE	Documentation (Ref.)
			Temp (C°)	Burnup Fissile (%)	Burnup Fertile (%)	Fast Fluence (x 10^{25} n/m^2)	Fissile	Fertile			
FPTE-1	GA/UKAEA	252.4	1184	2	NA	1.1	$(U\text{-}238)O_2$ TRISO	None	Test alternative design for GA fuel elements at expected reactor design conditions.	Yes	1-7
FPTE-3	GA/UKAEA	644.9	979	8	NA	2.9	$(U\text{-}238)O_2$ TRISO	None	↓	Yes	1-7
FTE-13	GA/EPRI	511.9	1490			2.3	PuO_2 TRISO $(Th,Pu)O_2$ TRISO $(Th,U)C_2$ TRISO	ThO_2 BISO ThC_2 TRISO	Obtain fabrication experience with Pu fuels, test fuel rod containing Pu particles and rods at representative conditions, and evaluate analytical methods for predicting isotope reaction rates for physics models initially and at end of life for Pu fuels.	Yes	1-8

2. DESCRIPTION OF TEST ELEMENTS

2.1. FUEL TEST ELEMENTS (FTEs), FUEL BED TEST ELEMENTS (FBTEs), RECYCLE TEST ELEMENTS (RTEs)

The FTEs, FBTEs, and RTEs consisted of a bottom connector, a bottom reflector, a stack of three or six fuel bodies, and a top reflector, all partially or entirely enclosed in a graphite sleeve (Fig. 2-1). The test elements had the same external appearance and dimensions as the standard Peach Bottom fuel elements. The FTEs and FBTEs contained three 787-mm (31-in.) long fuel bodies. The RTEs contained six fuel bodies, each of which was 394 mm (15.5 in.) in length. All of the fuel bodies, with the exception of those contained in FTE-18, were fabricated from Great Lakes Carbon Corporation H-327 nuclear-grade graphite.

The fuel bodies had eight (Fig. 2-2), six (Fig. 2-3), or three (Fig. 2-4) fuel holes arranged in a "telephone dial" configuration. Except in FTE-18,* the fuel holes contained fuel rods** or blended beds of fuel particles. Fuel particles and other "spine samples," including the metallic fission product diffusion samples (Section 9), were irradiated in the center hole of many of the fuel bodies. Several types of fuel particles were tested in the test elements. Tables 2-1 and 2-2 identify these fuel particle types and the test elements in which they were irradiated.

Each FTE and FBTE was instrumented with a Chromel/Alumel (C/A) thermocouple and a tungsten/rhenium (W/Re) thermocouple. (FTE-18 had two W/Re thermocouples.) The locations of these thermocouples in the elements are

---

*In FTE-18, fuel particles and graphite were molded together in three fuel zones. Each fuel body was a monolithic structure.

**Fuel particles bonded together by a carbonaceous matrix.

shown in Figs. 2-2 through 2-4. Some of the test elements were located in core locations equipped with purge gas sampling lines. These elements were monitored for fission gas release.

2.2. FORT ST. VRAIN PROOF TEST ELEMENT 2 (PTE-2)

PTE-2 consisted of seven graphite components. From bottom to top, these included a bottom connector, a bottom reflector, four fuel bodies, and a top reflector. Fuel bodies one, three, and four were made from H-327 nuclear-grade graphite. Fuel body two was fabricated from Speer 9567 nuclear-grade graphite. The bottom portion of the test element was cylindrical. The remainder of the element had a hexagonal geometry. Figure 2-5 shows the completed assembly.

Figure 2-6 shows a cross-sectional view of PTE-2. The arrangement of coolant and fuel holes in PTE-2 approximated the geometry of a FSV fuel block. The fuel irradiated in PTE-2 was similar, but not identical, to the fuel being irradiated in the Fort St. Vrain reactor.

PTE-2 included a C/A thermocouple and a W/Re thermocouple for monitoring irradiation temperatures. The locations of these thermocouples are shown in Fig. 2-6.

2.3. FUEL PIN TEST ELEMENTS (FPTEs)

The fuel element contained a single stack of four fuel pins keyed together within a standard Peach Bottom graphite sleeve. Below the pins at the bottom end were a connector and a reflector. Above the pins at the top was a reflector with a handling knob. The fuel pins were maintained concentric in the graphite sleeve by three longitudinal ribs. Each fuel pin consisted of a series of annular fuel compacts stacked around a central graphite tube and surrounded by an outer graphite fuel tube.

The designs of FPTE-1 and FPTE-3 were somewhat different. In FPTE-3, cooling was accomplished by two independent gas streams inside the element

sleeve. Coolant entered the element in the region of the lower reflector via two groups of gas ports drilled through the sleeve. The lower group supplied coolant to a central cooling channel inside the inner graphite tube, and the upper ports supplied coolant to an annular coolant channel formed by the sleeve and the exterior of the fuel pins. In FPTE-1, coolant flow inside the element was through an annular channel only. In addition, the fuel pins in FPTE-1 were shorter than in FPTE-3, resulting in a shorter fueled length. The designs of FPTE-1 and FPTE-3 are shown in Figs. 2-7 through 2-9.

The fuel compacts for the elements consisted of low-enriched UO_2 particles dispersed in a graphite matrix. The particles were 800-μm-diameter UO_2 kernels of 80% to 90% theoretical density, coated with layers of pyrolytic carbon (PyC) and SiC to give a final coated particle size of 1200 μm. The element contained no thorium.

Both elements were instrumented with two thermocouples. Neither element was purged.

TABLE 2-1
FUEL TYPES[a] IRRADIATED IN THE PEACH BOTTOM TEST ELEMENTS

Fissile[b]	Fertile	Test Elements
(4.2 Th,U)O_2	--	RTE-1, -5, -7
(4.0 Th,U)O_2	ThC_2	RTE-2, -4
UO2	ThC_2	RTE-5, -7
(2.0 Th,U)O_2	ThC_2	RTE-1, -2, -4, -5, -6, -7, -8
(2.0 Th,U)O_2	ThO_2	RTE-1, -5, -7
UC2	ThC_2	FTE-1, -2, -5, FBTE-2, -5, RTE-1, -2, -4, -5, -6, -8
UC_2 TRISO	ThC_2	FTE-3, -4, -5, -6, -8, -14, -15, FBTE-3, RTE-1, -2, -4, -5, -6, -7, -8
UO_2	ThO_2	RTE-1, -5, -6, -7
UC_2	ThO_2	RTE-1, -5, -7
UC_2 TRISO	ThC_2 TRISO	FTE-14, -15, RTE-1, -5, -7, -8
(2.0 Th,U)O_2 TRISO	ThC_2	
(2.0 Th,U)C_2	ThC_2	FTE-1, -2, -5, FBTE-1, -5, -6
(2.0 Th,U)C_2 TRISO	ThC_2 TRISO	FTE-1, -2, -5, FBTE-4, -5, PTE-2
(2.75 Th,U)C_2 TRISO	ThC_2	FTE-3, -4, -6, -9
(1.0 Th,U)C_2 TRISO	ThC_2 TRISO	FTE-10, -16, -17
(2.75 Th,U)O_2	ThO_2	FTE-12
(2.75 Th,U)C_2 TRISO	ThC_2 TRISO	FTE-3, -4, -6, -13
UO_2 TRISO	ThO_2	FTE-3, -4, -6, -7, -14, -15, RTE-1
UO_2 TRISO	ThC_2	FTE-14, -15
UC_2 TRISO	ThO_2 TRISO	FTE-14, -15
(1.0 Th,U)O_2 TRISO	ThC_2	FTE-14, -15
UO_2 TRISO	ThO_2 TRISO	FTE-14, -15
UO2 TRISO	ThC_2 TRISO	FTE-14, -15
PuO_2 TRISO	ThO_2	FTE-13
(3.0 Th,Pu)O_2 TRISO	ThO_2	FTE-13
(1.0 Th,U)O_2	None	FTE-18
UO_2 TRISO	None	FPTE-1, -3

[a]All particles are BISO except where noted. See Fig. 2-10 for a description of BISO and TRISO particles.

[b](x.x Th,U): x.x = thorium/uranium ratio.

TABLE 2-2
FUEL TYPES[a] IRRADIATED IN PEACH BOTTOM TEST ELEMENT SPINE SAMPLES

Fissile[b]	Fertile	Test Elements
UC_2	--	FTE-1, -2, -3, -4, -5, -6
UC_2 TRISO	--	FTE-1, -2, -3, -4, -5, -6, -14, -15
UO_2	--	FTE-1, -2, -3, -4, -5, -6, -14, -15
(4.1 Th,U)C_2	--	FTE-1, -2, -3, -4, -5, -6
(1.0 Th,U)C_2	--	FTE-1, -2, -3, -4, -5, -6
(4.1 Th,U)C_2 TRISO	--	FTE-1, -2, -3, -4, -5, -6
(18.0 Th,U)C_2 TRISO	--	FTE-1, -2, -3, -4, -5, -6
(1.0 Th,U)C_2 TRISO	--	FTE-1, -2, -3, -4, -5, -6
(1.0 Th,U)O_2	--	FTE-1, -2, -3, -4, -5, -6
UO_2 TRISO	--	FTE-1, -2, -3, -4, -5, -6, -14, -15
--	ThC_2	FTE-1, -2, -3, -4, -5, -6, -14, -15
--	ThC_2 TRISO	FTE-1, -2, -3, -4, -5, -6
--	ThO_2	FTE-1, -2, -3, -4, -5, -6, -14, -15
--	ThO_2 TRISO	FTE-14, -15
UO_2 TRISO	ThO_2	FTE-1, -2, -3, -4, -5, -6
(1.0 Th,U)C_2 TRISO	ThC_2 TRISO	FTE-1, -2, -3, -4, -5, -6
UO_2	ThO_2	FTE-5
UC_2 TRISO (VSM)	--	FTE-14, -15
UC_2 TRISO (WAR)	--	FTE-14, -15
(1.0 Th,U)O_2 TRISO	--	FTE-14, -15
(2.0 Th,U)O_2 TRISO	--	FTE-14, -15
UCO TRISO (WAR)	--	FTE-14, -15

[a] All particles are BISO except where noted. See Fig. 2-10 for a description of BISO and TRISO particles.

[b] (x.x Th,U): x.x = thorium/uranium ratio.

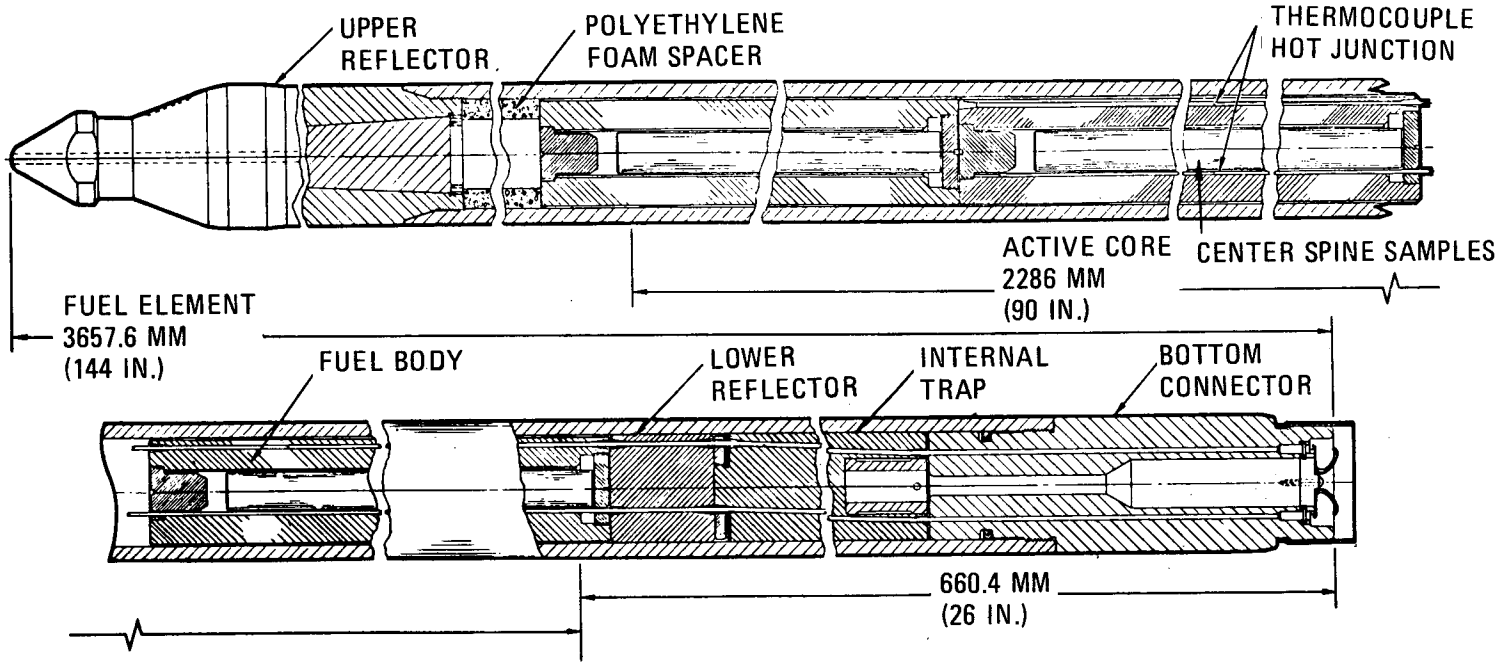

Fig. 2-1. FTE, FBTE, and RTE design

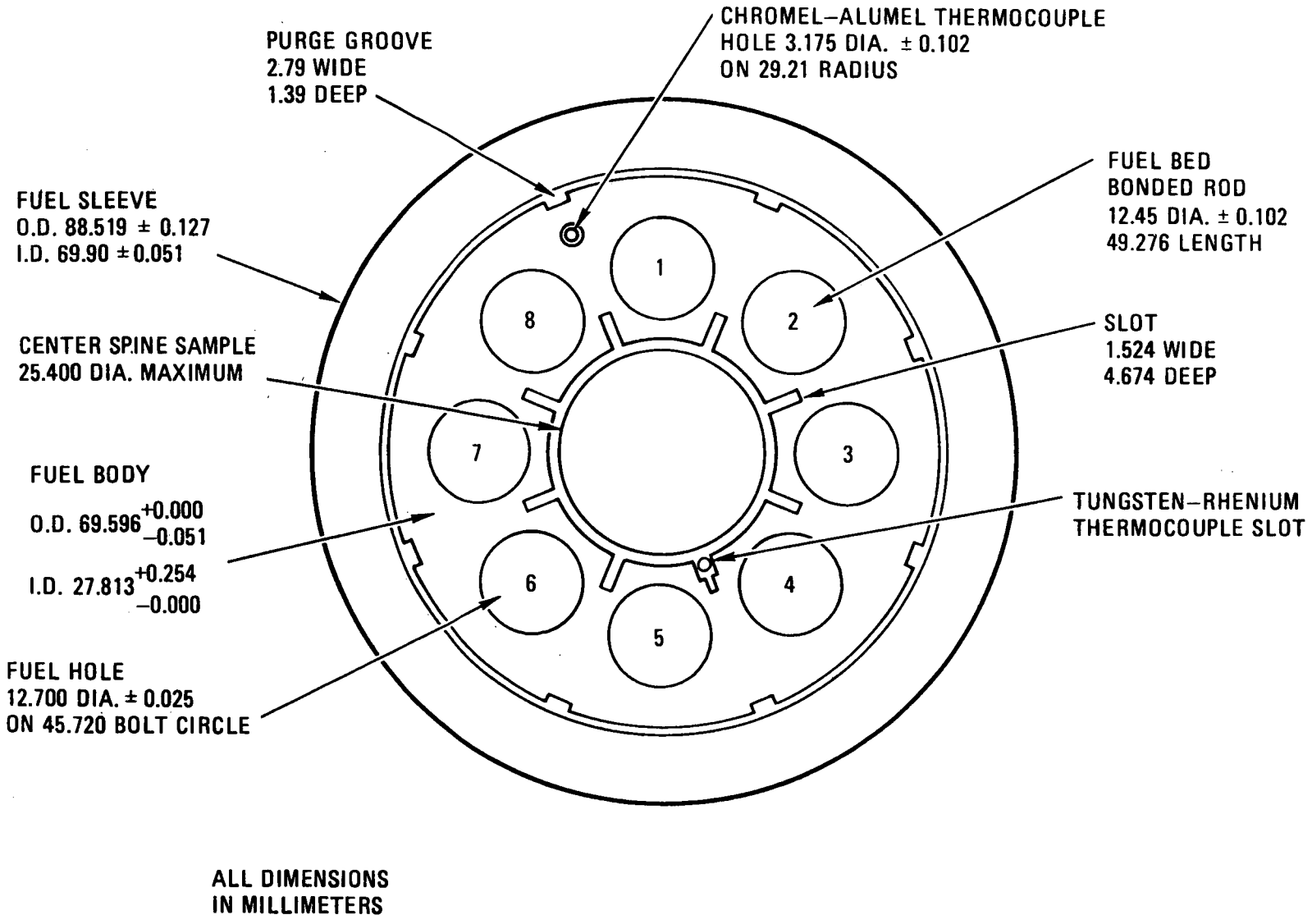

Fig. 2-2. Radial cross-sectional view of an eight-hole telephone dial element

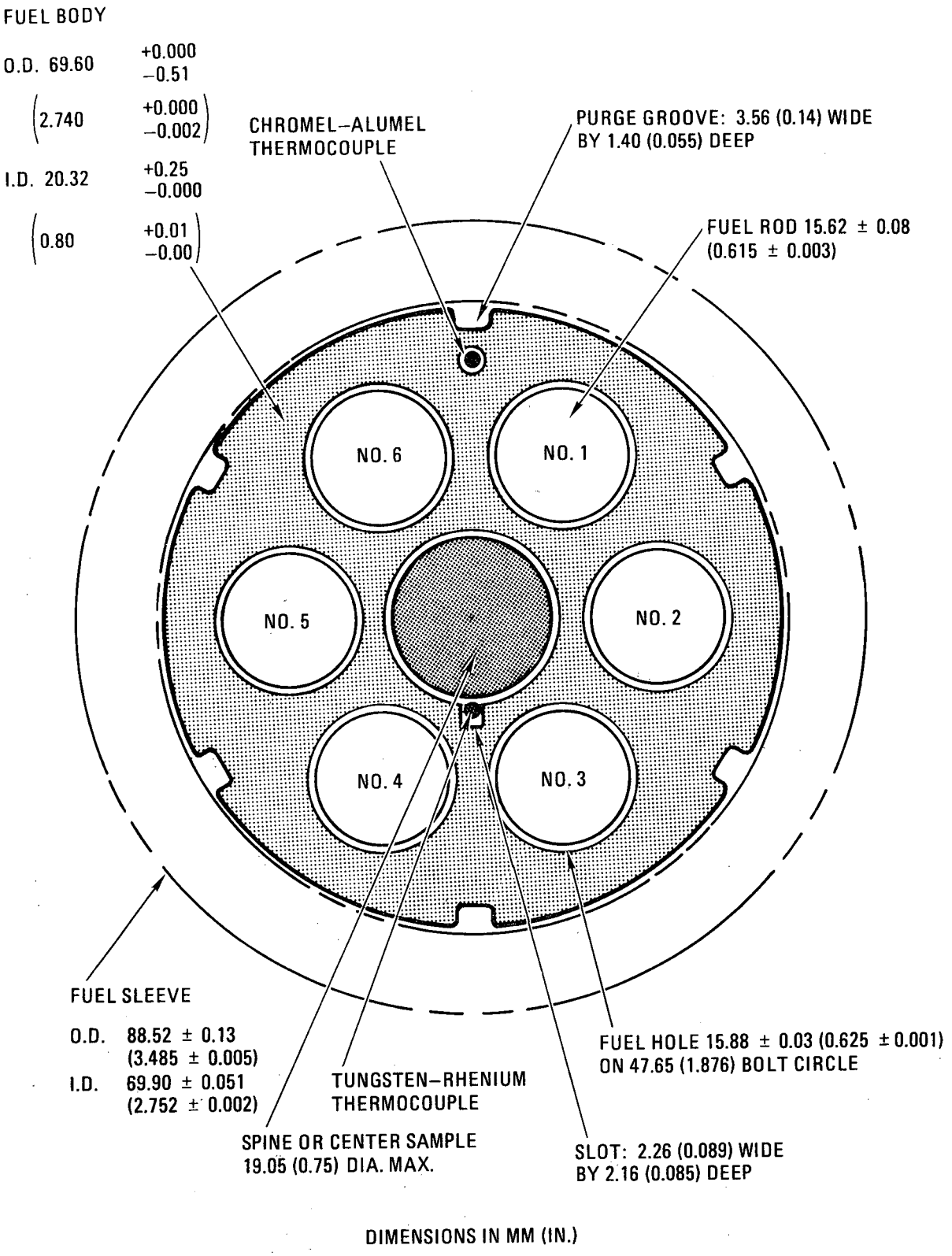

Fig. 2-3. Radial cross-sectional view of a six-hole telephone dial test element

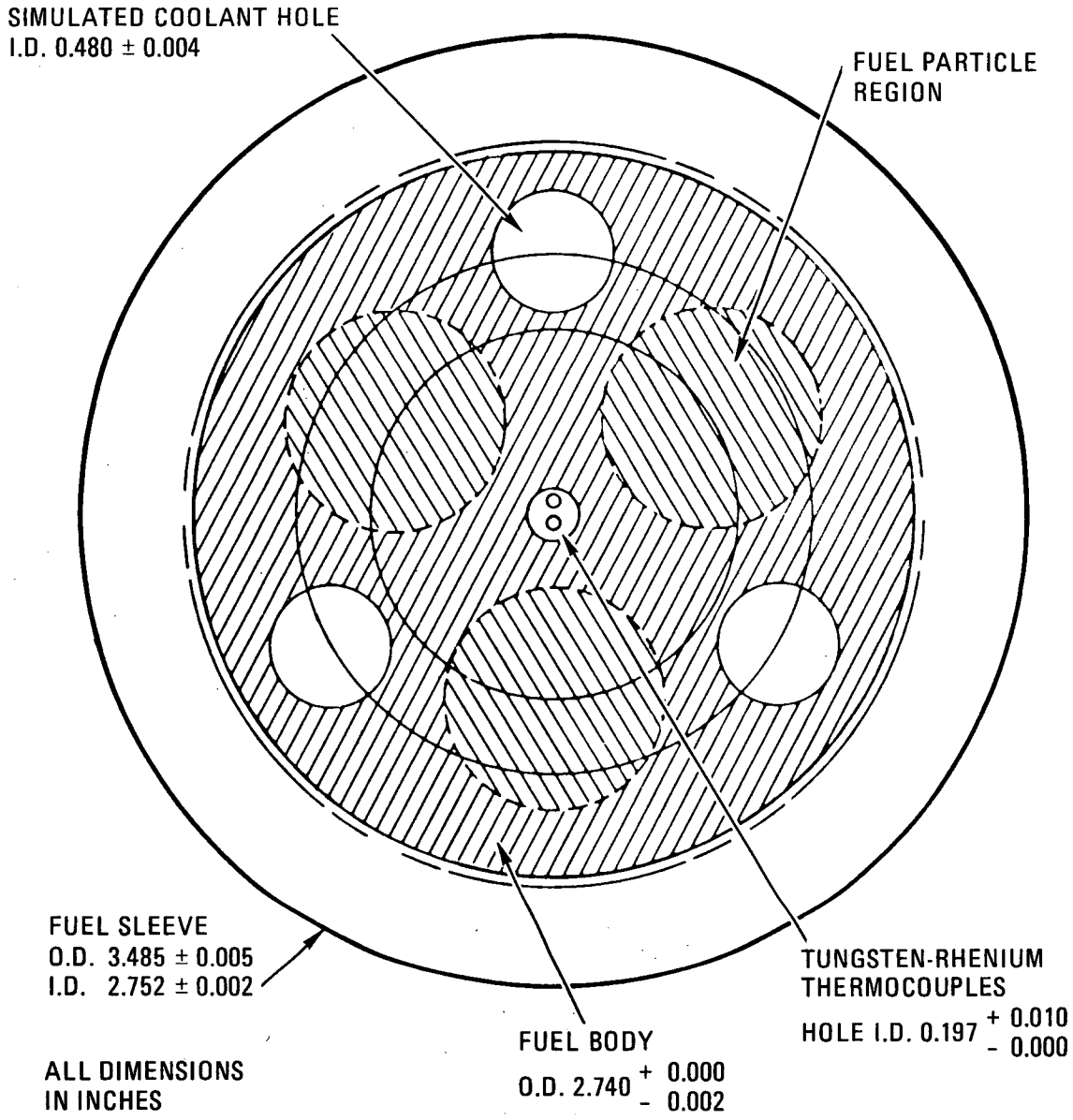

Fig. 2-4. Radial cross-sectional view of FTE-18

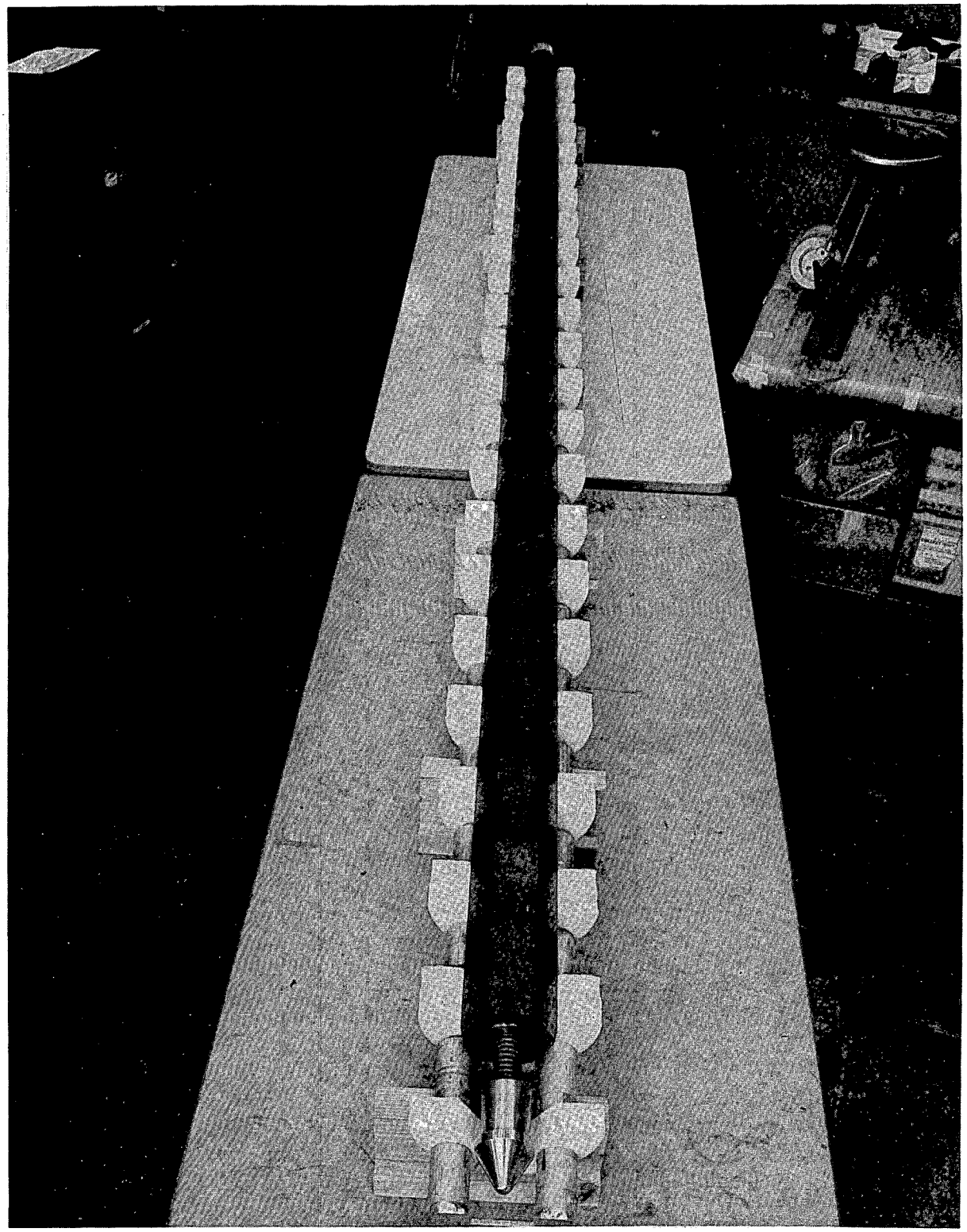

Fig. 2-5. Completed PTE-2 assembly

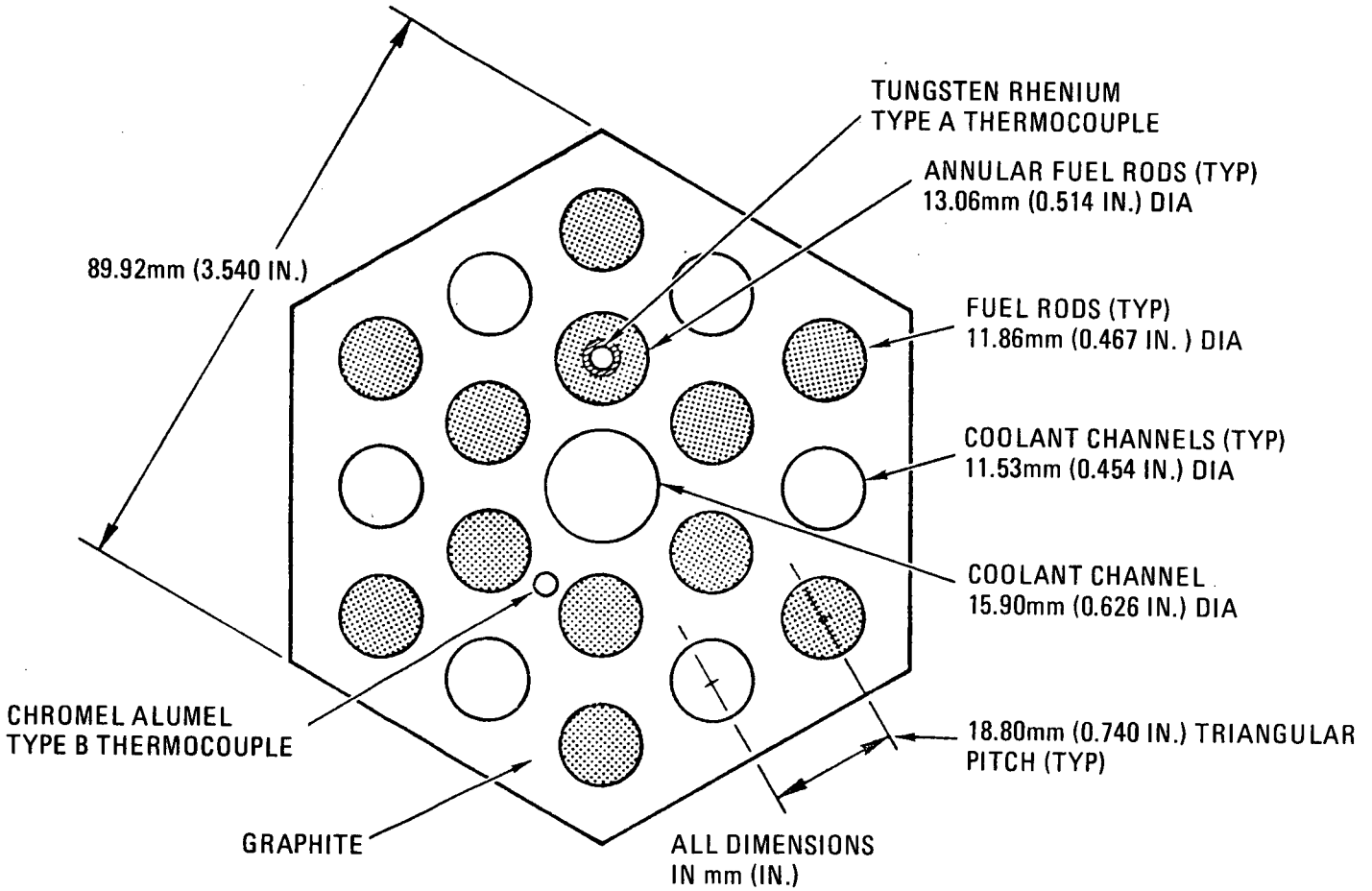

Fig. 2-6. Radial cross-sectional view of PTE-2

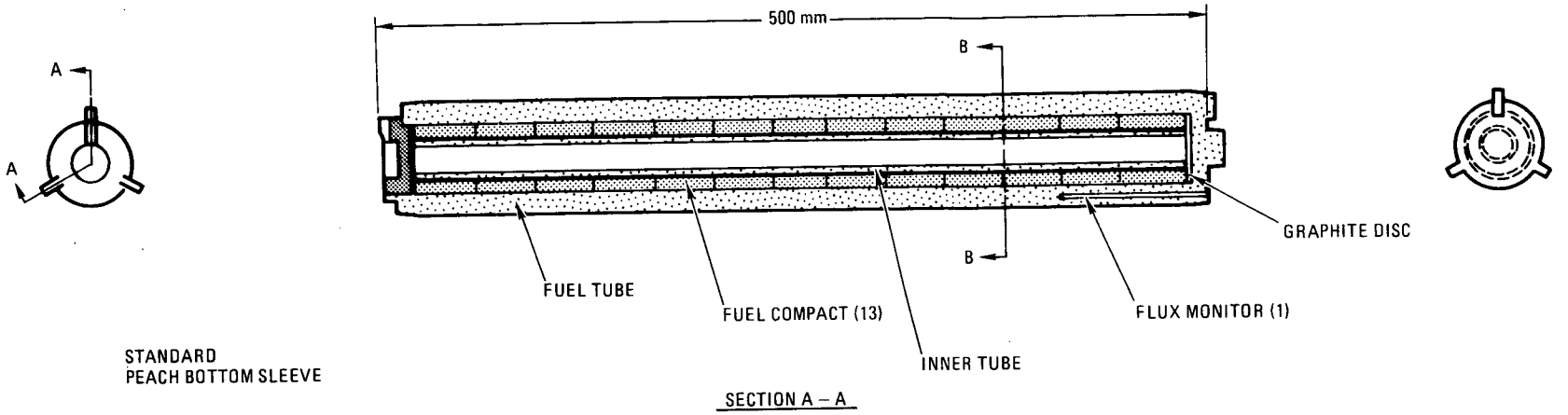

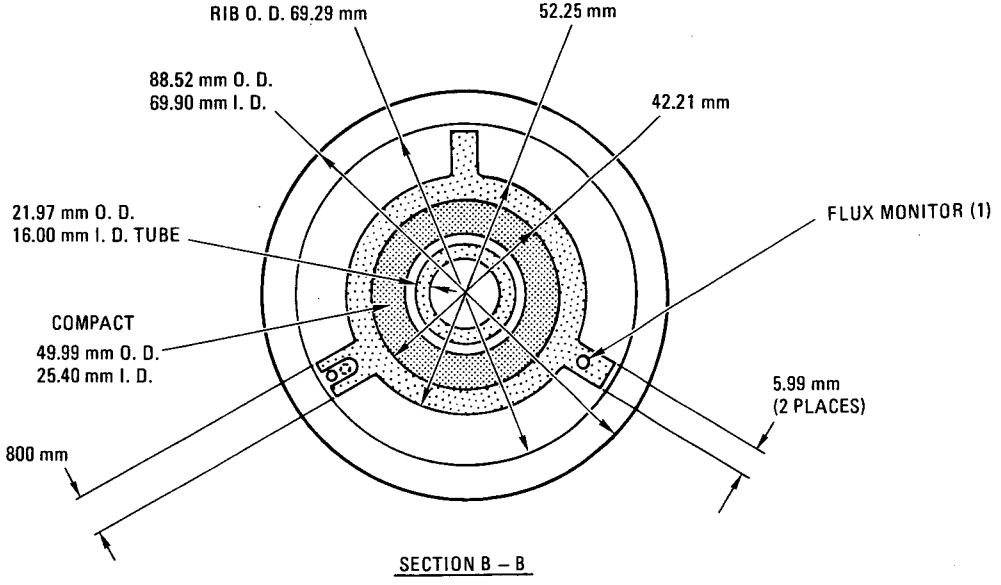

Fig. 2-7. Cross-sectional views of FPTE-1

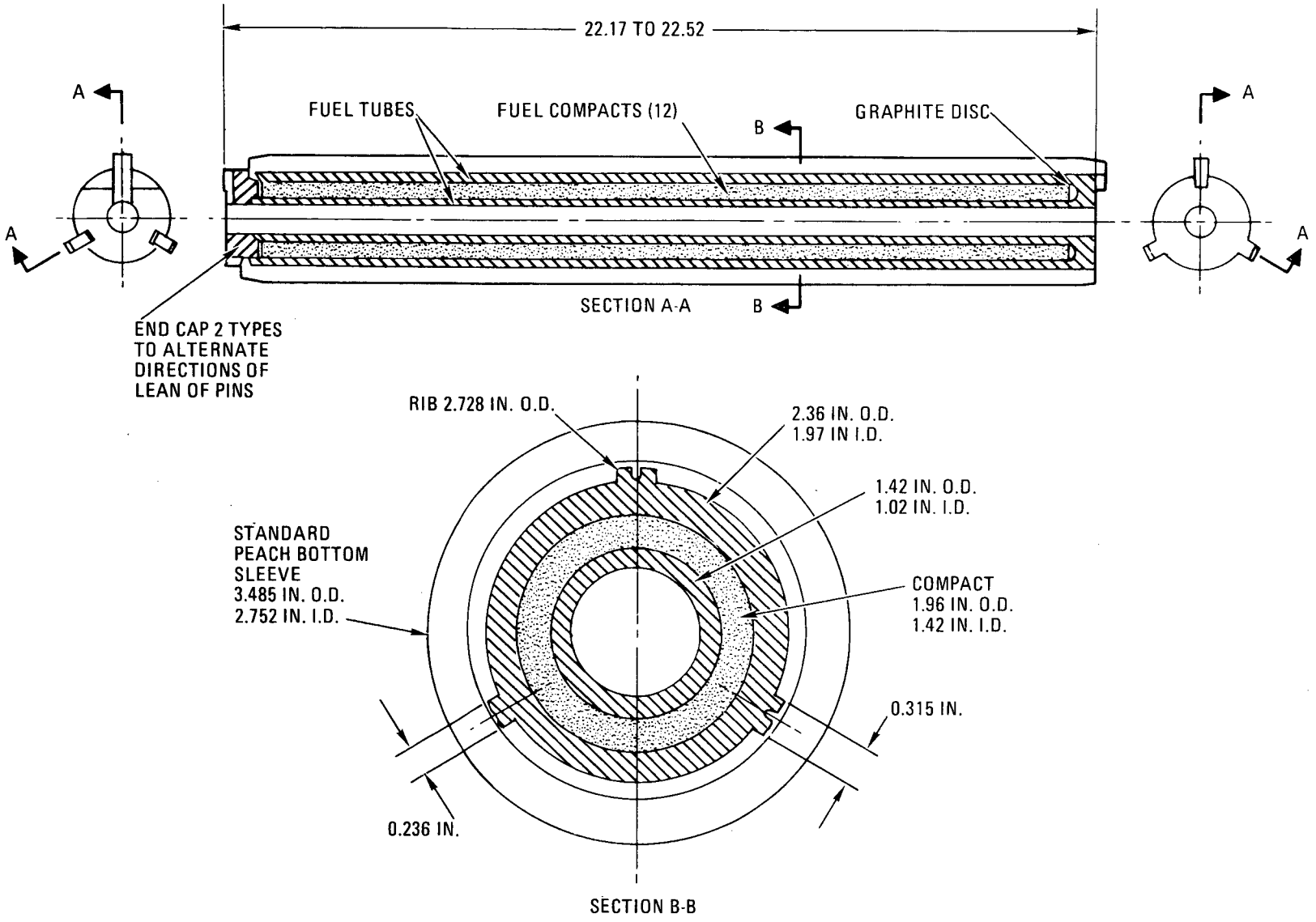

Fig. 2-8. Cross-sectional views of FPTE-3

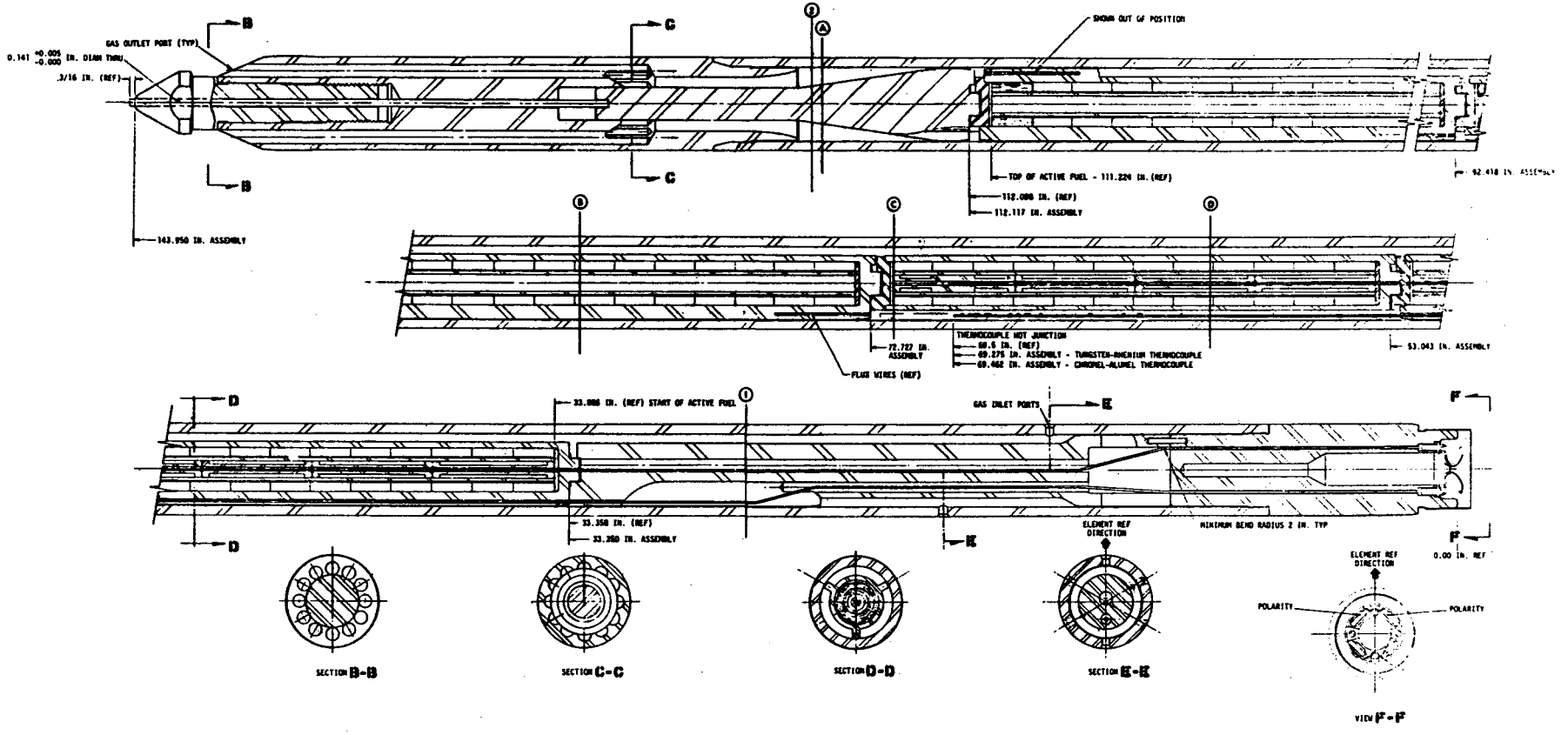

Fig. 2-9. Fuel pin test element assembly

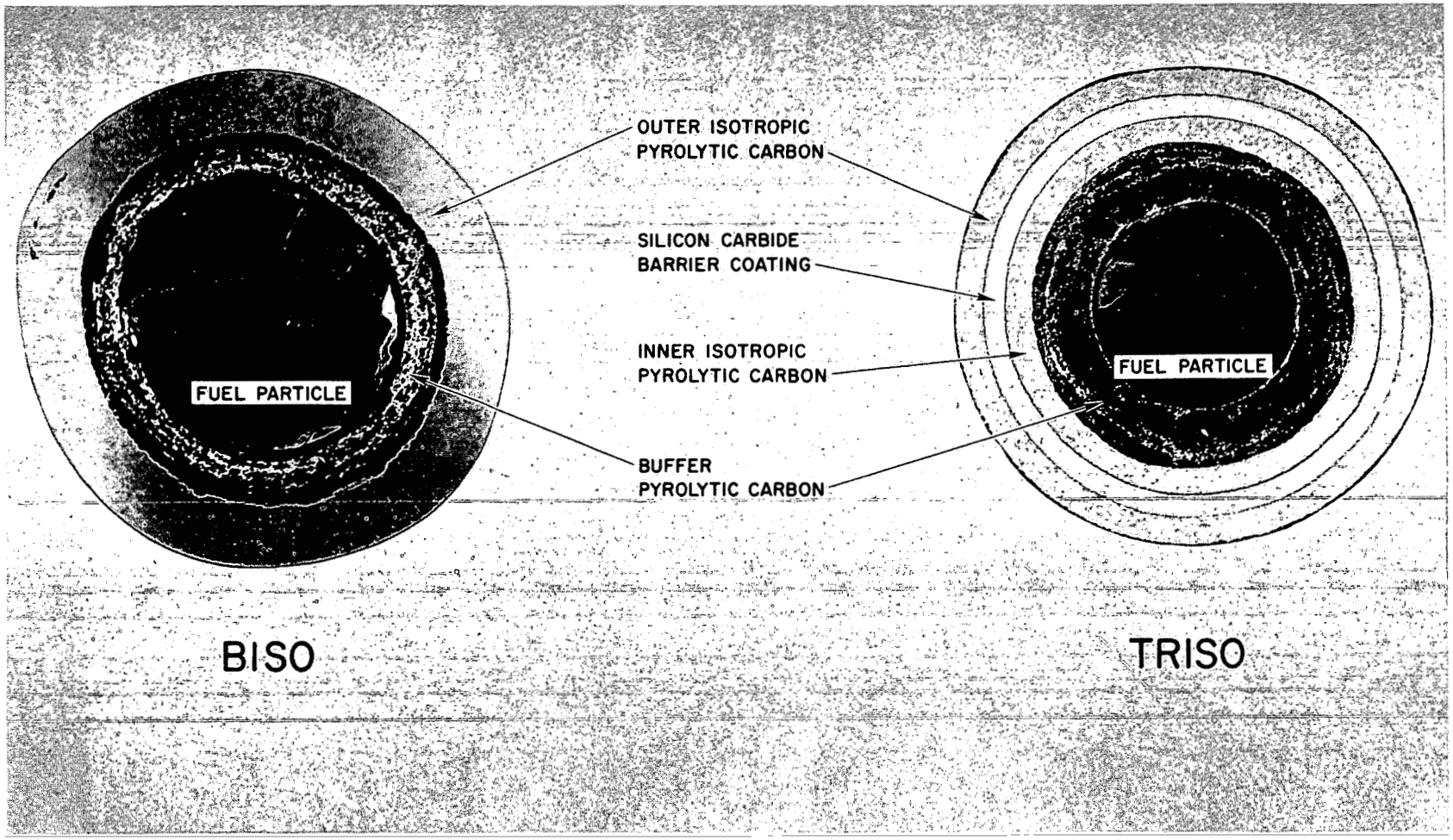

Fig. 2-10. Cross-sectional views of TRISO- and BISO-coated particles

3. IRRADIATION CONDITIONS

3.1. COMPUTER SIMULATION OF TEST ELEMENT IRRADIATIONS

Computer simulations of the test element irradiations were performed using the GAUGE, FEVER, TREVER, and TAC-2D computer codes. A brief description of these codes is given below.

GAUGE (Ref. 3-1) is a two-dimensional, four-group diffusion-depletion code which collapses a reactor core into one layer and calculates nuclide densities as a function of time and radial core location. The GAUGE code was used to calculate radial power distributions for the Peach Bottom core.

FEVER (Ref. 3-2) is a one-dimensional, multigroup diffusion-depletion code which calculates nuclide densities in fuel regions or subregions as a function of time and axial core location. The FEVER code was used to calculate axial power profiles for the Peach Bottom core.

TREVER (Ref. 3-3) is a one-dimensional heat transfer code for calculating radial temperature profiles in HTGR fuel elements. The code repeats these calculations at any number of specified axial locations, thereby generating axial temperature profiles as well. The TREVER versions used for the thermal analyses of Peach Bottom test elements were modified versions of the large HTGR (LHTGR) TREVER code, which has since been replaced by the SURVEY (Ref. 3-4) code for core performance evaluations. Several Peach Bottom TREVER versions were required to model the various test element geometries.

TAC-2D (Ref. 3-5) is two-dimensional, finite difference heat transfer code which calculates the radial or axial heat transfer characteristics

for specific geometries. TAC-2D was used to generate the temperature shaping factors required by TREVER to account for the influence of geometry on the heat transfer characteristics of the test elements.

The reactor operating history for Peach Bottom Core 2 is detailed in Ref. 3-6. For the computer simulation of Core 2, the irradiation history was divided into 22 periods of steady state operation. Figures 3-1 and 3-2 show the core operating parameters used in the TREVER thermal analyses.

3.2. FEEDBACK OF NUCLEAR MEASUREMENTS INTO THERMAL CALCULATIONS

As discussed in Section 4.1.2, measured fission product distributions can be used to establish axial power and fluence profiles for individual fuel elements. Since power profiles can vary significantly from element to element and since physics calculations do not exactly predict axial power distributions (Section 4.5 and Ref. 3-7), measured power profiles should be fed back into thermal calculations to obtain more reliable temperatures. Theoretically, thermal calculations could be further improved by correcting element average power predictions using factors obtained from comparison of measured (Section 4.2) and predicted fuel particle burnup. A brief discussion of a method for feeding back nuclear measurements into thermal calculations is presented below.

Predicted axial power profiles can be corrected using factors obtained from a comparison of predicted and measured time-averaged axial power profiles:

$$(APF_{z,t})_{corr.} = (APF_{z,t})_{pred.} \times f_z \ ,$$

where $APF_{z,t}$ is the axial power factor at axial location z and time t and

$$f_z = \frac{(APF_{z,\bar{t}})_{meas}}{(APF_{z,\bar{t}})_{pred}} \ .$$

In addition, measured end-of-life (EOL) power distributions can be directly substituted for predicted EOL distributions.

Element average power predictions can be corrected using factors obtained via comparison of measured and calculated fuel burnup and time-averaged axial power profiles. The correction factor is given by the equation

$$CF = \frac{(CPF)_{meas}}{(CPF)_{pred}} = \frac{(F_z)_{meas}}{(F_z)_{pred}} \times \frac{(APF_{z,\bar{t}})_{pred}}{(APF_{z,\bar{t}})_{meas}} ,$$

where CPF = element average power,

F_z = composite fuel burnup at axial location z,

$APF_{z,\bar{t}}$ = time-averaged axial power factor at axial location z.

The above equation is based on the direct proportionality of fuel particle burnup and power, which at a given axial location is equal to the product of the element average power and the local axial power factor.

Successful application of the concept described above requires that the uncertainty in the nuclear measurements be less than the uncertainty in the predictions, which has been established to be approximately ±10% (1σ) (Ref. 3-7). This concept was applied to the analyses of FTE-14 and FTE-15 (Ref. 3-8), the last of the Peach Bottom test elements to undergo extensive PIE and evaluation. In FTE-14, for which an 8% underprediction in the element average power was established and corrected, the agreement between the predicted and measured temperatures for the W/Re thermocouple (Section 5) was within 1° C on a time-averaged basis and within ±14° C (1σ) for all TREVER time intervals. Unfortunately, the other three thermocouples in FTE-14 and FTE-15 failed, preventing further comparison of calculated and measured temperatures.

FTE-18 represents a second case in which feedback of nuclear measurements improved the quality of temperature calculations. Gamma spectrometry performed by KFA (Ref. 3-9) on FTE-18 confirmed the conclusion of the thermal analysis by GA (Ref. 3-10) that the power for the element had been underpredicted. Temperatures for FTE-18 have been recalculated using the gamma spectrometric data and are presented in Appendix A of this report.

3.3. SUMMARY OF IRRADIATION CONDITIONS

Key parameters for the Peach Bottom test element irradiations are summarized in Tables 3-1 and 3-2. Temperature and neutron fluences are presented in Table 3-1, and fuel particle burnups are given in Table 3-2. Figures 3-3 through 3-8 show typical radial temperature profiles for each of the test element geometries irradiated in Peach Bottom Core 2.

REFERENCES

3-1. Wagner, M. R., "GAUGE, a Two-Dimensional Few Group Neutron Diffusion Depletion Program for a Uniform Triangular Mesh," USAEC Report GA-8307, March 1968.

3-2. Todt, F. W., and L. J. Todt, "FEVER/M1, a One-Dimensional Depletion Program for Reactor Fuel Cycle Analyses," GA unpublished data, October 22, 1969.

3-3. Saurwein, J. J., "Peach Bottom Test Element Thermal Analyses with TREVER Code," GA unpublished data.

3-4. Georghiou, D. L., "SURVEY, A Computer Code for the Thermal and Fuel Performance Analysis of High-Temperature Gas-Cooled Reactors, User's Manual," GA unpublished data, November 1978.

3-5. Peterson, J. F., "TAC-2D, A General Purpose Two-Dimensional Heat Transfer Computer Code, User's Manual," USAEC Report GA-8868, September 6, 1969.

3-6. Scheffel, W. J., N. L. Baldwin, and R. W. Tomlin, "Operating History Report for the Peach Bottom HTGR, Volume I, Reactor Operating History," ERDA Report GA-A13907, August 31, 1976.

3-7. Saurwein, J. J., and C. F. Wallroth, "Nuclear and Thermal Design Verification for the Peach Bottom High-Temperature Gas-Cooled Reactor," DOE Report GA-A14726, September 1978.

3-8. Holzgraf, J. F., et al., "Postirradiation Examination and Evaluation of Peach Bottom Fuel Test Elements FTE-14 and FTE-15," DOE Report GA-A13944, February 1979.

3-9. Schröder, R., et al., "PBR-B1 Gammaspektrometrische Nachunterguchungen," Kernforschungsanlage Jülich, Institut für Reaktorwerkstoffe, IRW-TN-23/78, February 13, 1979.

3-10. Wallroth, C. F., et al., "Postirradiation Examination and Evaluation of Peach Bottom Molded Fuel Test Element FTE-18," Report GA-A13699, June 1, 1976.

TABLE 3-1
IRRADIATION TEMPERATURES AND FAST NEUTRON EXPOSURES FOR PEACH BOTTOM TEST ELEMENTS

Element	Body No.	Temperature (°C)																Average Fluence ($\times 10^{25}$ n/m^2)	
		Envelope								Time Averaged									
		Fuel Extremes		Fuel		Body		Sleeve		Fuel		Body		Sleeve		Coolant			
		Peak	Min.	Max.[a]	Min.[b]	Max.[a]	Min.[b]	Max.[a]	Min.[b]	Avg[c]	RMS[d]	Avg[c]	RMS[d]	Avg[c]	RMS[d]	Avg[c]	RMS[d]	Fast	Thermal
FTE-1	1	1167	488	959	687	761	668	623	537	851	153	741	124	594	89	405	42	0.9	1.1
	2	1316	819	1272	891	1018	865	850	710	1118	36	978	35	801	37	570	48	1.1	1.4
	3	1251	819	1161	875	998	858	900	761	1052	50	962	33	851	16	709	30	0.7	0.9
Element peak/min., mean,[e] RMS[f]		1316	488							1007[e]	148[f]	894[e]	133[f]	749[e]	125[f]	561[e]	124[f]	0.9	1.1
FTE-2	1	1077	458	882	627	719	612	597	501	769	129	679	105	554	75	400	36	1.3	1.2
	2	1212	737	1163	802	948	782	786	651	1004	38	889	34	733	34	544	42	1.7	1.6
	3	1157	748	1066	795	926	782	820	700	956	44	882	30	784	17	667	27	1.0	1.0
Element peak/min., mean, RMS		1212	748							910	130	817	118	690	110	537	115	1.3	1.3
FTE-3	1	1096	471	914	651	735	599	601	495	770	125	661	97	542	71	385	32	0.4	0.4
	2	1167	740	1134	808	922	749	767	630	970	29	839	28	702	31	514	38	0.5	0.6
	3	1103	728	1016	785	886	746	794	668	909	42	828	26	740	16	625	24	0.3	0.4
Element peak/min., mean, RMS		1167	471							883	114	776	101	661	97	508	103	0.4	0.5
FTE-4	1	1146	498	947	727	757	657	619	509	822	136	692	105	554	74	385	33	1.4	1.9
	2	1280	851	1219	938	984	867	817	679	1067	39	906	39	737	40	526	43	1.9	2.8
	3	1236	846	1137	931	968	871	858	760	1021	53	911	33	798	19	658	30	1.3	1.8
Element peak/min., mean, RMS		1280	498							970	138	836	123	896	115	523	117	1.5	2.1
FTE-5	1	1185	464	959	612	757	541	618	436	824	127	684	98	553	66	399	33	2.6	3.6
	2	1379	633	1297	752	1046	669	862	542	1095	50	922	43	741	43	536	42	3.7	5.3
	3	1272	607	1167	779	1022	712	909	614	1033	63	917	40	798	23	662	29	2.5	3.5
Element peak/min., mean, RMS		1379	464							984	145	841	129	697	115	532	113	2.9	4.1
FTE-6	1	1196	482	1021	660	800	600	657	487	858	132	713	103	568	73	385	33	2.1	2.6
	2	1382	753	1302	832	1044	761	857	630	1103	42	930	42	750	42	521	43	2.8	3.8
	3	1429	747	1347	811	1130	763	978	677	1075	57	949	36	819	21	656	32	2.0	2.5
Element peak/min., mean, RMS		1429	482							1012	142	864	127	712	117	521	116	2.3	3.0
FTE-7	1	1333	486	1089	679	849	597	688	464	919	161	763	124	601	84	403	36	1.7	2.8
	2	1481	808	1446	878	1134	780	945	596	1213	38	1020	36	805	37	551	45	2.5	4.1
	3	1374	719	1279	826	1089	755	969	644	1096	63	968	40	837	20	681	29	2.3	2.7
Element peak/min., mean, RMS		1481	486							1076	158	917	136	748	118	545	119	2.2	3.2
FTE-8	1	1154	448	954	604	762	542	626	438	814	134	689	105	557	72	399	33	1.7	2.9
	2	1283	699	1253	763	1010	689	851	551	1058	32	905	32	735	60	536	41	2.4	4.2
	3	1209	1041	1138	743	989	691	888	604	985	47	884	29	779	17	656	27	2.2	2.7
Element peak/min., mean, RMS		1283	448							952	132	826	117	690	107	531	110	2.1	3.2
FTE-9	1	1108	474	946	653	740	584	617	474	789	125	663	97	541	68	392	32	2.0	2.5
	2	1257	752	1216	826	973	759	808	626	1028	35	874	35	718	37	527	42	2.7	3.8
	3	1252	743	1180	820	999	777	874	693	998	54	891	34	783	21	653	29	2.0	2.4
Element peak/min., mean, RMS		1257	474							939	134	809	121	681	112	524	112	2.2	2.9
FTE-10	1	1202	477	1004	681	792	610	647	493	872	149	731	118	587	82	409	39	1.8	2.6
	2	1320	886	1289	955	1136	904	753	582	1115	29	1019	26	658	26	530	28	2.6	3.9
	3	1287	793	1215	866	1027	807	894	707	1019	50	903	30	784	17	640	32	2.4	2.6
Element peak/min., mean, RMS		1320	477							1002	136	884	139	676	96	526	100	2.2	3.0
FTE-12	1	1166	473	978	671	774	603	637	487	818	133	693	105	561	72	398	32	1.8	2.4
	2	1311	798	1273	875	1032	795	850	648	1062	32	908	32	739	35	531	40	2.6	3.7
	3	1277	757	1204	824	1025	777	897	690	990	48	888	30	779	17	650	26	2.4	2.4
Element peak/min., mean, RMS		1311	473							957	132	830	117	693	106	526	108	2.2	2.8
FTE-13	1	1146	491	864	763	704	676	583	530	814	130	690	103	566	73	401	35	1.6	2.2
	2	1490	709	1154	1041	970	941	725	673	1098	85	955	85	699	32	534	37	2.2	3.4
	3	1234	787	1031	945	901	876	796	757	988	43	888	26	776	16	655	30	1.6	2.2
Element peak/min., mean, RMS		1490	491							967	150	844	138	677	102	530	109	1.8	2.6

TABLE 3-1 (Continued)

Element	Body No.	Temperature (°C)																Average Fluence ($\times 10^{25}$ n/m^2)	
		Envelope								Time Averaged									
		Fuel Extremes		Fuel		Body		Sleeve		Fuel		Body		Sleeve		Coolant			
		Peak	Min.	Max.[a]	Min.[b]	Max.[a]	Min.[b]	Max.[a]	Min.[b]	Avg[c]	RMS[d]	Avg[c]	RMS[d]	Avg[c]	RMS[d]	Avg[c]	RMS[d]	Fast	Thermal
FTE-14	1	1278	533	1037	689	797	652	657	530	842	138	717	108	575	76	398	36	1.1	1.2
	2	1574	896	1432	997	1146	942	886	719	1199	62	1037	62	783	41	548	45	1.4	1.8
	3	1480	942	1393	1036	1179	992	934	782	1196	56	1074	45	840	19	681	29	1.0	1.1
Element peak/min., mean, RMS		1574	533							1079	192	943	178	733	125	542	121	1.1	1.4
FTE-15	1	1337	519	1071	678	806	612	669	471	846	137	700	104	562	73	390	32	1.5	1.9
	2	1624	848	1481	958	1170	878	899	618	1193	59	1020	60	763	38	526	41	2.0	3.1
	3	1491	855	1373	980	1158	928	905	678	1153	58	1038	45	805	19	648	27	1.6	1.9
Element peak/min., mean, RMS		1624	519							1064	181	919	172	710	117	521	111	1.7	2.3
FTE-16	1	1229	496	1029	689	832	633	672	505	848	142	723	113	576	79	407	39	1.5	2.1
	2	1397	784	1241	877	1089	836	760	580	1067	40	970	39	659	31	525	26	2.2	3.2
	3	1259	740	1150	793	993	751	863	668	974	48	875	29	759	16	632	31	1.6	2.1
Element peak/min., mean, RMS		1397	496							963	127	856	125	665	90	521	97	1.8	2.5
FTE-17	1	978	440	832	591	679	531	575	445	686	97	592	77	500	56	394	30	1.4	2.2
	2	1107	688	1074	759	896	691	760	583	884	30	772	32	654	34	519	38	2.0	3.4
	3	1054	695	1005	750	886	707	803	644	853	31	781	19	711	16	629	24	2.0	2.2
Element peak/min., mean, RMS		1107	440							808	106	715	100	622	97	514	101	1.8	2.6
FTE-18	1	1229	644	1090	719	909	681	611	477	900	87	795	65	536	25	376	7	1.6	1.9
	2	1448	837	1372	891	1140	834	764	572	1129	110	988	87	658	37	446	10	2.1	3.0
	3	1546	957	1515	983	1280	920	885	662	1251	126	1101	103	757	48	532	19	2.3	3.4
	4	1562	1013	1559	1020	1337	960	972	742	1295	133	1152	111	833	58	618	28	2.3	3.3
	5	1571	1006	1567	1015	1351	965	1024	784	1280	136	1153	114	883	67	696	38	2.0	2.7
	6	1558	984	1514	992	1322	952	1042	803	1224	127	1120	107	908	72	756	47	1.3	1.8
Element peak/min., mean, RMS										1180	121	1052	99	762	54	570	135		
RTE-1	1	1140	540	942	674	722	583	587	453	823	102	676	74	539	48	369	15	1.7	2.2
	2	1480	751	1334	865	1013	740	781	548	1131	56	917	48	701	36	436	23	2.7	3.8
	3	1640	877	1505	979	1170	848	905	636	1271	34	1048	31	809	28	521	25	3.0	4.4
	4	1640	934	1505	1016	1199	894	957	696	1291	33	1086	26	868	22	607	24	3.0	3.3
	5	1449	896	1351	982	1115	871	948	720	1202	48	1035	34	873	22	681	18	2.6	3.5
	6	1230	826	1176	875	1017	806	911	711	1062	20	955	14	851	14	733	12	1.7	2.2
Element peak/min., mean, RMS		1640	540							1130	158	953	140	774	122	558	131	2.4	3.4
RTE-2	1	888	451	777	534	636	524	537	438	664	78	592	62	490	41	369	13	1.7	1.9
	2	1276	730	1221	806	914	716	726	567	1045	50	835	41	653	31	429	20	2.8	3.2
	3	1260	722	1223	765	968	744	804	609	1016	29	887	26	714	24	502	21	3.1	3.6
	4	1392	861	1352	891	1065	818	876	677	1167	30	978	24	794	21	576	20	2.9	3.5
	5	1377	745	1326	780	1084	766	920	669	1044	34	940	27	801	20	641	16	2.4	2.7
	6	1234	775	1182	800	1008	762	887	683	1005	29	905	20	802	14	689	11	1.5	1.8
Element peak/min., mean, RMS		1392	451							990	162	856	131	709	115	534	114	2.4	2.8
RTE-4	1	988	519	842	638	663	584	544	474	762	106	640	76	519	51	372	16	1.1	1.2
	2	1118	668	1063	743	842	722	683	578	931	52	811	44	646	35	444	24	1.8	2.0
	3	1262	788	1226	837	981	813	794	662	1066	30	931	28	751	27	531	25	1.9	2.2
	4	1327	939	1297	969	1054	892	889	740	1188	27	1017	23	835	22	616	23	1.8	2.1
	5	1307	900	1262	951	1037	881	905	761	1158	38	1005	27	861	20	688	18	1.4	1.6
	6	1075	805	1052	825	940	814	869	745	976	19	913	15	831	14	741	12	0.9	1.1
Element peak/min., mean, RMS		1327	519							1014	154	886	136	740	126	565	132	1.5	1.7
RTE-5	1	946	471	825	601	640	526	533	426	729	79	601	56	494	37	366	13	2.3	2.8
	2	1240	654	1143	756	869	650	694	505	987	49	798	41	630	32	426	21	3.7	5.0
	3	1314	720	1242	801	968	690	784	563	1077	29	885	26	713	24	501	22	4.1	5.7
	4	1393	759	1291	858	1025	747	849	628	1131	35	948	29	782	25	579	22	4.0	5.5
	5	1322	812	1230	865	999	768	860	662	1089	35	937	25	804	20	649	18	3.4	4.5
	6	1225	786	1134	841	962	781	854	688	1016	31	909	21	810	15	703	13	2.1	2.9
Element peak/min., mean, RMS		1393	471							1005	141	846	126	706	117	537	120	3.3	4.4

TABLE 3-1 (Continued)

Element	Body No.	Temperature (°C)																Average Fluence ($\times 10^{25}$ n/m^2)	
		Envelope								Time Averaged									
		Fuel Extremes		Fuel		Body		Sleeve		Fuel		Body		Sleeve		Coolant			
		Peak	Min.	Max.[a]	Min.[b]	Max.[a]	Min.[b]	Max.[a]	Min.[b]	Avg[c]	RMS[d]	Avg[c]	RMS[d]	Avg[c]	RMS[d]	Avg[c]	RMS[d]	Fast	Thermal
RTE-6	1	944	505	866	614	669	551	560	442	732	78	606	56	490	36	366	13	2.4	3.0
	2	1173	701	1118	743	872	651	697	505	956	46	790	38	624	31	426	20	3.8	5.2
	3	1378	808	1341	846	1041	729	824	593	1141	32	938	29	746	27	505	25	4.1	5.9
	4	1293	766	1260	804	1024	720	855	615	1108	26	946	23	748	22	587	21	4.0	5.7
	5	1266	782	1227	811	1014	740	879	646	1084	34	950	25	814	20	656	18	3.5	4.6
	6	1209	830	1161	860	983	803	873	699	1041	30	932	21	828	15	712	14	2.3	3.0
Element peak/min., mean, RMS		1378	505							1010	145	860	131	716	121	542	124	3.4	4.6
RTE-7	1	952	496	792	606	623	550	517	454	717	94	606	68	498	46	368	15	0.7	0.7
	2	1198	716	1095	798	839	712	672	568	979	53	806	43	641	35	435	22	1.1	1.1
	3	1286	826	1200	878	942	790	763	642	1083	29	903	27	730	25	515	23	1.1	1.2
	4	1299	867	1234	902	982	822	816	689	1107	25	942	21	786	20	593	21	1.1	1.2
	5	1222	828	1164	879	964	817	832	712	1060	33	932	24	808	19	659	16	0.8	0.9
	6	1091	797	1040	825	906	785	820	712	973	21	888	15	803	13	707	11	0.5	0.6
Element peak/min., mean, RMS		1299	496							986	140	846	122	711	115	546	121	0.9	1.0
RTE-8	1	937	481	807	568	656	550	552	438	681	75	607	60	498	40	367	13	2.4	3.0
	2	1170	654	1114	697	875	629	699	490	921	46	775	40	615	31	426	20	3.8	5.2
	3	1287	766	1253	796	986	687	802	559	1072	29	883	26	710	24	500	22	4.2	5.9
	4	1413	847	1374	894	1086	772	881	644	1187	29	988	25	806	23	582	24	4.1	5.8
	5	1225	771	1192	796	1016	739	889	647	1067	31	945	24	812	20	657	18	3.6	4.7
	6	1164	790	1126	820	972	760	883	675	1020	24	920	19	821	16	713	13	2.4	3.0
Element peak/min., mean, RMS		1413	481							991	165	853	133	710	123	541	124	3.4	4.6
FBTE-1	1	1147	667	989	649	756	581	629	475	831	132	685	99	556	68	397	31	2.5	3.1
	2	1334	714	1278	833	991	738	819	616	1084	60	898	37	732	37	526	40	3.6	4.2
	3	1352	942	1283	791	1049	746	918	664	1029	67	899	37	785	24	648	28	3.0	3.1
Element peak/min., mean, RMS		1352	667							981	143	827	120	691	109	524	108	3.1	3.6
FBTE-2	1	1220	478	1012	653	770	572	627	460	849	137	698	104	563	71	398	32	2.5	3.3
	2	1366	685	1324	808	1035	707	841	581	1103	58	920	38	746	38	531	41	3.6	5.0
	3	1335	678	1246	800	1030	751	892	663	1044	68	916	38	797	24	655	28	3.0	3.2
Element peak/min., mean, RMS		1336	478							999	144	844	124	702	111	528	110	3.0	3.8
FBTE-3	1	1177	442	966	591	778	528	635	429	812	132	683	103	553	69	400	33	2.5	3.8
	2	1326	663	1292	718	1057	643	885	527	1064	37	903	36	735	38	539	43	3.6	5.5
	3	1260	651	1190	741	1048	681	937	597	1014	49	904	31	795	21	667	29	3.0	3.6
Element peak/min., mean, RMS		1326	442							963	138	830	123	694	113	535	115	3.0	4.3
FBTE-4	1	1088	479	907	666	732	618	597	503	820	141	706	110	570	78	399	34	0.8	0.7
	2	1219	779	1189	844	963	781	787	642	1067	31	920	31	751	33	535	41	1.1	1.0
	3	1142	737	1065	796	920	758	807	671	976	46	887	29	781	15	652	25	0.7	0.6
Element peak/min., mean, RMS		1219	479							955	134	838	116	701	106	529	109	0.8	0.8
FPTE-1	1	1031	586	891	676	628	534	402	376	783	72	586	42	394	18	390	17	0.9	0.8
	2	1184	818	1142	841	774	644	476	440	993	19	717	17	469	21	456	20	1.1	1.2
	3	1168	804	1123	842	793	667	538	494	987	30	741	11	532	15	522	17	1.0	1.0
	4	1039	716	954	754	737	637	572	526	862	40	700	15	566	6	572	12	0.7	0.6
Element peak/min., mean, RMS		1184	586							906	99	686	64	490	68	485	71	0.9	0.9
FPTE-3	1	852	441	714	545	565	438	403	354	658	81	517	49	386	18	369	13	1.8	2.3
	2	969	637	930	674	727	523	491	399	852	30	654	28	459	22	426	19	2.8	3.8
	3	979	705	975	717	796	574	581	445	908	5	725	13	531	19	494	19	2.6	3.6
	4	957	854	908	696	792	591	646	493	857	33	733	10	592	14	559	18	1.7	2.2
Element peak/min., mean, RMS		979	441							819	106	657	91	492	79	462	74	2.2	3.0

TABLE 3-1 (Continued)

Element	Body No.	Temperature (°C)																Average Fluence ($\times 10^{25}$ n/m^2)	
		Envelope								Time Averaged									
		Fuel Extremes		Fuel		Body		Sleeve		Fuel		Body		Sleeve		Coolant			
		Peak	Min.	Max.[a]	Min.[b]	Max.[a]	Min.[b]	Max.[a]	Min.[b]	Avg[c]	RMS[d]	Avg[c]	RMS[d]	Avg[c]	RMS[d]	Avg[c]	RMS[d]	Fast	Thermal
PTE-2	1	638	458	670	541	573	477			627	77	541	58			366	15	1.0	NC[g]
	2	909	643	998	759	853	661			915	76	787	74			480	50	1.8	NC
	3	1007	894	1166	878	1041	804			1068	16	964	29			647	43	1.6	NC
	4	1018	988	1149	875	1073	834			1059	10	998	7			741	13	0.9	NC
Element peak/min., mean, RMS		1018	458							942	166	840	167			560	134	1.4	NC

[a] Maximum time-averaged temperature.

[b] Minimum time-averaged temperature.

[c] Average time-averaged temperature for fuel body.

[d] Root mean square deviation of all calculated temperatures for fuel body.

[e] Average time-averaged temperature for fuel element.

[f] Root mean square deviation of all calculated temperatures for the fuel element.

[g] NC = not calculated.

TABLE 3-2
FUEL PARTICLE BURNUPS FOR PEACH BOTTOM TEST ELEMENTS

Element I.D.	Body No.	Burnup					
		Fissile		Fertile		Composite	
		Mean (% FIMA)	RMS (% FIMA)	Mean (% FIMA)	RMS (% FIMA)	Mean (% FIMA)	RMS (% FIMA)
FTE-1	1	15.37	4.91	0.09	0.05	1.88	0.62
	2	19.49	0.92	0.15	0.02	2.41	0.12
	3	13.03	2.56	0.05	0.03	1.57	0.33
Total		15.96	4.20	0.10	0.06	1.95	0.54
FTE-2	1	21.39	6.81	0.23	0.13	2.35	0.80
	2	26.89	1.38	0.37	0.05	3.03	0.18
	3	17.85	3.43	0.12	0.08	1.89	0.41
Total		22.04	5.82	0.24	0.14	2.42	0.70
FTE-3	1	7.83	2.06	0.03	0.01	1.42	0.38
	2	9.87	0.44	0.04	0.00	1.80	0.08
	3	6.51	1.38	0.02	0.01	1.18	0.25
Total		8.07	2.00	0.03	0.01	1.47	0.37
FTE-4	1	28.25	6.34	0.43	0.21	4.69	1.16
	2	35.25	1.13	0.68	0.07	5.97	0.23
	3	25.11	4.60	0.24	0.15	4.05	0.83
Total		29.54	6.26	0.45	0.24	4.91	1.16
FTE-5	1	43.63	12.06	1.32	0.63	7.94	2.40
	2	54.94	1.24	2.17	0.13	10.42	0.31
	3	41.91	6.58	1.05	0.48	7.44	1.43
Total		46.83	9.84	1.52	0.66	8.60	2.08
FTE-6	1	36.14	7.42	0.89	0.42	8.10	1.85
	2	44.60	0.97	1.47	0.08	10.29	0.27
	3	33.86	5.53	0.72	0.33	7.50	1.39
Total		38.20	7.09	1.03	0.45	8.63	1.80
FTE-7	1	36.99	7.59	0.69	0.33	5.64	1.32
	2	45.65	1.00	1.15	0.07	7.22	0.19
	3	34.66	5.66	0.56	0.26	5.21	0.99
Total		39.10	7.25	0.80	0.35	6.02	1.29
FTE-8	1	31.37	12.35	0.78	0.52	8.65	3.55
	2	47.84	0.93	1.75	0.07	13.62	0.28
	3	40.18	5.44	1.12	0.36	11.18	1.67
Total		39.79	10.31	1.22	0.55	11.15	3.04
FTE-9	1	35.54	7.29	0.79	0.38	5.56	1.32
	2	43.86	0.96	1.31	0.08	7.15	0.20
	3	33.30	5.44	0.64	0.29	5.13	1.00
Total		37.57	6.97	0.92	0.40	5.95	1.30

TABLE 3-2 (Continued)

Element I.D.	Body No.	Burnup					
		Fissile		Fertile		Composite	
		Mean (% FIMA)	RMS (% FIMA)	Mean (% FIMA)	RMS (% FIMA)	Mean (% FIMA)	RMS (% FIMA)
FTE-10	1	30.30	11.93	0.70	0.47	6.57	2.72
	2	46.22	0.90	1.58	0.06	10.44	0.22
	3	38.81	5.26	1.01	0.33	8.51	1.31
Total		38.44	9.96	1.10	0.49	8.51	2.35
FTE-12	1	29.29	11.53	0.51	0.34	4.07	1.71
	2	44.67	0.87	1.16	0.04	6.54	0.14
	3	37.52	5.08	0.74	0.24	5.29	0.84
Total		37.16	9.63	0.80	0.36	5.30	1.49
FTE-13	1	ND[(a)]	ND	ND	ND	ND	ND
	2	ND	ND	ND	ND	ND	ND
	3	ND	ND	ND	ND	ND	ND
Total							
FTE-14	1	18.70	4.34	0.21	0.10	1.86	0.48
	2	23.86	0.73	0.35	0.02	2.45	0.09
	3	16.93	3.22	0.16	0.08	1.66	0.36
Total		19.83	4.30	0.24	0.11	1.99	0.48
FTE-15	1	29.20	6.17	0.57	0.28	3.19	0.81
	2	36.66	0.69	0.97	0.05	4.23	0.11
	3	27.52	4.71	0.47	0.22	2.94	0.63
Total		31.13	6.00	0.67	0.30	3.45	0.82
FTE-16	1	31.23	6.61	0.55	0.27	4.24	1.03
	2	39.18	0.75	0.93	0.05	5.54	0.14
	3	29.45	5.03	0.46	0.21	3.98	0.79
Total		33.28	6.41	0.65	0.29	4.58	1.02
FTE-17	1	32.42	6.86	0.63	0.31	3.77	0.95
	2	40.68	0.78	1.07	0.06	4.98	0.13
	3	30.57	5.22	0.53	0.24	3.49	0.73
Total		34.56	6.65	0.74	0.33	4.08	0.95
FTE-18	1	28.61	4.12	0.57	0.17	5.72	0.90
	2	36.86	1.09	1.08	0.10	7.72	0.35
	3	39.27	0.26	1.28	0.01	8.26	0.06
	4	38.46	0.59	1.19	0.05	8.04	0.15
	5	34.57	1.65	0.89	0.10	7.08	0.38
	6	27.21	0.42	0.48	0.13	5.39	0.55
Total		34.16	5.14	0.92	0.32	7.03	1.21
FBTE-1	1	41.47	11.49	1.30	0.62	7.10	2.17
	2	52.25	1.18	2.14	0.13	9.37	0.28
	3	37.39	8.96	0.93	0.48	6.18	1.68
		43.69	10.25	1.46	0.63	7.55	2.08

TABLE 3-2 (Continued)

Element I.D.	Body No.	Burnup					
		Fissile		Fertile		Composite	
		Mean (% FIMA)	RMS (% FIMA)	Mean (% FIMA)	RMS (% FIMA)	Mean (% FIMA)	RMS (% FIMA)
FBTE-2	1	41.76	11.55	1.76	0.83	13.52	3.96
	2	52.57	1.19	2.88	0.18	17.49	0.48
	3	40.10	6.29	1.40	0.63	12.78	2.30
Total		44.81	9.45	2.01	0.88	14.60	3.37
FBTE-3	1	44.43	12.31	1.59	0.75	10.19	3.05
	2	55.97	1.27	2.61	0.16	13.33	0.38
	3	42.67	6.69	1.26	0.57	9.58	1.80
Total		47.69	10.04	1.82	0.80	11.03	2.63
FBTE-4	1	12.93	4.15	0.09	0.05	2.63	0.86
	2	16.38	0.79	0.15	0.02	3.36	0.17
	3	10.94	2.14	0.05	0.03	2.20	0.45
Total		13.42	3.54	0.10	0.06	2.73	0.74
FBTE-5	1	44.07	12.13	1.33	0.63	6.10	1.89
	2	55.48	1.23	2.18	0.13	8.13	0.25
	3	42.37	6.65	1.06	0.48	5.67	1.17
Total		47.31	9.91	1.52	0.66	6.64	1.68
FBTE-6	1	15.61	4.29	0.10	0.04	1.60	0.45
	2	19.68	0.44	0.16	0.01	2.05	0.05
	3	15.02	2.35	0.08	0.03	1.52	0.26
Total		16.77	3.51	0.11	0.05	1.72	0.38
RTE-1	1	32.82	6.52	0.60	0.29	7.01	1.53
	2	45.82	1.69	1.46	0.17	10.28	0.47
	3	49.32	0.34	1.78	0.03	11.23	0.08
	4	47.81	0.96	1.64	0.09	10.82	0.26
	5	42.17	2.50	1.17	0.18	9.32	0.64
	6	31.59	3.26	0.50	0.19	6.68	0.80
Total		41.59	7.71	1.19	0.52	9.22	1.95
RTE-2	1	27.43	8.76	0.53	0.29	6.08	2.03
	2	42.68	1.49	1.41	0.17	9.93	0.44
	3	45.28	0.24	1.70	0.02	10.69	0.06
	4	43.01	1.10	1.51	0.09	10.07	0.30
	5	36.78	2.47	1.01	0.18	8.39	0.65
	6	27.19	2.87	0.38	0.17	5.91	0.73
Total		37.06	8.36	1.09	0.52	8.51	2.13
RTE-4	1	18.09	6.76	0.16	0.10	2.63	1.02
	2	30.19	1.15	0.49	0.07	4.59	0.22
	3	31.88	0.24	0.58	0.01	4.90	0.04
	4	29.43	1.11	0.48	0.04	4.47	0.19
	5	23.97	2.05	0.28	0.06	3.55	0.33
	6	16.97	1.86	0.07	0.05	2.41	0.30
Total		25.09	6.62	0.34	0.20	3.76	1.08

TABLE 3-2 (Continued)

Element I.D.	Body No.	Burnup					
		Fissile		Fertile		Composite	
		Mean (% FIMA)	RMS (% FIMA)	Mean (% FIMA)	RMS (% FIMA)	Mean (% FIMA)	RMS (% FIMA)
RTE-5	1	35.89	11.30	0.92	0.43	6.05	2.02
	2	55.17	1.90	2.22	0.26	9.99	0.50
	3	58.43	0.30	2.71	0.04	10.88	0.08
	4	56.38	1.03	2.47	0.13	10.38	0.26
	5	49.90	2.90	1.76	0.27	8.82	0.65
	6	37.86	3.72	0.77	0.29	6.21	0.79
Total		48.94	10.27	1.81	0.79	8.72	2.16
RTE-6	1	36.51	11.51	1.03	0.48	7.00	2.34
	2	56.19	1.93	2.49	0.29	11.54	0.56
	3	59.49	0.30	3.03	0.05	12.54	0.09
	4	57.35	1.06	2.76	0.15	11.95	0.30
	5	50.68	2.98	1.96	0.30	10.16	0.75
	6	38.47	3.72	0.85	0.32	7.19	0.89
Total		49.78	10.47	2.02	0.88	10.06	2.48
RTE-7	1	11.35	4.23	0.05	0.03	1.49	0.57
	2	18.86	0.71	0.16	0.02	2.55	0.11
	3	19.87	0.16	0.19	0.01	2.70	0.02
	4	18.30	0.70	0.15	0.01	2.47	0.10
	5	14.89	1.27	0.09	0.02	1.98	0.18
	6	10.56	1.15	0.02	0.02	1.37	0.16
Total		15.64	4.12	0.11	0.06	2.10	0.58
RTE-8	1	36.58	11.53	1.04	0.49	7.16	2.39
	2	56.40	1.97	2.53	0.30	11.80	0.58
	3	59.78	0.31	3.09	0.05	12.85	0.10
	4	57.69	1.07	2.82	0.15	12.26	0.31
	5	50.97	3.00	2.00	0.31	10.43	0.77
	6	38.66	3.76	0.88	0.33	7.37	0.92
Total		50.01	10.54	2.06	0.90	10.31	2.54
FPTE-1	1	1.43	0.50	Element did not contain fertile fuel.			
	2	2.08	0.03				
	3	1.85	0.13				
	4	1.22	0.19				
Total		1.64	0.43				
FPTE-3	1	6.20	1.29	Element did not contain fertile fuel.			
	2	8.20	0.17				
	3	7.84	0.32				
	4	5.78	0.81				
Total		7.01	1.30				
PTE-2		ND	ND	ND	ND	ND	ND

(a) ND = not determined.

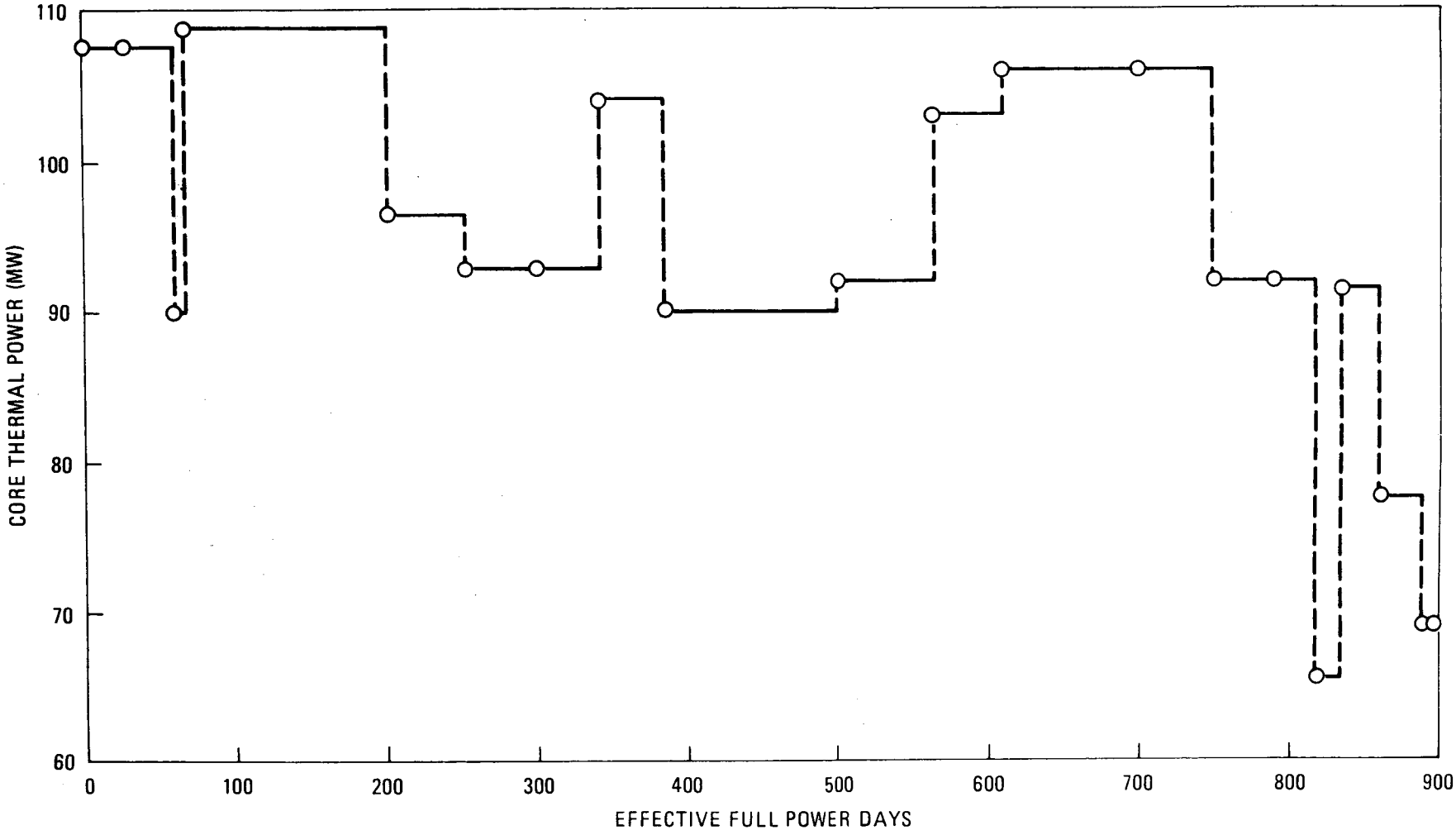

Fig. 3-1. Peach Bottom Core 2 thermal power, TREVER simulation

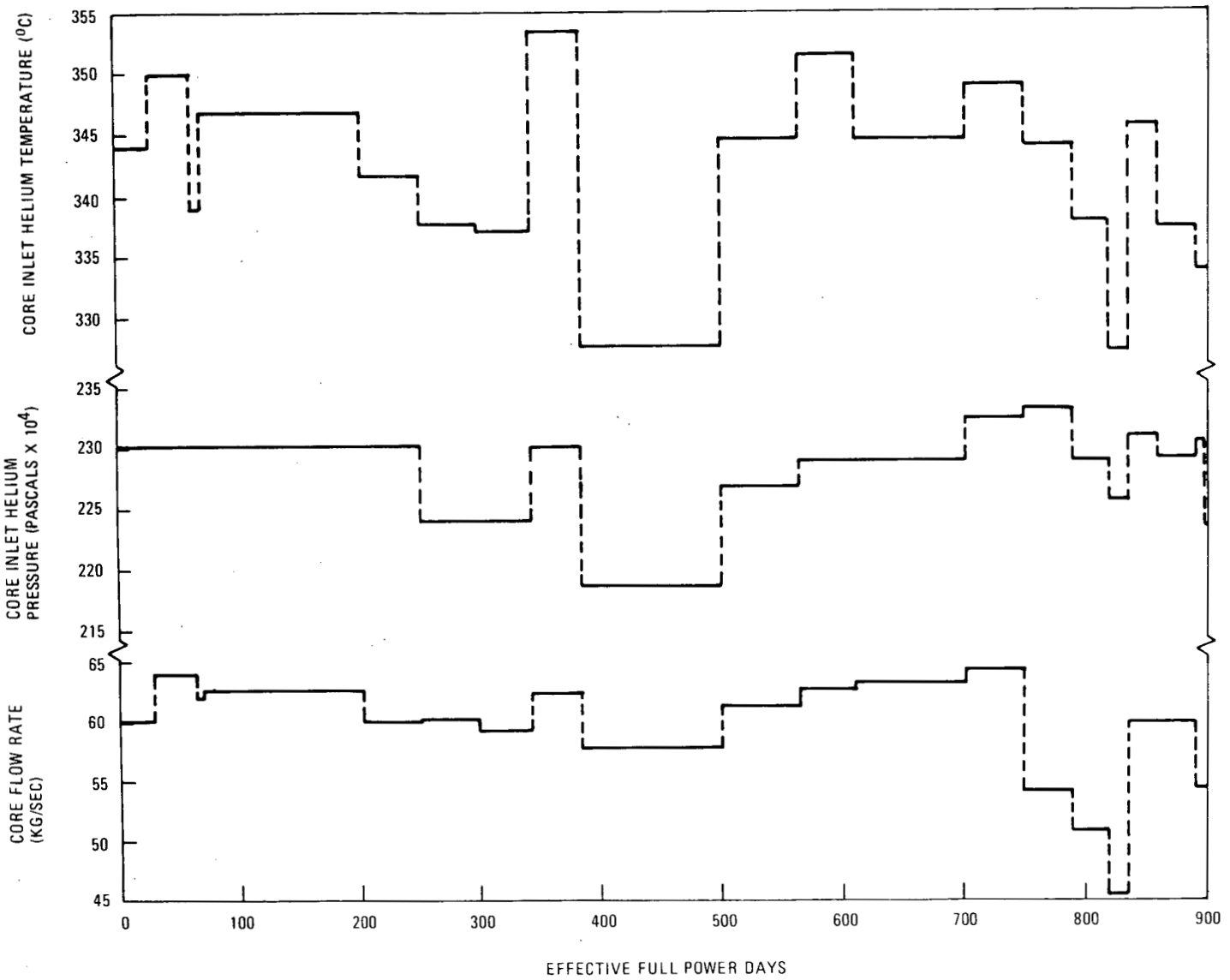

Fig. 3-2. Peach Bottom Core 2 operating parameters, TREVER simulation

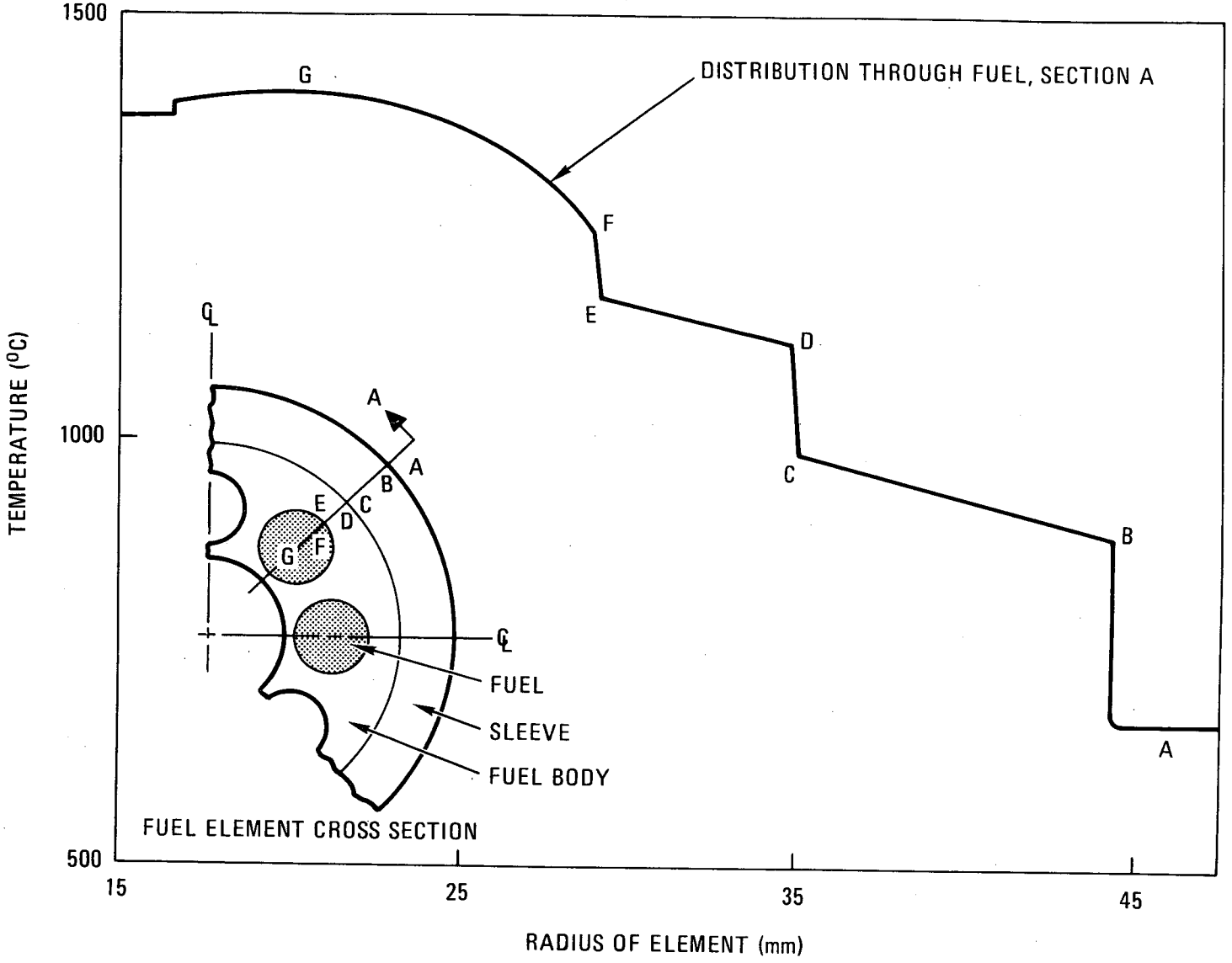

Fig. 3-3. Typical radial temperature profile for test elements having eight-hole teledial geometry

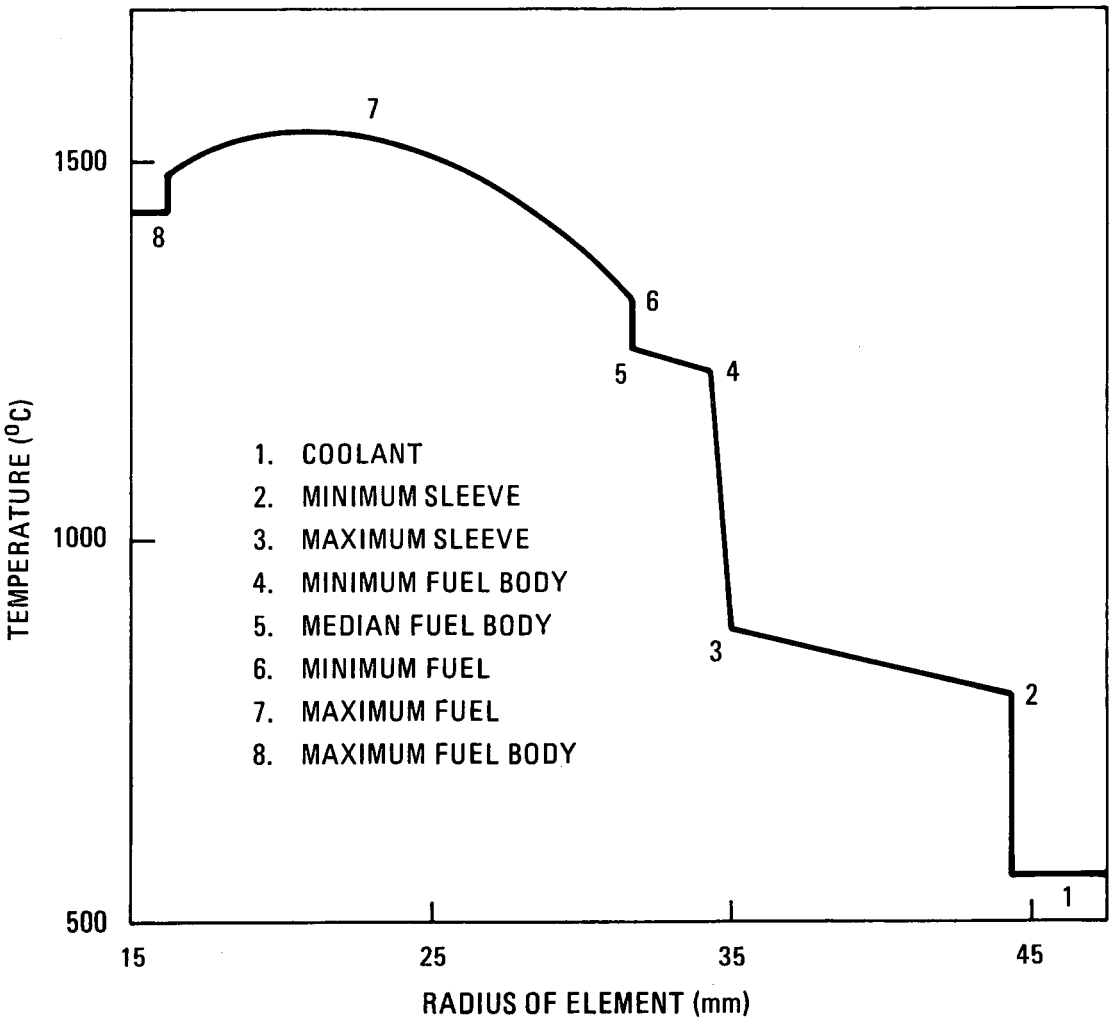

Fig. 3-4. Typical radial temperature profile for test elements having six-hole teledial geometry

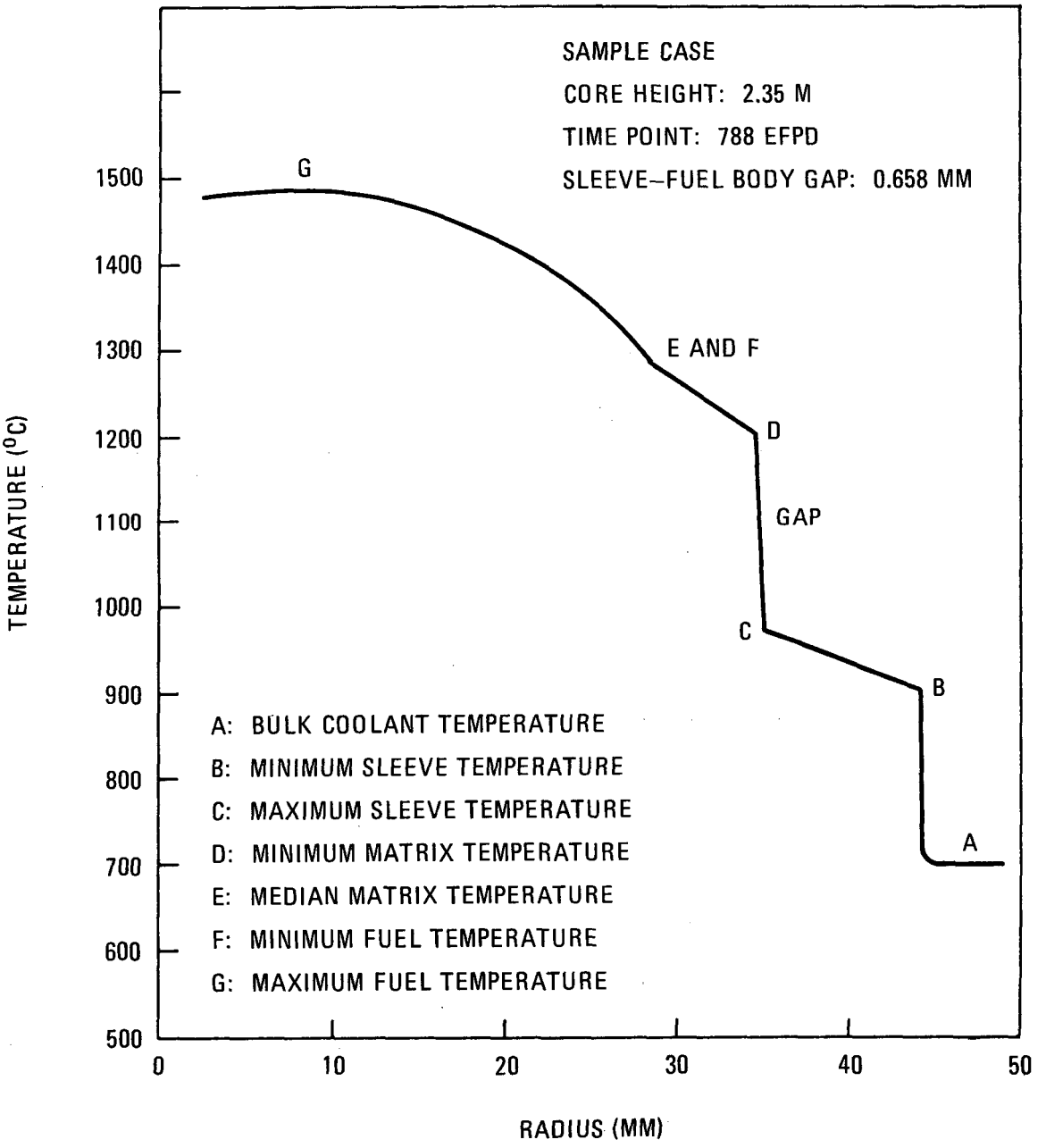

Fig. 3-5. Typical radial temperature profile for molded block element (FTE-18)

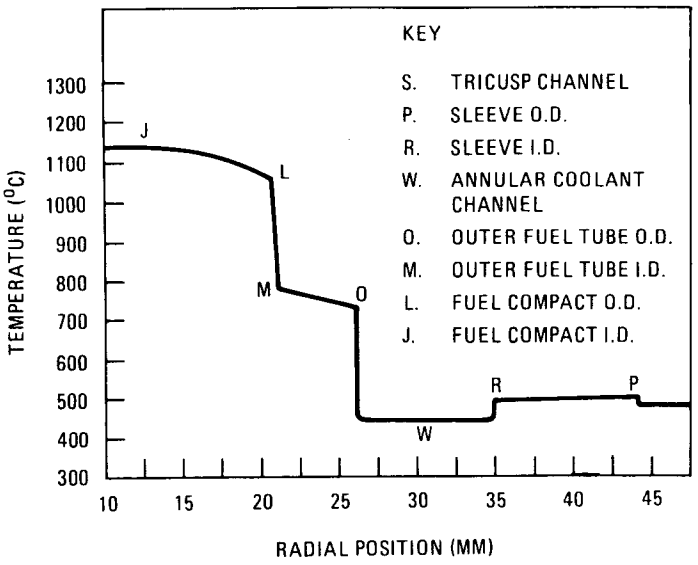

Fig. 3-6. Typical radial temperature profile for FPTE-1

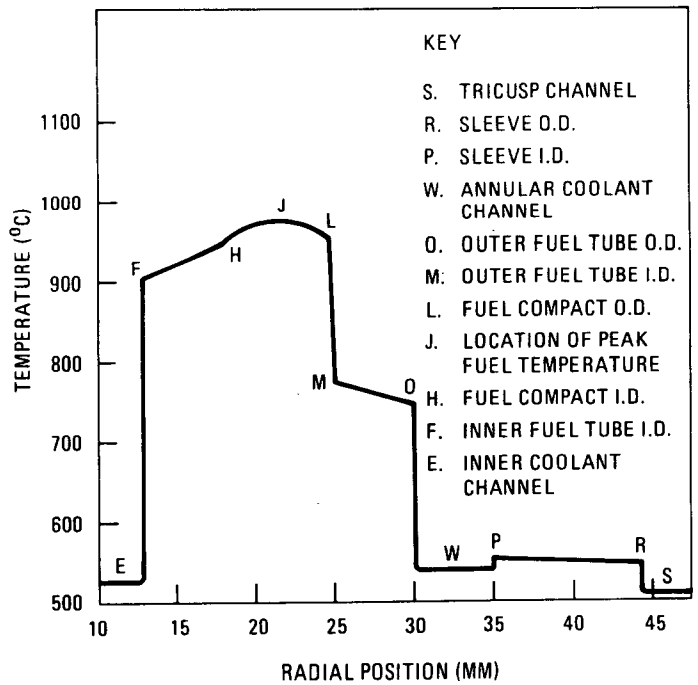

Fig. 3-7. Typical radial temperature profile for FPTE-3

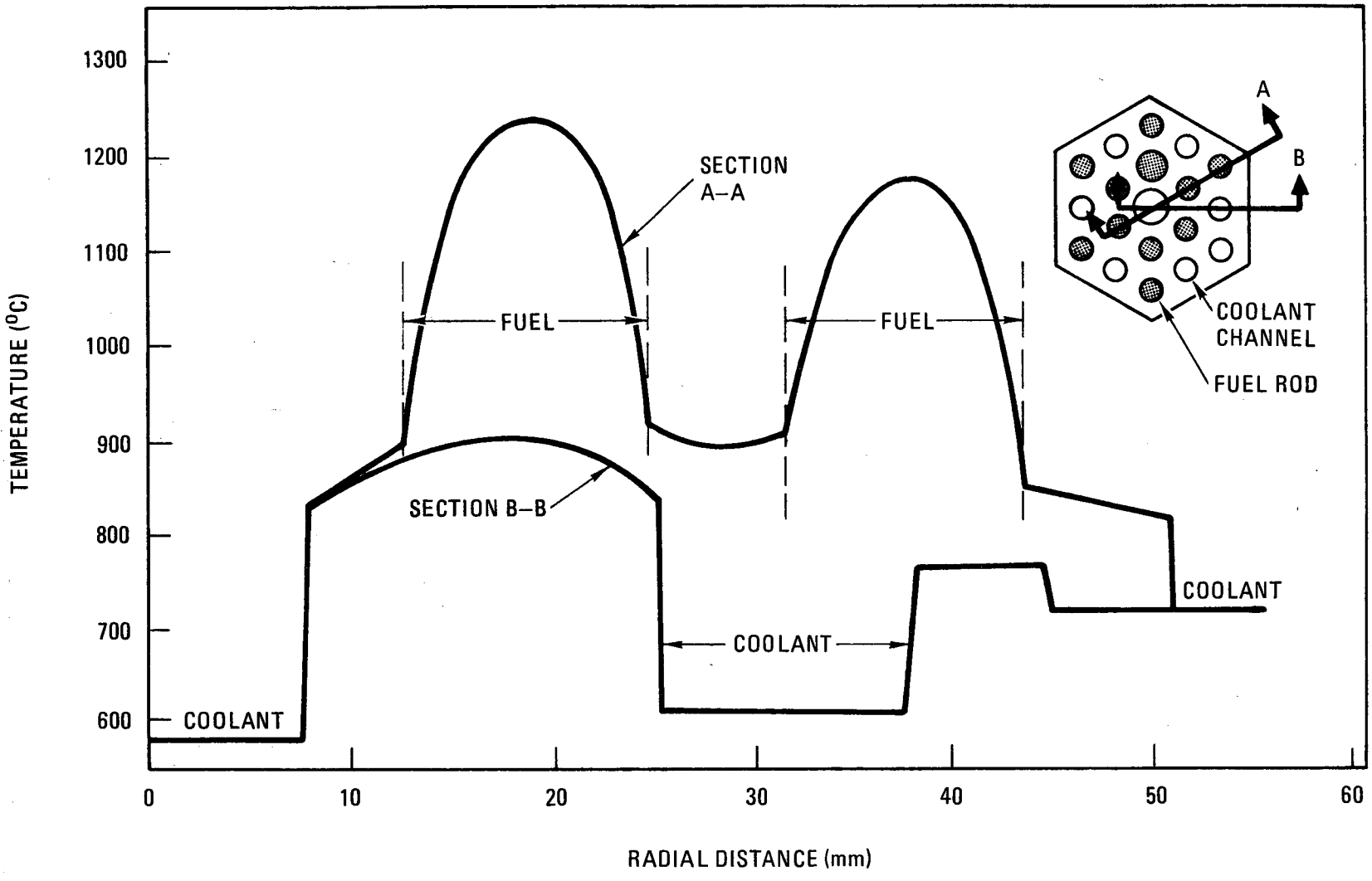

Fig. 3-8. Typical radial temperature profile for FSV PTE-2

4. NUCLEAR MEASUREMENTS

Gamma spectroscopic and destructive burnup measurements were performed on many of the Peach Bottom test elements to better define irradiation conditions and verify nuclear design calculations. Improvement of temperature predictions via feedback of nuclear measurements into thermal calculations was discussed in Section 3.2. This section discusses the nuclear measurements and compares them with design code predictions.

4.1. GAMMA SPECTROSCOPIC MEASUREMENTS

Gamma spectroscopic measurements were made at Peach Bottom for nearly all the test elements irradiated in Core 2. Test elements which were removed from the core and gamma scanned prior to final shutdown of Core 2 were scanned only for total activity using a sodium-iodide detector. Elements scanned after final shutdown were scanned for individual fission products using a high-resolution Ge(Li) detector. The Peach Bottom gamma scanning is described in Ref. 4-1. In addition to these measurements, gamma spectroscopic measurements on fuel and graphite components from many of the test elements were performed during PIE at GA, ORNL, and KFA. A gamma spectroscopic examination of the Peach Bottom test elements provided data on fuel stack length, axial power and neutron flux profiles, power generation, and fission product mobility.

4.1.1. Fuel Stack Length

Fuel stack lengths were determined for each gamma scanned fuel element using the strip charts of total activity or of single nuclide activities. A typical strip chart is shown in Fig. 4-1. A comparison of fuel body stack lengths determined from the destructive PIE and from the EOL gamma scanning of FTE-6 (Ref. 4-2) was performed to qualify the validity of the gamma scanning

method. This comparison, shown in Table 4-1, indicated no statistical differences between stack lengths determined via the two techniques.

4.1.2. Axial Power and Thermal Flux Profiles

Since Cs-137 is a fission product of both U-235 and U-233 and has a half life (30.1 yr) which is much longer than the irradiation period for the test elements, the activity of Cs-137 measured for a given sample is proportional to the number of fissions which occurred in the sample. The normalized axial distribution of Cs-137 within an element is therefore representative of the time-averaged axial power profile provided that the Cs-137 was contained in the fuel. The axial distributions of the short-lived isotopes Ba-La-140 (12.8 days) and Zr-95 (65.5 days) within an element are representative of the EOL axial power profile.

Cs-134 is formed indirectly from fission through the decay of Xe-133 to Cs-133, followed by neutron activation via capture of neutrons primarily in the 0.38 to 2.82 J (2.38 to 17.6 eV) energy range. The quantity of Cs-134 formed in a given fuel rod is dependent on both the fission rate and the neutron flux. These are not necessarily synonymous since the fission rate is dictated by heavy metal atom densities and fission cross sections, as well as by neutron flux. The dependence on the fission rate can be removed by dividing the measured activity of Cs-134 by the measured activity of Cs-137. The normalized Cs-134/Cs-137 axial profile is therefore representative of the time-averaged thermal flux (or the thermal fluence) distribution provided that the Cs-137 and Cs-134 are contained in the fuel and the Cs-134 activity is corrected for decay (762.9-day half life) during irradiation. In taking the Cs-134/Cs-137 profile to be equivalent to the thermal fluence distribution, it is assumed that the axial distribution of neutrons in the epithermal range has approximately the same shape as the axial distribution of thermal neutrons (<0.38 aJ). The normalized Cs-134/Cs-137 profile is also representative of the time-averaged axial profile for elements, or fuel stacks, in which the fuel loadings are uniform over the length of the element.

The relationships between the Cs-134/Cs-137, Cs-137, time-averaged power, and thermal fluence distributions are illustrated in Fig. 4-2. High thorium loadings in fuel body 1 of FTE-14 relative to fuel bodies 2 and 3 caused the predicted time-averaged power profile for fuel stacks 1 and 2 to peak in fuel body 1. This is reflected in the Cs-137 profile but not in the Cs-134/Cs-137 profile. The Cs-134/Cs-137 profile resembles the predicted thermal fluence profile, which is not perturbed by the non-uniform thorium loadings since single fuel stacks contain too little fuel to dictate the shape of the local flux distribution.

The hot cell gamma scans of individual fuel stacks were particularly useful in establishing power and flux profiles for the fuel elements. The Peach Bottom scans were of more limited use because of the complicated scanning geometry. The geometry for the Peach Bottom scans is shown in Fig. 4-3. The geometrical configuration was very sensitive to the exact position of the collimator with respect to the fuel element. A slight tilt or eccentricity of the collimator axis or any rotational or pendulum type movement of the element would give significantly different fractional fuel areas. Except for test elements which had azimuthally uniform fuel loadings and no spine samples, the uncertainty associated with the scanning geometry and the nonrepresentativeness of the area under surveillance precluded the use of the Peach Bottom scans for determining power and flux profiles. However, the Peach Bottom scans for elements such as FTE-6, which contained power-producing and neutron-absorbing spine samples, demonstrated the necessity of considering the effect of spine samples on power profiles in order to accurately calculate temperatures. The perturbation of the axial power profile by spine samples in FTE-6 is clearly seen from the Cs-137 profile shown in Fig. 4-4.

4.1.3. Absolute Power

The power generated within a sample can be calculated from the number of Cs-137 atoms produced during irradiation using the equation

$$P = \frac{3.2 \times 10^{-11} N}{yt} ,$$

where P = power, W,

N = number of Cs-137 atoms produced during irradiation,

y = effective fission yield for Cs-137 from U-233 and U-235,

t = irradiation time, s,

3.2×10^{-11} = W-s/ fission.

The number of Cs-137 atoms produced during irradiation is obtained by converting the measured Cs-137 activity, in counts per minute (CPM), to Cs-137 atoms and then correcting for decay during and after irradiation (see Section 3.4.2.4. of Ref. 4-3). The conversion of CPM to atoms is achieved using a calibration factor (or factors) which accounts for the efficiency of the detector, the geometrical spreading of the gamma radiation, and absorption of gamma radiation within the sample and between the sample and the detector.

Calibration of the hot cell gamma scanning performed at GA was accomplished using fuel rods of known burnup from capsules P13R (Ref 4-4) and P13Q (Ref. 4-5) for 12.7-mm (0.5-in.) and 15.9-mm (0.625-in.) diameter rods, respectively. The Peach Bottom scanning configuration was calibrated via cross-calibration of Peach Bottom scans with calibrated hot cell scans for FTE-6 and FTE-15 (Ref. 4-1).

4.1.4. Determination of Nuclide Mobility

The ratio of fission product inventories is approximately constant along a fuel element for an unfailed and retentive fuel variety such as TRISO-coated fuel. Alternatively, for failed or non-retentive fuel, the ratio of mobile to non-mobile fission product inventories will vary with the amount of mobile fission products that escapes from the fuel. The following method is outlined for determining fission product

mobility within a fuel element. Although the method is specifically described for Cs-137, it is equally applicable to cerium, ruthenium, and other mobile species which do not diffuse through intact TRISO coatings.

1. Determine the average Cs-137/Zr-95 ratio for a retentive fuel variety having no detectable fuel failure (as determined by metallography and fission gas release measurements). Determine the variance in the Cs-137/Zr-95 ratios and test for significance using the axial variability test.

2. If testing fuels with different thorium and uranium inventories than the reference fuel, correct the reference Cs-137/Zr-95 ratio using the equation

$$\left(\frac{\text{Cs-137}}{\text{Zr-95}}\right)_s \sim \frac{Y_{Cs,5} + \frac{N_3 \times \sigma_{f,3}}{N_5 \times \sigma_{f,5}} \times Y_{Cs,3}}{Y_{Zr,5} + \frac{N_3 \times \sigma_{f,3}}{N_5 \times \sigma_{f,5}} \times Y_{Zr,3}}$$

where $(\text{Cs-137/Zr-95})_s$ = corrected Cs-137/Zr-95 ratio for fuel with no cesium loss,

$\sigma_{f,5}$ = fission cross section for U-235 (580 barns),

$\sigma_{f,3}$ = fission cross section for U-233 (525 barns),

N_j = atomic concentration for U-23j

$Y_{i,j}$ = fission yield for isotope i from fission of U-23j.

3. Calculate the Cs-137 loss from the Cs-137/Zr-95 ratio for the reference fuel and the Cs-137/Zr-95

ratio for the fuel with suspected cesium loss assuming a linear relationship between the Cs-137/Zr-95 ratio and cesium loss.

4.2. BURNUP MEASUREMENTS

Destructive and non-destructive techniques including radiochemistry (Refs. 4-6 and 4-7), mass spectrometry (Refs. 4-7 and 4-8), isotope dilution mass spectrometry (Ref. 4-9), and gamma spectrometry (Refs. 4-10 and 4-11) were employed to measure the fuel burnup in Peach Bottom test elements. A summary of these methods and associated error analyses is given in Ref. 4-3. The first three methods were applied to loose fuel particles from spine samples and the last was applied to fuel rods. One or more of these methods were used to measure fuel burnup in test elements FTE-3, FTE-4, FTE-5, FTE-6, FTE-13, FTE-14, FTE-15, FTE-18, and FPTE-1. The measurements for FTE-13, FTE-18, and FPTE-1 were performed at ORNL, KFA, and Springfields Nuclear Power Development Laboratories, respectively. All other measurements were performed at GA.

4.2.1. Fissile and Fertile Particle Burnup

Destructively measured burnups for fissile and fertile fuel from Peach Bottom test elements are presented in Tables 4-2 and 4-3, respectively. All burnups are expressed in percent FIMA (fissions per initial metal atom). Table 4-2 includes a comparison of fissile particle burnups determined via the spectrometric methods (mass spectrometry and IDMS) and the radiochemical method. Application of the group agreement test to the data indicates that the probability is less than 0.05 that the differences between the burnups determined via the different techniques are due to measurement errors alone. It is concluded that there is a statistically significant bias of $-3.21 \pm 1.29\%$ (1σ) in the radiochemical method relative to the spectrometric methods, at least for this sample population.

Table 4-4 compares measured fissile and fertile fuel burnups with the corresponding burnup predictions. The measured fissile burnups given in Table 4-4 are averages of the burnups determined via mass spectrometry and IDMS. These methods have the lowest measurement errors, and the average of the two is believed to provide the most accurate estimate of the burnup in fissile fuel. The measured burnups for fertile fuel were determined via radiochemistry using Cs-137 as a burnup monitor. This comparison indicates that both the fissile and fertile burnup predictions are significantly biased as a group on the low side relative to measured burnups. Table 4-4 also shows that the relative differences between the measurements and predictions for individual samples vary significantly with axial core location. These differences are plotted as a function of axial position for fissile and fertile burnup in Figs. 4-5 and 4-6, respectively. Linear regression lines have been calculated for the data and included in both figures. In each case, the relative difference between measurements and predictions was negatively correlated with axial position. The burnup was overpredicted in fuel body 1 and underpredicted in fuel bodies 2 and 3 for both fissile and fertile fuel. The element average bias in predicted burnup relative to actual burnup was -4.1% for fissile fuel and -3.0% for fertile fuel, as determined from the regression lines presented in Figs. 4-5 and 4-6.

4.2.2. Composite Burnup

The composite (combined fissile and fertile) burnups in fuel rods from test elements FTE-4, FTE-6, FTE-14, and FTE-15 were determined from gamma spectroscopic measurements as described in Ref. 4-3. In order to verify these data, composite burnups were derived from the fissile and fertile burnups determined from the more accurate destructive measurements on spine sample fuel. The composite burnups determined from destructive measurements on spine samples are compared with the corresponding gamma spectroscopically determined burnups in Table 4-5. The comparison is made in two groups. The composite burnups for the eight-hole teledial elements, FTE-4 and FTE-6, are compared as one group, and the burnups for the six-hole teledial elements, FTE-14 and FTE-15, are compared as a second group. This was done because a different calibration was used

for the six-hole and eight-hole teledial elements to obtain absolute fission product inventories from CPM (Section 4.1.3).

The comparison of the Group I burnups indicates that the gamma spectroscopically determined burnups have a statistically significant* bias of +8.1% relative to the burnups established by destructive methods. Although the gamma spectroscopically determined burnups for both FTE-14 and FTE-15 appear to be biased relative to destructively measured burnup, they are not significantly biased as a group. Since the destructive measurements are considered to be the most representative of the true burnup, the calibration for the scanning of fuel rods from eight-hole teledial test elements is concluded to be 8.1% too high. No error could be concluded for the calibration of the six-hole element fuel rod scans as a group.

Table 4-6 compares the gamma spectroscopically measured composite burnups for FTE-4, FTE-6, FTE-14, and FTE-15 with the corresponding predictions. The measured burnups for FTE-4 and FTE-6 fuel rods were corrected to account for the 8.1% error in the calibration for the gamma scanning of eight-hole-element fuel rods. The measured burnups for FTE-14 and FTE-15 were also corrected for their biases relative to destructively measured burnups as shown in Table 4-5. For the entire population of fuel rods considered, the predicted burnups were biased by -3.6 ± 0.9% (1σ) relative to measured burnups. This bias is consistent with the biases established for fissile (-4.1%) and fertile (-3.0%) fuel in Figs. 4-5 and 4-6. The RMS variation in the disagreement between measurements and predictions was ±9.4%. This value is interpreted to be the 1σ uncertainty associated with local point burnup predictions for the fuel test elements.

---

*Although the criterion for significance is not satisfied with $\sqrt{m}\,\bar{d} = 1.8 < 1.96$, significance at the 95% confidence level is assumed based on the observation that the RMS variation in the group of relative differences indicates that the errors estimated for the gamma spectroscopically determined burnups are conservative.

4.3. ISOTOPIC ANALYSIS

Uranium isotopic concentrations in relative atom percent for both fissile and fertile particles were determined from mass spectrometric measurements on loose particles from test elements FTE-3, FTE-4, FTE-5, FTE-6, FTE-14, and FTE-15 and were compared with predictions based on GAUGE and FEVER code simulations of Peach Bottom Core 2. The measurements and predictions are compared in Table 4-7. The relative differences are expressed in terms of a bias which is defined as

$$\% \text{ Bias} = [(\text{Calc}/\text{Meas}) - 1] \times 100 \ .$$

The error for each bias is the progressed uncertainty for the measurements. Usually two to four independent measurements (individual particles) were made at a specific core location and combined into a single value. The ranges of the observed differences are summarized in Table 4-8.

Figures 4-7 through 4-10 show the relative differences between predicted and measured isotopic concentrations as a function of axial core location for fissile and fertile fuel. The results of the comparisons of predicted and measured isotopic concentrations are summarized below.

1. The U-235 concentration in fissile fuel was slightly overpredicted at the top of the core and slightly underpredicted at the bottom. The U-235, U-236, and U-238 concentrations were overpredicted in the bottom of the core and underpredicted at the top. These trends suggest that the calculated thermal flux profile was skewed toward the bottom of the core, since higher fluxes would result in more fissions (and therefore less U-235) and increased formation of U-236 via neutron activation. Underprediction of neutron fluxes in the top part of the core would result in less fissions (more U-235) and decreased formation of U-236.

2. The U-233 concentration in fertile fuel was overpredicted by a few percent at the bottom and center of the core and underpredicted at the top. The U-234 and U-235 concentration predictions for fertile fuel were biased in the opposite direction from the U-233 concentration predictions. This suggests that the capture cross section for U-233 was underestimated at the bottom and middle of the core and overestimated at the top.

3. The U-234 concentrations in fertile fuel were less underpredicted in FTE-15 than in FTE-14. The concentrations of bred U-235 were less underpredicted in FTE-14 than in FTE-15. (The fuel burnups in FTE-15 were higher than in FTE-14.) This suggests that the assumed capture cross section for U-234 was too small.

It is concluded that the fissile material was fairly well modeled by GAUGE/FEVER, although some difficulty in calculating the U-236 inventory is apparent. The burnup in fertile fuel was not as well modeled. The effectiveness of GAUGE/FEVER calculations in predicting burnup for fissile and fertile fuel in the Peach Bottom test elements is quantified in Section 4.2.2. The data provided in this section help identify the reasons for the errors in the predictions.

4.4. URANIUM LOADING MEASUREMENTS

In order to obtain an estimate of the uncertainty in the historically reported uranium loadings for the Peach Bottom test elements, delayed neutron activation analysis (DNAA) uranium measurements were made on historical fuel rods representing the fuel rods irradiated in several test elements. The results of these measurements are compared with historically reported uranium loadings in Table 4-9. Various statistical tests have been applied to check for significance in the relative differences between measured and reported values.

The relative differences between measured and reported uranium loadings in 14 of 23 rod batches could not be attributed at the 0.05 significance level to measurement error. For the entire group of rods, the reported uranium loadings are biased by -2.0 ± 0.2% (1σ) relative to the measured values. The RMS variation in the relative differences is ±3.2%. The RMS variation is interpreted as the 1σ uncertainty in the fuel test element uranium loadings. It is doubtful whether the -2.0% bias in the historically reported uranium loadings represents an actual 2% overloading of uranium into the test elements. This may instead be indicative of an inherent bias in the measurement technique.

The loading of thorium into the fuel rods was not controlled as stringently as the loading of uranium. Consequently, the uncertainty in the thorium loadings can be assumed to be greater than ±3.2% (1σ). A ±5% uncertainty on heavy metal loadings was assumed in calculating the errors associated with gamma spectroscopically determined burnups to allow for thorium loading variations.

4.5. NUCLEAR DESIGN VERIFICATION

The predictive accuracy for local point GAUGE/FEVER burnup calculations for the Peach Bottom test elements is estimated to be ±9.4% (1σ) based on a comparison of predictions and gamma spectroscopic burnup measurements for a group of 153 fuel rods from test elements FTE-4, FTE-6, FTE-14, and FTE-15 (Section 4.2.3. and Table 4-6). Corrections based on burnups determined via the more accurate destructive measurement techniques (i.e., mass spectrometry and IDMS for fissile fuel and radiochemistry for fertile fuel) were applied to the gamma spectroscopic burnup measurements to improve the accuracy of the data. Because of the relatively few test elements involved in the comparison, the -3.6 ± 0.9% (1σ) bias determined in the predictions relative to the measurements is not considered to represent a bias in the predictions for all test elements. The predictive accuracy estimated for test element local point burnup calculations is consistent with the ±10% (1σ) predictive accuracy concluded for local point power calculations for Peach Bottom regular fuel elements (Ref. 4-12).

The bias in predicted burnups relative to measurements was observed to vary systematically as a function of the axial core location. As a group, the predictions for FTE-4, FTE-6, FTE-14, and FTE-15 were biased by +4.5 ± 1.7% (1σ), -7.6 ± 1.2% (1σ), and -7.9 ± 1.6% (1σ) in fuel bodies 1, 2, and 3, respectively. This trend of overprediction at the bottom of the core and underprediction at the middle and top of the core was also seen in the burnup predictions for both fissile and fertile fuel. For fissile fuel, the bias in the predictions relative to destructively measured burnup varied from about +6% at the bottom of the core to -15% at the top, with a mean bias of -4.1% (Fig. 4-5). For fertile fuel, the bias varied from about +24% at the bottom of the core to -30% at the top, with a mean bias of -3.0% (Fig. 4-6).

A semi-independent* estimate of the accuracy of burnup predictions for the test elements was obtained using the Peach Bottom gamma scans. The element average burnups for eight test elements which had uniform axial fuel loadings were derived from the total Cs-137 inventory in each element as determined from the Peach Bottom scans. These element average burnups are compared with GAUGE predictions in Table 4-10. For this group of test elements, the accuracy in the burnup predictions was determined to be ±12.2% (1σ) with an apparent bias of -12.5 ± 2.2% (1σ) in the predictions relative to measurements. However, if the measured burnups are reduced by 8.1% to account for the error (Section 4.2.3 and Table 4-8) in the calibration for the hot cell scanning of fuel rods from eight-hole teledial test elements, the bias becomes -5.4 ± 2.2% (1σ), which is supportive of the -3.6% bias obtained from the hot cell scans of fuel rods in FTE-4, FTE-6, FTE-14 and FTE-15.

It should be noted that the statements about the test element burnup predictions in the above paragraphs are not necessarily indicative of the

*The estimate is not completely independent of the first estimate since the Peach Bottom test element scanning geometry was calibrated using the hot cell scanning results (Section 4.1.3.).

overall accuracy of the nuclear predictions for Peach Bottom Core 2, nor should they be considered indicative of the accuracy of nuclear design calculations in general. The reason is that the GAUGE/FEVER codes used to simulate Peach Bottom Core 2 were not set up to explicitly model the test elements (they were assumed to be regular Peach Bottom fuel elements having the appropriate fuel loadings). References 4-1 and 4-12 should be referred to for discussions concerning nuclear design verification in Peach Bottom.

REFERENCES

4-1. Holzgraf, J. F., F. McCord, and C. F. Wallroth, "Gamma Spectroscopic Examination of Peach Bottom HTGR Core Components," DOE Report GA-A13453, April 1978.

4-2. Wallroth, C. F., J. F. Holzgraf, and D. D. Jensen, "Postirradiation Examination of Peach Bottom Fuel Test Element FTE-6," ERDA Report GA-A13943, September 1977.

4-3. Wallroth, C. F., et al., "Postirradiation Examination of Peach Bottom Fuel Test Element FTE-14," ERDA Report GA-13452, July 1977.

4-4. Scott, C. B., D. P. Harmon, and J. F. Holzgraf, "Postirradiation Examination of Capsules P13R and P13S," ERDA Report GA-13827, October 8, 1976.

4-5. Young, C. A., and C. B. Scott, "Postirradiation Examination of Capsule P13Q," ERDA Report GA-A14174, September 1977.

4-6. "Standard Method of Test for Atom Percent Fission on Uranium Fuel (Radiochemical Method)," ASTM Procedures E219-69, American Society for Testing Materials, March 21, 1969.

4-7. Crockett, T., "Atom Percent Fission in Fissile and Fertile Fuel Particles," GA unpublished data.

4-8. "Standard Method of Test for Atom Percent Fission in Uranium and Plutonium Fuel (Mass Spectrometric Method)," ASTM Procedure E244-69, American Society for Testing Materials, March 21, 1969.

4-9. Jones, Ralph J. (ed.), "Method 2.505, Mass-Spectrometric Isotopic Analysis of Uranium in Irradiated-Fuel Dissolver Solution Using the Isotopic-Dilution Technique," in Selected Measurement Methods for Plutonium and Uranium in the Nuclear Fuel Cycle, USAEC Report TID-7029, 1963.

4-10. Holzgraf, J. F., and T. L. Emrich, "BETSY, a Computer Program to Evaluate Fuel Rod Gamma Spectroscopy for Fission Product Inventory and Burnup," GA unpublished data.

4-11. Schröder, R., et al., "PBR-B1 Gammaspektrometrische Nachunterguchungen," Kernforschungsanlage Jülich, Institut für Reaktorwerkstoffe, IRW-TN-23/78, February 13, 1979.

4-12. Saurwein, J. J., and C. F. Wallroth, "Nuclear and Thermal Design Verification for the Peach Bottom High-Temperature Gas-Cooled Reactor," DOE Report GA-A14726, September 1979.

TABLE 4-1
COMPARISON OF FUEL STACK LENGTHS DETERMINED FROM GAMMA SPECTROSCOPY AND METROLOGY

Fuel Body	Composite Fuel Stack Length (in.)		Length from Gamma Scanning (in.)		Relative Difference $z = x_2/x_1 - 1$ (%)		Test 1 $D = z/\xi_z$	Test 2 D^2	Test Results
	x_1	ξ[a]	x_2	ξ[a]	z	ξ_z			
1	26.7653	0.1070	26.6678	0.1296	0.37	0.63	0.58	0.33	Not significant
2	26.6527	0.1181	26.7290	0.1092	-0.29	0.60	-0.48	0.22	Not significant
3	26.6349	0.1224	26.6546	0.0874	-0.07	0.56	0.13	0.02	Not significant

[a] 2σ error.

TABLE 4-2
FISSILE PARTICLE BURNUP MEASUREMENTS FOR PEACH BOTTOM FUEL TEST ELEMENTS

FTE No.	Spine Sample I.D.	Axial Core Location (mm)	Mass Spectrometry + IDMS								Radiochemistry								Burnup Comparison z=(R/M)-1		
			ASTM Eq. 1 (at. %)		ASTM Eq. 2 (at. %)		ASTM Eq. 3 (at. %)		Average (at. %)		Chemical U				IDMS U		Average (at. %)				
											Cs-137 (at. %)		Zr (at. %)		Cs-137 (at. %)						
			Avg	±1σ	Avg	±1σ	Avg	±1σ	Avg	±1σ	Avg	±1σ	Avg	±1σ	Avg	±1σ	Avg	±1σ	z (%)	ε (±1σ) (%)	d=z/ε
3	TS5-5	2676	7.28	0.47	7.44	0.26	7.31	0.37	7.34	0.22	6.36	0.30	--	--	--	--	6.36	0.30	-13.35	4.84	-2.76
4	TS4-5	2669	26.49	0.70	24.09	0.49	25.86	0.55	25.48	0.53	26.84	1.53	26.61	1.41	22.16	0.63	25.20	1.44	-1.10	6.01	-0.18
4	TS28-5	2638	26.24	0.19	25.10	0.74	25.94	0.24	25.78	0.53	31.37	0.93	29.78	1.14	--	--	30.58	0.93	18.62	4.35	4.28
5	TS3-5	2027	56.99	0.24	53.41	0.88	55.36	0.43	55.25	0.91	59.01	1.33	--	--	--	--	59.01	1.33	6.81	2.98	2.29
6	TS6-5	2684	35.17	0.35	34.71	0.61	34.98	0.31	34.96	0.27	35.81	1.72	30.69	3.71	33.64	1.32	33.38	1.88	-4.52	5.43	-0.83
14	TS4-6	1642	25.04	0.48	25.69	0.71	25.21	0.39	25.31	0.35	23.21	0.67	--	--	22.84	0.73	23.02	0.51	-9.05	2.38	-3.80
14	TS2-6	1164	23.23	0.46	22.94	0.66	23.15	0.38	23.11	0.31	21.33	1.12	--	--	21.80	0.90	21.56	0.74	-6.71	3.44	-1.95
14	TS7-3	2377	22.74	0.48	22.79	0.66	22.78	0.39	22.77	0.30	21.36	1.20	--	--	19.42	0.63	20.39	0.96	-10.45	4.38	-2.39
15	TS5-6	1854	38.62	0.45	38.58	0.87	38.61	0.42	38.61	0.36	36.28	1.70	--	--	36.49	2.05	36.38	1.33	-5.78	3.55	-1.63
15	TS5-6	1166	34.12	0.47	33.94	0.83	34.06	0.41	34.04	0.35	32.06	2.00	--	--	31.84	1.97	31.95	1.41	-6.14	4.25	-1.44
15	TS8-3	2424	33.47	0.49	33.52	0.83	33.48	0.42	33.49	0.35	32.75	1.69	--	--	31.78	2.00	32.26	1.35	-3.67	4.15	-0.88
$\bar{z}$, $\bar{\epsilon}$, $\bar{d}$																			-3.21	±2.88	-0.84
RMS_z, $S_{\bar{z}}$																			1.11	2.23	

TABLE 4-3
FERTILE PARTICLE BURNUP MEASUREMENTS
FOR PEACH BOTTOM FUEL TEST ELEMENTS

FTE No.	Spine Sample I.D.	Core Location (mm)	Number of Samples	Radiochemistry					
				Cs-137 (at. %)		Zr (at. %)		Average (at. %)	
				Avg	±1σ	Avg	±1σ	Avg	±1σ
4	TS16-3	2574	9	0.39	0.06	--	--	--	--
5									
6	TS18-3	2589	5	0.88	0.03	0.74	0.03	0.81	0.07
14	TS2-5	1164	4	0.25	0.02	--	--	--	--
14	TS7-2	2387	5	0.29	0.01	--	--	--	--
15	TS2-5	1166	5	0.68	0.06	--	--	--	--
15	TS7-2	2392	5	0.68	0.03	--	--	--	--
15	TS6-6	1937	5	0.85	0.03	--	--	--	--

TABLE 4-4
COMPARISON OF MEASURED AND CALCULATED FISSILE AND FERTILE BURNUPS

Fissile FIMA								Fertile FIMA							
FTE No.	Core Location (mm)	% FIMA Meas. Avg	% FIMA Meas. ±1σ	% FIMA Calc.	z=(C/M)-1 z(%)	z=(C/M)-1 ε(%)	d=z/ε	FTE No.	Core Location (mm)	% FIMA Meas. Avg	% FIMA Meas. ±1σ	% FIMA Calc.	z=(C/M)-1 z(%)	z=(C/M)-1 ε(%)	d=z/ε
3	2676	7.34	0.22	6.32	-13.90	±2.58	-5.39	4	2574	0.39	0.06	0.28	-28.21	±11.04	-2.56
4	2669	25.48	0.53	23.38	-8.24	±1.91	-4.31	5	1933	2.36	0.03	2.19	-7.20	±1.18	-6.10
4	2638	25.78	0.53	23.76	-7.84	±1.90	-4.13	6	2589	0.88	0.03	0.74	-15.91	±2.87	-5.54
5	2027	55.25	0.91	53.34	-3.46	±1.59	-2.18	14	1164	0.25	0.02	0.25	0	±8.00	0
6	2684	34.96	0.27	30.35	-13.19	±0.67	-19.69	14	2387	0.29	0.01	0.21	-27.59	±2.50	-11.04
14	1642	25.31	0.35	24.09	-4.82	±1.32	-3.65	15	1166	0.68	0.06	0.83	+22.06	±10.77	+2.05
14	1164	23.11	0.31	23.13	+0.09	±1.34	+0.07	15	2392	0.68	0.03	0.66	-2.94	±4.28	-0.69
14	2377	22.77	0.30	19.37	-14.93	±1.12	-13.33	15	1937	0.85	0.03	0.86	+1.18	±3.57	+0.33
15	1854	38.61	0.36	36.82	-4.62	±0.89	-5.19								
15	1166	34.04	0.35	35.63	+4.66	±1.08	+4.31								
15	2424	33.49	0.35	30.25	-9.69	±0.94	-10.31								
$\bar{z}$, $\bar{\varepsilon}$, $\bar{d}$					-6.90	±1.49	-5.80	$\bar{z}$, $\bar{\varepsilon}$, $\bar{d}$					-7.33	±6.60	-2.94
$RMS_{\bar{z}}$, $S_{\bar{z}}$					5.78	±0.45		$RMS_{\bar{z}}$, $S_{\bar{z}}$					15.53	±2.33	

TABLE 4-5
COMPARISON OF COMPOSITE BURNUP DETERMINED
FROM DESTRUCTIVE METHODS[a] AND GAMMA SPECTROSCOPY

FTE No.	Axial Location (mm)	Fuel Stack	Destructive FIMA[a]		Gamma Spectroscopy FIMA		Relative Difference $z=(\gamma/D)-1$ (%)		
			% FIMA	±1σ (%)	% FIMA	±1σ (%)	z	$\pm\varepsilon_z$ (1σ)	$d=z/\varepsilon_z$
4	2565	3	5.29	0.05	6.14	0.65	16.1	12.3	1.31
4	2615	3	4.99	0.05	5.57	0.59	11.6	11.9	0.97
4	2565	7	6.68	0.06	6.67	0.70	-0.1	10.5	-0.01
4	2615	7	6.31	0.06	6.76	0.71	7.1	11.3	0.63
4	$\bar{z}$, $\bar{\varepsilon}_z$, $\bar{d}$						8.7	11.5	0.72
	RMS, $\varepsilon_{\bar{z}}$, $\sqrt{m}\,\bar{d}$[b]						±6.0	5.8	1.45
6	2684	3,4	9.17	0.10	10.33	1.11	12.6	12.2	1.03
6	2684	5,6	9.53	0.10	10.37	1.05	8.8	11.1	0.79
6	2684	7,8	13.24	0.13	13.30	1.58	0.4	12.0	0.03
6	$\bar{z}$, $\varepsilon_{\bar{z}}$, $\bar{d}$						7.3	11.8	0.62
	RMS, $\varepsilon_{\bar{z}}$, $\sqrt{m}\,\bar{d}$ (b)						±5.1	6.8	1.07
4,6	$\bar{z}$, $\varepsilon_{\bar{z}}$, $\bar{d}$						8.1	11.6	0.68
	RMS, $\varepsilon_{\bar{z}}$, $\sqrt{m}\,\bar{d}$[b]						±5.7	4.4	1.80
14	1164	1	1.80	0.03	2.01	0.18	11.7	10.2	1.15
	1642	1	3.24	0.04	4.08	0.28	25.9	8.8	2.95
	2387	1	3.20	0.04	3.37	0.25	5.3	7.9	0.67
14	$\bar{z}$, $\varepsilon_{\bar{z}}$, $\bar{d}$						14.3	9.0	1.59
	RMS, $\varepsilon_{\bar{z}}$, $\sqrt{m}\,\bar{d}$[b]						±8.6	5.2	2.75
15	1166	1	2.94	0.06	2.66	0.27	-9.5	9.4	-1.01
	1854	1	5.73	0.05	5.67	0.46	-1.0	8.1	-0.12
	2424	1	4.92	0.05	4.70	0.48	-4.5	9.8	-0.46
15	$\bar{z}$, $\varepsilon_{\bar{z}}$, $\bar{d}$						-5.0	9.1	-0.53
	RMS, $\varepsilon_{\bar{z}}$, $\sqrt{m}\,\bar{d}$ (b)						±3.5	5.3	0.92
14,15	$\bar{z}$, $\varepsilon_{\bar{z}}$, $\bar{d}$						4.6	9.1	0.53
	RMS, $\varepsilon_{\bar{z}}$, $\sqrt{m}\,\bar{d}$[b]						±11.7	3.7	1.30

[a] Composite FIMA calculated from fissile FIMA determined by mass spectrometry and IDMS and fertile FIMA determined by radiochemistry using Cs-137 as a burnup monitor.

[b] If $\sqrt{m}\,d > 1.96$, there is a 95% probability that there is a real bias between the parameters being compared (group agreement test). The best estimate of the bias is $\bar{z}$.

TABLE 4-6
COMPARISON OF COMPOSITE BURNUP DETERMINED FROM GAMMA SPECTROSCOPY
AND COMPOSITE BURNUP PREDICTIONS

FTE No.	Fuel Stacks	Relative Difference [(Calc/Meas)-1](%)															
		Fuel Body 1				Fuel Body 2				Fuel Body 3				Total Element			
		No. Rods	$\bar{z}$	RMS_z	$\varepsilon_{\bar{z}}$	No. Rods	$\bar{z}$	RMS_z	$\varepsilon_{\bar{z}}$	No. Rods	$\bar{z}$	RMS_z	$\varepsilon_{\bar{z}}$	No. Rods	$\bar{\bar{z}}$	RMS_z	$\varepsilon_{\bar{\bar{z}}}$
4(a)	3,4	3	8.8	±0.4	±6.7	8	-9.1	±3.2	±3.1	4	-14.7	±3.1	±4.5	15	-5.0	±10.3	±2.9
	5,6	3	15.4	±11.2	±7.1	3	-11.6	±0.7	±4.9	1	-11.4	--	±9.4	7	-2.5	±14.2	±4.2
	7,8	1	5.6	--	±11.1	6	-8.0	±5.5	±3.7	2	-4.3	±3.2	±7.1	9	-2.2	±6.8	±4.6
	$\bar{\bar{z}}$, $\varepsilon_{\bar{\bar{z}}}$	7	9.9	±7.6	±4.9	17	-9.6	±4.0	±2.3	7	-10.1	±5.0	±4.2	31	-3.2	±10.9	±2.3
6(a)	3,4	7	-7.7	±5.1	±3.7	7	-12.2	±2.0	±3.5	7	-12.5	±4.2	±3.5	21	-10.8	±4.6	±2.1
	5,6	7	-4.6	±6.8	±3.8	7	-11.7	±2.9	±3.5	7	-12.1	±2.4	±3.5	21	-9.5	±5.7	±2.1
	7,8	7	-0.9	±3.5	±3.9	7	-12.1	±5.2	±3.7	7	-5.2	±6.0	±4.2	21	-6.1	±6.8	±2.3
	$\bar{\bar{z}}$, $\varepsilon_{\bar{\bar{z}}}$	21	-4.4	±6.0	±2.2	21	-12.0	±3.6	±2.1	21	-9.9	±5.6	±2.2	63	-8.8	±6.1	±1.2
14(b)	1	11	5.2	±12.9	±2.6	9	-3.0	±3.5	±2.3	6	-4.2	±2.0	±3.0	26	-0.7	±8.8	±1.5
15(c)	1	11	7.4	±10.3	±3.0	11	-5.7	±2.8	±2.7	11	-7.5	±2.8	±2.7	33	-1.9	±9.2	±1.6
Total		50	4.5	±11.0	±1.7	58	-7.6	±4.9	±1.2	45	-7.9	±4.8	±1.6	153	-3.6	±9.4	±0.9

(a) Correction determined for calibration of 8-hole test element gamma scans in Table 4-8 applied (i.e., $F'_\gamma = F_\gamma/1.081$).

(b) Correction determined for FTE-14 fuel rod scans in Table 4-8 applied (i.e., $F'_\gamma = F_\gamma/1.143$).

(c) Correction determined for FTE-15 fuel rod scans in Table 4-8 applied (i.e., $F'_\gamma = F_\gamma/0.95$).

TABLE 4-7
RELATIVE DIFFERENCES BETWEEN CALCULATED AND MEASURED NUCLIDE CONCENTRATIONS IN PEACH BOTTOM FUEL TEST ELEMENTS

FTE No.	Axial Core Location (mm)	Bias in Isotopic Concentrations [(Calc/Meas)-1]										Number of Samples	Fuel Particle Type
		U-233		U-234		U-235		U-236		U-238			
		Bias (%)	1σ (%)	Bias (%)	1σ (%)	Bias (%)	1σ (%)	Bias (%)	1σ (%)	Bias (%)	1σ (%)		
Fissile Fuel													
3	2672	--	--	-21.4		+1.3		-18.2		-9.7		2	UC_2 TRISO
3	2640	--	--	-18.7		+1.2		-18.4		-7.6		2	UO_2 TRISO
4	2669	--	--	-16.0		-0.1		-5.3		-3.0		4	UC_2 TRISO
4	2638	--	--	-15.4	±0.3	+1.2	0.0	-7.1	±0.2	-3.1	±0.2	2	UO_2 TRISO
5	2027	--	--	+24.9		+0.9		-1.0		-5.1		2	UC_2 TRISO
6	2684	--	--	-26.8	±0.4	+3.3	±0.1	-14.8	±0.3	-5.5	±0.5	2	UC_2 TRISO
14	1164	--	--	+5.5	±0.5	-0.9	0.0	+9.6	±0.2	0.0	±0.3	1	UC_xO_y TRISO
14	1642	--	--	+11.5	±0.6	-0.2	0.0	+1.6	±0.4	-1.0	±0.2	1	UC_xO_y TRISO
14	2377	--	--	-1.6	±1.3	+1.3	±0.1	-11.6	±0.3	-3.2	±0.4	1	UC_xO_y TRISO
15	1166	--	--	+12.3	±1.1	-2.5	±0.1	+12.7	±0.5	+2.5	±0.8	1	UC_xO_y TRISO
15	1854	--	--	+15.3	±1.0	+0.4	±0.1	-2.0	±0.4	-1.9	±0.8	1	UC_xO_y TRISO
15	2424	--	--	-7.4	±0.5	+1.8	±0.1	-9.4	±0.5	-3.1	±0.7	1	UC_xO_y TRISO
Fertile Fuel													
3	2577	+0.3		+8.7		-84.5		(a)	--	(a)	--	2	
4	2574	-1.0	0.0	+22.2	±0.5	+37.6	±10.2	(a)	--	(a)	--	2	ThC_2 TRISO
5	1930	+1.5		-1.9		-52.1		(a)	--	(a)	--	2	ThC_2 TRISO
6	2589	-1.3	0.0	+16.0	±0.6	+34.6	±7.4	(a)	--	(a)	--	2	ThC_2 TRISO
14	1164	±1.0	0.0	-19.5	±0.2	-28.9	±7.9	(a)	--	(a)	--	5	ThC_2 BISO
14	2377	+0.8	0.0	-12.4	±0.3	-33.8	±0.3	(a)	--	(a)	--	5	ThC_2 BISO
15	1166	+1.1	±0.1	+1.5	±0.2	-52.4	±5.2	(a)	--	(a)	--	5	ThC_2 BISO
15	1937	+3.7	±0.8	-13.5	±0.7	-80.0	±6.0	(a)	--	(a)	--	5	ThC_2 BISO
15	2392	+1.3	±0.2	+1.5	±0.4	-54.0	±5.4	(a)	--	(a)	--	5	ThC_2 BISO

(a) Measured, but no prediction available.

TABLE 4-8
MAXIMUM AND MINIMUM RELATIVE
DIFFERENCES BETWEEN CALCULATED
AND PREDICTED ISOTOPIC CONCENTRATIONS

Fuel Type	Isotopic Concentration Bias [(Calc/Meas)-1](%)				
	U-233	U-234	U-235	U-236	U-238
Fissile, max.	NA[a]	+15.6	+3.3	+12.5	+1.9
Fuel particle, min.	NA[a]	-26.8	-2.4	-14.8	-5.5
Fertile, max.	+3.7	+22.2	+37.6	Measured, but no predictions available	
Fuel particle, min.	-1.3	-19.5	-80.0		

[a] NA = not applicable.

TABLE 4-9
DNAA URANIUM MEASUREMENTS OF
PEACH BOTTOM HISTORICAL FUEL RODS

Rod Batch I.D.	No. Rods Measured	Uranium Loadings			Relative Diff. [(Calc/Meas)-1]		Tests		Results	Irradiation
		Meas (g)	$\pm S_{\bar{x}}$ (g)	Calc Target (g)	z	$\pm S_z$	$D=z/S_z$	D^2		
6	2	0.614	0.0064	0.615	+0.0016	0.0104	0.156	0.024		FTE-5 Stack 1,2
9	2	0.758	0.0058	0.763	+0.0066	0.0077	0.856	0.733		RTE 1,2
10	2	0.6285	0.0090	0.625	-0.0056	0.0142	-0.391	0.153		RTE 3,4
11	2	0.6335	0.0075	0.625	-0.0134	0.0117	-1.149	1.320		RTE 5,6,7,8
12	2	0.618	0.0030	0.615	-0.0049	0.0048	-1.005	1.010		RTE-5, Stack 3,4
15	2	0.7635	0.0042	0.763	-0.0007	0.0055	-0.119	0.014		RTE 1,2
16	2	0.6475	0.0031	0.625	-0.0347	0.0046	-7.519	56.541	Significant	RTE 3,4
17	2	0.6485	0.0011	0.625	-0.0362	0.0016	-22.167	491.37	Significant	RTE 5,6,7,8
26	3	0.6450	0.0037	0.615	-0.0465	0.0055	-8.504	72.31	Significant	FTE-5 Stack 5,6
29	2	0.658	0.0012	0.615	-0.0654	0.0017	-38.34	1469.86	Significant	FTE-5 Stack 7,8
11399	2	0.5995	0.0030	0.553	-0.0776	0.0046	-16.80	282.35	Significant	FTE-4 Stack 5,6
11400	2	0.690	0.0012	0.656	-0.0493	0.0016	-29.80	888.149	Significant	FTE-6 Stack 5,6
11402	2	0.573	0.022	0.553	-0.0349	0.0371	-0.942	0.887		FTE-4 Stack 3,4
11410	4	0.6213	0.0027	0.656	+0.0559	0.0046	12.172	148.16	Significant	FTE-6 Stack 1,2
11411	2	0.661	0.0010	0.656	-0.0076	0.0015	-5.038	25.383	Significant	FTE-6 Stack 7,8
11413	3	0.7847	0.0040	0.739	-0.0582	0.0048	-12.132	147.17	Significant	RTE-1
11419	2	0.6430	0.0016	0.656	+0.0202	0.0025	7.964	63.43	Significant	RTE-1
11421	3	0.7367	0.0037	0.739	+0.0031	0.0050	0.620	0.384		RTE-1
11422	1	0.736	0.0028	0.739	+0.0041	0.0038	1.067	1.139		RTE-1
11435	1	0.778	0.0034	0.739	-0.050	0.0042	-12.076	145.83	Significant	RTE-1
11704	2	0.6875	0.0018	0.656	-0.046	0.0025	-18.34	336.37	Significant	FTE-6 Stack 3,4
11705	4	0.541	0.0017	0.553	+0.022	0.0032	6.906	47.69	Significant	FTE-4 Stack 1,2
11706	2	0.5785	0.0029	0.553	-0.044	0.0047	-9.199	84.61	Significant	FTE-4 Stack 7,8
$\bar{x}_1$, S_x		0.6628	0.0060	0.6492	-0.0201	0.0097	-6.686	186.61		
RMS_1, $S_{\bar{x}}$		0.0671	0.0013	0.0671	0.0316	0.0020	11.863	±345.80		
					10.15>1.39 sign. axial variation		32.06 >1.96 sign. group agreement test	186.61 >1.39 sign. group goodness to fit		

TABLE 4-10
BURNUP COMPARISON FOR TEST ELEMENTS
SCANNED DURING PHASE I OF PEACH BOTTOM EOL PROGRAM

Element I.D.	GAUGE Position (Patch/Hex.)	Total FIMA			Relative Difference, [(C/M)-1]=z		Comparison	
		GAUGE (%)	Meas. (%)	$S_M(1\sigma)$ (%)	z	$S_z(1\sigma)$	Test 1 $D = z/S_z$	Test 2 D^2
C02-01 (FTE-6)	6/5	8.25	7.48	±0.57	+0.103	±0.084	1.220	1.490
D14-08 (FTE-8)	88/1	9.32	10.42	±0.71	-0.106	±0.061	-1.732	3.000
C14-08 (FTE-5)	88/1,83/1	9.31	11.01	±0.66	-0.155	±0.051	-3.057	9.343
A02-01 (FTE-17)	4/5	4.11	5.44	±0.43	-0.244	±0.060	-4.094	16.760
E05-04 (FBTE-1)	17/6	10.22	10.91	±0.74	-0.063	±0.064	-1.000	1.000
F14-08 (FTE-7)	68/1	5.82	7.12	±0.46	-0.183	±0.053	-3.474	12.066
A11-11 (FBTE-2)	34/5	10.17	14.87	±0.89	-0.316	±0.041	-7.714	59.509
F06-01 (FTE-12)	22/5	5.39	5.57	±0.40	-0.032	±0.070	-0.460	0.211
Mean $\bar{x}$, $\bar{S}_x$		7.824	9.103	±0.629	-0.125	±0.062	-2.539	12.922
RMS, $S_{\bar{x}}$ Test		±2.225	±3.049	±0.222	±0.122	±0.022	±2.545	±18.479

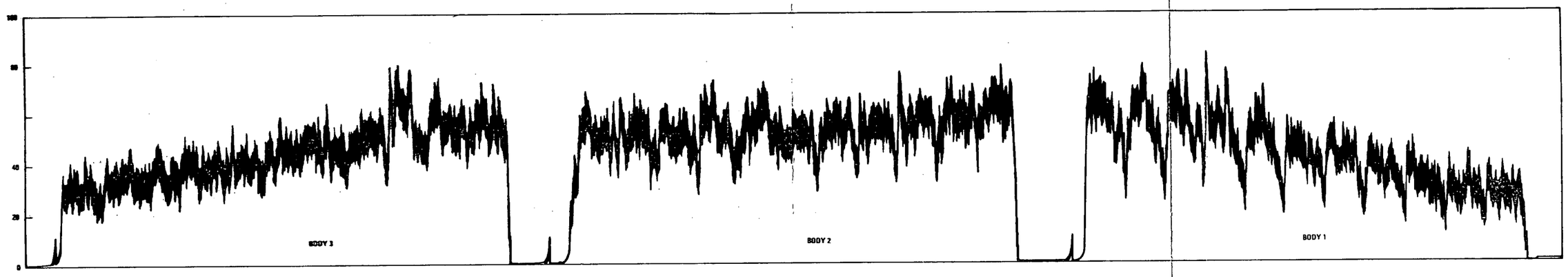

Fig. 4-1. Typical gamma scan strip chart (FTE-14)

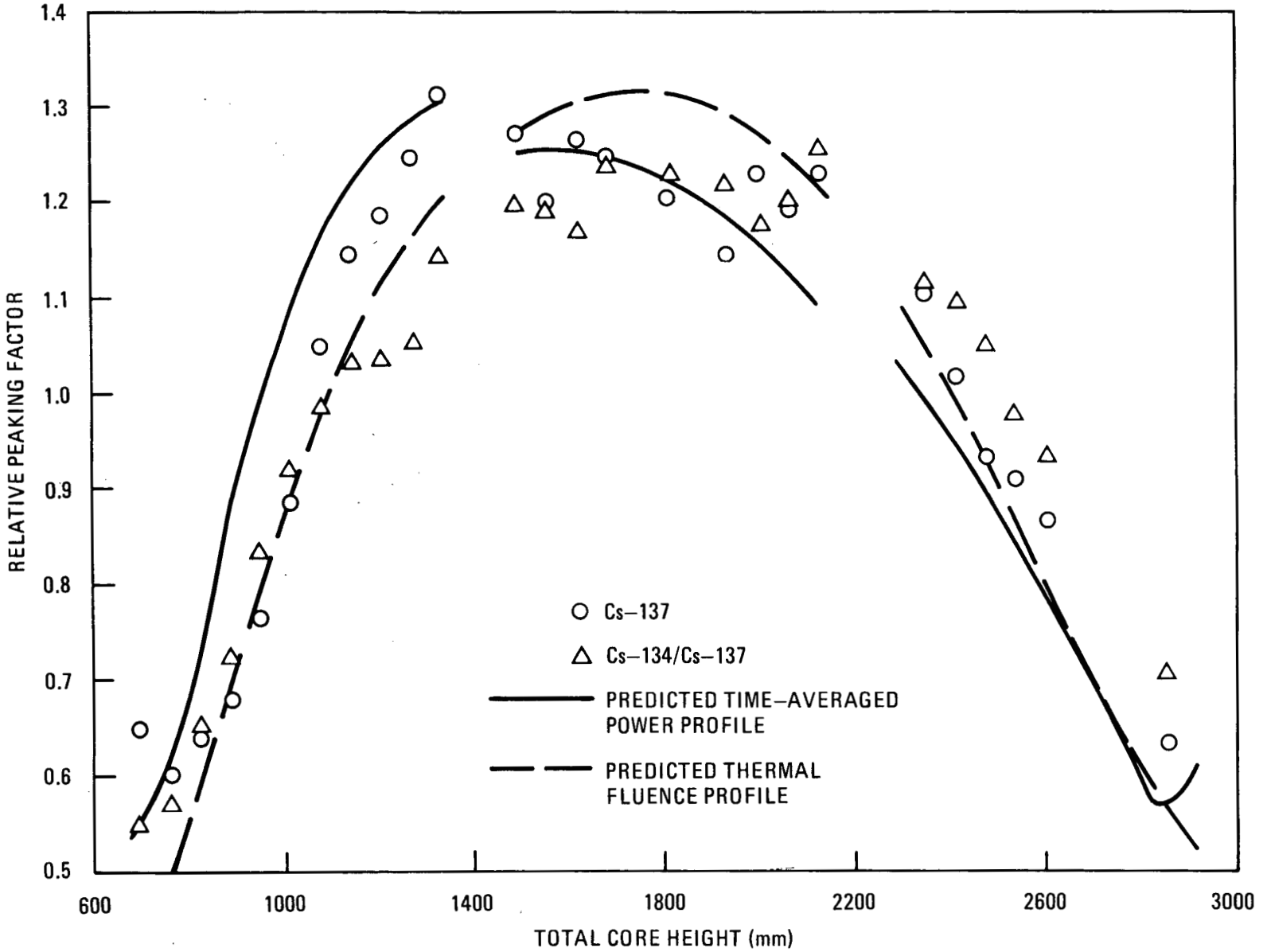

Fig. 4-2. Comparison of Cs-137 and Cs-134/Cs-137 profiles for FTE-14 with predicted time-averaged power and thermal fluence profiles

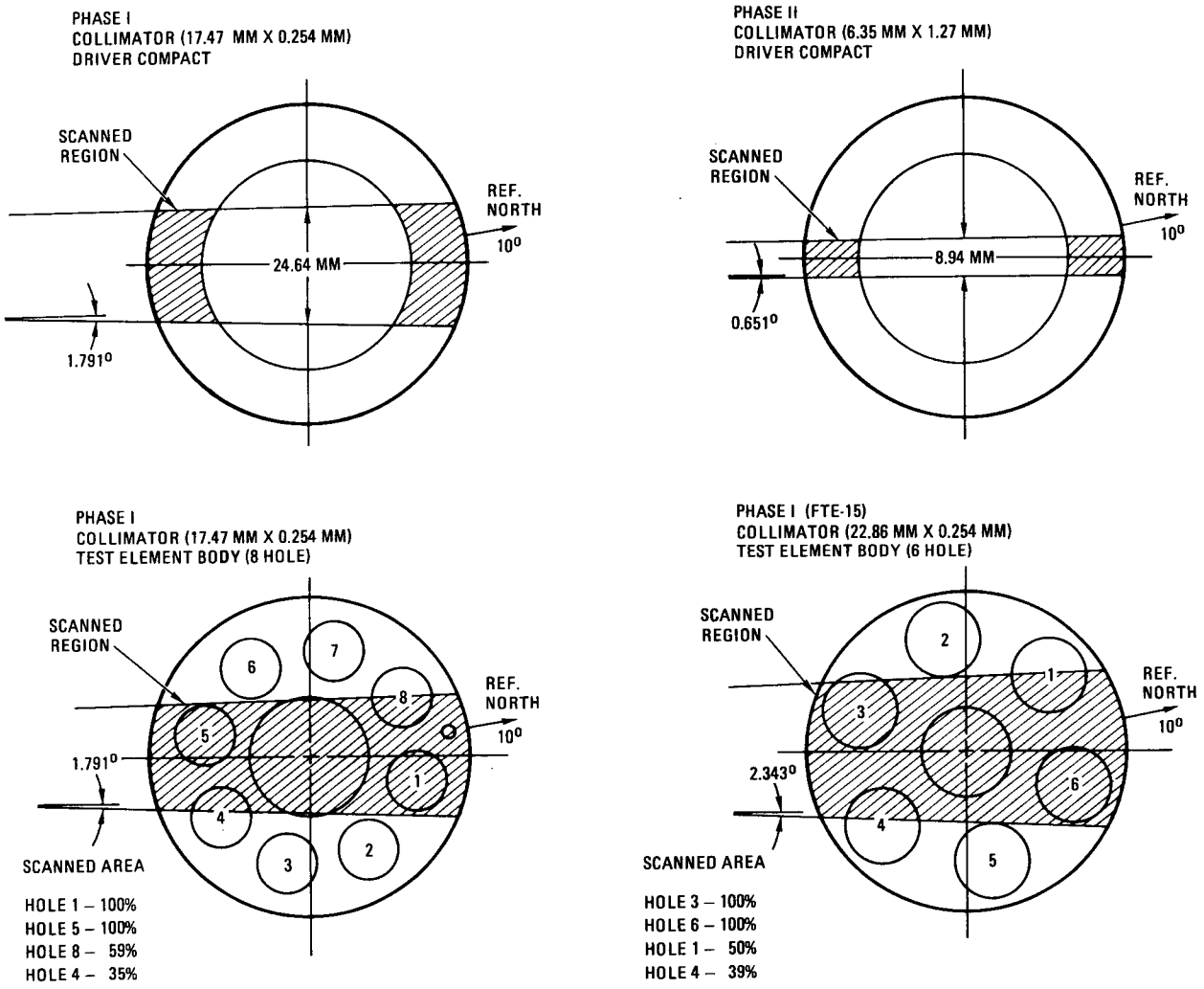

Fig. 4-3. Effective scanning paths of Peach Bottom EOL gamma scanning

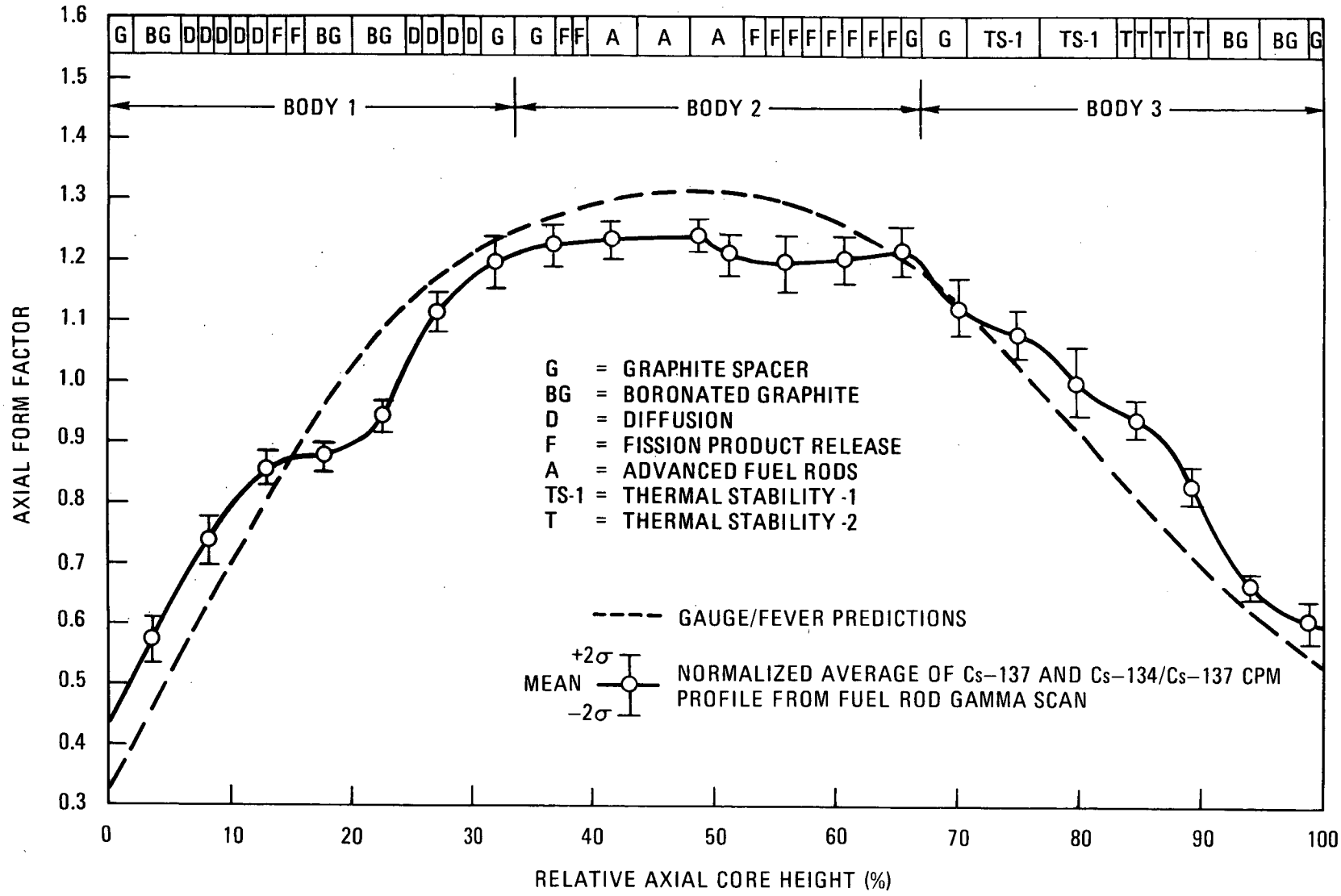

Fig. 4-4. FTE-6 normalized, predicted, and measured fluence profiles determined from fuel stack 3 and 5 gamma scans

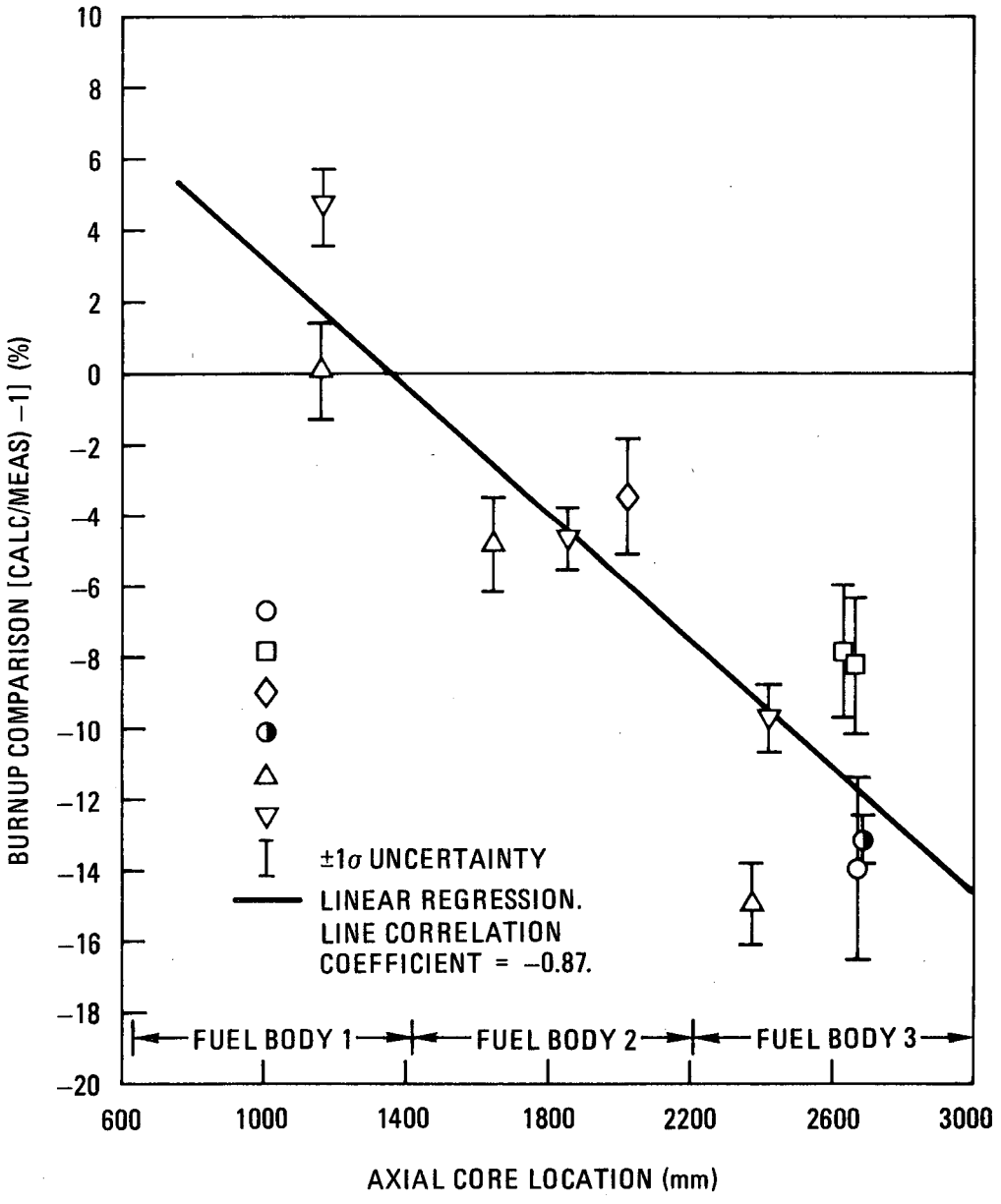

Fig. 4-5. Comparison of calculated and measured fissile burnups

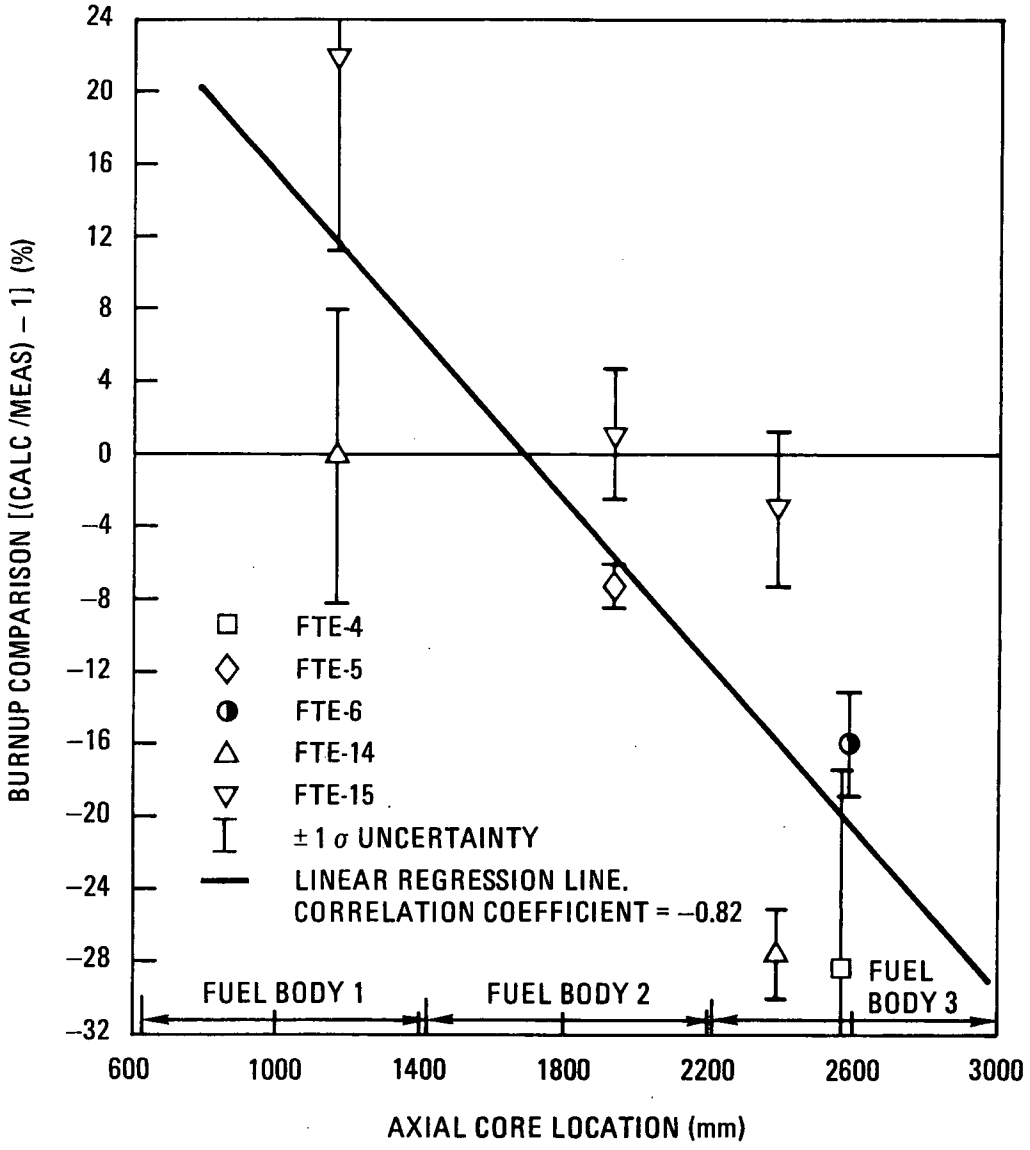

Fig. 4-6. Comparison of calculated and measured fertile burnups

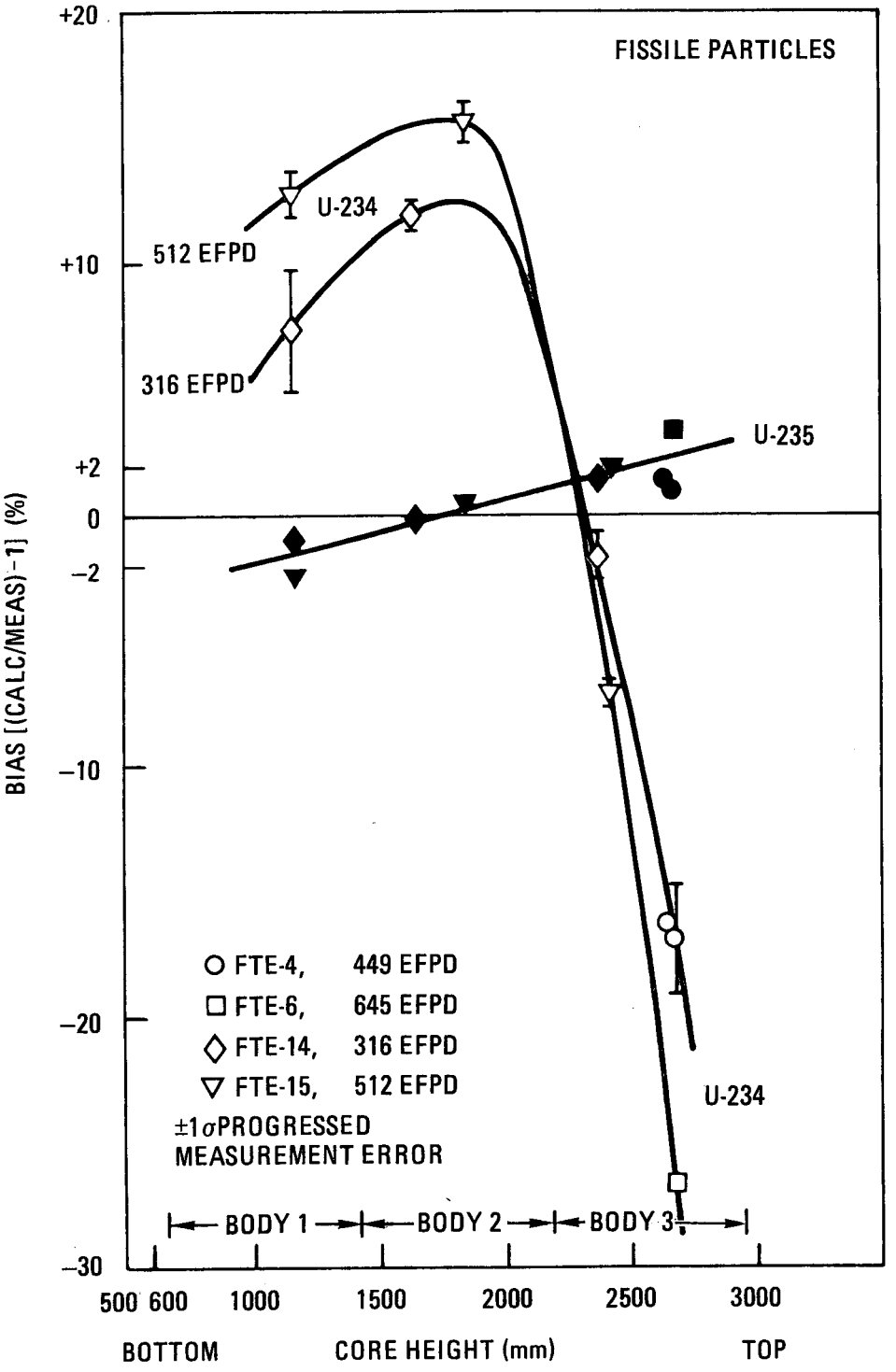

Fig. 4-7. Relative difference between calculated and measured U-234 and U-235 concentration for fissile particles from Peach Bottom fuel test elements

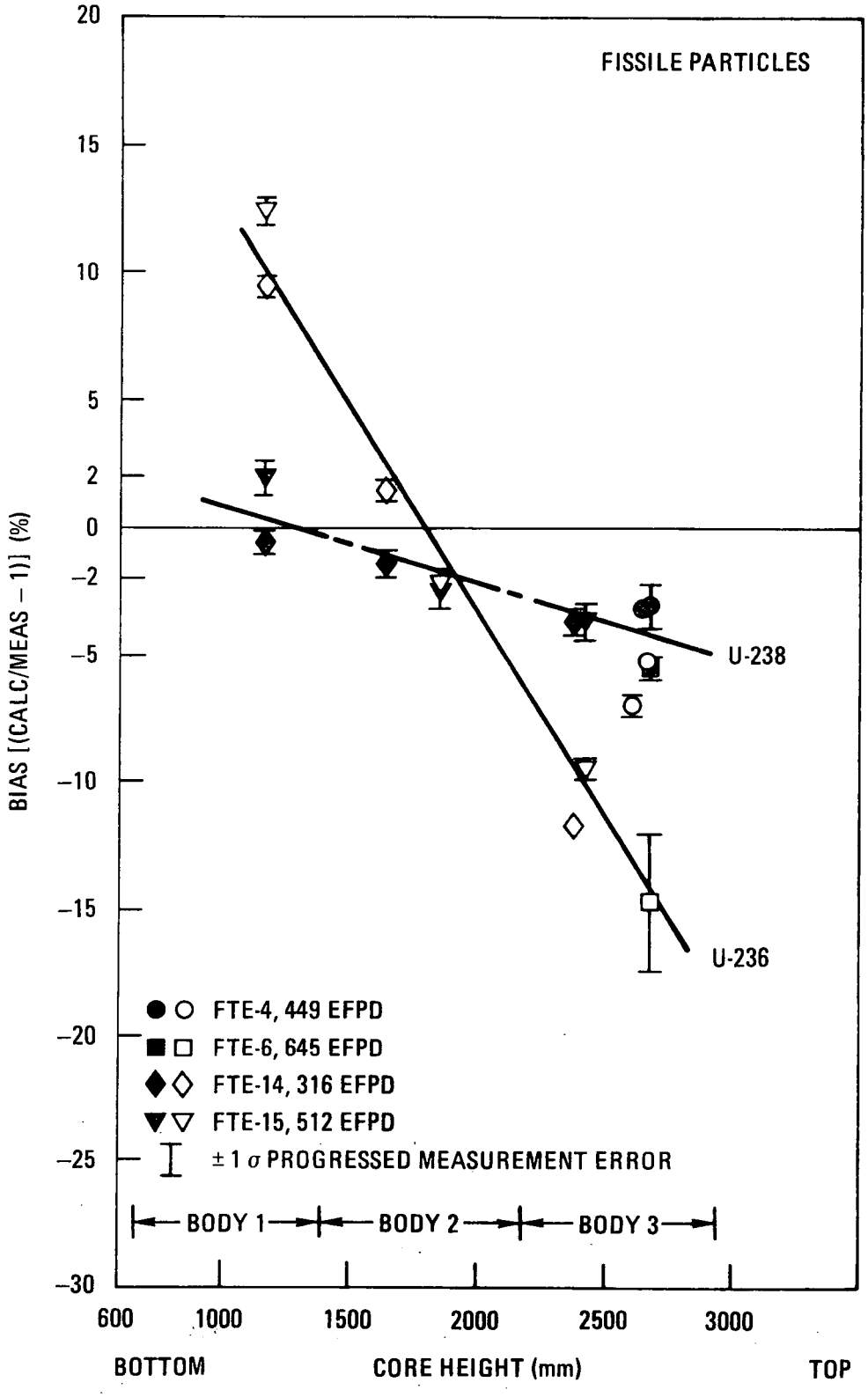

Fig. 4-8. Relative difference between calculated and measured U-236 and U-238 concentration for fissile particles from Peach Bottom fuel test elements

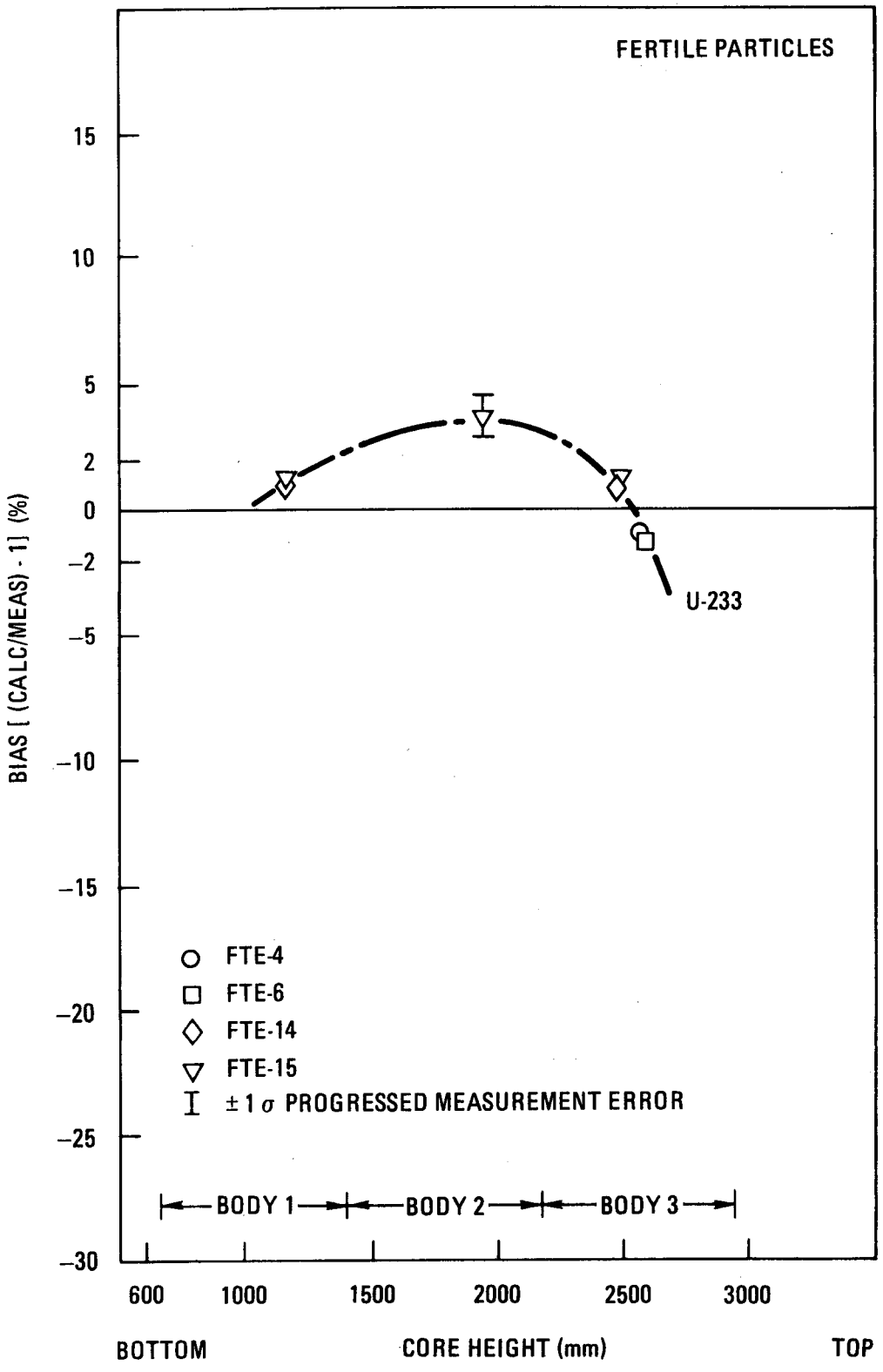

Fig. 4-9. Relative difference between calculated and measured U-233 concentration for fertile particles from Peach Bottom fuel test elements

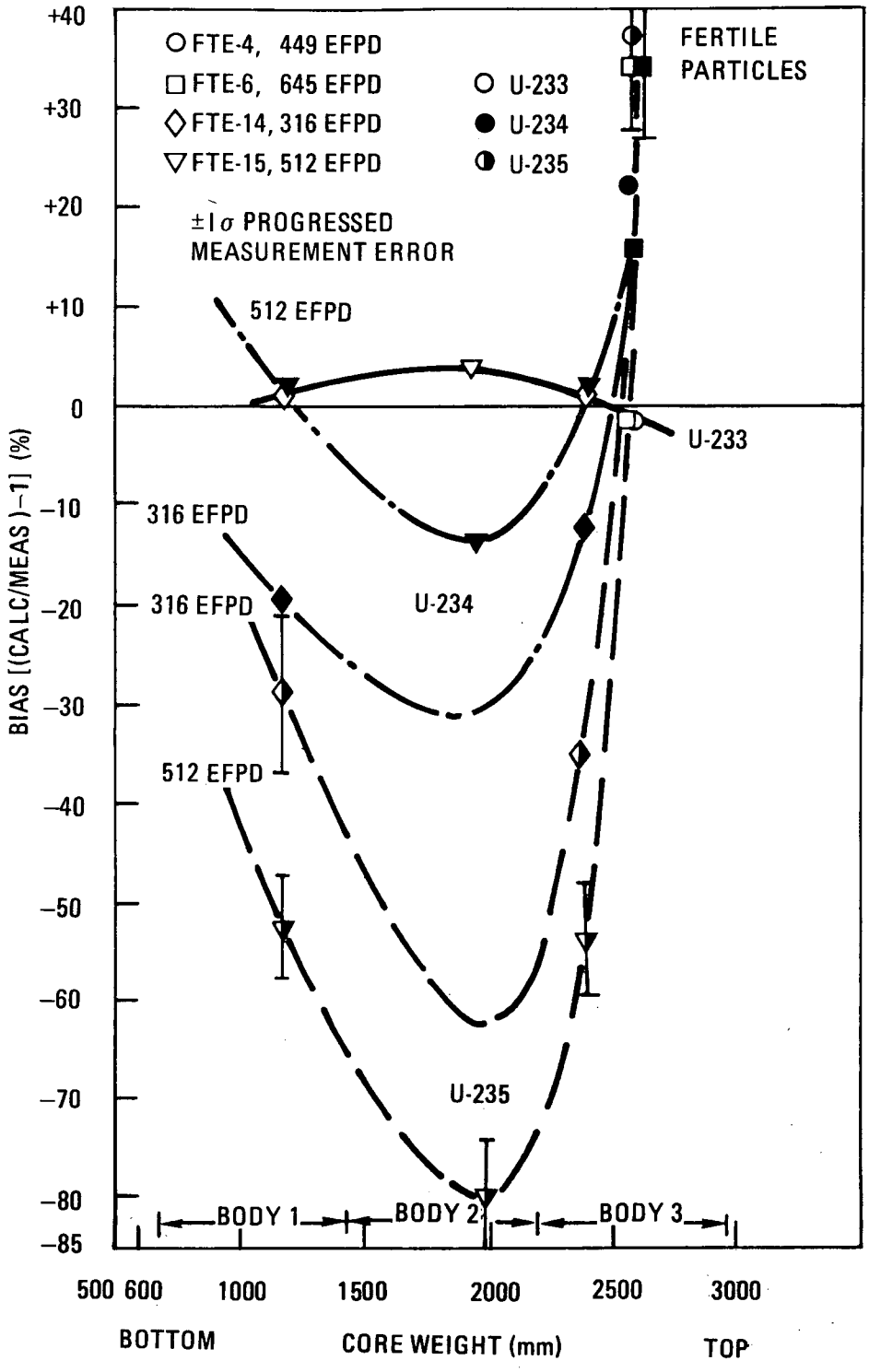

Fig. 4-10. Relative difference between calculated and measured U-233, U-234, and U-235 concentration for fertile particles from Peach Bottom fuel test elements

5. THERMAL DESIGN VERIFICATION

5.1. TEMPERATURE MEASUREMENTS

Twenty-five of the 33 test elements contained thermocouples for monitoring in-pile temperatures: in most cases, a C/A type located near the outer perimeter of the fuel body, where temperatures were generally less than 1100°C, and a W/Re type situated in a slot in the inner surface of the annular fuel body, where temperatures close to fuel centerline temperatures were experienced. The locations of these thermocouples are shown in Figs. 2-4, 2-5, 2-6, and 2-9. In a few of the test elements, a second W/Re type thermocouple was substituted for the less temperature resistant C/A type and positioned to monitor fuel temperatures. The hot junctions of the thermocouples were generally positioned at, or near, 1918 mm total core height, the axial location at which peak fuel temperatures were expected.

Temperature readings were recorded on a weekly basis and had to be corrected for the following:

1. Changes in cold junction temperature (standoff pin temperature). This correction was done automatically at the reactor site.
2. Adjustment in calibration equipment for the W/Re type, for which readings were 22°C too high because of change from the W-5% Re/W-26% type to the W-3% Re/W-25% Re type between Core 1 and Core 2.
3. Decalibration of the W/Re type due to effect on emf output of neutron bombardment and transmutation.

The derivation of the recalibration formula used on Peach Bottom W/Re thermocouples is discussed in Section 5.2.

The performance of each thermocouple is summarized in Table 5-1. Reliable readings have been defined as measurements from the axial location where the thermocouple hot junction was supposed to be located. Although a thermocouple was considered to have failed once it stopped giving reliable readings, many thermocouples did not fail entirely but apparently short circuited and continued to give measurements from an axial location lower in the core. It is not always clear when a thermocouple malfunctioned, and there is no way to know for certain whether the thermocouple hot junction was exactly at the axial location where it was supposed to be. In evaluating the thermocouple data, it was assumed that all readings were reliable unless thermocouple failure was clearly indicated. Indications of obvious failure include sudden and unexpected large reductions in recorded temperature followed by continuous low readings, marked deviation from the temperature trend established by the other thermocouple in the element (if functional) and by thermocouples in other elements having a similar environment, and temperature readings so far below expected temperatures that they are unbelievable. Some likely reasons for thermocouple failure are:

1. Structural defectiveness or improper installation.
2. Thermal shock resulting from rapid and large changes in temperature, such as those caused by startup and shutdown or by sudden changes in local or total core power.
3. Excessive temperature.

The temperature levels at which thermocouple performance is jeopardized are indicated by the following observations:

1. The highest temperature recorded by a C/A thermocouple in the Peach Bottom core was approximately 1180°C (in E05-01), and the thermocouple failed immediately afterward. The highest temperature recorded by a C/A thermocouple in a test element was approximately 1100°C in FTE-9 and FBTE-2.

2. Uncorrected W/Re thermocouple readings between 1300° and 1350°C were recorded for FTE-13, FTE-14, and FTE-18. The actual temperatures were 50° to 150°C higher as determined from recalibration (see Section 5.2). Barring failure for reasons 1 or 2 cited above, the C/A thermocouples and the W/Re thermocouples should perform dependably up to temperatures of about 1100° and 1400°C, respectively.

5.2. THERMOCOUPLE RECALIBRATION

Thermocouple recalibration has been carried out on a group of six thermocouples recovered from Peach Bottom test elements, including two each from FTE-5, FTE-18, and FPTE-3. Five of these were W-3% Re/W-25% Re (Type W) thermocouples and one was a C/A (Type K) thermocouple. The C/A thermocouple, for which no decalibration was expected, was included as a control test for the recalibration experiment. Resistance measurements for the thermocouples were consistent with preirradiation values, indicating that all were intact after irradiation. Each thermocouple was inserted into a furnace at known temperatures ranging from 680° to 980°C, and the actual and indicated temperatures were recorded (Ref. 5-1). The recalibration results are shown in Fig. 5-1, which plots the actual temperature T_a versus the indicated temperature T_i. The recalibration results for each thermocouple have been analyzed via linear regression by the method of least squares under the assumption of 0°C as the cold junction temperature:

$$T_a = T_o + K \times T_i \quad ,$$

with the regression constants being

$$T_o = 1/n \sum T_a - K/n \sum T_i$$

and

$$K = \frac{\sum T_i T_a - \left(\sum T_i \sum T_a\right)/n}{\sum T_i^2 - \left(\sum T_i\right)^2/n}$$

The correlation coefficients are in all cases very close or equal to 1.0 (see Fig. 5-1), indicating a strong linear correlation for the covered temperature range. This temperature range corresponds to irradiation temperatures from 1020° to 1320°C based on a cold junction temperature of 340°C and encompasses the irradiation temperatures experienced by the majority of the thermocouples. An additional measurement at an actual furnace temperature of 420°C made with thermocouple FPTE-3B shows that the linear correlation also holds at lower temperatures. It is therefore concluded that the recalibration results can be extrapolated to higher temperatures as well. (These temperatures were not achievable during recalibration because of a furnace limitation.) The standard deviations along the regression lines range from ±1° to ±8°C and average ±4°C, which is within the estimated ±8°C error associated with the test equipment. The nearly identical decalibration experienced by the two identical thermocouples from FTE-18 shows decalibration to be a systematic effect for the Type W thermocouples. A reproducibility of ±8°C is concluded for the decalibration effect. This represents about 1% of the cold junction to hot junction temperature rise for the test element thermocouples. As expected, no decalibration was found for the C/A thermocouple, which supports the validity of the recalibration exercise.

The regression constants T_o and K are correlated with the thermal fluence ψ in Figs. 5-2 and 5-3, respectively. A second-order fit was used for the intercept T_o and a first-order fit was used for the slope K. As can be seen, the thermocouples from FTE-5 and FTE-18 follow a certain pattern, but the FPTE-3 thermocouples are somewhat different. The dissimilar decalibration of the thermocouples can be attributed to the following factors. First, the hot junctions of the FPTE-3 thermocouples were inserted about 7 mm directly into fuel compacts, while the FTE-5 and FTE-18 thermocouples were surrounded by graphite and about 7 mm away from the nearest fuel zone. The lower thermal neutron microflux in the fuel compacts resulted in less decalibration in the FPTE-3 thermocouples. Second, the active core lengths of the FPTE-3 thermocouples (648 mm and 1210 mm) were different from those of the FTE-5 and FTE-18 thermocouples (1257 mm).

Since the decalibration resulting from thermal neutron bombardment is accumulated over the thermocouple length, the thermocouple with the shortest active core length experienced the least calibration.

The following recalibration formula has been developed for all Type W Peach Bottom thermocouples:

$$T_a = a(\psi + b\psi^2) + (1 + c\psi)(T_i - T_s) + T_s,$$

where $a = -1.303 \times 10^{-4}\ gh^{1.667}$ (see Fig. 5-4),

$b = -0.0669$,

$c = 2.916 \times 10^{-3}\ gh^{0.4544}$ (see Fig. 5-5),

g = geometry factor to account for location of thermocouple hot junction in fuel ($g = 1.0$) or in graphite ($g - 1.64$),

h = thermocouple length within the active core (mm),

T_i = indicated temperature (°C),

T_s = standoff pin temperature (cold junction) (°C),

T_a = actual temperature (°C),

ψ = thermal neutron fluence in 10^{25} n/m^2 [$(E < 382$ J)].

In developing the above equation, it was assumed that fluence and temperature gradients were similar for all Peach Bottom regular fuel elements and test elements and would correlate with the thermocouple length within the active core. Under this assumption, the effect of these factors on thermocouple decalibration is accounted for by the h term in the recalibration formula. In instrumented regular fuel elements, the thermocouples were situated within slots in the graphite spine directly adjacent to fuel compacts. Because of this geometrical configuration, the geometry factor for regular fuel element thermocouples was taken to be 1.32, the average of the geometry factors for thermocouples surrounded by graphite ($g = 1.64$) and those surrounded by fuel ($g = 1.0$).

The error (1σ) associated with the recalibration formula is given by the equation

$$S \cong \sqrt{S_1^2 + S_2^2 + S_3^2 + S_4^2} \quad ,$$

where $S_1 = [a + 2\,b\psi + C(T_i - T_s)]\, S_\psi$,

$S_2 \cong 0.8\psi$,

$S_3 = 1.09 \times 10^{-3}\, \psi (T_i - T_s)$,

$S_4 \cong 0.4\psi$,

$S_\psi = 0.096\psi$ or 0.076ψ.

The error terms S_1, S_2, S_3, and S_4 are the errors resulting from the uncertainties on the thermal neutron fluence, regression for terms a and b, the term $K - 1 + c\psi$, and the geometry factor g, respectively. A 6.8% (1σ) error on the thermal fluence was determined from calibrated gamma spectroscopy on 48 standard Peach Bottom fuel elements (Ref. 5-2). This error applies to FPTE-3 as well. For elements like FTE-5 and FTE-18 for which burnup and gamma spectroscopic measurements have been fed back into the nuclear calculations, the uncertainty on the thermal neutron fluence can be reduced to 3.4% (1). Consequently, the error of the fluence term S_ψ is 9.6% and 7.6% when applied to non-recalibrated thermocouples from elements without and with burnup measurements, respectively.

5.3. COMPARISON OF CALCULATED AND MEASURED TEMPERATURE

A comparison of calculated and measured temperatures was performed for Peach Bottom test elements and is summarized in Table 5-2. Measured temperatures were obtained by time averaging the readings for individual thermocouples over each TREVER time interval (Section 3). A total of 261 measured temperatures obtained from 28 thermocouples in 20 fuel elements were compared with predictions.

The agreement between measured and calculated temperature is within ±82°C (1σ) with no significant bias between measurements and predictions.

These results are in close agreement with the results for regular Peach Bottom fuel elements (Ref. 5-3). The agreement between measured and calculated temperatures for these elements was within ±78°C (1σ) with an apparent bias of +27°C (predicted - measured) ±7°C (1σ).

As another check on thermal calculations, measured and calculated temperature differences (ΔT) between the C/A thermocouple and W/Re thermocouple positions were compared. This comparison is shown in Table 5-3. Unfortunately, the large number of thermocouple failures (particularly failure of the C/A type) limited the quantity of data available for comparison with predictions to 34 measurements in five test elements. The disagreement between measurements and predictions was fairly high, ±42°C (1σ). However, no significant bias was found, which indicates that there was no systematic underprediction or overprediction of the heat flux or effective conductance.

REFERENCES

5-1. McNair, J. M., "Calibration of Peach Bottom Test Element Thermo-Couples," GA unpublished data.

5-2. Holzgraf, J. F., F. McCord, and C. F. Wallroth, "Gamma Spectroscopic Examination of the Peach Bottom HTGR Reactor Core Components," DOE Report GA-A13453, April 1978.

5-3. Saurwein, J. J., and C. F. Wallroth, "Nuclear and Thermal Design Verification for the Peach Bottom High-Temperature Gas-Cooled Reactor," DOE Report GA-A14726, September 1979.

TABLE 5-1
SUMMARY OF THERMOCOUPLE PERFORMANCE IN PEACH BOTTOM TEST ELEMENTS

Test Element	Thermocouple Type	Hot Junction Location [Total Core Height (mm)]	Duration of Reliable Readings (EFPD)	Remarks
FTE-1	C/A	1918	0	Beginning of life (BOL) failure.
	W/Re	1918	0-252	OK throughout life.
FTE-2	C/A	1918	0-385	OK throughout life.
	W/Re	1918	0-385	OK throughout life.
FTE-3	C/A	1918	252-262	Functional but appears to have short-circuited shortly after 262 EFPD.
	W/Re	1918	0	Functional but appears to have short-circuited at BOL.
FTE-4	C/A	1918	0	BOL failure.
	W/Re	1918	252-701	OK throughout life.
FTE-5	C/A	1918	0	Functional but appears to have short-circuited immediately after BOL.
	W/Re	1918	0	Very erratic from 0-250 EFPD and then failed completely. Reading of 1337°C obtained at 228 EFPD.
FTE-6	C/A	1918	0	Reading of 941°C at BOL and then short-circuited. Functional throughout life.
	W/Re	1918	252-897	OK throughout life.
FTE-7	C/A	1918	0	Functional but short-circuited at BOL.
	W/Re	1918	252-897	OK throughout life.
FTE-8	C/A	1918	0	Functional but short-circuited at BOL.
	W/Re	1918	252-897	OK throughout life.
FTE-9	C/A	1918	252-897	OK throughout life.
	W/Re	1918	252-897	OK throughout life.
FTE-10	W/Re	1918	0	Readings obtained but clearly incorrect. Apparently BOL failure.
	W/Re	2388	328-897	No readings for first 75 EFPD but then OK.

TABLE 5-1 (Continued)

Test Element	Thermocouple Type	Hot Junction Location [Total Core Height (mm)]	Duration of Reliable Readings (EFPD)	Remarks
FTE-12	C/A	2009	252-?	Readings after 460 EFPD not available.
	W/Re	2009	300-426	Readings somewhat erratic prior to 300 EFPD but then stabilized. Reading of 1402°C obtained at 426 EFPD followed by thermocouple failure.
FTE-13	W/Re	1918	385-818	OK until 818 EFPD and then short-circuited.
	W/Re	1918	385-897	OK throughout life.
FTE-14	C/A	1766	0	BOL failure.
	W/Re	1766	385-701	OK throughout life.
FTE-15	C/A	1766	0	Functional but short-circuited at BOL. Complete failure at 700 EFPD.
	W/Re	1766	0	Functional but very erratic until 780 EFPD and then failed. Reading of 1300°C obtained at 600 EFPD.
FTE-16	W/Re	1918	385-897	OK throughout life.
	W/Re	1918	385-750	Readings available at regular intervals until 436 EFPD. Subsequent readings only at 667 EFPD and 750 EFPD.
FTE-17	W/Re	1918	0	Functional but short-circuited at BOL.
	W/Re	1732	385-897	OK throughout life.
FTE-18	W/Re	1918	385-897	OK throughout life.
	W/Re	1918	0	BOL failure.
FBTE-1	C/A	1918	0-?	OK through 422 EFPD. Readings after 422 EFPD not available.
	W/Re	1918	252-?	Apparent malfunction prior to 252 EFPD. Then recovered and OK through 422 EFPD. Readings after 422 EFPD not available.

TABLE 5-1 (Continued)

Test Element	Thermocouple Type	Hot Junction Location [Total Core Height (mm)]	Duration of Reliable Readings (EFPD)	Remarks
FBTE-2	C/A W/Re	1918 1918	0-407 0-252, 385-897	Failed completely after 407 EFPD. OK except from 252-385 EFPD when element was at core location A02-01. Short-circuit or poor contact between thermocouple leads and standoff pin resulted in erroneous readings during this time interval.
FBTE-3	C/A W/Re	1918 1918	0-318 0-897	Complete failure after 318 EFPD. OK throughout life.
FBTE-4	C/A W/Re	1918 1918	0-252 0-252	OK throughout life but somewhat erratic. OK throughout life.
FBTE-6	C/A W/Re		0 0	Functional but short-circuited at BOL. Reading of 1377°C obtained at 1 EFPD and then readings dropped drastically indicating deterioration of thermocouple.
FPTE-1	C/A W/Re	1765 1765	0-252 0-252	OK throughout life. OK throughout life.
FPTE-3	W/Re W/Re	1869 1308	252-897 0	OK throughout life. Functional but likely short-circuit at BOL. Complete failure after 378 EFPD.
PTE-2	C/A W/Re		0-252 0	OK throughout life. Reading of 1360°C obtained at BOL followed by thermocouple deterioration.

TABLE 5-2
COMPARISON OF MEASURED AND PREDICTED TEMPERATURES
IN PEACH BOTTOM FUEL TEST ELEMENTS

Thermocouple	Predicted Temperature - Measured Temperature (°C)																		
	Time Interval (EFPD)																		
	0-27.0	27.0-62.7	62.7-68.6	68.6-202.1	202.1-252.4	252.4-298.0	298.0-342.9	342.9-385.4	385.4-499.6	499.6-564.1	564.1-610.2	610.2-701.2	701.2-748.0	748.0-788.0	788.0-818.0	818.0-835.0	835.0-858.0	858.0-889.7	889.7-896.9	0-896.9
FTE-1 W/Re	86	46	32	16	0															25
FTE-2 C/A	2	-25	-50	31	-39	-32	-68	-66												-17
FTE-2 W/Re	31	8	25	-20	-30	5	40	-29												-5
FTE-4 W/Re						51	42	116	108	69	149	135								99
FTE-6 W/Re						-151	-75	-19	-36	-104	-2	21	56	31	49	-11	-4	-27	-20	-26
FTE-7 W/Re						165	92	80	69	43	89	44	61	60	12	80	85	-53	-45	61
FTE-8 W/Re						59	7	8	15	-5	33	0	30	30	-2	53	72	-58	-50	14
FTE-9 W/Re						-119	-52	-33	-45	-44	9	-33	4	-30	-65	15	38	-49	-47	-36
FTE-9 C/A						-100	-55	-47	-37	-71	-28	-35	-17	-22	-93	64	-5	-35	-15	-40
FTE-10 W/Re							-10	-100	7	-9	30	18	45	30	-3	83	142	69	65	18
FTE-12 W/Re						-49	-67	-112												-75
FTE-12 C/A						-52	14	-26												-21
FTE-13 W/Re (A)									-118	-177	-92	-81	-123	-60	-132					-113
FTE-13 W/Re (B)									-90	-174	-93	-83	-91	-67	-135	-65	-54	-195	-171	-106
FTE-14 W/Re									-11	-14	22	12								-1
FTE-16 W/Re (A)									-132	-99	-1	-33	-12	-7	-58	0	45	-43	-43	-54
FTE-17 W/Re									-235	-259	-209	-174	-136	-83	-95	-58	6	-111	-112	-165
FTE-18 W/Re (A)									-78	-88	-1	-18	-59	5	-80	-10	18	-130	-122	-52
FBTE-1 W/Re						-27	-1	-38												-22
FBTE-1 C/A	-27	6	-46	41	5	-50	27	3												10
FBTE-2 W/Re	-5	61	-7	9	12				144	136	185	189	201	206	118	133	194	82	137	113

TABLE 5-2 (Continued)

Thermocouple	Predicted Temperature - Measured Temperature (°C) Time Interval (EFPD)																		
	0-27.0	27.0-62.7	62.7-68.6	68.6-202.1	202.1 252.4	252.4-298.0	298.0-342.9	342.9-385.4	385.4-499.6	499.6-564.1	564.1-610.2	610.2-701.2	701.2-748.0	748.0-788.0	788.0-818.0	818.0-835.0	835.0-858.0	858.0-889.7	889.7-869.9	0-896.9
FBTE-2 C/A	-9	7	-44	54	27	-76	50	0												18
FBTE-3 W/Re	59	9	-2	18	31	82	29	42	65	37	62	31	115	148	96	175	179	70	70	61
FBTE-3 C/A	142	70	7	118	67	79														97
FBTE-4 W/Re	-78	-36	15	-48	-48															-48
FBTE-4 C/A	-56	-16	-97	25	-11															0
FPTE-1 W/Re	-44	-71	-59	-68	-21															-56
FPTE-3 W/Re (A)						84	61	52	67	69	95	50	91	90	72	73	80	5	10	66
No. of Measurements	11	11	11	11	11	16	16	16	16	16	16	16	14	14	14	13	13	13	13	261
Mean	9	5	-21	16	-1	0	-8	-12	-19	-38	13	-4	9	21	-26	40	59	-38	-27	-1
RMS	±62	±40	±39	±48	±33	±84	±50	±58	±95	±104	±91	±78	±90	±79	±78	±69	±74	±78	±81	±78
RMS/$\sqrt{n}$																				±5

TABLE 5-3
COMPARISON OF MEASURED AND PREDICTED TEMPERATURE RISES
IN PEACH BOTTOM FUEL TEST ELEMENTS

	Predicted ΔT - Measured ΔT (°C)																		
	Time Interval (EFPD)																		
Test Element	0-27.0	27.0-62.7	62.7-68.6	68.6-202.1	202.1-252.4	252.4-298.0	298.0-342.9	342.9-385.4	385.4-499.6	499.6-564.1	564.1-610.2	610.2-701.2	701.2-748.0	748.0-788.0	788.0-818.0	818.0-835.0	835.0-858.0	858.0-889.7	889.7-896.9	0-EOL
FTE-2	29	33	75	-51	9	37	108	37												
FTE-9						-20	3	14	-8	27	38	2	21	-8	28	-49	43	-14	-32	
FBTE-1						23	-28	-41												
FBTE-2	4	54	37	-45	-15															
FBTE-3	-83	-60	-9	-100	-36	3														
No. of Measurements	3	3	3	3	3	4	3	3	1	1	1	1	1	1	1	1	1	1	1	34
Mean	-17	9	34	-65	-14	11	28	3	-8	27	38	2	21	-8	28	-49	43	-14	-32	2
RMS	±48	±50	±34	±25	±18	±21	±58	±33												±42
RMS/$\sqrt{n}$																				±7

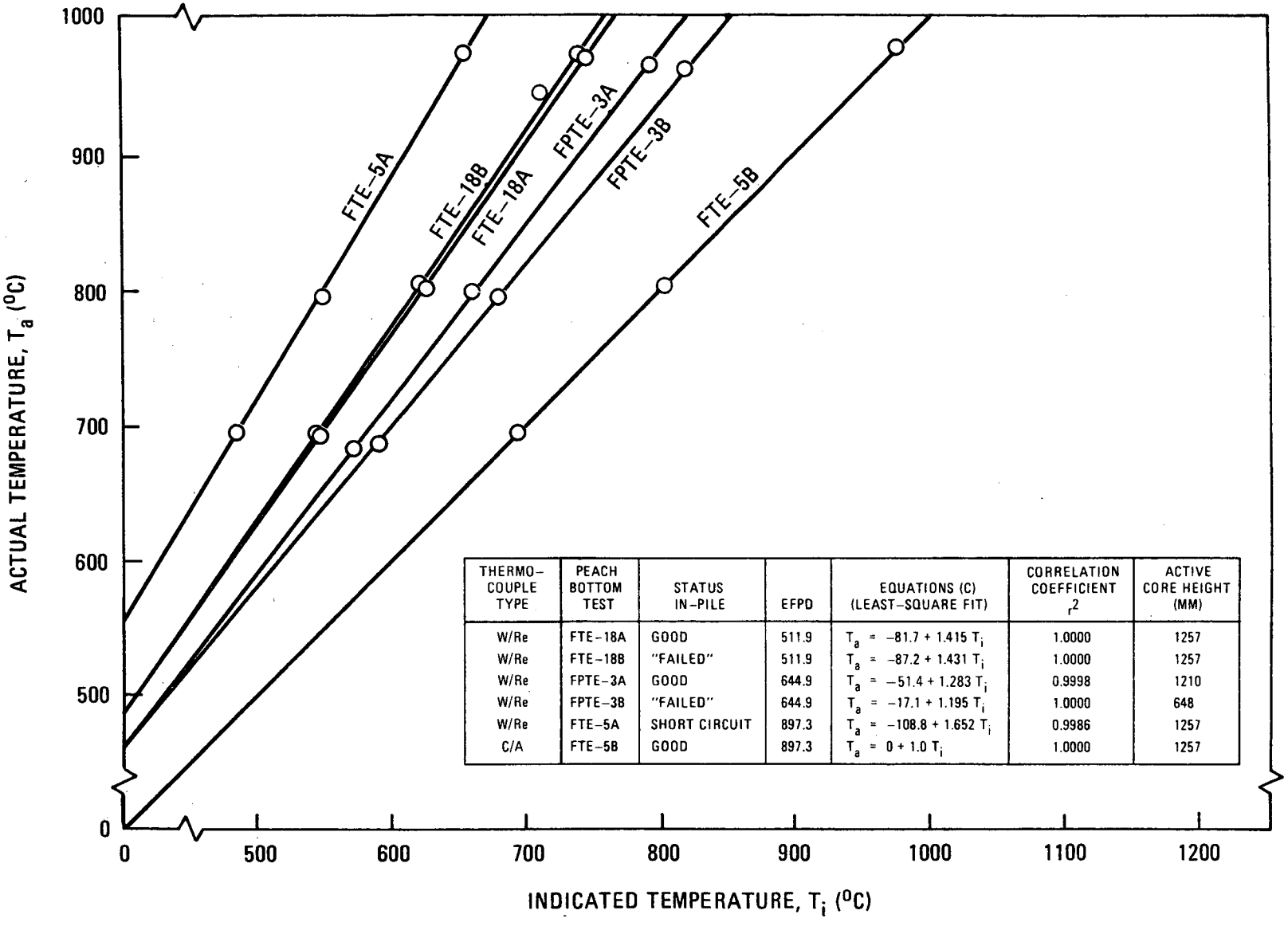

THERMO-COUPLE TYPE	PEACH BOTTOM TEST	STATUS IN-PILE	EFPD	EQUATIONS (C) (LEAST-SQUARE FIT)	CORRELATION COEFFICIENT r^2	ACTIVE CORE HEIGHT (MM)
W/Re	FTE-18A	GOOD	511.9	$T_a = -81.7 + 1.415\ T_i$	1.0000	1257
W/Re	FTE-18B	"FAILED"	511.9	$T_a = -87.2 + 1.431\ T_i$	1.0000	1257
W/Re	FPTE-3A	GOOD	644.9	$T_a = -51.4 + 1.283\ T_i$	0.9998	1210
W/Re	FPTE-3B	"FAILED"	644.9	$T_a = -17.1 + 1.195\ T_i$	1.0000	648
W/Re	FTE-5A	SHORT CIRCUIT	897.3	$T_a = -108.8 + 1.652\ T_i$	0.9986	1257
C/A	FTE-5B	GOOD	897.3	$T_a = 0 + 1.0\ T_i$	1.0000	1257

Fig. 5-1. FTE-18, FPTE-3, and FTE-5 thermocouple EOL recalibration results

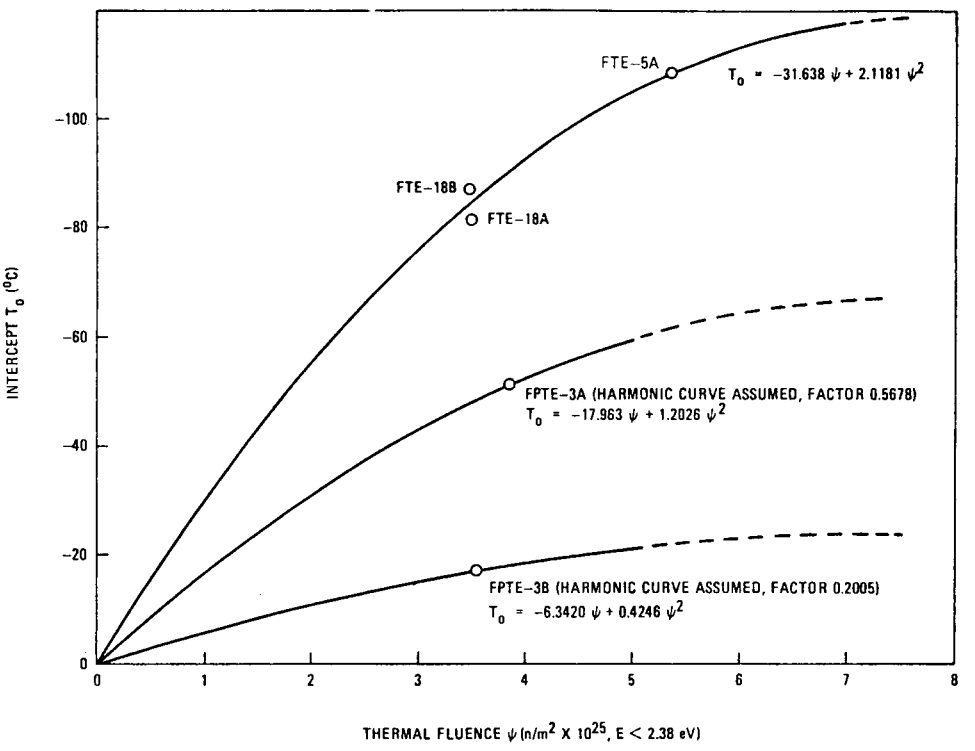

Fig. 5-2. Peach Bottom thermocouple recalibration term T_o

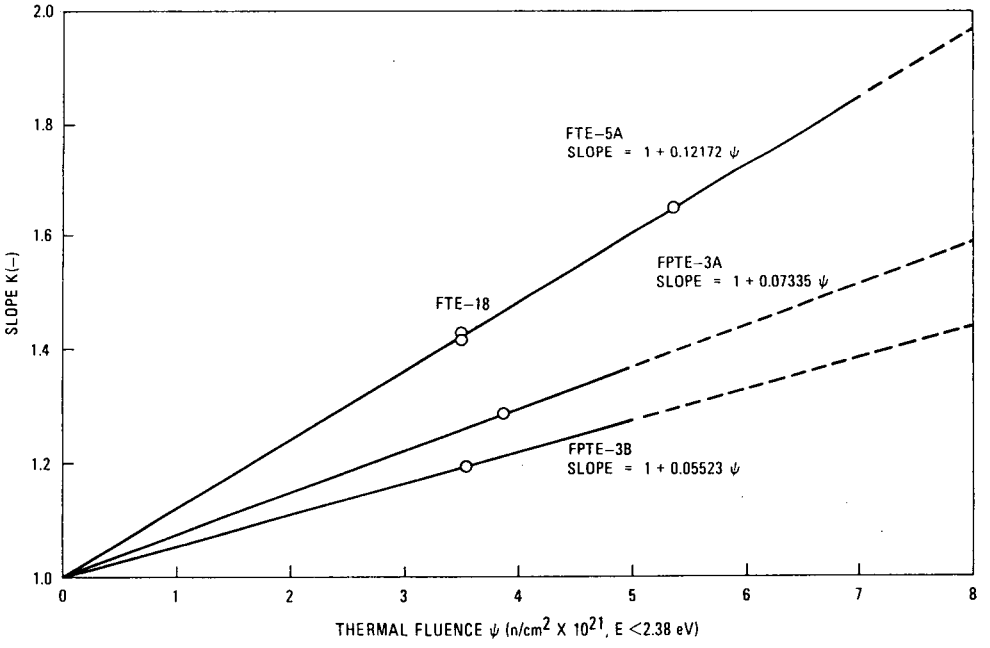

Fig. 5-3. Peach Bottom thermocouple recalibration term K

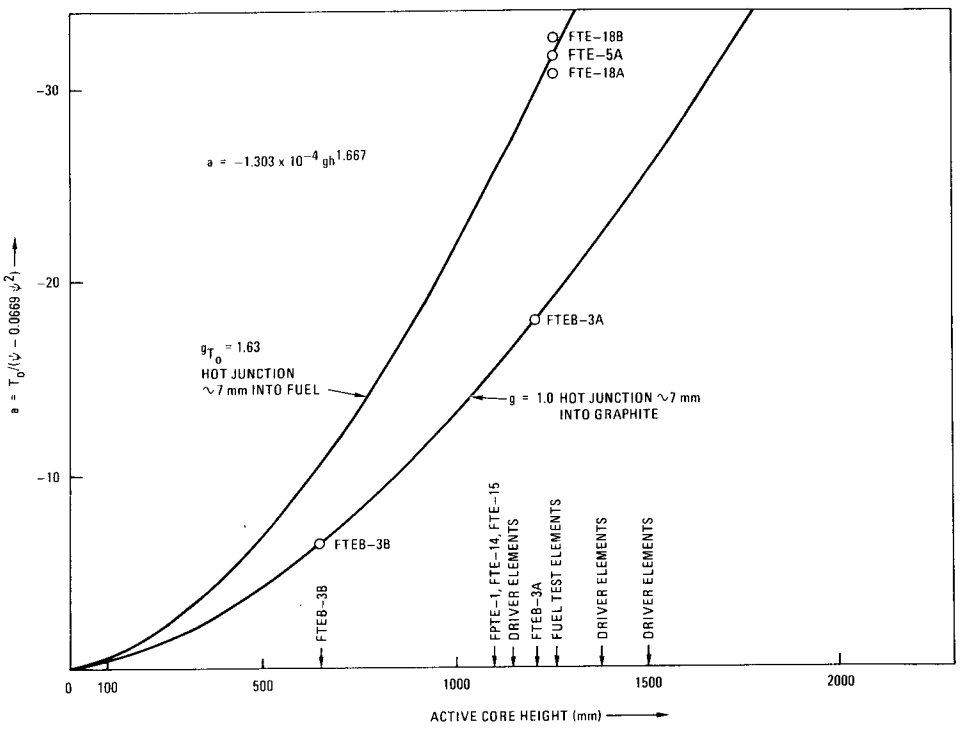

Fig. 5-4. Height correction for Type W Peach Bottom thermocouple recalibration term T_o

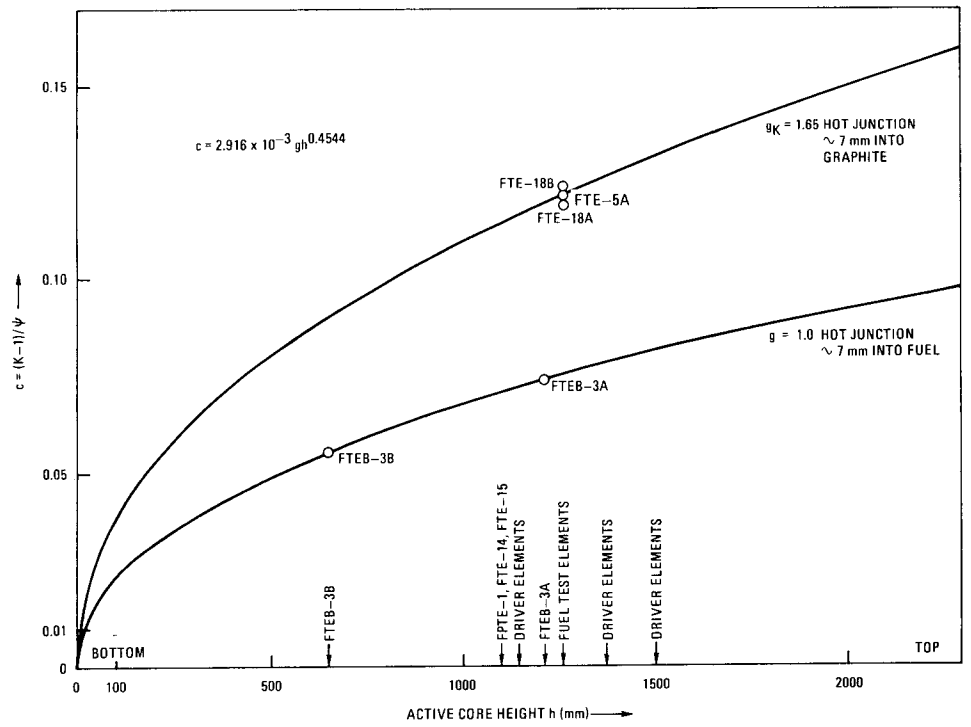

Fig. 5-5. Height correction for Type W Peach Bottom thermocouple recalibration term K

6. MATERIAL STRAIN EVALUATION

This section reports the results of the material strain evaluation for the Peach Bottom test elements. These results were obtained from a systematic computerized analysis of the dimensional measurements for the test elements using STAT, STRAIN, GAPS, and DRWDIM, a series of computer codes developed specifically for this task. These codes employ the statistical methods described in Ref. 6-1 to reduce test element dimensional data and compare the resultant strains with TREVER (Section 3) code predictions. A schematic showing the flow of information through these codes and providing a brief description of each is given in Fig. 6-1. The STAT, STRAIN, GAPS, and DRWDIM codes are described in Ref. 6-2.

6.1. GRAPHITE

6.1.1. Total Element and Sleeve

Total element length changes for a number of Peach Bottom test elements are given in Table 6-1. These data indicate that the element length initially expanded and then began shrinking with additional exposure. Net reductions in length were observed for all elements irradiated longer than 500 EFPD.

Sleeve strains were determined from postirradiation measurements of the inner and outer sleeve diameters and nominal preirradiation dimensions obtained from repeated measurements on archive material. Diametral strains* ranged from about +0.1% adjacent to the top and bottom reflectors to approximately -0.7% near the midpoint of the element having

---

*Material strains presented in this report are defined as follows:

$$\varepsilon(\%) = \left(\frac{X_{\text{postirradiation}}}{X_{\text{preirradiation}}} - 1 \right) \times 100 \ .$$

the highest neutron exposure. For most of the examined elements, measured sleeve strains are scattered around the predicted strain profiles obtained from the TREVER code. A typical comparison of measured and predicted strains is shown in Fig. 6-2. Because of the relatively large uncertainties in measured sleeve strains resulting from the absence of preirradiation measurements, a systematic comparison of measured and predicted strains was not performed.

6.1.2. Fuel Bodies

A large body of H-327 graphite axial and radial strain data for irradiation temperatures between 650° and 1150°C and fast neutron fluences from 0.3×10^{25} to 4.2×10^{25} n/m^2 $[(E > 29\ fJ)_{HTGR}]$ has been assembled from measurements on 50 irradiated fuel bodies from 13 Peach Bottom test elements. These data are compared with the design curves for irradiation-induced strain in H-327 graphite in Figs. 6-3 through 6-8.* Except for axial strains in fuel bodies which experienced average irradiation temperatures less than 1000°C, radial and axial strains in the large H-327 graphite fuel bodies are systematically lower than the design data. Discrepancies between measurements and design data are particularly apparent at fast neutron fluences greater than 2.5×10^{25} n/m^2 $[(E > 29\ fJ)_{HTGR}]$ and decrease with temperature rather than increase. However, the measurements are generally within the 95% confidence intervals of the design curves.

*Some liberty has been taken in comparing the measured strains with the design curves for irradiation-induced strain. The measured strains include creep strains and elastic strains as well as irradiation-induced strains. However, the creep strains and elastic strains for the test elements were relatively small, so the measured strains should be approximately equal to the irradiation-induced strains (at room temperature).

6.2. FUEL RODS

Postirradiation fuel rod dimensional measurements were performed by ORNL and GA on 1666 fuel rods from 16 Peach Bottom test elements. Preirradiation measurements were performed on 1166 of these rods. Postirradiation characterization consisted of diameter measurements at the top, middle, and bottom of the rod and one length measurement. These measurements were performed at two rotational positions, 90 deg apart, resulting in eight measurements per rod. Preirradiation measurements were performed in a similar manner but at only one rotational position, resulting in four measurements per rod. Fuel rod strains were computed from these preirradiation and postirradiation measurements using the STAT code.

In order to reduce the data into a manageable and presentable form, the strains for all fuel rods consisting of the same fuel blend in a given fuel body were averaged and correlated with fuel stack average temperatures and fast neutron fluences. These data are presented in Table 6-2. Anisotropy results, strain predictions, and comparisons of measured and predicted strains are also given in Table 6-2. Strain predictions are based on strain-fluence correlations developed using the SHRINK and FSVROD codes. The calculations performed by these codes are based on models which assume the dimensional change in a fuel rod to be isotropic and controlled by dimensional changes in the constituent fuel particles. TRISO particle volume changes are calculated based on the assumption that the SiC layer is dimensionally stable under normal HTGR operating conditions and that particle dimensional change is the result of irradiation densification effects in the OPyC layer. BISO particle volume changes are calculated with models which account for an OPyC layer shrinking against an internal buildup of fission gas pressure.

The dimensional change of a fuel rod during irradiation is dependent on the irradiation conditions and the properties of the fuel rod constituents. Of primary importance among the latter are the relative quantities of TRISO, BISO, and shim particles in the rod. Also important are the size of the particles, the thickness and density of the OPyC layers in the particles,

and the composition of the matrix. Fuel rods used in the recycle test elements were manufactured both at GA and at ORNL. The fuel rods used in all other test elements were manufactured at GA. The matrix for the rods made by GA was a blend of 27% to 30% natural flake 6353 graphite filler and 73% to 70% Allied Chemical Company 15V coal tar pitch (FSV matrix). The matrix for the rods fabricated at ORNL was a blend of 35 wt % fine Poco graphite in 15V pitch. Because of the higher filler content, the ORNL matrix had a somewhat higher density than the matrix used in the GA rods. None of the test element fuel rods contained shim particles.

Material properties, irradiation conditions, and measured strains for fuel rods containing all TRISO or all BISO coated fuel are listed in Tables 6-3 and 6-4. These tables were prepared in order to identify groups of fuel rods having the same, or similar, material properties so that the influence of irradiation conditions (i.e., fast neutron exposure and temperature) on fuel rod strain could be isolated. Plots of irradiation strain versus fast neutron fluence for three such groups are shown in Figs. 6-9, 6-10, and 6-11. The irradiation strain for each of these groups of fuel rods is observed to increase in the negative direction with fast neutron fluence, rapidly at first and then more and more slowly with additional neutron exposure. Although the scatter in the available data and the absence of data at fluences greater than 4.2×10^{25} n/m^2 make it difficult to be certain, the strain appears to reach a maximum and then to start declining at a fluence of about 3.0×10^{25} n/m^2. The irradiation strain is also observed to increase with irradiation temperature, as indicated by the data in the 700° to 900°C and 900° to 1100°C temperature ranges. However, the data in the 900° to 1100°C and 1100° to 1300°C ranges suggest that this temperature dependence is, at least for the fuel rods under observation in Figs. 6-10 and 6-11, restricted to temperatures of less than about 1000°C.

Within the range of fast neutron fluence (0.3×10^{25} to 4.2×10^{25} n/m^2) and stack average irradiation temperatures (700° to 1300°C) experienced by Peach Bottom test element fuel rods, maximum strains were approximately -2.0% for rods containing all TRISO fuel particles and -3.5% for rods

containing all BISO fuel particles with diameters in the 550- to 1000-μm range. Fuel rods containing small-diameter (≈350-μm), BISO-coated UO_2 and UC_2 particles experienced unusually high strains, with some rods shrinking as much as 7.5%. These rods were fabricated by GA for the recycle test elements. It is interesting to note that fuel rods fabricated by ORNL which contained UO_2 particles with properties similar to those of the UO_2 and UC_2 particles in the GA rods did not exhibit such large strains. This disparity in dimensional stability is most likely a result of differences in the irradiation-induced behavior of the matrix phases in the GA and ORNL rods. However, no explanation accounting for such large behavioral differences is immediately obvious.

Fuel rod dimensional changes were generally observed to be slightly anisotropic, with the radial strain exceeding the axial strain in most of the rods fabricated by GA and vice versa in rods fabricated by ORNL. With strain anisotropy expressed as axial strain divided by radial strain, the average strain anisotropies for GA and ORNL rods were 93.5% ± 9.6% and 118.7% ± 11.4%, respectively.

Pyrolytic carbon coatings on fuel particles are structurally symmetric and cannot contribute to fuel rod anisotropy. However, the matrix phases within a fuel rod are composed of inherently anisotropic graphite particles. Preferential alignment of these particles during fuel rod fabrication is the most probable explanation for the strain anisotropy observed in the test element fuel rods. The systematic difference in the strain anisotropies exhibited by the GA and the ORNL rods can be attributed to the use of different materials and fabrication techniques, which resulted in preferential alignment of anisotropic constituents with respect to the radial direction in one case and in the axial direction in the other. An alternative explanation, which cannot be ruled out, is that the difference in strain anisotropies is an artifact of a bias, or biases, in the fuel rod measuring techniques employed by GA and ORNL.

Whereas most of the test element fuel rods were only slightly anisotropic, a number of fuel rods fabricated by GA for the Phase 3 test

element (FTE-14, FTE-15, and FTE-16) were considerably anisotropic (see Table 6-2). A survey of the material properties for these rods provided no clues as to the reason for the extreme anisotropies. These fuel rods were omitted in calculating the average strain anisotropy for the GA fuel rods.

A comparison of measured and predicted fuel rod strains was performed and is summarized in Table 6-5. This comparison indicates that fuel rods containing all TRISO fuel generally shrank more than predicted and fuel rods containing all, or mostly, BISO fuel generally shrank less than predicted. These results and those from numerous capsule irradiation experiments performed by GA (Refs. 6-3 through 6-7) point out the need for improved models to better predict fuel rod dimensional changes. Considerable efforts have already been made (Refs. 6-8, 6-9) and are continuing in this area. The strain data for the Peach Bottom test element fuel rods constitute a large body of data obtained under actual operating conditions that can be used to verify these new models.

REFERENCES

6-1. Wallroth, C. F., et al., "Postirradiation Examination of Peach Bottom Fuel Test Element FTE-4," ERDA Report GA-A13452, July 1977.

6-2. Saurwein, J. J., "STAT, GAPS, STRAIN, DRWDIM, A System of Computer Codes for Analyzing HTGR Fuel Test Element Metrology Data," ERDA Report GA-A14274, August 1977.

6-3. Scott, C. B., and D. P. Harmon, "Postirradiation Examination of Capsules HRB-4, HRB-5, and HRB-6," ERDA Report GA-A13267, November 28, 1975.

6-4. Young, C. A., and C. B. Scott, "Postirradiation Examination of Capsule P13Q," ERDA Report GA-A14174, September 1977.

6-5. Scott, C. B., and D. P. Harmon, "Postirradiation Examination of Capsule F-30," Report GA-A13208, April 1, 1975.

6-6. Johnson, W. R., et al., "Postirradiation Examination of Capsules HT-24 and HT-25," ERDA Report GA-A13486, October 8, 1976.

6-7. Scott, C. B., D. P. Harmon, and J. F. Holzgraf, "Postirradiation Examination of Capsules P13R and P13S," ERDA Report GA-A13827, October 8, 1976.

6-8. Kovacs, W. J., and D. P. Harmon, "Irradiation-Induced Dimensional Changes in HTGR Fuel Rods," GA unpublished data.

6-9. Kaae, J. E., et al., "The Mechanical Behavior of BISO Coated Fuel Particles During Irradiation, Parts I and II," Nucl. Technol. 35, 359-378 (1977).

TABLE 6-1
PEACH BOTTOM TEST ELEMENT LENGTH DATA

Fuel Element	Strain (%)	Error (σ) (%)	Exposure (EFPD)	Mean Fast Fluence (10^{25} n/m^2)	Mean Sleeve Temp. (°C)
FTE-3	+0.07	±0.08	133	0.43	661
FTE-14	+0.07	±0.08	317	1.15	730
FTE-4	+0.35	±0.08	449	1.53	696
FTE-15	-0.79	±0.08	512	1.68	709
FTE-13	-0.19	±0.08	512	1.81	677
FTE-18	-0.19	±0.08	512	1.94	683
FTE-6	-0.62	±0.08	645	2.30	712
RTE-1	-0.50	±0.08	645	2.44	773
FTE-5	-0.39	±0.08	897	2.99	686
RTE-5	-0.48	±0.08	897	3.28	706
RTE-6	-0.52	±0.08	897	3.37	716
RTE-8	-0.17	±0.08	897	3.41	710

TABLE 6-2
PEACH BOTTOM FUEL ROD STRAIN DATA

Element I.D.	Body No.	Hole No.	No. of Rods	Fast Fluence (10^{25} n/m^2)	Avg. Fuel Rod Temp. (°C)	Fuel Vol. TRISO (%)	Content BISO (%)	Strain Calc (%)	Strain Meas[a] (%)	Strain (C/M)-1 (%)	Anisotropy Ax./Rad. (%)	Comments
FTE-3	1	1,2	10	0.41	772	24	76	-1.357	-1.221	12.97	108.5	
		3,4	6		769	85	15	-0.849	-0.751	20.47	86.8	
		5,6	6		768	100	0	-0.724	-0.627	18.91	95.5	
		7,8	9		772	74	26	-1.311	-0.840	64.51	73.4	
	2	1,2	11	0.54	971	24	76	-1.660	-1.909	-12.54	97.9	
		3,4	7		968	85	15	-1.013	-1.279	-20.64	92.1	
		5,6	7		967	100	0	-0.849	-1.086	-21.69	98.7	
		7,8	10		972	74	26	-1.545	-1.333	15.91	81.1	
	3	1,2	6	0.34	909	24	76	-1.030	-1.446	-30.44	105.2	
		3,4	6		908	85	15	-0.683	-0.951	-29.21	93.7	
		5,6	6		908	100	0	-0.595	-0.863	-31.58	84.7	
		7,8	6		910	74	26	-1.075	-1.084	-1.67	73.8	
FTE-4	1	1,2	5	1.40	831	22	78	-3.087	-2.107	46.83	99.2	
		3,4	5		823	78	22	-1.968	-1.475	38.26	86.1	
		7,8	5			64	36				84.2	
		5,6	5		812	100	0	-0.947	-1.063	-4.71	107.8	
	2	1,2	15	1.94	1079	22	78	-3.727	-2.810	32.86	95.7	
		3,4	6		1068	78	22	-2.331	-2.077	12.46	82.1	
		7,8	5			64	36				84.3	
		5,6	15		1055	100	0	-1.170	-1.597	-26.59	102.0	
	3	1,2	5	1.26	1028	22	78	-3.077	-2.482	23.09	103.4	
		3,4	5		1022	78	22	-1.964	-1.914	2.65	96.1	
		7,8	4			64	36				78.6	
		5,6	5		1014	100	0	-0.940	-1.488	-37.17	91.2	
FTE-5	1	1,2	24	2.73	825	0	100	-4.407	-4.521	-0.12	97.3	(b)
		3,4	22		845	0	100				106.7	(b)
		5,6	15		810	64	36	-3.049	-2.975	3.65	93.4	(b)
		7,8	12		815	100	0	-1.677	-1.228	51.50	73.3	(b)
	2	1,2	27	3.67	1088	0	100	-4.837	-6.421	-24.54	91.7	(b)
		3,4	18		1135	0	100				108.2	(b)
		5,6	27		1075	64	36	-3.450	-3.331	3.66	81.0	(b)
		7,8	16		1082	100	0	-1.924	-1.688	15.24	76.8	(b)
	3	1,2	17	2.58	1032	0	100	-4.436	-6.670	-33.49	NA	(b,c,d)
		3,4	10		1057	0	100				NA	(b,c,d)
		5,6	12		1022	64	36	-3.020	-3.440	-12.21	NA	(b,c,d)
		7,8	15		1020	100	0	-1.741	-1.830	-4.86	NA	(b,c,d)
FTE-6	1	1,2	21	2.10	870	26	74	-3.359	-2.297	47.94	93.2	
		3,4	21		855	93	7	-1.635	-1.541	10.49	92.6	
		5,6	21		850	100	0	-1.328	-1.486	-9.61	96.3	
		7,8	21		858	80	20	-1.983	-1.764	15.02	88.6	
	2	1,2	28	2.83	1117	26	74	-3.981	-2.875	38.70	92.4	
		3,4	28		1099	93	7	-1.785	-2.083	-13.67	93.7	
		5,6	28		1094	100	0	-1.559	-1.917	-18.15	91.5	
		7,8	25		1103	80	20	-2.153	-2.362	-8.69	82.8	
	3	1,2	21	1.98	1084	26	74	-3.520	-3.112	13.10	91.0	
		3,4	20		1072	93	7	-1.664	-2.078	-19.70	96.3	
		5,6	21		1068	100	0	-1.350	-1.988	-32.19	96.2	
		7,8	12		1074	80	20	-1.980	-2.240	-11.62	90.5	
FTE-13	2	1,7,8	28	2.24	1091	23	77	-3.406	-2.358	50.23	114.8	
		2,3,6	28		1091	14	86	-3.672	-2.828	30.62	114.9	
		4,5	13		1091	20	80	-3.414	-2.655	32.65	115.6	
FTE-14	1	1,2,3	3	1.05	847	23	77	-2.274	-1.869	22.71	159.3	
	2	1	5	1.42	1206	23	77	-2.443	-2.271	7.90	95.4	
	3	1	3	0.97	1198	23	77	-1.875	-2.107	-11.83	102.7	
	2	2	5	1.42	1182	100	0	-1.007	-1.274	-20.74	90.5	
	3	6	3	0.97	1200	100	0	-0.084	-1.413	-40.64	73.7	
	2	3	5	1.42	1210	25	75	-2.541	-2.076	22.48	100.0	
	3	3	3	0.97	1196	25	75	-1.931	-1.775	7.67	101.1	
	1	4	3	1.05	840	22	78	-1.919	-1.807	7.83	153.8	
	2	4	5	1.42	1185	55	45	-2.355	-2.299	2.78	108.9	
	3	4	3	0.97	1181	55	45	-1.852	-1.990	-7.56	102.9	
	2	5	5	1.42	1207	21	79	-2.881	-2.773	4.23	99.0	
	3	5	3	0.97	1198	21	79	-2.147	-2.410	-11.81	90.7	
	2	6	5	1.42	1206	100	0	-0.734	-1.226	-39.79	62.5	
	3	2	3	0.97	1201	100	0	-0.841	-1.210	-30.25	50.5	
FTE-15	1	1	11	1.47	854	23	77	-2.864	-2.429	18.12	144.1	
	2	1	11	2.00	1195	27	73	-2.900	-2.398	20.93	98.3	
	3	1	11	1.55	1160	27	73	-2.461	-2.226	10.06	94.2	
	2	2	10	2.00	1182	100	0	-1.127	-0.877	72.05	107.8	
	3	2	7	1.55	1154	100	0	-1.032	-0.979	21.28	105.2	

TABLE 6-2 (Continued)

Element I.D.	Body No.	Hole No.	No. of Rods	Fast Fluence (10^{25}n/m^2)	Avg. Fuel Rod Temp. (°C)	Fuel Vol. Content TRISO (%)	Fuel Vol. Content BISO (%)	Strain Calc (%)	Strain Meas [a] (%)	Strain (C/M)-1 (%)	Anisotropy Ax./Rad. (%)	Comments
FTE-15 (cont'd)	1	3	2	1.47	842	22	78	-2.469	-2.042	23.34	150.1	
	2	3	11	2.00	1207	25	75	-3.088	-2.103	46.99	104.7	
	3	3	6	1.55	1167	25	75	-2.647	-1.988	33.08	105.4	
	1	4	5	1.47	837	22	78	-2.419	-2.169	13.10	161.1	
	2	4	5	2.00	1171	55	45	-2.925	-2.210	32.68	102.7	
	3	4	7	1.55	1144	55	45	-2.579	-1.976	30.84	92.4	
	1	5	6	1.47	848	23	77	-2.560	-2.050	24.61	154.6	
	2	5	3	2.00	1199	21	79	-3.238	-2.576	25.72	102.7	
	3	5	6	1.55	1165	21	79	-2.716	-2.083	36.63	85.0	
	2	6	11	2.00	1204	100	0	-0.937	-0.946	0.85	63.7	
	3	6	11	1.55	1130	100	0	-0.854	-1.209	-28.54	79.8	
FTE-16	2	1	14	2.33	1008	100	0	-1.825	-2.004	-7.21	156.5	
	2	2	14	2.23	1059	100	0	-1.825	-1.456	28.18	145.8	
	2	3	14	2.23	1083	100	0	-1.825	-1.612	13.82	119.9	
	2	4	14	2.23	1046	100	0	-1.825	-1.748	5.50	153.7	
	2	5	14	2.23	1086	100	0	-1.825	-1.407	32.77	157.8	
	3	5	14	1.64	990	100	0	-1.689	-1.818	-6.55	157.0	
	2	6	14	2.23	1103	100	0	-1.825	-1.315	40.59	151.8	
	2	7	14	2.23	1103	100	0	-1.825	-1.234	49.52	100.5	
	2	8	14	2.23	1049	100	0	-1.825	-1.574	20.51	149.1	
RTE-1	1	1,5	6	1.70	777	0	100	-2.932	-2.310	27.76	111.8	
	2	1,5	6	2.70	1060	0	100	-3.562	-3.039	17.75	111.6	
	3	1,5	6	3.00	1193	0	100	-3.574	-2.764	30.44	110.2	
	4	1,5	6	2.96	1218	0	100	-3.594	-3.021	19.05	117.3	
	5	1,5	6	2.59	1181	0	100	-3.909	-2.813	39.11	128.4	
	6	1,5	6	1.66	1055	0	100	-3.341	-2.682	24.26	114.7	
	1	2,6	6	1.70	823	69	31	-2.205	-1.655	35.37	NA	(b,c)
	2	2,6	7	2.70	1118	69	31	-2.632	-2.673	-0.91	NA	(b,c)
	3	2,6	7	3.00	1258	69	31	-2.712	-2.802	-1.89	NA	(b,c)
	4	2,6	6	2.96	1282	69	31	-2.721	-2.876	-3.92	NA	(b,c)
	5	2,6	7	2.59	1197	0	100	-4.285	-5.324	-1.11	NA	(b,c)
	6	2,6	7	1.66	1067	0	100	-3.647	-3.481	30.00	NA	(b,c)
	1	3,7	6	1.70	835	0	100	-3.130	-1.994	57.74	106.9	
	2	3,7	6	2.70	1156	0	100	-3.827	-2.589	48.52	114.2	
	3	3,7	6	3.00	1289	0	100	-3.850	-2.852	35.16	111.8	
	4	3,7	6	2.96	1308	0	100	-3.870	-2.830	37.63	119.1	
	5	3,7	7	2.59	1198	0	100	-4.369	-4.217	22.83	NA	(b,c)
	6	3,7	7	1.66	1065	100	0	-1.373	-2.397	-27.93	NA	(b,c)
	1	4,8	6	1.70	858	0	100	-2.923	-2.161	38.60	132.3	
	2	4,8	6	2.70	1190	0	100	-3.605	-2.809	28.86	110.0	
	3	4,8	6	3.00	1342	0	100	-3.626	-3.006	24.25	134.1	
	4	4,8	6	2.96	1356	0	100	-3.644	-2.407	52.14	118.4	
	5	4,8	7	2.59	1230	26	74	-3.865	-3.217	35.23	NA	(b,c)
	6	4,8	7	1.66	1080	26	74	-3.198	-2.330	38.42	NA	(b,c)
RTE-2	2	1,3,5,7	24	2.83	1045	0	100	-4.094	-2.810	47.20	107.9	
	4	7	6	2.94	1167	0	100	-4.127	-7.734	-46.50	NA	(b,c,d)
	6	1	6	1.49	1005	75	25	-2.212	-3.244	-31.83	NA	(b,c,d)
RTE-4	5	1,3,5,7	24	1.43	1158	0	100	-3.122	-2.584	20.95	NA	(c)
RTE-6	1	1	7	2.42	732	0	100	-3.724	-3.294	17.17	NA	(b,c,d)
	2	1	7	3.79	956	65	35	-3.175	-3.000	6.30	NA	(b,c,d)
	4	1	7	4.00	1108	65	35	-3.210	-3.406	-5.62	NA	(b,c,d)
	5	1	7	3.50	1084	65	35	-3.132	-3.472	-9.57	NA	(b,c,d)
	3	1,3,5,7	24	4.15	1141	0	100	-3.901	-3.267	19.70	112.0	
	6	1,5,7	16	2.34	1041	0	100	-3.694	-1.943	101.30	96.0	
RTE-5	5	1,2	7	3.40	1088	0	100	-4.058	-4.486	-9.38	NA	(b,c)
	6	1,2	7	2.14	1020	0	100	-3.679	-4.281	-14.07	NA	(b,c)
	1	3,4	6	2.33	736	0	100	-3.433	-2.286	50.08	112.1	
	2	3,4	6	3.73	1009	0	100	-3.757	-2.586	47.14	122.5	
	3	3,4	6	4.11	1104	0	100	-3.663	-2.653	38.96	134.8	
	4	3,4	6	3.98	1160	0	100	-3.720	-2.801	33.93	128.7	
	5	3,4	7	3.40	1073	0	100	-4.187	-7.361	-43.06	NA	(b,c)
	6	5,6	7	2.14	1014	0	100	-3.826	-6.224	-38.38	NA	(b,c)
	5	7,8	6	3.40	1115	0	100	-3.993	-3.274	22.27	120.2	
	6	3,4	6	2.14	1031	0	100	-3.626	-3.000	21.20	132.0	
	1	5,6	7	2.33	707	65	35	-2.631	-2.441	11.54	NA	(b,c)
	2	5,6	7	3.73	942	65	35	-3.225	-3.797	-14.93	NA	(b,c)
	3	5,6	7	4.11	1028	65	35	-3.275	-2.625	26.47	NA	(b)
	4	5,6	7	3.98	1083	65	35	-3.278	-4.239	-22.54	NA	(b,c)
	5	5,6	7	3.40	1080	0	100	-4.004	-6.716	-40.30	NA	(b,c)

TABLE 6-2 (Continued)

Element I.D.	Body No.	Hole No.	No. of Rods	Fast Fluence (10^{25} n/m^2)	Avg. Fuel Rod Temp. (°C)	Fuel Vol. Content		Strain			Anisotropy Ax./Rad. (%)	Comments
						TRISO (%)	BISO (%)	Calc (%)	Meas[a] (%)	(C/M)-1 (%)		
RTE-5 (cont'd)	1	7,8	6	2.33	747	0	100	-3.479	-1.522	160.67	94.9	
	2	7,8	6	3.73	1024	0	100	-3.949	-2.127	87.38	123.2	
	3	7,8	6	4.11	1112	0	100	-3.899	-1.885	113.74	133.7	
	4	7,8	6	3.98	1164	0	100	-3.940	-2.239	77.59	116.4	
	6	7,8	7	2.14	997	100	0	-1.638	-2.454	-32.95	NA	(b,c)
	1	1,2	6	2.33	727	0	100	-3.392	-2.243	51.19	109.3	
	2	1,2	6	3.73	974	0	100	-3.741	-2.762	37.83	123.8	
	3	1,2	6	4.11	1062	0	100	-3.680	-2.484	48.97	124.3	
	4	1,2	6	3.98	1116	0	100	-3.724	-2.446	54.49	146.7	
RTE-7	3	1,2	7	1.15	1081	0	100	-2.725	-3.500	-22.06	NA	(b,c)
	5	1,2	6	0.85	1062	0	100	-2.215	-2.029	9.76	NA	(c)
	6	1,2	12	0.51	974	0	100	-1.492	-1.324	13.20	NA	(c)
	3	3,4	6	1.15	1077	0	100	-2.719	-2.598	5.80	NA	(c)
	5	3,4	6	0.85	1053	0	100	-2.173	-2.042	8.66	NA	(c)
	6	3,4	12	0.51	967	0	100	-1.459	-1.535	-3.33	NA	(c)
	1	5,6	12	0.66	730	0	100	-1.587	-0.823	116.40	NA	(c)
	3	5,6	6	1.15	1106	0	100	-2.888	-2.284	30.45	NA	(c)
	5	5,6	7	0.85	1053	62	38	-1.799	-2.700	-33.60	NA	(b,c)
	1	7,8	7	0.66	709	100	0	-0.882	-0.972	11.10	NA	(b,c)
	3	7,8	5	1.15	1066	100	0	-1.313	-2.473	-46.82	NA	(b,c)
	5	7,8	6	0.85	1073	0	100	-2.260	-1.997	24.84	NA	(c)
	6	7,8	12	0.51	981	0	100	-1.517	-1.468	10.19	NA	(c)
RTE-8	2	1,5,7	19	3,83	921	100	0	-1.817	-1.932	-5.67	NA	(b,c,d)
	5	1,5,7	21	3.55	1067	100	0	-1.814	-2.026	-10.36	NA	(b,c,d)
	3	1,5,7	21	4.20	1072	0	100	-4.088	-6.118	-32.98	NA	(b,c,d)
	4	1,3,5,7	24	4.06	1187	0	100	-3.929	-3.325	18.28	118.7	(b,c,d)
	6	1,5,7	20	2.38	1020	65	35	-2.738	-2.886	-4.91	NA	(b,c,d)

(a) Unless otherwise indicated, measured strain is the average of the axial and radial strains.
(b) Nominal preirradiation data.
(c) Diametrical strain only.
(d) Fuel was cured in place (CIP process).

TABLE 6-3
MATERIAL PROPERTIES, IRRADIATION CONDITIONS, AND MEASURED STRAIN FOR FUEL RODS CONTAINING TRISO-COATED FISSILE AND FERTILE FUEL PARTICLES

Test Element I.D.	Fuel Body	Fuel Holes	Fissile Particles (TRISO)					Fertile Particles (TRISO)					Irrad. Temp. (°C)	Fast Fluence ($1 \times 10^{25} n/m^2$)	Strain, $\Delta x/x$ (%)
				Particle		OPyC Coating			Particle		OPyC Layer				
			% of Rod Vol.	Type	Dia. (μm)	Thick. (μm)	Density (g/cm^3)	% of Rod Vol.	Type	Dia. (μm)	Thick. (μm)	Density (g/cm^3)			
FTE-3	1	5,6	53	$(Th,U)C_2$	509	44	1.80	9	ThC_2	663	41	1.79	768	0.41	-0.627[a]
	2	5,6											967	0.54	-1.086[a]
	3	5,6											908	0.34	-0.863[a]
FTE-4	1	5,6	48					14					812	1.40	-1.063[a]
	2	5,6											1055	1.94	-1.597[a]
	3	5,6											1014	1.26	-1.488[a]
FTE-6	1	5,6	57					5					850	2.10	-1.486[a]
	2	5,6											1094	2.83	-1.917[a]
	3	5,6											1068	1.98	-1.988[a]
FTE-14	2	2	16	UC_2	536	38	1.80	46	ThC_2	649	38	1.81	1182	1.42	-1.274
	2	6	15	UO_2	579	37	1.83	47	ThO_2	670	25	1.81	1206	1.42	-1.226
	3	2							ThO_2	670	25	1.81	1200	0.97	-1.443
	3	6							ThC_2	649	38	1.81	1201	0.97	-1.210
FTE-15	2	2	16	UC_2	536	38	1.80	44					1182	2.00	-0.877
	3	2	16	UC_2	536	38	1.80	44					1154	1.55	-0.979
	3	6	15	UO_2	579	37	1.83	47					1130	1.55	-1.209
	2	6	14	UO_2	579	37	1.83	36	ThO_2	670	25	1.81	1204	2.00	-0.946
FTE-16	2	1-8	44	$(Th,U)C_2$	N.A.	N.A.	N.A.	21	ThC_2	N.A.	N.A.	N.A.	1067	2.23	-1.544[a]
	3	5	44	$(Th,U)C_2$	489	45	1.79	21	ThC_2	656	43	1.80	990	1.64	-1.818[a]
RTE-1	6	3,7	46	UC_2	331	27	1.71	26	ThC_2	685	36	1.86	1065	1.66	-2.397
RTE-5	6	7,8	40	UC_2	347	32	1.73	22	ThC_2	654	41	1.79	997	2.14	-2.454
RTE-7	1	7,8											709	0.66	-0.972
	3	7,8											1066	1.15	-2.473
RTE-8	2	1,5,7											921	3.83	-1.932
	5	1,5,7											1067	3.55	-2.026

[a] Data plotted in Fig. 6-9.

TABLE 6-4
MATERIAL PROPERTIES, IRRADIATION CONDITIONS, AND MEASURED STRAIN FOR FUEL RODS CONTAINING BISO-COATED FISSILE AND FERTILE FUEL PARTICLES

Test Element I.D.	Fuel Body	Fuel Holes	Fissile Particles (BISO)					Fertile Particles (BISO)					Irrad. Temp. (°C)	Fast Fluence ($1 \times 10^{25} n/m^2$)	Strain, $\Delta x/x$ (%)
				Particle		OPyC Layer			Particle		OPyC Layer				
			% of Rod Vol.	Type	Dia. (μm)	Thick. (μm)	Density (g/cm^3)	% of Rod Vol.	Type	Dia. (μm)	Thick. (μm)	Density (g/cm^3)			
RTE-1	1	1,5	66	$(4Th,U)O_2$	772	129	1.91	--	--	--	--	--	777	1.70	-2.310[a]
	2	1,5	↓	↓	↓	↓	↓	--	--	--	--	--	1060	2.70	-3.039[a]
	3	1,5	↓	↓	↓	↓	↓	--	--	--	--	--	1193	3.00	-2.764[a]
	4	1,5	↓	↓	↓	↓	↓	--	--	--	--	--	1218	2.96	-3.021[a]
	5	1,5	54	$(2Th,U)O_2$	793	128	1.86	11	ThC_2	NA	NA	NA	1181	2.59	-2.813
	6	1,5	↓	↓	↓	↓	↓	↓	ThC_2	↓	NA	NA	1055	1.66	-2.682
	1	3,7	↓	↓	↓	↓	↓	↓	ThO_2	↓	66	1.99	835	1.70	-1.994
	2	3,7	↓	↓	↓	↓	↓	↓	↓	↓	↓	↓	1156	2.70	-2.589
	3	3,7	56	$(2Th,U)O_2$	806	141	1.85	9	↓	↓	↓	↓	1289	3.00	-2.852
	4	3,7	56	$(2Th,U)O_2$	806	141	1.85	9	↓	↓	↓	↓	1308	2.96	-2.830
	1	4,8	44	UO_2	328	60	1.89	21	↓	↓	↓	↓	858	1.70	-2.161
	2	4,8	↓	↓	↓	↓	↓	↓	↓	↓	↓	↓	1190	2.70	-2.809
	3	4,8	↓	↓	↓	↓	↓	↓	↓	↓	↓	↓	1342	3.00	-3.006
	4	4,8	↓	↓	↓	↓	↓	↓	↓	↓	↓	↓	1356	2.96	-2.407
	5	2,6	38	UC_2	331	73	1.78	27	ThC_2	597	67	1.85	1197	2.57	-5.324
	6	2,6	↓	↓	↓	↓	↓	↓	ThC_2	597	67	1.85	1067	1.66	-3.481
	5	3,7	↓	↓	↓	↓	↓	↓	ThO_2	696	81	1.78	1198	2.59	-4.217
RTE-2	2	1,3,5,7	39	$(2Th,U)O_2$	793	128	1.86	26	ThC_2	NA	NA	NA	1045	2.83	-2.810
	4	7	49	UC_2	340	74	1.84	16	ThC_2	614	71	1.88	1167	2.94	-7.734
RTE-4	5	1,3,5,7	37	$(2Th,U)O_2$	754	122	1.91	28	ThC_2	580	66	1.88	1158	1.43	-2.584[b]
RTE-5	1	1,2	65	$(4Th,U)O_2$	783	135	1.92	--	--	--	--	--	727	2.33	-2.243[a]
	2	1,2	↓	↓	↓	↓	↓	--	--	--	--	--	974	3.73	-2.762[a]
	3	1,2	↓	↓	↓	↓	↓	--	--	--	--	--	1062	4.11	-2.484[a]
	4	1,2	↓	↓	↓	↓	↓	--	--	--	--	--	1116	3.98	-2.446[a]
	5	1,2	37	UO_2	371	60	NA	27	ThC_2	580	66	1.88	1088	3.40	-4.486
	6	1,2	37	UO_2	371	60	NA	27	ThC_2	580	66	1.88	1020	2.14	-4.281
	1	3,4	37	$(2Th,U)O_2$	754	122	1.91	27	ThO_2	633	70	1.91	736	2.33	-2.286[b]
	2	3,4	↓	↓	↓	↓	↓	↓	↓	↓	↓	↓	1009	3.73	-2.586[b]
	3	3,4	↓	↓	↓	↓	↓	↓	↓	↓	↓	↓	1104	4.11	-2.653[b]
	4	3,4	↓	↓	↓	↓	↓	↓	↓	↓	↓	↓	1160	3.98	-2.801[b]
	5	3,4	40	UC_2	340	74	1.84	22	ThC_2	614	71	1.88	1073	3.40	-7.361
	6	5,6	40	UC_2	340	74	1.84	22	ThC_2	614	71	1.88	1074	2.14	-6.224
	5	7,8	35	$(2Th,U)O_2$	751	123	1.91	30	ThC_2	580	66	1.88	1115	3.40	-3.274[b]
	6	3,4	35	$(2Th,U)O_2$	751	123	1.91	30	ThC_2	580	66	1.88	1031	2.14	-3.000[b]
	1	7,8	36	UO_2	328	60	1.89	32	ThO_2	645	62	1.94	747	2.33	-1.522
	2	7,8	↓	↓	↓	↓	↓	↓	↓	↓	↓	↓	1024	3.73	-2.127
	3	7,8	↓	↓	↓	↓	↓	↓	↓	↓	↓	↓	1112	4.11	-1.885
	4	7,8	↓	↓	↓	↓	↓	32	ThO_2	633	70	1.91	1164	3.98	-2.239
RTE-6	1	1	40	UC_2	340	74	1.84	22	ThC_2	614	71	1.88	723	2.42	-3.294
	3	1,3,5,7	35	$(2Th,U)O_2$	751	123	1.91	31	ThC_2	580	66	1.88	1141	4.15	-3.267[b]
	6	1,5,7	35	UO_2	328	60	1.89	30	NA	NA	NA	NA	1041	2.34	-1.943

TABLE 6-4 (Continued)

Test Element I.D.	Fuel Body	Fuel Holes	Fissile Particles (BISO)					Fertile Particles (BISO)					Irrad. Temp. (°C)	Fast Fluence ($1 \times 10^{25} n/m^2$)	Strain, $\Delta x/x$ (%)
				Particle		OPyC Layer			Particle		OPyC Layer				
			% of Rod Vol.	Type	Dia. (μm)	Thick. (μm)	Density (g/cm^3)	% of Rod Vol.	Type	Dia. (μm)	Thick. (μm)	Density (g/cm)			
RTE-7	3	1,2	37	UO_2	371	60	NA	27	ThC_2	614	71	1.88	1081	1.15	-3.500
	5	1,2	65	$(4Th,U)O_2$	783	135	1.92	--	--	--	--	--	1062	0.85	-2.029[a]
	6	1,2	65	$(4Th,U)O_2$	783	135	1.92	--	--	--	--	--	974	0.51	-1.324[a]
	3	3,4	35	$(2Th,U)O_2$	751	123	1.91	31	ThC_2	580	66	1.88	1077	1.15	-2.598[b]
	5	3,4	37		754	122		28	ThO_2	645	62	1.94	1053	0.85	-2.042[b]
	6	3,4	37		754	122				645	62	1.94	967	0.51	-1.535[b]
	1	5,6	36	UO_2	328	60	1.89			NA	66	1.99	730	0.66	-0.823
	3	5,6											1106	1.15	-2.284
	5	7,8						32	ThO_2	633	70	1.91	1073	0.85	-1.997
	6	7,8						32	ThO_2				981	0.51	-1.468
RTE-8	3	1,5,7	40	UC_2	340	74	1.84	22	ThC_2	614	71	1.88	1072	4.20	-6.118
	4	1,3,5,7	35	$(2Th,U)O_2$	751	123	1.91	31	ThC_2	580	66	1.88	1187	4.06	-3.325[b]
FTE-5	1	1,2	25	UC_2	340	74	1.84	37					825	2.73	
	2	1,2											1088	3.67	
	3	1,2											1022	2.58	

[a] Data plotted in Fig. 6-10.
[b] Data plotted in Fig. 6-11.

TABLE 6-5
SUMMARY COMPARISON OF MEASURED AND
CALCULATED FUEL ROD STRAIN

Fuel Rod Composition	Temperature (°C)	Fast Fluence (10^{25} n/m^2)	Number of Rods	Measured Strain (%)	Strain Comparison, (Calc/Meas)-1 (%)
All TRISO-coated fuel (GA matrix)	700-900	0.0-1.0	13	-0.800	15.0
		1.0-2.0	5	-1.063	-4.7
		2.0-3.0	33	-1.357	20.9
		3.0-4.0	0	ND[a]	ND
	900-1100	0.0-1.0	13	-0.974	-26.6
		1.0-2.0	53	-1.989	-34.1
		2.0-3.0	50	-2.067	-18.7
		3.0-4.0	56	-1.882	-0.3
	1100-1300	0.0-1.0	6	-1.311	-35.4
		1.0-2.0	49	-1.085	0.8
		2.0-3.0	0	ND	ND
		3.0-4.0	0	ND	ND
BISO- and TRISO-coated fuel: TRISO fuel constitutes >50% of fuel volume (GA matrix)	700-900	0.0-1.0	15	-0.689	19.7
		1.0-2.0	16	-1.565	36.8
		2.0-3.0	64	-2.180	10.2
		3.0-4.0	0	ND	ND
	900-1100	0.0-1.0	36	-1.469	-13.8
		1.0-2.0	58	-2.312	-9.6
		2.0-3.0	60	-2.803	-10.3
		3.0-4.0	62	-3.411	-1.8
	1100-1300	0.0-1.0	3	-1.990	-7.6
		1.0-2.0	12	-2.137	16.8
		2.0-3.0	43	-2.530	4.8
		3.0-4.0	14	-3.104	-3.7
BISO- and TRISO-coated fuel: BISO fuel constitutes >50% of fuel volume (ORNL matrix)	700-900	0.0-1.0	10	-1.221	12.9
		1.0-2.0	35	-2.071	22.4
		2.0-3.0	21	-2.297	47.9
		3.0-4.0	0	ND	ND
	900-1100	0.0-1.0	17	-1.677	-21.5
		1.0-2.0	48	-2.683	26.9
		2.0-3.0	69	-3.497	37.8
		3.0-4.0	0	ND	ND
	1100-1300	0.0-1.0	9	-2.097	-5.3
		1.0-2.0	63	-2.277	23.1
		2.0-3.0	35	-3.046	37.0
		3.0-4.0	0	ND	ND

TABLE 6-5 (Continued)

Fuel Rod Composition	Temperature (°C)	Fast Fluence (10^{25} n/m^2)	Number of Rods	Measured Strain (%)	Strain Comparison, (Calc/Meas)-1 (%)
All BISO-coated fuel: Rods containing small (≈350μm) BISO-coated UC_2 and UO_2 particles made by GA are not included. (ORNL matrix)	700-900	0.0-1.0	12	-0.823	116.4
		1.0-2.0	18	-2.155	41.4
		2.0-3.0	18	-2.017	87.3
		3.0-4.0	0	ND	ND
	900-1100	0.0-1.0	54	-1.732	10.6
		1.0-2.0	12	-2.640	15.0
		2.0-3.0	52	-2.698	46.9
		3.0-4.0	24	-2.490	55.3
	1100-1300	0.0-1.0	0	ND	ND
		1.0-2.0	30	-2.434	25.7
		2.0-3.0	54	-2.788	35.0
		3.0-4.0	84	-2.736	47.4
All BISO-coated fuel: Rods containing small (≈350μm) BISO-coated UC_2 and UO_2 particles made by GA. (GA matrix)	700-900	0.0-1.0	0	ND	ND
		1.0-2.0	0	ND	ND
		2.0-3.0	53	-3.907	8.5
		3.0-4.0	0	ND	ND
	900-1100	0.0-1.0	0	ND	ND
		1.0-2.0	14	-3.490	4.0
		2.0-3.0	41	-5.725	-28.6
		3.0-4.0	80	-6.096	-27.5
	1100-1300	0.0-1.0	0	ND	ND
		1.0-2.0	0	ND	ND
		2.0-3.0	20	-5.758	-8.3
		3.0-4.0	0	ND	ND

(a) ND = not determined.

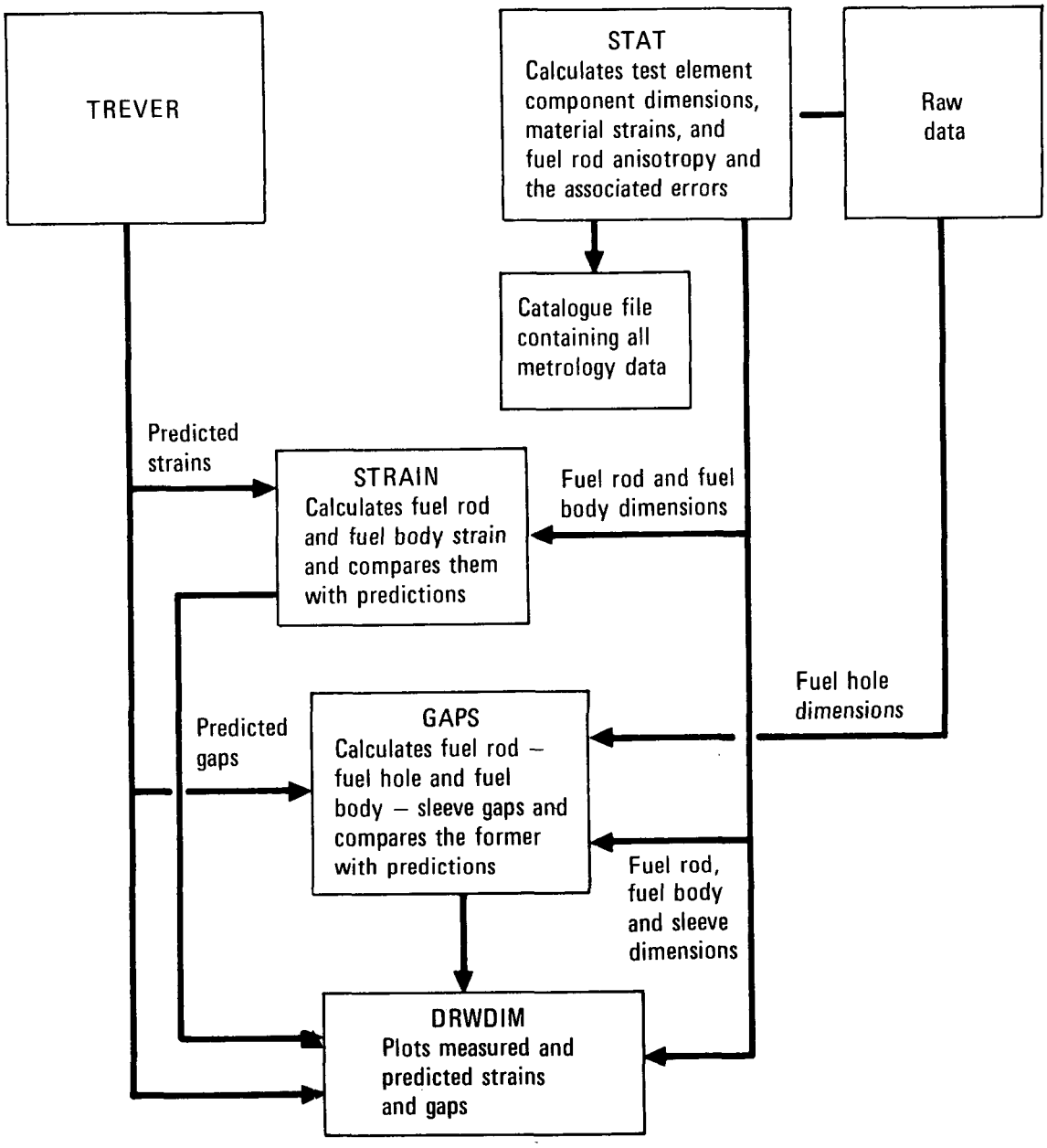

Fig. 6-1. Flow of information through metrology data reduction system

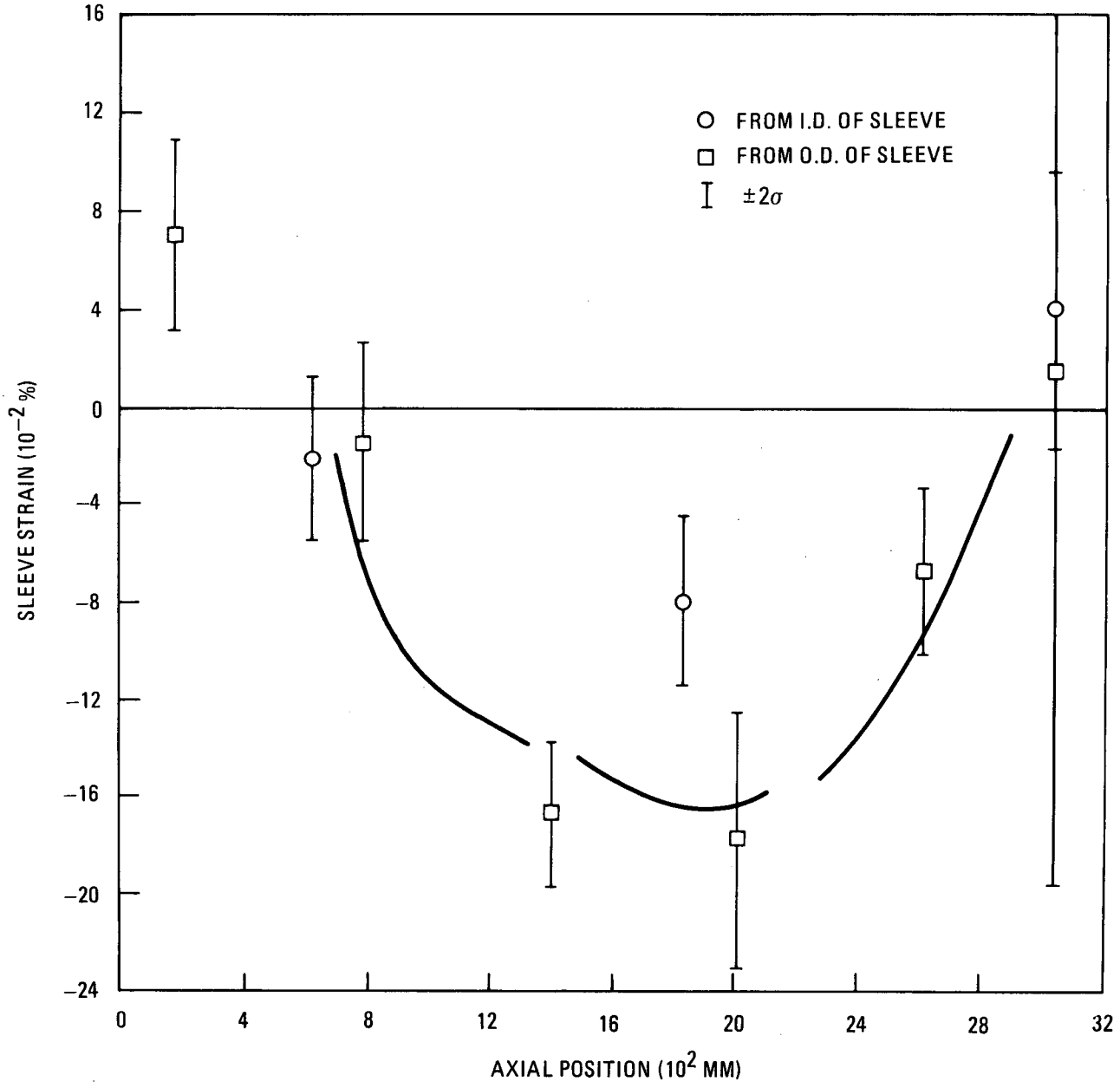

Fig. 6-2. Typical comparison of measured and calculated sleeve strain for a Peach Bottom test element

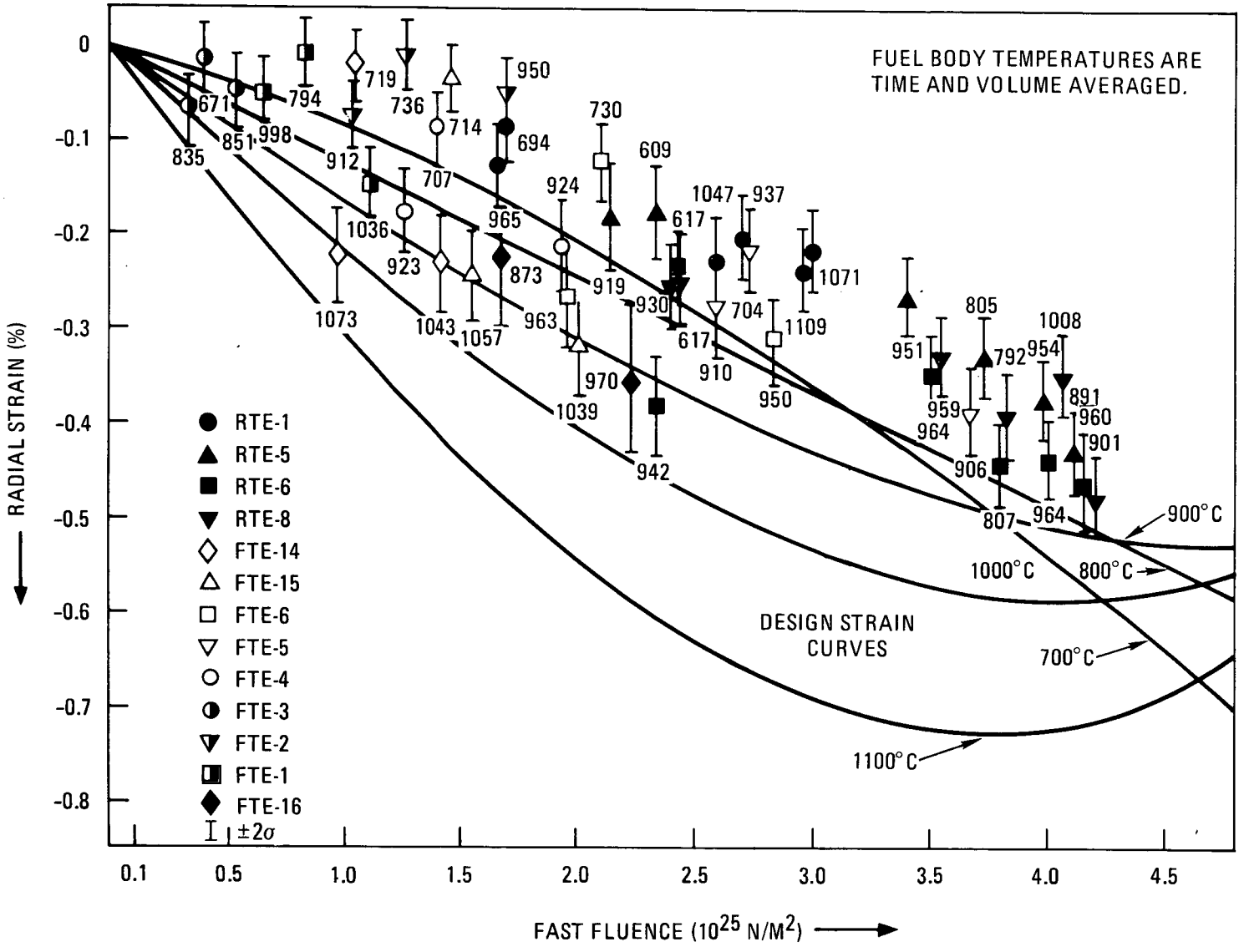

Fig. 6-3. Radial strain versus fast neutron fluence for H-327 graphite fuel bodies irradiated in Peach Bottom test elements

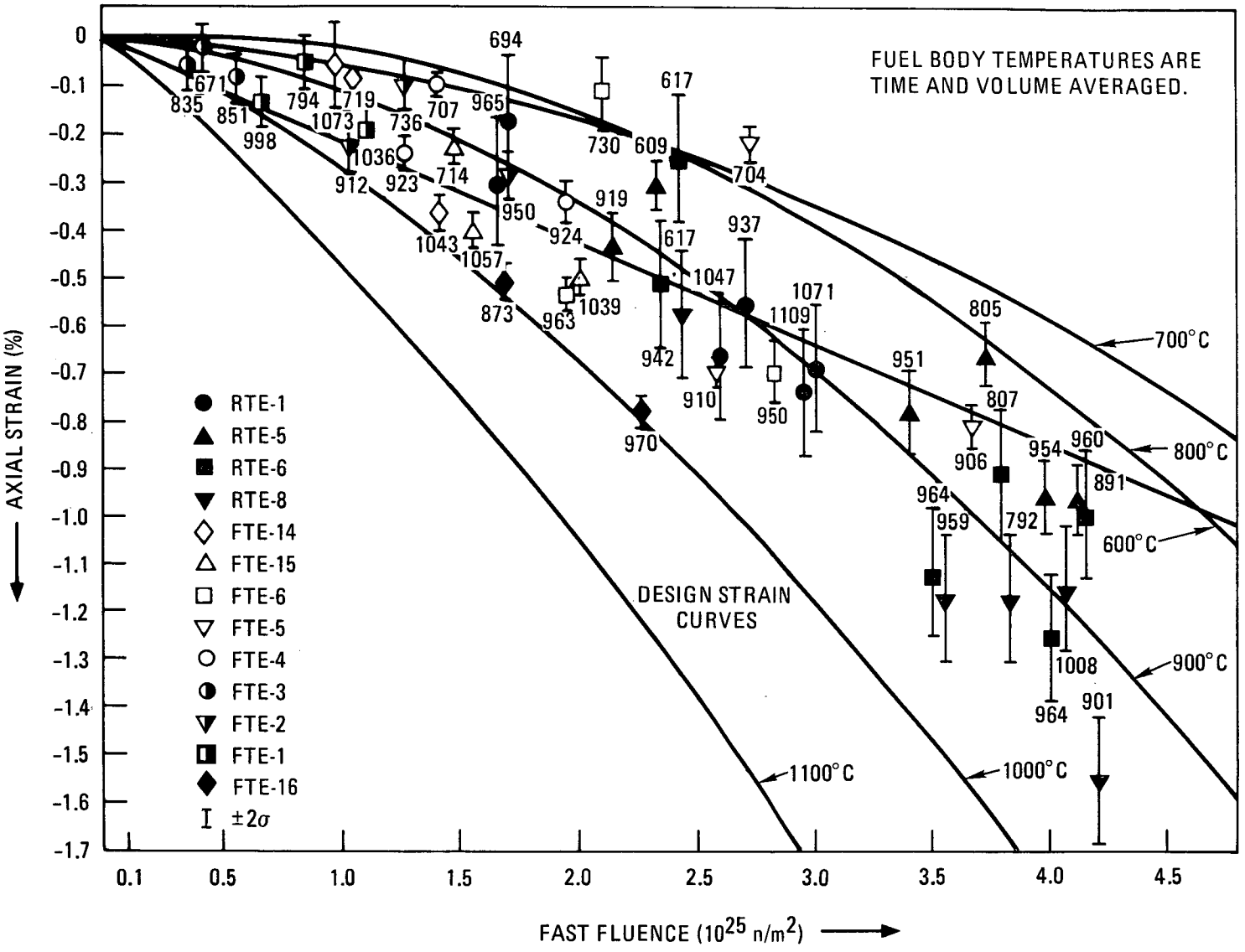

Fig. 6-4. Axial strain versus fast neutron fluence for H-327 graphite fuel bodies irradiated in Peach Bottom test elements

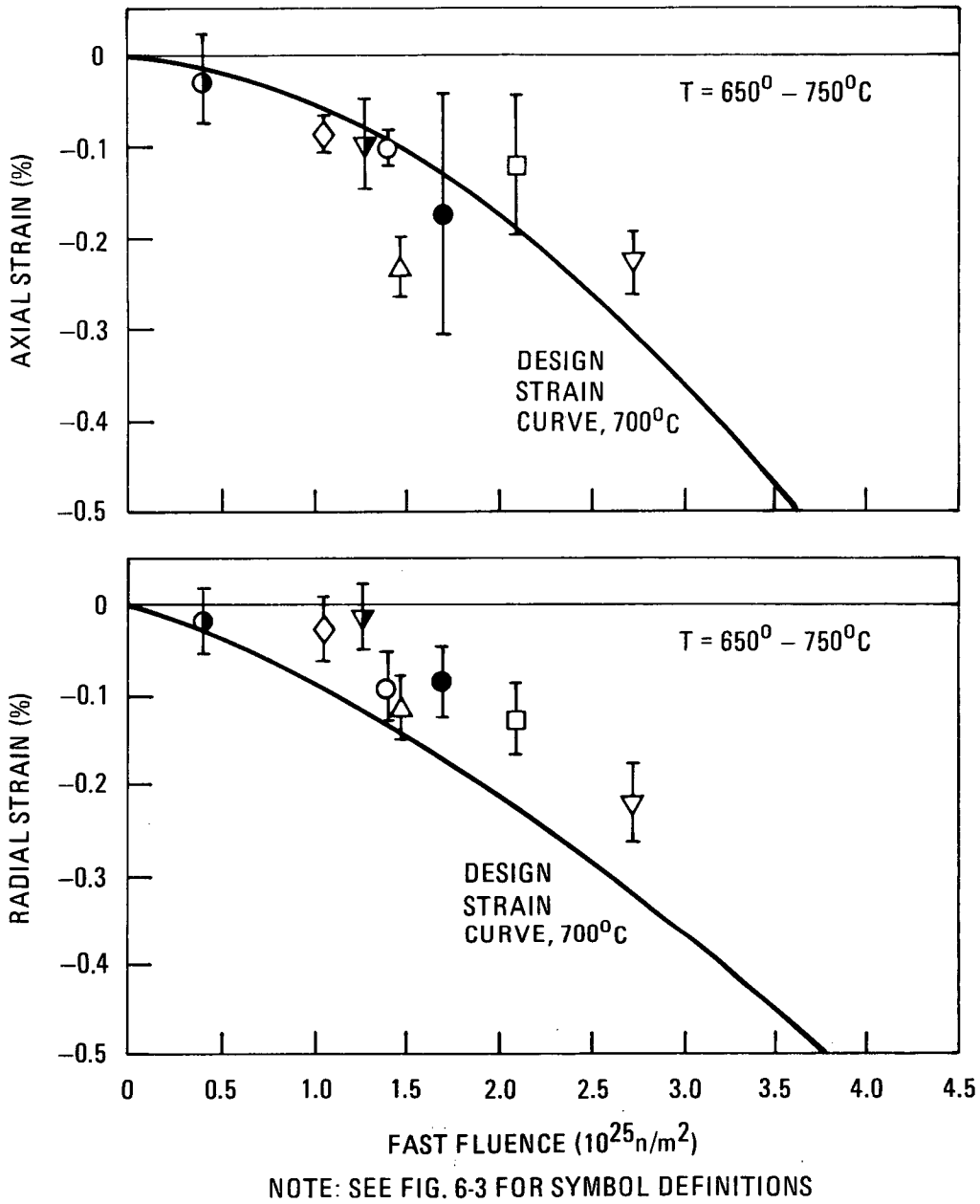

Fig. 6-5(a). Axial and radial strain versus fast neutron fluence for H-327 graphite fuel bodies irradiated in Peach Bottom test elements at 650° to 750° C

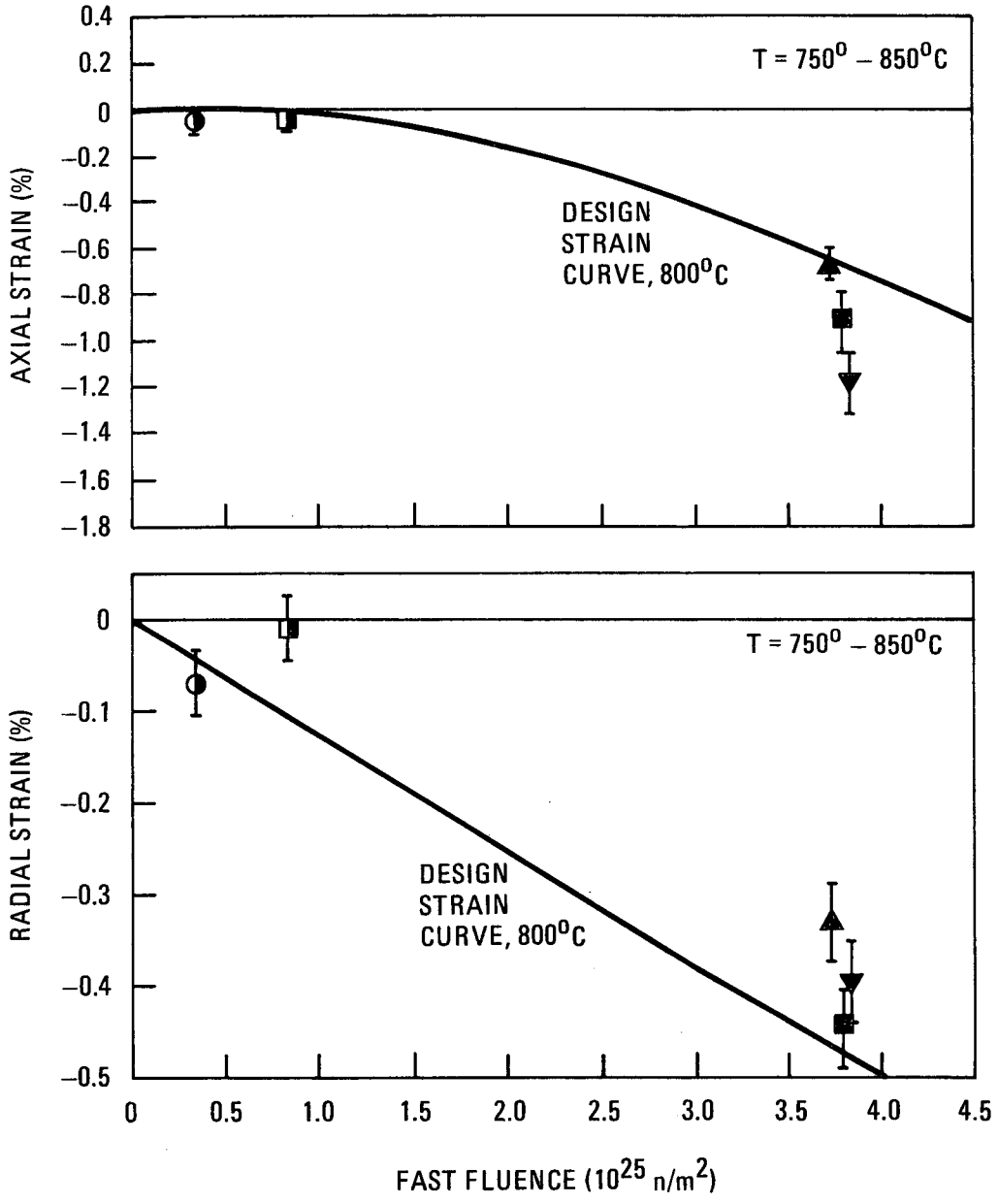

Fig. 6-5(b). Axial and radial strain versus fast neutron fluence for H-327 graphite fuel bodies irradiated in Peach Bottom test elements at 750° to 850°C

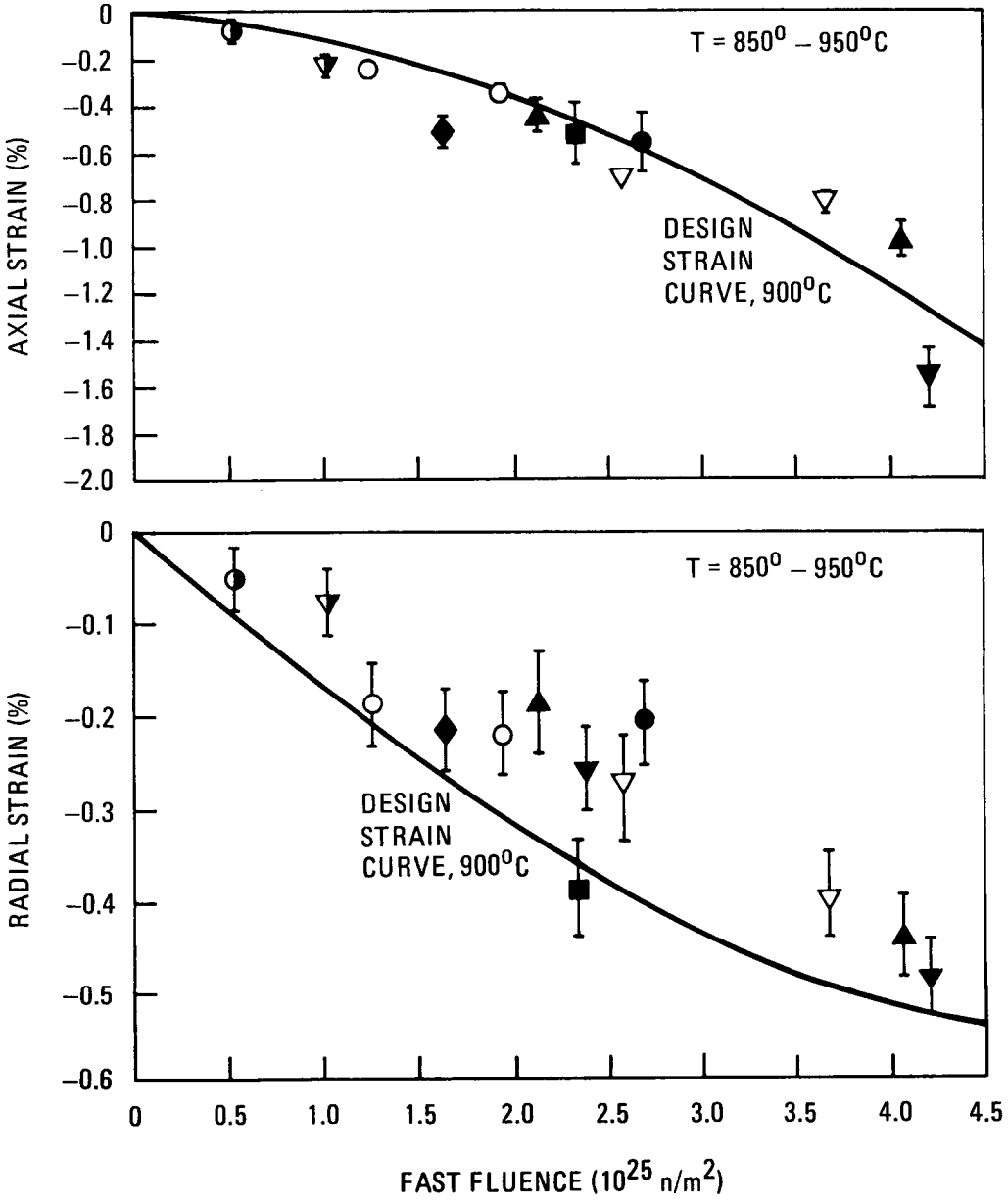

Fig. 6-5(c). Axial and radial strain versus fast neutron fluence for H-327 graphite fuel bodies irradiated in Peach Bottom test elements at 850° to 950°C

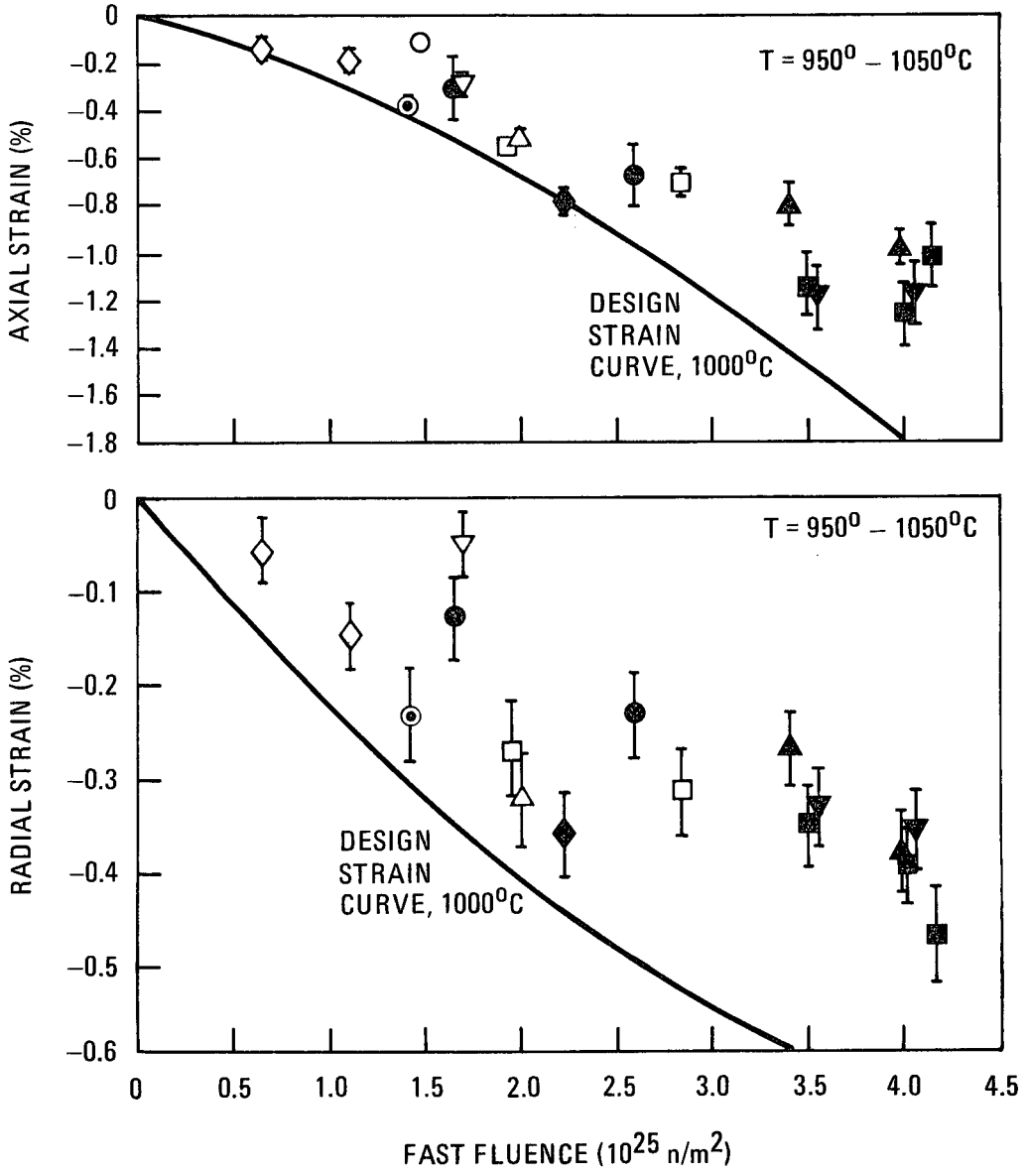

Fig. 6-5(d). Axial and radial strain versus fast neutron fluence for H-327 graphite fuel bodies irradiated in Peach Bottom test elements at 950° to 1050°C

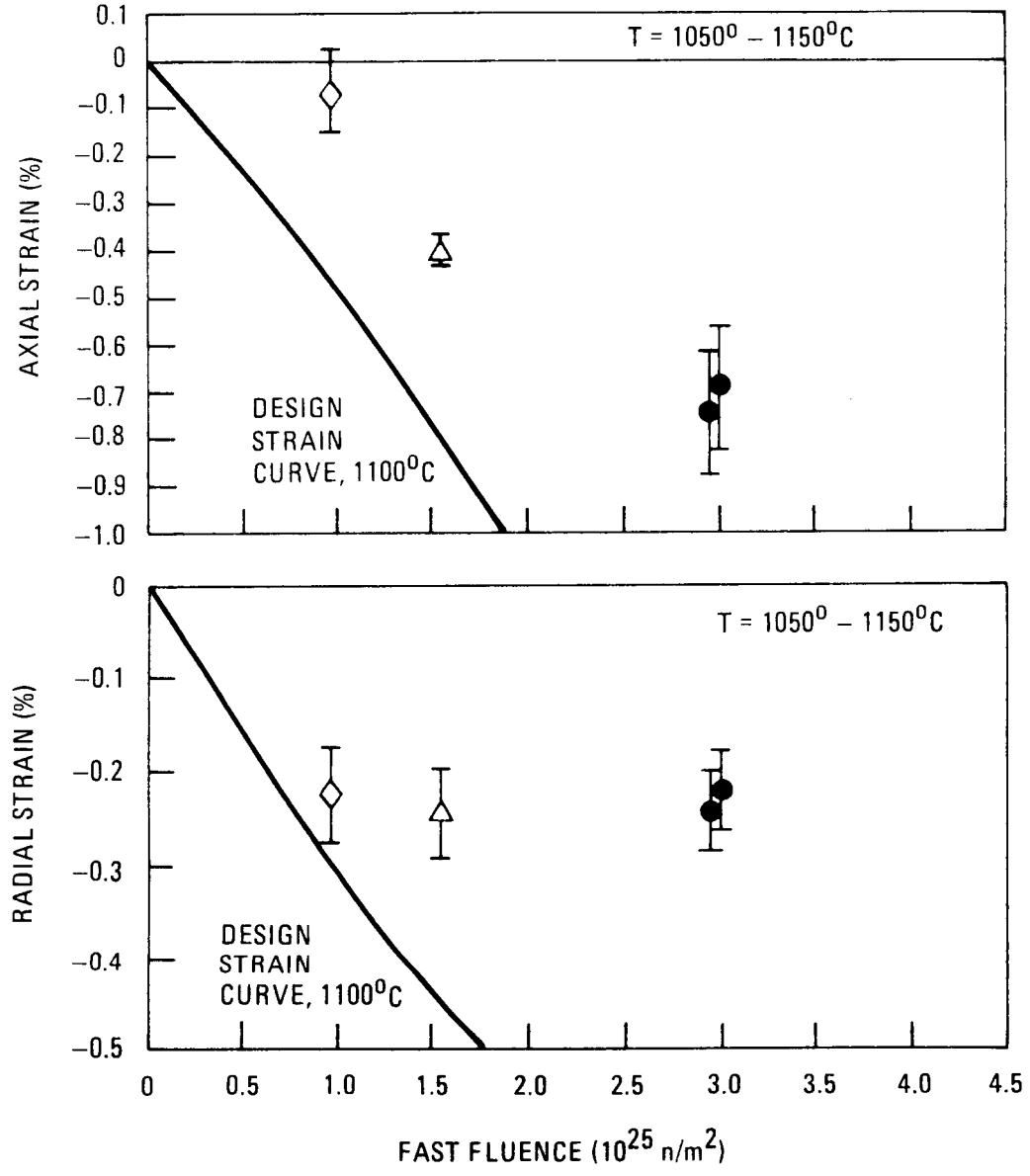

Fig. 6-5(e). Axial and radial strain versus fast neutron fluence for H-327 graphite fuel bodies irradiated in Peach Bottom test elements at 1050° to 1100°C

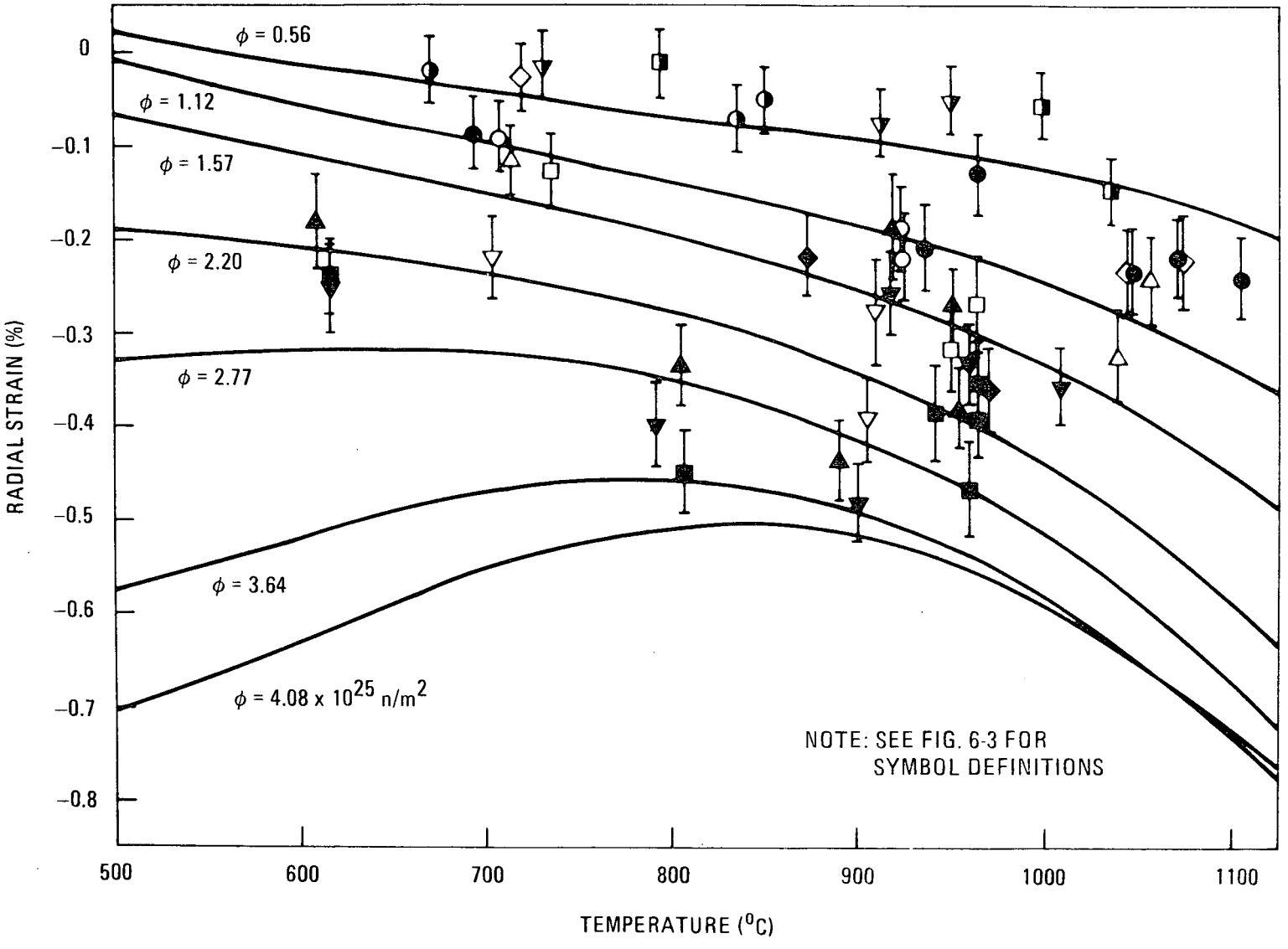

Fig. 6-6. Radial strain versus irradiation temperature for H-327 graphite fuel bodies irradiated in Peach Bottom test elements

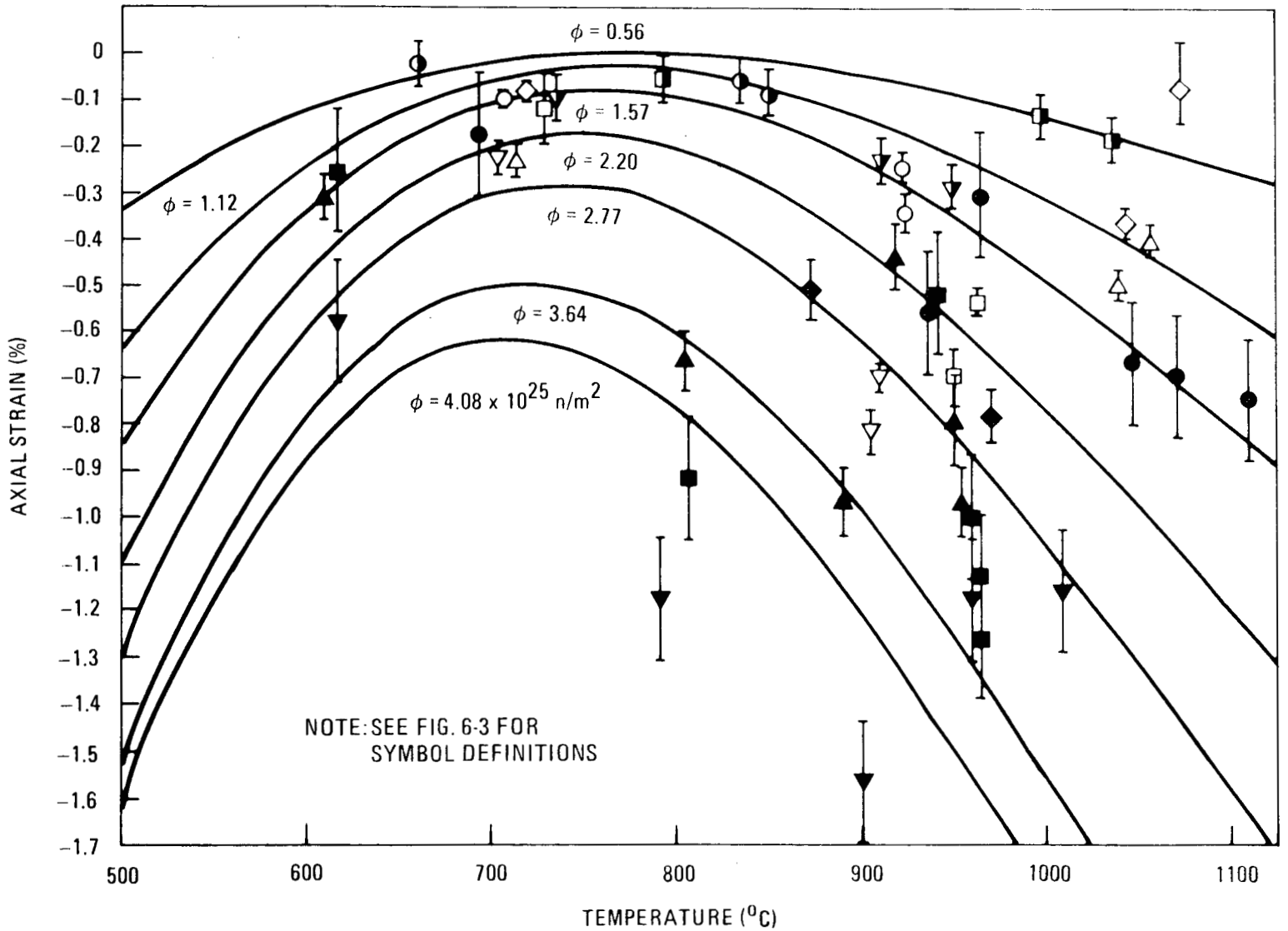

Fig. 6-7. Axial strain versus irradiation temperature for H-327 graphite fuel bodies irradiated in Peach Bottom test elements

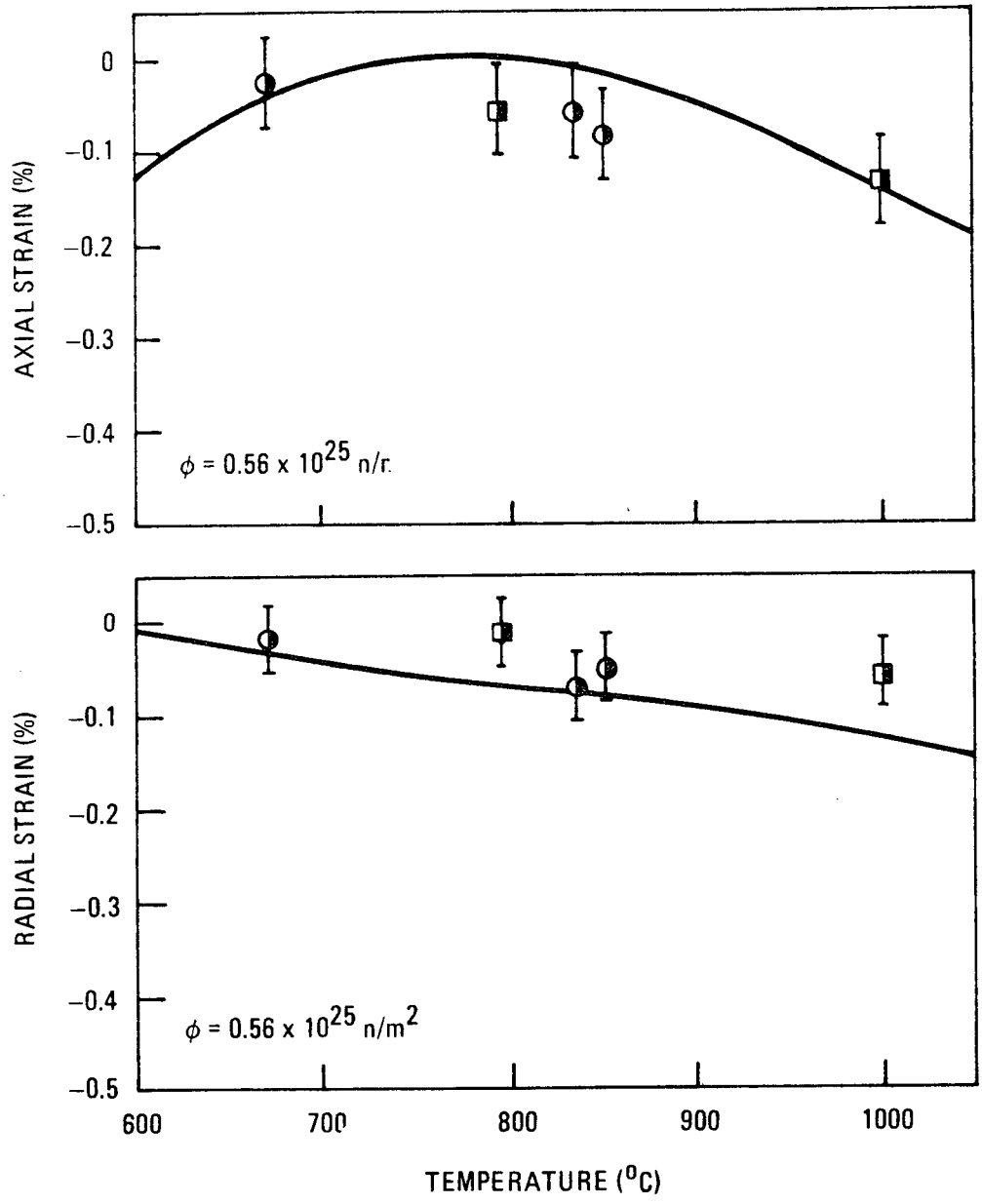

NOTE: SEE FIG. 6-3 FOR SYMBOL DEFINITIONS

Fig. 6-8(a). Axial and radial strain versus irradiation temperature for H-327 graphite fuel bodies irradiated in Peach Bottom test elements to a fast neutron fluence of ≈0.56 x 10^{25} n/m^2

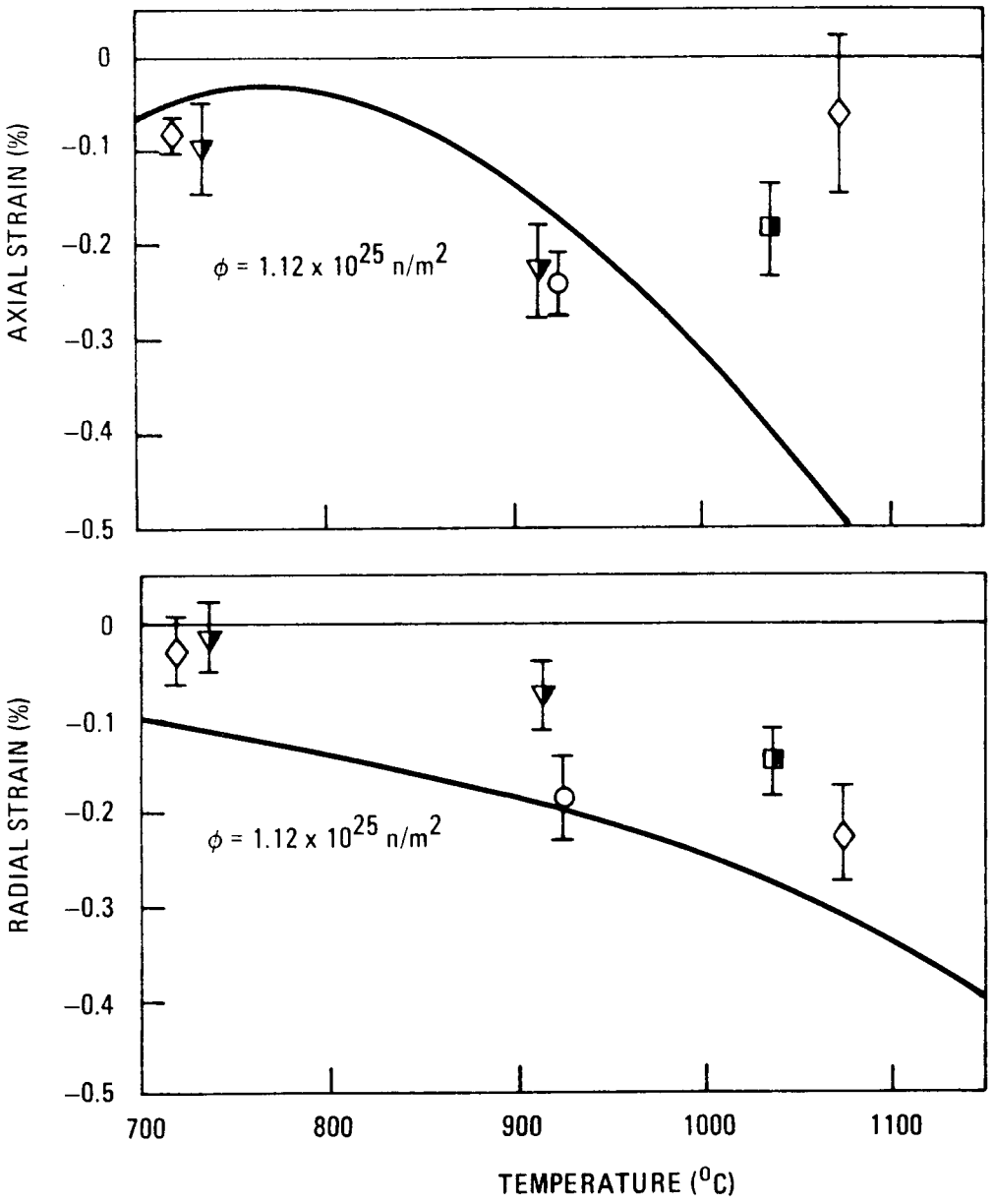

Fig. 6-8(b). Axial and radial strain versus irradiation temperature for H-327 graphite fuel bodies irradiated in Peach Bottom test elements to a fast neutron fluence of $\approx 1.12 \times 10^{25}$ n/m^2

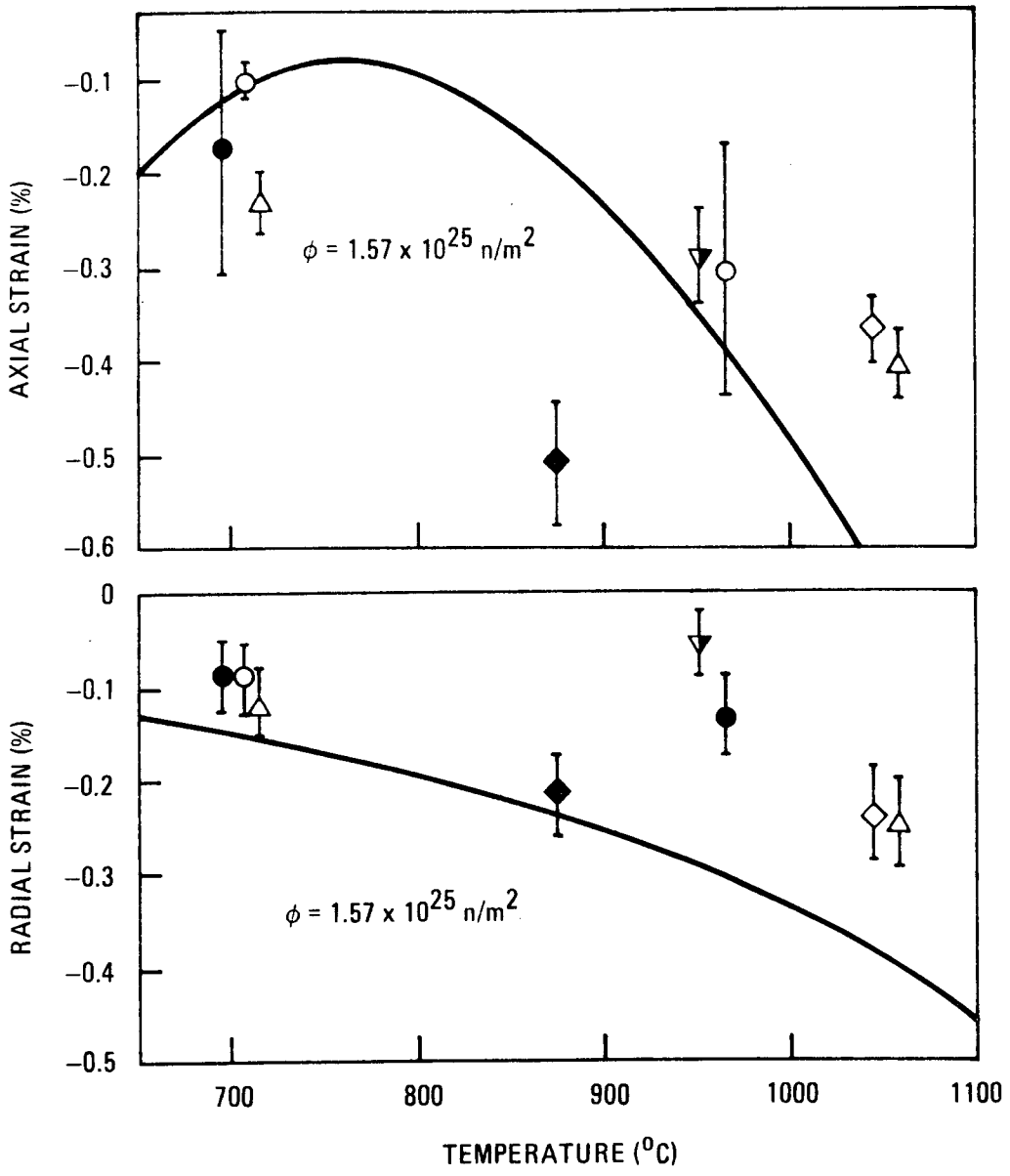

Fig. 6-8(c). Axial and radial strain versus irradiation temperature for H-327 graphite fuel bodies irradiated in Peach Bottom test elements to a fast neutron fluence of ≈1.57 x 10^{25} n/m^2

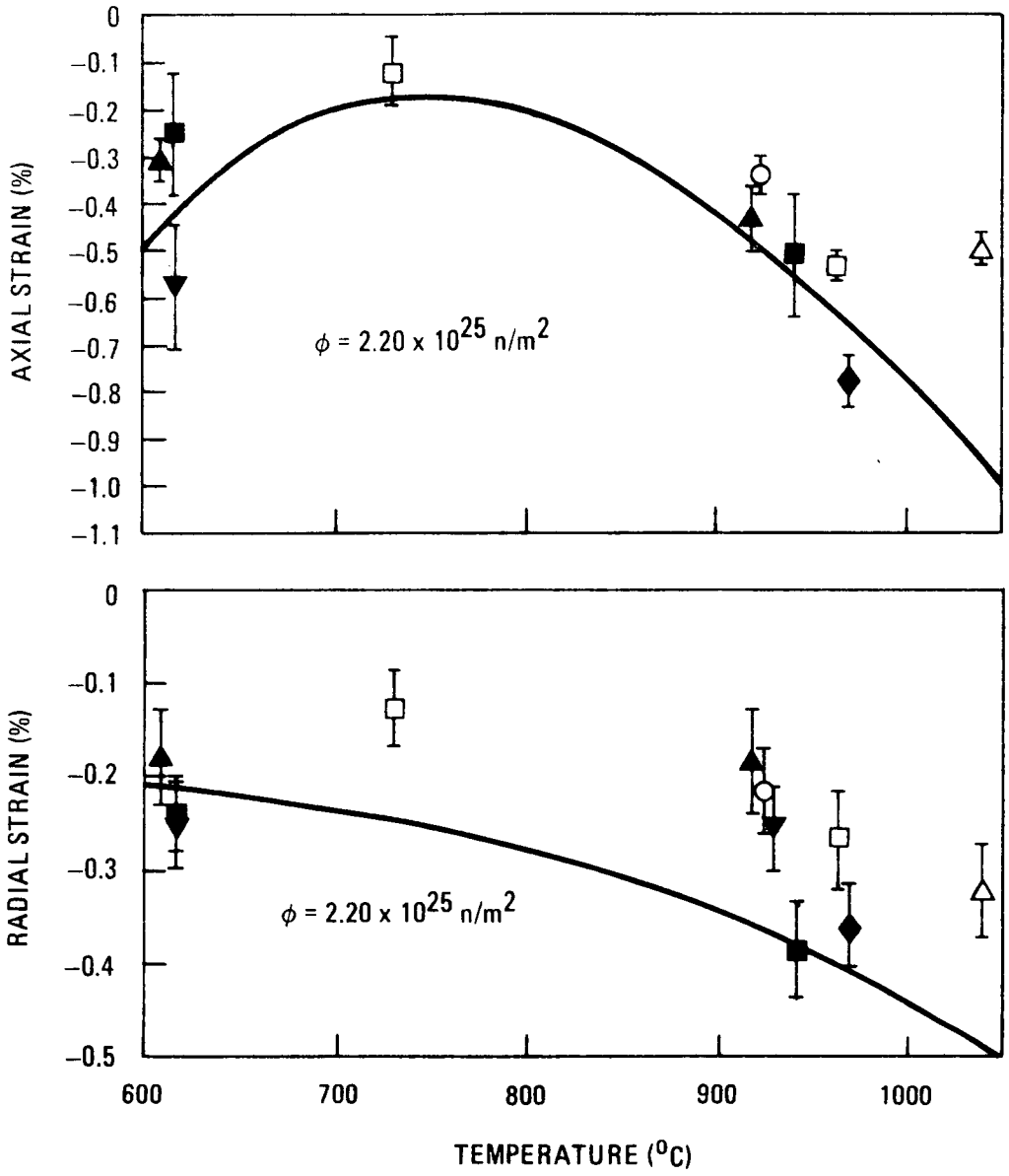

Fig. 6-8(d). Axial and radial strain versus irradiation temperature for H-327 graphite fuel bodies irradiated in Peach Bottom test elements to a fast neutron fluence of ≈2.20 x 10^{25} n/m^2

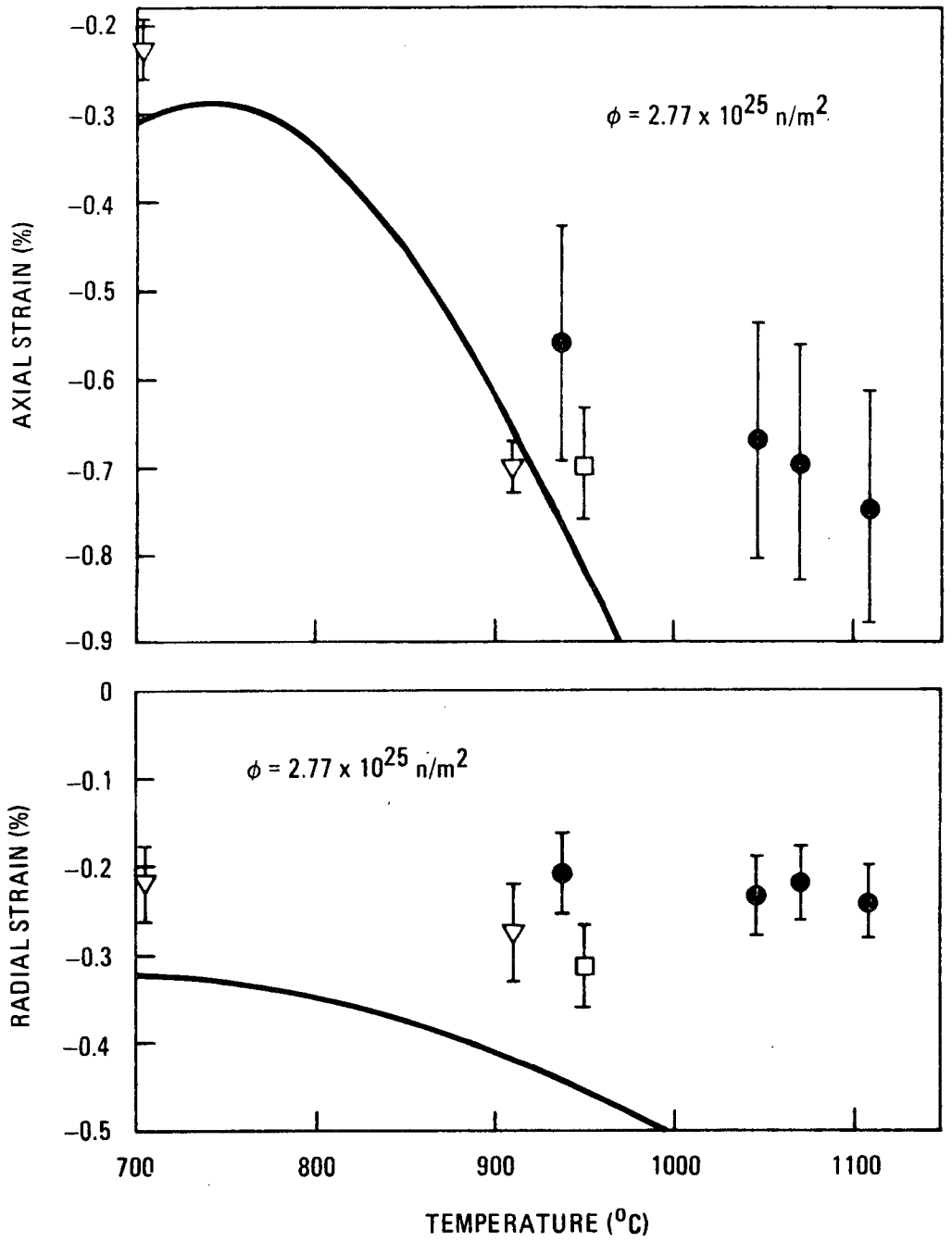

Fig. 6-8(e). Axial and radial strain versus irradiation temperature for H-327 graphite fuel bodies irradiated in Peach Bottom test elements to a fast neutron fluence of ≈2.77 x 10^{25} n/m^2

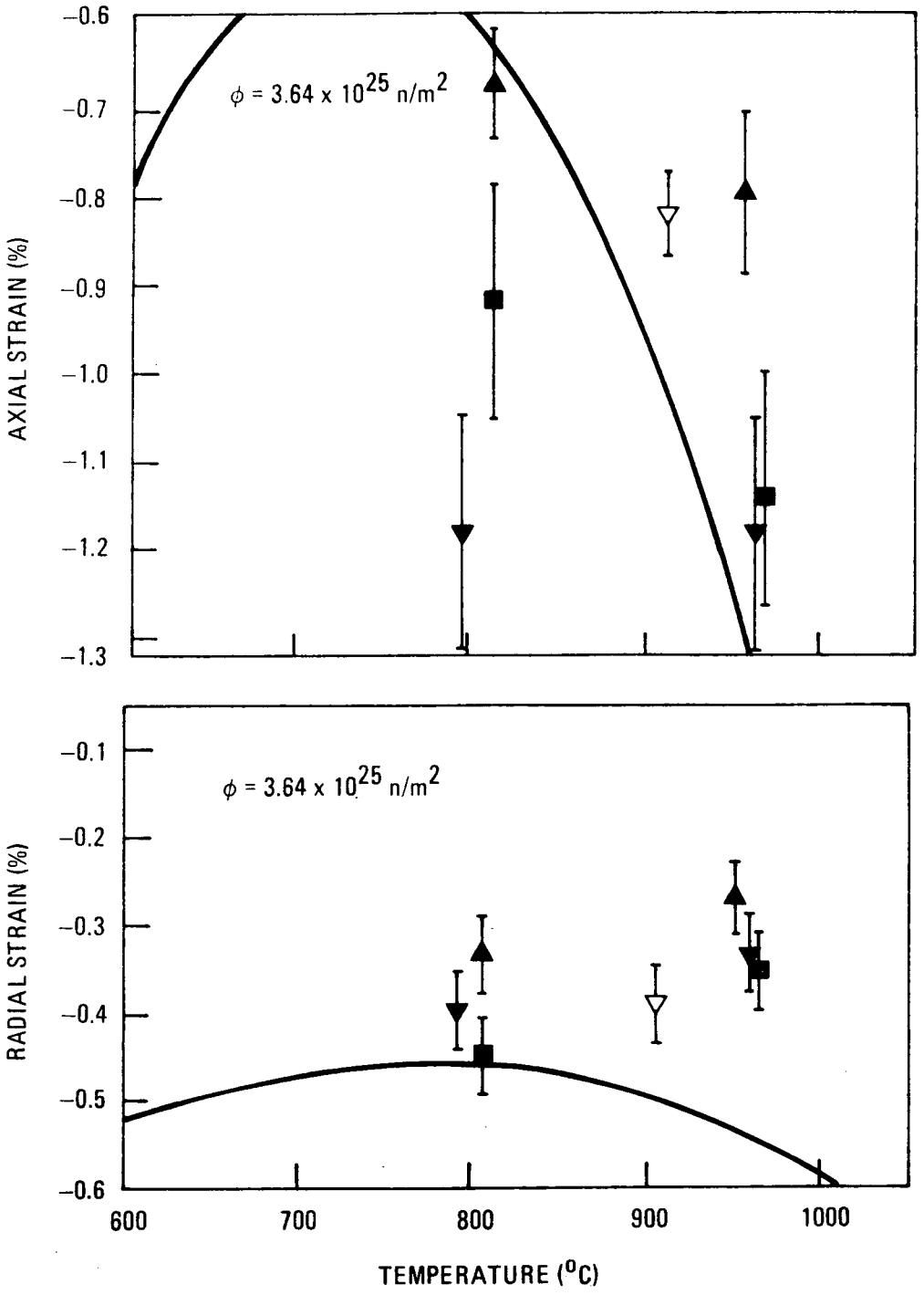

Fig. 6-8(f). Axial and radial strain versus irradiation temperature for H-327 graphite fuel bodies irradiated in Peach Bottom test elements to a fast neutron fluence of ≈3.64 x 10^{25} n/m^2

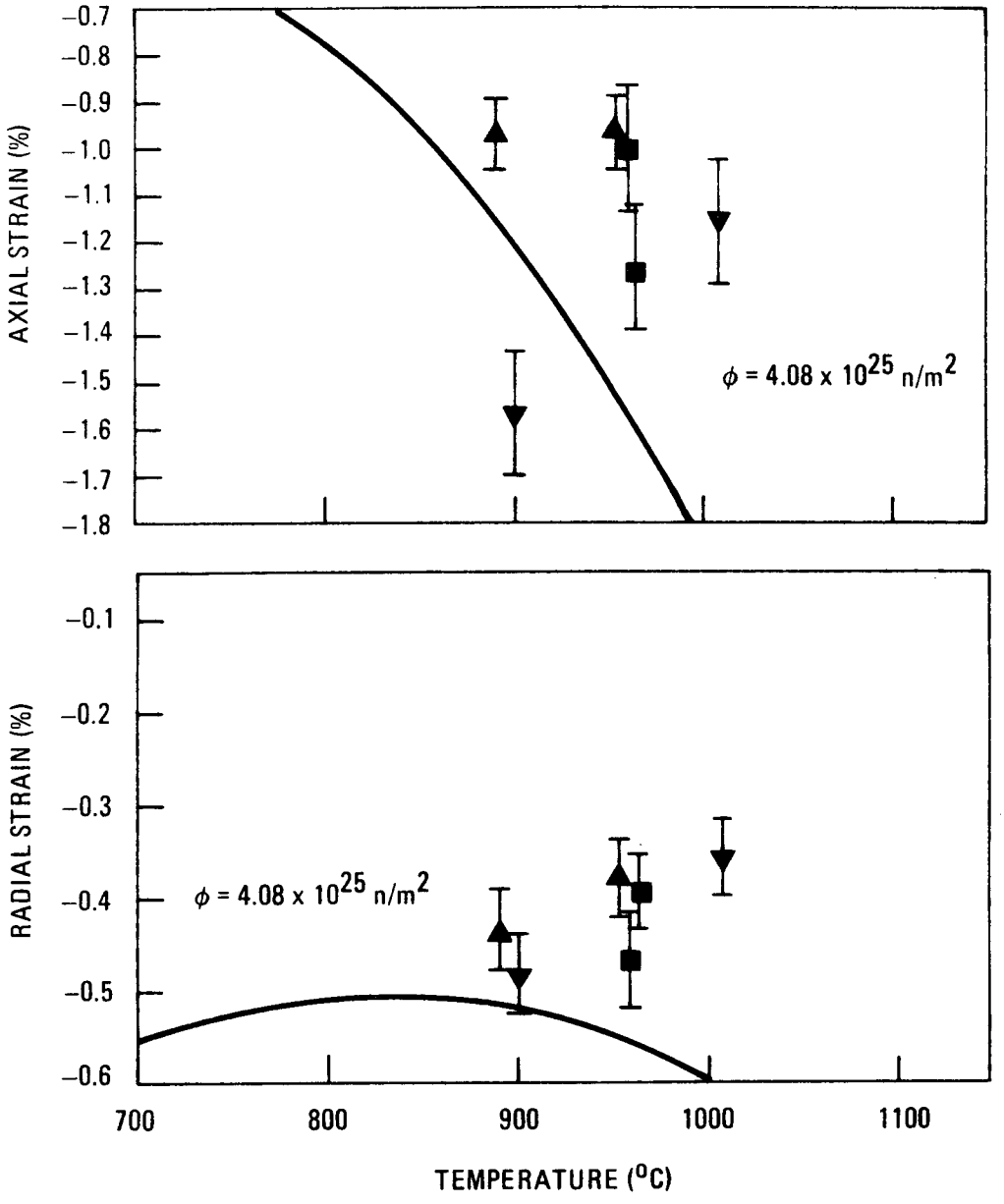

Fig. 6-8(g). Axial and radial strain versus irradiation temperature for H-327 graphite fuel bodies irradiated in Peach Bottom test elements to a fast neutron fluence of $\approx 4.08 \times 10^{25}$ n/m^2

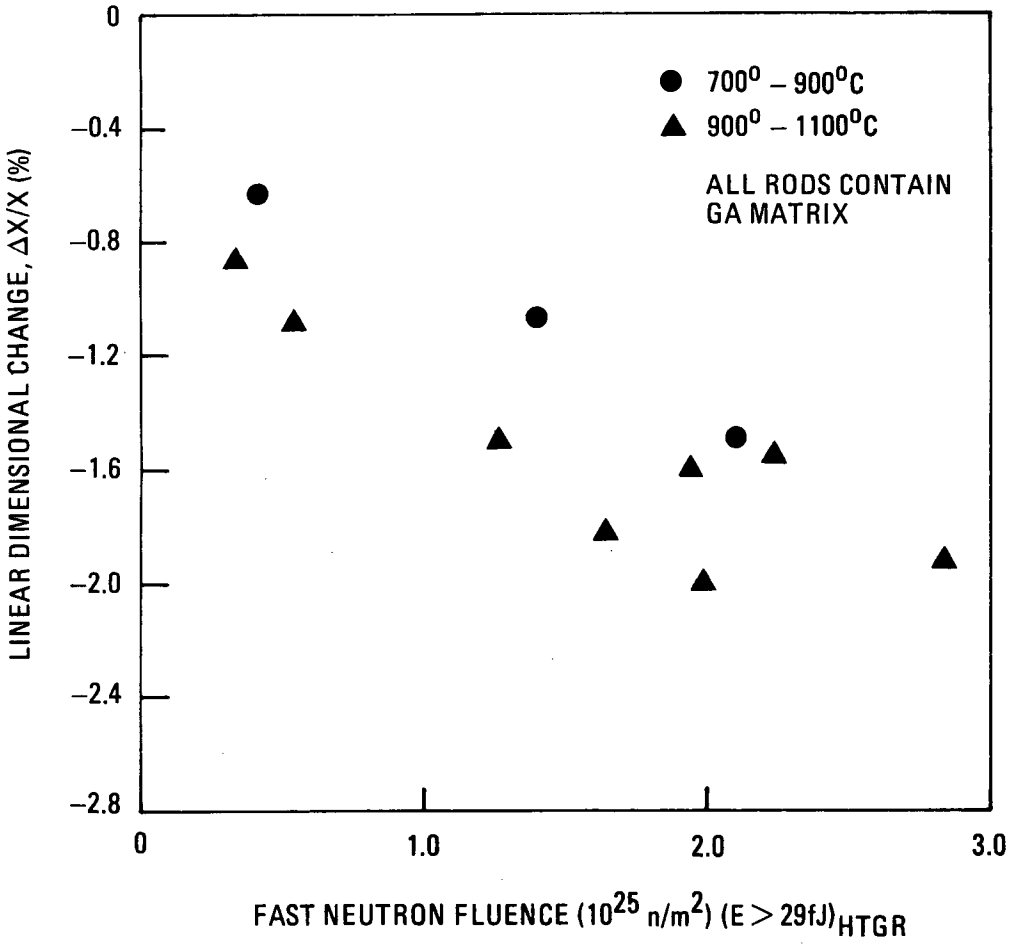

Fig. 6-9. Linear dimensional change of all-TRISO particle [≈50 vol % $(Th,U)C_2$ and 12 vol % ThC_2] fuel rods irradiated in Peach Bottom test elements FTE-3, -9, -6, and -16

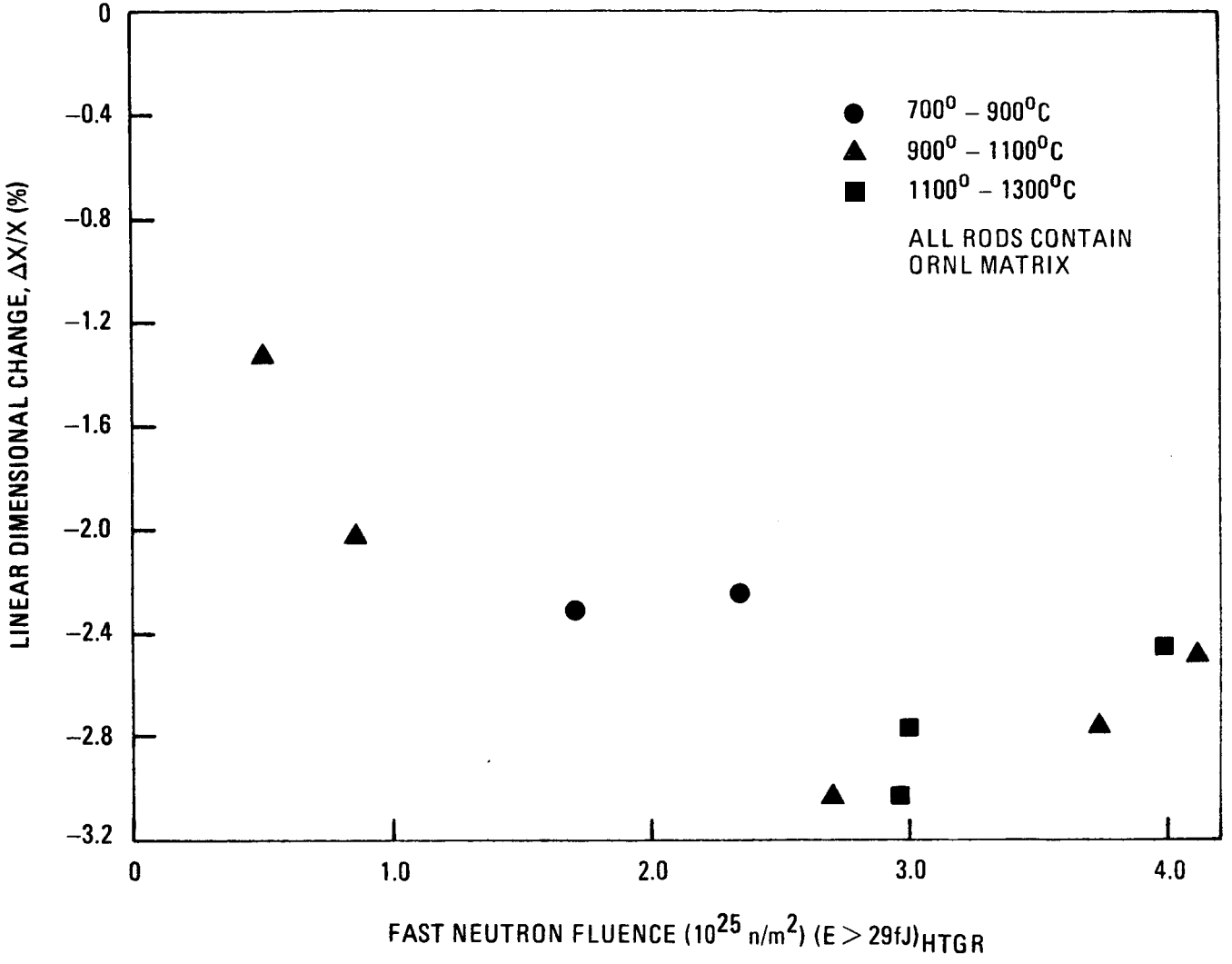

Fig. 6-10. Linear dimensional change of all-BISO particle [≈65 vol % $(4Th,U)O_2$] fuel rods irradiated in Peach Bottom test elements RTE-1, -5, and -7

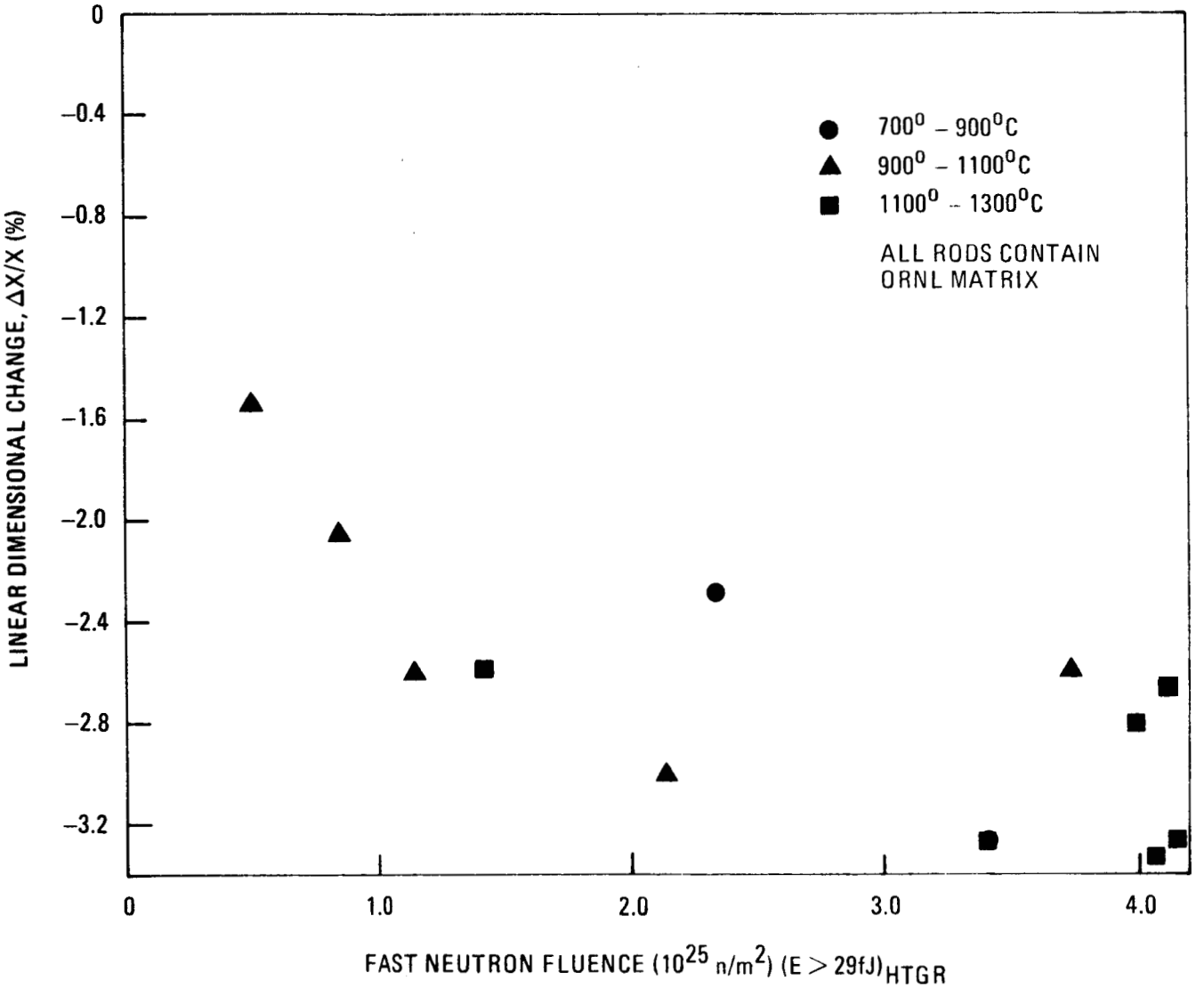

Fig. 6-11. Linear dimensional change of all-BISO particle [≈37 vol % $(2Th,U)O_2$ and 20 vol % ThC_2 or ThO_2] fuel rods irradiated in Peach Bottom test elements RTE-4, -5, -6, -7, and -8

7. STRESS ANALYSIS

7.1. RESIDUAL STRESS CALCULATIONS

The methods and material properties used in the stress analysis are described in previous fuel test element PIE and evaluation reports (Refs. 7-1, 7-2, 7-3, 7-4). Stress calculations were performed for 10 test elements to determine:

1. The distribution of thermal and irradiation-induced operating stresses as a function of time, fluence, and axial position.

2. The maximum operating and shutdown stresses at BOL, during irradiation, and at EOL.

Four fuel body configurations were analyzed:

A. Eight-hole teledial (FTE-1,-2,-3,-4,-5,-6) (Fig. 7-1).
B. Six-hole teledial (FTE-14,-15) (Fig. 7-2).
C. Twelve-fuel-hole hexagonal (PTE-2) (Fig. 7-3).
D. Three-fuel-zone molded teledial (FTE-18) (Fig. 7-4).

The finite element model for each configuration was a sector of unit thickness taken at the midplane of a fuel body. The sector angle of each finite element mesh and the number of nodes and elements are tabulated below.

Configuration	Sector Angle (deg)	Nodes	Elements
Eight-hole teledial	22.5	334	524
Six-hole teledial	30	450	713
Twelve-hole hexagonal	30	515	758
Three-fuel-zone teledial	60	301	495

Temperature and stress distributions at the midplane of each fuel body were calculated using GTEPC-2D (Ref. 7-5), a computer program for viscoelastic analysis of graphite. GTEPC uses a standard viscoelastic solid for stress calculations in which the coefficients of springs and dashpots are functions of temperature and fluence. Thermal boundary conditions were determined from the one-dimensional TREVER (Ref. 7-6) calculations. GTEPC temperature field calculations were verified with TAC 2D (Ref. 7-7) and with TREVER calculations to within ±40°C. Temperatures calculated with TREVER were determined to be within ±82°C (1σ) of measured temperatures (Section 5).

All elements were made of H-327 graphite except FTE-18, which was made from NUKEM A3-3 matrix material. Material properties data used in the stress and thermal analysis of H-327 graphite bodies were obtained from Refs. 7-8 and 7-9, and irradiation-induced creep data were taken from Ref. 7-10. The material properties data used in the analyses of FTE-18 were obtained from Ref. 7-11. The coefficient of irradiation-induced creep for the A3-3 matrix material is described in Ref. 7-4.

7.1.1. Initial Thermal Stress

A summary of initial thermal stresses is given in Table 7-1 for midplane locations of fuel bodies for each element. Except in FTE-18, which contained six fuel bodies, and in FTE-1, maximum initial thermal stresses occurred in fuel body 2. The location of maximum stress varied with the configuration of the fuel body. This stress was located at the central spine sample hole (element 1, Fig. 7-1) in FTE-1 and FTE-2, at the fuel hole surface adjacent to the slot (element 288) in the remaining eight-hole elements, at the outer fuel hole surface in PTE-2 and FTE-14 and -15 (elements 669 and 230, respectively), and at the outer edge of the simulated coolant hole (element 1) in FTE-18.

Comparison of the stress results with the ultimate tensile strength (UTS) values for H-327 graphite in Table 7-2 shows that initial thermal stresses are less than the ultimate strength values. For example, the

in-plane tensile stress for FTE-1 is 7% of the corresponding strength. The strength is obtained by correcting the initial strength at room temperature for the effects of temperature and fast fluence according to Ref. 7-8:

$$UTS_i = UTS_o\left(\frac{E_i * E_T}{E_o^2}\right)^n \quad ,$$

where $n = 0.4$ for radial orientation,

$n = 0.67$ for axial orientation,

E_o = elastic modulus for unirradiated H-327 graphite at room temperature (Table 7-2),

UTS_o = UTS of unirradiated H-327 graphite at room temperature (Table 7-2),

E_i = elastic modulus of irradiated H-327 graphite at room temperature (Table 7-3, Fig. 7-5),

E_T = elastic modulus at elevated temperature T,

$= E_o\ (1 + 1.5 \times 10^{-4}\ \Delta T)$,

ΔT = temperature - 298 K, and

UTS_i = UTS of irradiated H-327 graphite at temperature T.

The initial tensile strength of test elements made of H-327 graphite was assumed to be the strength at the midlength edge of the log. The midlength edge location was selected because the test element bodies were generally machined from the outer portion of the log (Ref. 7-12). This may slightly overestimate the strength, since some bodies were taken from a point midway between the outer portion of the log (designated as edge) and the central portion of the log (Fig. 7-6). On the other hand, the test elements were machined from logs with strengths greater than the mean (Table 7-4). For example, tensile strengths of specimens taken from the midlength-center of each log measured 12.0 to 17.9 MPa, well above the mean strength of 11.2 MPa for all logs. In summary, the midlength-edge strength is believed to be the best estimate of tensile strength at the midplane of test element fuel bodies. For the initial compressive strength, which was not characterized as a function of position in the log, a conservative minimun

value of 27.6 MPa was used. Calculated compressive stresses were found to be small in comparison with the UCS value and were not included in the tables.

The tensile, compressive, and bending strengths of FTE-18 fuel bodies are given in Table 7-5. The tensile strengths of these molded blocks were 1/3 those of H-327 graphite bodies. This low tensile strength is the primary reason for the high stress factors noted for FTE-18 in Table 7-1 and Tables 7-6 through 7-9.

7.1.2. Peak Stress During Life

The stress distribution changed rapidly with time owing to increasing irradiation strain in hotter areas of the fuel body. The higher-temperature areas near the center of the body reversed from initial compressive stress to a state of tensile stress at EOL, while cooler areas near the element sleeve went into compression. This stress reversal was predicted by the GTEPC-2D code at the midplane of all test element fuel bodies. During shutdown at EOL, both tensile and compressive stresses increased significantly relative to operating stresses at EOL. During shutdown, the hotter areas of the fuel body, which were in tension, wanted to shrink more than the body as a whole but were restrained. This resulted in higher tensile stresses. The cooler areas, which were in compression, wanted to shrink less than the body as a whole. This resulted in increased compressive stresses in these areas.

Peak operating and shutdown stress values during the irradiation life of the test elements are given in Tables 7-6 and 7-7, respectively. The tabulated stresses are peak stresses experienced during irradiation (including EOL) of the test elements, as obtained from stress predictions. Peak EOL stresses are similarly presented in Tables 7-8 and 7-9.

Except in FTE-5, -6, -15, and -18, peak operating and shutdown stresses occurred at EOL. Peak operating stresses generally occurred in body 2 of the elements and were always less than the strength.

Tensile shutdown stresses for FTE-1 and FTE-2 were higher than those in all other H-327 graphite fuel elements. The maximum in-plane stress-strength ratios were 1.69 and 1.77 for body 2 of FTE-1 and FTE-2, respectively. For some eight-hole elements (FTE -1, -2, and -4) during operation and for all six of the elements of this type during shutdown, maximum in-plane tensile stresses were located at the inner safety slot (element 359). The slot was a safety feature designed to confine graphite breakage, caused by swelling of fuel rods or loose beds, to the inside diameter of the elements. It should be noted, however, that the stresses were not properly calculated. The applied elasticity model contained a theoretical singularity of infinite stress at the notch, which should have been evaluated by another method, such as fracture mechanics.

Because of this inherent error in the analysis, stress distributions for the eight-hole elements (except FTE-1) were reviewed to identify other locations having high stresses. In every case, the next-highest stress was found at the fuel hole surface adjacent to the central spine (element 10, Fig. 7-1). These stresses were generally 30% to 40% less than calculated at the notch, but in some cases were still greater than the UTS. Stress-strength ratios in excess of 1.0 were calculated at this location in body 2 of FTE-2 (1.30), FTE-4 (1.04), and FTE-6 (1.13). These results suggest that the calculations are slightly conservative or that the UTS is a conservative criterion for failure, since cracks were only observed in body 2 of FTE-2.

The stress-strength ratio of 4.28 in body 4 of FTE-18 was the highest calculated for any of the test elements. One reason for the high stress-strength ratios calculated for FTE-18 is that the unirradiated UTS values at room temperature reported in Ref. 7-4 were used (the other nine elements were compared with the irradiated UTS at operating temperatures). The UTS is dependent on the $(E_i * E_T / E_o)$ factor in Eq. 7-1. If a factor of two increase in the elastic modulus is assumed for the material (this is the approximate increase for H-327 graphite at the irradiation temperature and neutron exposure for FTE-18), the maximum in-plane stress-strength ratio would be about 3.0. Indirect evidence indicates that no major cracking of the fuel bodies occurred. The locations of these high tensile stresses

were near the inner surface of the thermocouple and coolant holes, which were not accessible for detailed visual examination. However, no cracks or severe deformations were found at the outer surface of the fuel bodies, nor was evidence of increased fuel particle failure (e.g., because of matrix particle interaction) found from fission gas release measurements. Possible conclusions are that the stress calculations are conservative, the blocks displayed exceptional structural performance, or the UTS failure criterion is conservative.

Since residual stresses in irradiated fuel bodies represent a bending type stress field of inner tensile stresses and outer compressive stresses, the ultimate bending strength (UBS) is perhaps a better criterion for failure of the graphite fuel bodies. If the UBS given in Table 7-5 is substituted for the UTS, the maximum stress-strength ratio for FTE-18 is reduced to 1.27, a ratio more in line with the fact that no cracks were detected in the element. The UBS/UTS ratio for H-327 graphite is approximately 1.7 for the radial orientation (Ref. 7-13). Maximum stress-strength ratios calculated using the UBS would be less than 1.0 for all H-327 graphite elements. Except in FTE-2, this is consistent with the absence of structural damage.

The maximum axial stress-strength ratio for the H-327 graphite fuel bodies occurred in body 2 of FTE-2. A maximum stress-strength ratio of 0.82 was calculated at the fuel hole surface nearest the center of the fuel body (element 20). The maximum stress-strength ratio in FTE-18 was 3.28. The discussion concerning the high in-plane stress-strength ratios is also pertinent to the axial stress-strength ratios.

7.1.3. Graphite Failure in FTE-2

No structural damage was observed for any of the test element fuel bodies except body 2 of FTE-2. The various cracks in this fuel body are shown in photographs taken by the Kollmorgan periscope in the GA Hot Cell (Figs. 7-7 through 7-14). One external crack was observed along hole 1 in Figs. 7-7 and 7-8. Internal cracks in holes 1, 2, and 8 are shown in Figs. 7-9 through 7-12. Figures 7-13 and 7-14 show the failure at the safety slot

adjacent to fuel holes. The locations of internal cracks are diagrammed in Fig. 7-15.

FTE-1 and FTE-2 were predicted to experience the highest in-plane tensile stresses of any H-327 graphite fuel bodies. In addition, these two elements were unique among the analyzed Peach Bottom test elements, having loose particle fuel beds instead of fuel rods. It has been postulated that loose particle beds can densify, forming solid bridges across the fuel hole diameter. Thermal cycling can result in differential thermal strains between the fuel bed and graphite, producing stresses in excess of calculated graphite stresses. Although FTE-1 was predicted to have stresses nearly as high as those in FTE-2, no graphite failure occurred. The reason for this is not known.

7.1.4. Stress Analysis Conclusions

The conclusions from the stress analysis are as follows:

1. Visual examination of fuel bodies and slices taken during each element PIE revealed no structural damage of graphite due to residual stresses, except in FTE-2.

2. Neither six-hole teledial elements FTE-14 and FTE-15 nor hexagonal element PTE-2 can be considered a high-stress experiment, since the highest stresses in each element reached only ~50% of the UTS.

3. Each of the eight-hole teledial fuel test elements was predicted to achieve a stress-strength ratio $\geq$1.0 during its irradiation history. FTE-1 and FTE-2 were highest, with predicted EOL shutdown stresses at the safety slot of 169% and 177% of the calculated UTS at EOL. However, these high stresses were calculated at the root of a notch, where the models are known to be incorrect. Stresses $\geq$1.0 were also calculated at the inner

fuel hole surfaces in FTE-1, -2, -4, and -6. These high stress-strength ratios, combined with the observation of no failure except in FTE-2, suggest that the calculations and/or use of the UTS as the failure criterion is conservative.

4. FTE-18 was the highest calculated stress experiment, with stresses equivalent to those experienced by FTE-2. However, because the FTE-18 graphite material had a UTS that was only 1/3 the UTS of the H-327 graphite used in all other test element fuel bodies, the stress-strength ratio was extremely high, i.e., 4.28. However, no graphite failure was observed. The UBS is perhaps a better failure criterion since residual stresses in irradiated fuel bodies represent a bending type stress field of inner tensile and outer compressive stresses. Substituting the UBS for FTE-18 reduces the maximum stress-strength ratio to 1.27.

5. Axial cracks found in the center body of FTE-2 are postulated to have resulted from differential thermal strains between densified loose particle fuel beds and surrounding graphite, superimposed on high in-plane residual stresses (particularly at the safety slot and inner fuel hole surface).

7.2. DESTRUCTIVE STRESS EXAMINATION

An experimental program measured residual stress and strain distributions and additional load-carrying capacity in 21 H-327 graphite fuel bodies. The teledial fuel bodies represent eight test elements irradiated to fast neutron fluences up to 4.2×10^{25} n/m^2 $(E > 29\ fJ)_{HTGR}$ in the Peach Bottom reactor. The techniques employed included dimensional-change measurements, ring cutting, and four-point bend tests. A discussion of these techniques is presented in Ref. 7-14. The results obtained from irradiated samples were compared with the measurements on unirradiated control specimens to estimate irradiation-induced changes in material properties.

Irradiation conditions were obtained from computer simulations of the reactor operating history and were verified by gamma-spectroscopic measurements and thermocouple readings (Ref. 7-15). Where possible, test results were compared with analytical predictions (Ref. 7-16 and 7-17), using finite element methods and material properties data (Ref. 7-8). Test results were averaged over individual teledial bodies for comparison with predictions based on body-average irradiation conditions.

7.2.1. Ring Cut, Pressure Burst, and Diametral Compression Tests

Slices of 20-mm thickness were cut from 19 irradiated and nine unirradiated fuel bodies and subjected to radial-ring-cut, hydraulic burst, and diametral compression tests to determine in-plane stress and load-carrying capacity (Table 7-10).

A total of 33 unirradiated and 100 irradiated slices were subjected to radial ring cut tests. As expected, the diameter of the teledial ring and the distance between grooves on opposite sides of the cut were observed to decrease owing to release of compressive hoop stresses at the outer fiber and tensile hoop stresses at the inner fiber. In Figs. 7-16 and 7-17, results obtained from eight-hole-element slices are presented and compared with predictions obtained from a linear regression analysis. Apparently, in-plane stresses build up at a faster rate than predicted, reaching a peak at a fluence of approximately 0.5×10^{25} n/m^2 $[(E > 29\ fJ)_{HTGR}]$. With additional fast neutron exposure, the in-plane stresses decrease, possibly at a faster rate than predicted, although the scatter in the data makes it impossible to be certain. The average overprediction of in-plane stress over the fast fluence range 0.4 to 3.6×10^{25} n/m^2 $[E > 29\ fJ)_{HTGR}]$ experienced by the slices cut from eight-hole elements was 30%. Although the results for slices from six-hole elements were insufficient in quantity to permit a similar analysis, the in-plane stress for these specimens was found to be overpredicted by an average of 50%. These slices experienced fast fluences of 1 to 2×10^{25} n/m^2 $[(E > 29\ fJ)_{HTGR}]$.

Hydraulic burst and diametral compression tests were performed on 111 irradiated and 100 unirradiated slices. The results of these tests are presented in Figs. 7-18 and 7-19, respectively. The observed failure modes for both the six- and eight-hole teledial configurations agreed with the predicted failure modes for both tests. The six-hole slices failed at the outer fuel hole surface, which was predicted to be in compression. Consequently, the observed increase in burst pressure and failure load with neutron exposure is anticipated because of the irradiation-induced increase in graphite strength. The eight-hole slices failed at the inner surface of the fuel hole, which was predicted to be in tension. Consequently, the strength margin should decrease with neutron exposure until the irradiation-induced increase in graphite strength overcomes the irradiation-induced in-plane stress. This was observed, with the lowest in-plane strength occurring at about 0.5×10^{25} n/m^2 $[E > 29 \text{ fJ})_{HTGR}]$. This coincides with the peak in-plane stress, as determined from ring cutting (Figs. 7-16 and 7-17).

7.2.2. Four-Point Bend Tests

Thin strips from five eight-hole fuel bodies and thick strips from 14 six- and eight-hole bodies were subjected to four-point bend tests. In all, 208 tests were performed on irradiated strips and 88 on unirradiated samples (Table 7-11). The relative increases in Young's modulus and rupture modulus of thin strips with irradiation are compared in Fig. 7-20 with design data established by UTS tests on small graphite samples irradiated under accelerated conditions (Ref. 7-8). A similar presentation of the bend-test results for thick strips from eight different eight-hole bodies is shown in Fig. 7-21. Except for the rupture modulus of thick strips, which underwent a marginal increase of 5% compared with predictions of 45%, the observed increases are in line with design data. The good agreement for thin strips and the apparent overprediction of the maximum fiber strength for thick strips suggest that these strips contained nonlinear stress gradients. This resulted in net tensile stresses at the outer fiber after strip-cutting and an apparent reduction in rupture modulus. Nonlinear stress gradients can be deduced from the stress contour plots (Ref. 7-17) and from bowing differences between thick and thin strips. Thin strips showed smaller positive bow

and stress gradients, which is consistent with net tensile stresses at the outer fiber of adjacent thick strips.

7.2.3. Strip-Cutting Tests

About 230 irradiated strips and 25 control samples were cut from 14 irradiated and two unirradiated graphite fuel bodies. Strip elongation and bow were measured to determine the release of axial stresses (Table 7-12). Thick strip elongation was quite small (Figs. 7-22 and 7-23), while thin strip elongation peaked at a fast fluence of about 1.7×10^{25} n/m^2 [E > 29 fJ)$_{HTGR}$] (Fig. 7-24) and was strongly correlated with irradiation temperature (Fig. 7-25). These observations agree with predictions. However, the results also reveal thin strip elongation to be overpredicted by about 50%. This suggests a reduction in residual compressive stress at the neutral fiber.

Differential bow (i.e., before and after cutting) in thin and thick strips is shown in Figs. 7-26 through 7-29. Differential bow measurements for thin and thick strips were less than half of predicted values, and bow inversions relative to predictions were observed for all strip types. The onset of bow inversion ranged from fast fluences of 1.3×10^{25} n/m^2 [E > 29 fJ)$_{HTGR}$] for the thinnest strips to 3.6×10^{25} n/m^2 for the thickest strips. Strips with larger cross-strip temperature gradients (180°C) towards EOL had somewhat higher differential bow than strips with lower (~120°C) gradients. This is expected, since shutdown stresses are higher for larger temperature gradients. The maximum differential bow was observed at a fast fluence of about 1.7×10^{25} n/m^2 [(E > 29 fJ)$_{HTGR}$], which coincides with the maximum measured strip elongation.

It is hypothesized that the unexpected behavior of the strips can, at least in part, be attributed to creep-induced gradients in the coefficient of thermal expansion (CTE) (see Section 7.2.4). In the presence of cross-strip CTE gradients, the smaller the temperature gradient across the strip, the lower the fast fluence at which the bow inversion relative to predictions should occur. This was observed. The consequence of this

effect would be a reduction, relative to predictions, in residual stresses and stress gradients. This is consistent with ring-cutting results and thin strip elongations, as well as the strip-bowing results.

Perturbations originating from the cutting process were also investigated as a possible explanation for the behavior of the strips. A parameter study of saw-cutting feed rate and rotational blade speed yielded no significant variations in strip elongation and bowing, indicating that the cutting process was probably not the cause of the unexpected behavior.

7.2.4. Thermal Expansivity Measurements

Representative unirradiated control samples and 77 thin strip samples from four irradiated fuel bodies were subjected to thermal expansivity measurements (Fig. 7-30). The thermal expansivity was observed to vary systematically with azimuthal position on the body, being a maximum on the convex side of the bowed body and a minimum on the concave side, as shown in Figs. 7-31 through 7-34.

An initial hypothesis to explain the CTE variation (rejected later) was that the denser material had a lower CTE. An alternative hypothesis that CTE was influenced by creep strain was proposed after studying the anomalous bowing deformations of thin strips, which typically bowed in a direction opposite to that predicted. It was suspected that this was related to a spatial variation of CTE, so several of the bowed thin strips were heated uniformly to 1000°C. It was observed that the bow increased in the same inverted direction upon heating (Ref. 7-18). This indicated that the convex inner side of the thin strips had a higher CTE, resulting in even higher compressive stresses on the convex surface at operating temperatures than the already significant compressive stress which was relieved, as observed, by the inverted bowing of thin strips.

Attempts to reproduce the residual bowing behavior using stress analysis codes proved unsuccessful, although the codes included models for the variation of CTE with irradiation, which necessarily included the effect

of densification due to stress-free irradiation strain. The only obvious difference between these thin strip specimens and typical irradiation specimens was that the thin strips had been subjected to a spatially varying stress field (hence, creep) during their life, and the residual strain consisted, in part, of the spatial variation of creep strain. From these considerations it is conjectured that creep strain, rather than density, was the governing factor that influenced the unexpected behavior of the CTE.

Further evaluation revealed that the creep strain hypothesis is qualitatively consistent with inverted thin strip bowing. The cutting of the thin strips relieved a residual bending stress, so the convex side of the strips was under compression before cutting. The fuel bodies were in contact with the surrounding sleeves, which restrained the overall bowing, again putting the convex side of the body in compression. Assuming that the total creep strain had the same sign as the final stress state, the convex side would have had a compressive creep strain in both cases. As a result, the increase of CTE is correlated with an increase of compressive creep strain. This observation has been reported for a variety of graphites (Refs. 7-19 through 7-22), including H-327. A reduction of thermal expansivity under tensile creep strain has also been observed (Refs. 7-19 through 7-23). These sources indicate that 1% creep strain changes the thermal expansivity by about 15%.

These conjectures do not, by themselves, explain the inverted bowing of the thin strips, but they do indicate that a complete material model of graphite should probably include the observed CTE versus creep strain effect. It is possible that such a model, if employed in a time-dependent creep calculation, might reconcile the calculations with the experiments. Further effort will be required to modify the computer programs and test this theory.

7.2.5. Conclusions

The conclusions from the destructive stress examination are as follows:

1. Ring-cutting tests show in-plane stress to peak at a higher level and a lower fluence than predicted. A reduction in residual stress relative to predictions was observed at higher fluences from the more precise groove change measurements.

2. Pressure burst and diametral compression tests qualitatively verify predicted in-plane stress fields at the location of initial failure and the predicted net increase in graphite strength with irradiation.

3. Four-point bend test results show an increase in Young's modulus and rupture modulus with irradiation. Except for the rupture modulus in thick strips, observed increases are in line with the design data. The small increase in rupture modulus for thick strips is hypothesized as being due to the presence of residual tensile stress at the outer fiber after strip-cutting.

4. Strip elongation results confirm the release of compressive stress along the neutral fiber for both thin and thick strips. As predicted, strip elongation increased with temperature and reached a peak at a fast fluence of 1.7×10^{25} n/m^2 [E > 29 fJ)$_{HTGR}$]. The thin strip results indicate a reduction in residual stress relative to predictions.

5. Differential bow measurements for thin and thick strips were less than half of predicted values, and bow inversions relative to predictions were observed for all types. The fluence levels at which bow inversion began ranged from 1.3×10^{25} n/m^2 [E > 29 fJ)$_{HTGR}$] for thin strips to 3.6×10^{25} n/m^2 for thick strips.

6. Strips cut from graphite body sections suspected of contacting the surrounding graphite sleeve show systematic reductions in residual bow and increased CTE compared with neighboring strips. These observations suggest the presence of additional axial stress fields caused by restrained bow, which would result in greater than usual creep strain.

7. Increases in the CTE under compressive creep and decreases under tensile creep are hypothesized to be partially responsible for discrepancies between measurements and predictions at higher fluence levels. The effect of creep on CTE, which has been observed by several experimenters, was not included in the analytical model for graphite used for predicting residual stresses. Its inclusion could, at least partially, resolve the discrepancies at higher fluence levels noted in conclusions 1, 4, and 5.

8. The effects of compressive creep strain in increasing CTE are consistent with the higher CTE values measured in specimens taken from graphite body sections believed to have been compressed by restrained bow, as noted in conclusion 6.

REFERENCES

7-1. Wallroth, C. F., et al., "Postirradiated Examination of Peach Bottom Fuel Test Element FTE-4," ERDA Report GA-A13452, July 1977.

7-2. Wallroth, C. F., J. F. Holzgraf, and D. P. Jensen, "Post-irradiation Examination and Evaluation of Peach Bottom Fuel Test Element FTE-6," ERDA Report GA-A13943, September 1977.

7-3. Wallroth, C. F., et al., "Postirradiation Examination of Peach Bottom Fuel Test Elements FTE-14 and FTE-15," DOE Report GA-A13944, February 1979.

7-4. Wallroth, C. F., et al., "Postirradiation Examination and Evaluation of Peach Bottom Molded Fuel Test Element FTE-18," Report GA-A13699, June 1, 1976.

7-5. Tzung, F. K., "GTEPC-2D, A Computer Program for Two-Dimensional Graphite Thermal-Elastic-Plastic-Creep Analysis, User's Manual," Report GA-A13532, January 1978.

7-6. Saurwein, J. J., "Peach Bottom Test Element Thermal Analysis with TREVER Code," GA unpublished data, April 19, 1976.

7-7. Peterson, J. F., "TAC 2D-A General Purpose Two-Dimensional Heat Transfer Computer Code," Report GA-8868, September 6, 1969.

7-8. Scheffel, W. J., "Fuel Design Data Manual," GA unpublished data, August 30, 1979.

7-9. Smith, P. D., "Updates to Graphite Material Data Package," GA unpublished data, December 16, 1975.

7-10. Price, R. J., "Review of Irradiation-Induced Creep in Graphite Under HTGR Conditions," Report GA-A12332, November 1, 1972.

7-11. Cords, H., et al., "Temperatur und Spannungsanalyse der Experimente DR-B1/2/3," Kernforschungsanlage, Julich, Institut fur Reaktorwerkstaffe, IRW-TN-46/74, July 29, 1974.

7-12. Miller, C. M., "Tensile Strength Test Data of Graphite Logs for Peach Bottom Test Element Fuel Bodies," GA unpublished data.

7-13. Price, R., and L. Sevier, "A Comparison of Analytical and Experimental Results for Four Point Bend and Diametral Ring Compression Tests of H-327 Graphite," GA unpublished data, August 1978.

7-14. Wallroth, C. F., C. M. Miller, and J. J. Saurwein, "Residual Stress, Strain, and Strength Measurements in Peach Bottom Fuel Test Elements," DOE Report GA-A14704, May 1979.

7-15. Saurwein, J. J., and C. F. Wallroth, "Nuclear and Thermal Design Verification for the Peach Bottom HTGR," DOE Report GA-A14726, September 1979.

7-16. Homeyer, W. G., et al., "Residual Stresses in Peach Bottom Test Elements Analysis versus Experiment," ERDA Report GA-A14329, March 1977.

7-17. Tzung, F. K., and W. G. Homeyer, "Comparison of Residual Stress Predictions and Measurements for Graphite Bodies from Peach Bottom Fuel Test Elements," DOE Report GA-A14663, February 1978.

7-18. "HTGR Fuels and Core Development Program, Quarterly Progress Report for the Period Ending February 28, 1977," ERDA Report GA-A14298, March 1977, p. 9-42.

7-19. Brocklehurst, J. E., and R. G. Brown, "Constant Stress Irradiation Creep Experiments on Graphite in BR-2," Carbon 7, 487 (1969).

7-20. Gray, W. J., "Constant Stress Irradiation-Induced Creep of Graphite at High Fluences," Carbon 11, 383 (1973).

7-21. Kennedy, C. R., et al., "Results of Irradiation Creep Testing Graphite at 900°C," in Extended Abstracts of the 13th Biennial Conference on Carbon, American Carbon Society, 1977, p. 342.

7-22. Kennedy, C. R., et al., "Results of the 600°C Compressive Creep Irradiation Experiment," ORNL Abstract in 14th Biennial Conference on Carbon, June 25-29, 1979, p. 453.

7-23. Jouquet, G., et al., "Continuously Measured Irradiation Creep Strain of Two Reactor Grade Graphites," Kernforschungsanlage, Jülich, unpublished data, 1977.

7-24. "Preirradiation Data Compilation for FTE-18," NUKEM, 80/1527/72, April 7, 1972.

TABLE 7-1
INITIAL THERMAL STRESSES FOR PEACH BOTTOM TEST ELEMENT

Test Element	Initial Thermal Stress[a] (MPa) Peak	Mean[b]	RMS[b]	Fuel Body Sequence (Max.-Min. Stress)
In-Plane				
FTE-1 (element 1)	0.71	0.63	±0.07	123
FTE-2 (element 1)	0.65	0.62	±0.03	23[c]
FTE-3 (element 288)	2.14	1.62	±0.37	213
FTE-4 (element 288)	3.24	2.73	±0.37	231
FTE-5 (element 288)	3.81	2.88	±0.66	231
FTE-6 (element 288)	2.32	1.76	±0.40	231
FTE-14 (element 230)	3.63	2.96	±0.48	213
FTE-15 (element 230)	3.35	2.39	±0.74	231
PTE-2 (element 669)	3.78	--	--	2[d]
FTE-18 (element 1)	4.85	3.69	±1.03	342561
Stress-Strength Ratio				
FTE-1	0.07	0.06	±0.01	123
FTE-2	0.06	0.06	±0.00	23[c]
FTE-3	0.23	0.17	±0.04	213
FTE-4	0.33	0.28	±0.04	231
FTE-5	0.39	0.29	±0.07	231
FTE-6	0.24	0.18	±0.04	231
FTE-14	0.39	0.32	±0.05	213
FTE-15	0.36	0.25	±0.08	231
PTE-2	0.41	--	--	2
FTE-18	1.07	0.79	±0.22	342561
Axial				
FTE-1 (element 270)[e]	0.28	0.22	±0.04	123
FTE-2 (element 297)	0.34	0.31	±0.03	23[c]
FTE-3 (element 297)[f]	1.46	1.07	±0.28	231
FTE-4 (element 297)	2.30	1.92	±0.28	231
FTE-5 (element 297)	2.86	2.11	±0.54	231
FTE-6 (element 297)	1.59	1.17	±0.31	231
FTE-14 (element 446)[g]	3.23	2.29	±0.76	231
FTE-15 (element 446)[g]	3.00	2.06	±0.76	231
PTE-2 (element 758)	2.95	--	--	2
FTE-18 (element 1)	3.00	2.29	±0.63	342651

TABLE 7-1 (Continued)

Test Element	Initial Thermal Stress[a] (MPa) Peak	Mean[b]	RMS[b]	Fuel Body Sequence (Max.-Min. Stress)
	Stress-Strength Ratio			
FTE-1	0.01	0.01	±0.00	123
FTE-2	0.02	0.01	±0.00	23[c]
FTE-3	0.08	0.06	±0.02	231
FTE-4	0.13	0.11	±0.02	231
FTE-5	0.16	0.12	±0.03	231
FTE-6	0.16	0.12	±0.03	231
FTE-14	0.18	0.13	±0.04	231
FTE-15	0.17	0.11	±0.04	231
PTE-2	0.17	--	--	2
FTE-18	0.85	0.52	±0.14	342561

[a]The exposure sequence was noticeably different from the numerical order:

FTE	3	2	14	1	PTE-2	4	15,18	6	5
EFPD	133	252	316	385	404	449	512	645	897

[b]The mean and RMS are used to describe the variation of calculated peak stresses between the three fuel body positions and are not a representative statement for mean body stresses or of uncertainties in calculations.

[c]No stress analysis was done for body 1 of FTE-2, which was not available at the time (Ref. 7-15).

[d]Stress analysis was done for body 2 only of PTE-2, demonstrated by stress analyses of other fuel test elements as the position of maximum stress.

[e]Element 297 for body 1.

[f]Element 1 for body 2.

[g]Element 349 for body 1.

TABLE 7-2A
ULTIMATE TENSILE STRENGTH OF H-327 GRAPHITE AT ROOM TEMPERATURE

Block Position, Orientation	Ultimate Strength[a]			
	Mean		Standard Deviation	
	psi	MPa	psi	MPa
Ultimate Tensile Strength				
End center, axial	2180	15.031	435	3.000
End edge, axial[b]	2395	16.514	480	3.310
Midlength center, axial	1530	11.239	325	2.240
Midlength edge, axial[c]	2395	16.514	480	3.310
End center, radial	1350	9.308	270	1.862
End edge, radial[b]	1350	9.308	270	1.862
Midlength center, radial	940	6.481	190	1.310
Midlength edge, radial[c]	1290	8.895	260	1.793
Ultimate Compressive Strength[c]	$\geq$4000	>27,580		

[a] Ref. 7-9.

[b] End edge values were obtained by taking the midlength edge value for axial and the end center value for radial orientations. The standard deviation was calculated from 20% of the mean UTS value based upon characterization and quality assurance results.

[c] Used for unirradiated strength at room temperature in computing stress-to-strength ratios.

TABLE 7-2B
ELASTIC MODULUS OF H-327 GRAPHITE AT ROOM TEMPERATURE

Pointwise Block Position, Orientation	Elastic Modulus			
	Mean		Standard Deviation	
	10^6 psi	10^3 MPa	10^6 psi	10^3 MPa
End center, axial	1.42	9.79	0.3	2.07
End edge, axial[a]	2.02	13.93	0.6	4.14
Midlength center, axial	1.42	5.79	0.4	2.76
Midlength edge, axial[b]	2.02	13.93	0.6	4.14
End center, radial	0.754	5.20	0.3	2.07
End edge, radial[a]	0.669	4.61	0.3	2.07
Midlength center, radial	0.571	3.94	0.2	1.38
Midlength edge, radial[b]	0.774	5.34	0.3	2.07

[a] End edge values obtained by taking the midlength edge value for axial and the end center value for radial orientations.

[b] Used in stress calculations.

TABLE 7-3
PERCENTAGE CHANGE IN ELASTIC MODULUS OF H-327
GRAPHITE DURING NEUTRON IRRADIATION

Fast Neutron Fluence, ϕ (10^{25} n/m^2) (E > 29 fJ)$_{HTGR}$	Change in Elastic Modulus at Irradiation Temperature (%)			
	673 K	873 K	1173 K	1473 K
0	0	0	0	0
0.25	84.0	64.0	58.0	54.0
0.50	94.0	75.0	66.0	58.0
0.75	97.3	82.3	72.0	59.0
1.00	100.0	89.0	76.0	59.0
1.25	101.4	93.0	77.5	59.0
1.50	102.7	95.7	78.4	59.0
1.75	103.0	97.5	78.4	59.0
2.00	103.5	98.8	78.6	59.3
2.25	104.0	99.6	78.7	59.9
2.50	104.4	100.3	78.8	60.2
2.75	104.8	100.9	78.9	60.5
3.00	105.0	101.5	79.0	60.8
3.25	105.5	102.2	79.1	61.2
3.50	106.1	102.9	79.3	61.8
3.75	106.6	103.6	79.5	62.4
4.00	107.2	104.3	79.7	63.1
4.25	108.0	105.0	80.0	63.8
4.50	108.7	105.6	80.0	63.8
4.75	109.4	106.0	80.5	65.2
5.00	110.3	106.5	80.8	66.0
5.25	111.2	107.3	81.1	66.8
5.50	112.2	108.0	81.4	67.6
5.75	113.3	108.7	81.7	68.4
6.00	114.3	109.4	82.0	69.2
6.25	115.4	110.1	82.3	69.9
6.50	116.6	111.0	82.6	70.5
6.75	117.8	111.9	82.9	71.1
7.00	119.6	112.8	83.2	71.8
7.25	121.1	113.7	83.5	72.4
7.50	122.6	114.6	83.8	73.0
7.75	124.2	115.5	84.1	73.6
8.00	126.0	116.4	84.4	74.2

TABLE 7-4
TENSILE STRENGTHS FOR
PEACH BOTTOM TEST ELEMENT FUEL BODIES

Fuel Body	Sample I.D.	Tensile Strength	
		psi	MPa
FTE-1-1	721-10	2270	15.7
-2	954/0050-11	2190	15.1
-3	909/004-18	1940	13.4
FTE-2-1	909/0041-12	1940	13.4
-2	1947/0050-7	1740	12.0
-3	909/0041-16	1940	13.4
FTE-3-1	2513-32-3	2150	14.8
-2	721-42-10	2270	15.7
-3	738-39-2	1830	12.6
FTE-4-1	2181-31-3	1880	13.0
-2	738-33-10	1830	12.6
-3	738-30-2	1830	12.6
FTE-5-1	2124-35	1985	13.7
-2	2182-34	1880	13.0
-3	738-26	1830	12.6
FTE-6-1	2513-44-3	2150	14.8
-2	738-43-10	1830	12.6
-3	738-37-2	1830	12.6
FTE-14-1	4959-127	2040	14.1
-2	4959-129	2040	14.1
-3	1146-125	2590	17.9
FTE-15-1	2172-128	2015	13.9
-2	4959-130	2040	14.1
-3	4959-126	2040	14.1
FTE-16-1	2172-123	2015	13.9
-2	1146-122	2520	17.4
-3	2172-116	2015	13.9
FTE-18-1	None	641	4.4
-2	None	641	4.4
-3	None	512	3.5
-4	None	512	3.5
-5	None	764	5.3
-6	None	641	4.4
PTE-2-2	None	None	None
-3	None	None	None
FTE-18-1	None	641	4.4
-2	None	641	4.4
-3	None	512	3.5
-4	None	512	3.5
-5	None	764	5.3
-6	None	641	4.4

TABLE 7-5
FTE-18 ULTIMATE TENSILE AND COMPRESSIVE STRENGTH OF UNIRRADIATED MOLDED FUEL BODIES AT ROOM TEMPERATURE

Fuel Body	Ultimate Tensile Strength		Ultimate Compressive Strength		Ultimate Bending Strength	
	$UTS_{\perp}$ (psi)	$UTS_{\parallel}$ (psi)	$UCS_{\perp}$ (psi)	$UCS_{\parallel}$ (psi)	$UBS_{\perp}$ (psi)	$UBS_{\parallel}$ (psi)
1 Bottom	593	641	-4051	-4210	1693	1337
2	593	641	-4051	-4210	1693	1337
3	660	512	-4324	-4381	1678	1536
4	660	512	-4324	-4381	1678	1536
5	831	764	-4822	-4864	1778	1451
6 Top	593	641	-4051	-4210	1693	1337
Mean[a]	675	639	-4401	-4485	1719	1441
SD[a]	±116	±176	±458	±399	±178	±255

[a]Based on data in Ref. 7-24.

Note: $\perp$ perpendicular to pressing, radial to block
$\parallel$ parallel to pressing, axial to block.

TABLE 7-6
PEAK OPERATIONAL STRESSES DURING LIFE FOR
PEACH BOTTOM TEST ELEMENTS

Test Element	Operational Stress (MPa)			Fuel Body Sequence
	Peak	Mean[a]	±RMS[a]	
Tensile Stress				
In-Plane				
FTE-1 (element 359)	5.71	4.09	±1.25	321
FTE-2 (element 359)	4.78	4.62	±0.16	23
FTE-3 (element 288)[b]	1.14	0.83	±0.42	123
FTE-4 (element 359)	5.18	4.16	±0.80	231
FTE-5 (element 288)	6.37	5.13	±1.51	231
FTE-6 (element 288)	7.64	6.11	±1.11	231
FTE-14 (element 230)	3.63	2.96	±0.48	213
FTE-15 (element 230)	3.35	2.39	±0.74	231
PTE-2 (element 598)	0.66	--	--	2[c]
FTE-18 (element 33)	10.27	--	--	4[c]
Stress-Strength Ratio				
FTE-1	0.52	0.36	±0.12	321
FTE-2	0.41	0.39	±0.01	23
FTE-3	0.10	0.07	±0.04	123
FTE-4	0.43	0.34	±0.07	231
FTE-5	0.53	0.43	±0.13	231
FTE-6	0.64	0.50	±0.10	231
FTE-14	0.39	0.32	±0.05	213
FTE-15	0.36	0.25	±0.08	231
PTE-2	0.06	--	--	2[c]
FTE-18	2.26	--	--	4[c]
Axial				
FTE-1 (element 20)	4.97	4.73	±0.17	231[d]
FTE-2 (element 20)	6.23	6.01	±0.22	23
FTE-3 (element 20)[e]	2.55	1.56	±0.81	213
FTE-4 (element 20)	7.10	5.89	±0.86	231
FTE-5 (element 297)	9.36	7.03	±2.02	231
FTE-6 (element 297)	9.28	7.26	±1.44	231
FTE-14 (element 446)[f]	3.23	2.49	±0.54	231
FTE-15 (element 12)[f]	3.45	2.78	±0.75	231
PTE-2 (element 72)	1.91	--	--	2[c]
FTE-18 (element 8)	2.98	2.12	±0.70	143526

TABLE 7-6 (Continued)

Test Element	Operational Stress (MPa)			Fuel Body Sequence
	Peak	Mean	±RMS	
	Stress-Strength Ratio			
FTE-1	0.20	0.19	±0.01	321[d]
FTE-2	0.24	0.23	±0.01	23
FTE-3	0.10	0.06	±0.03	213
FTE-4	0.28	0.23	±0.03	231
FTE-5	0.37	0.28	±0.08	231
FTE-6	0.37	0.28	±0.06	231
FTE-14	0.18	0.13	±0.04	231
FTE-15	0.14	0.11	±0.03	231
PTE-2	0.07	--	--	2[c]
FTE-18	0.67	0.48	±0.16	143526

[a] The mean and RMS are used to describe the variation of calculated peak stresses between the three fuel body positions and are not a representative statement for mean body stresses or of uncertainties in calculations.

[b] Element 359, body 2.

[c] The stress analysis of PTE-2 and principal in-plane stresses in FTE-18 were determined only for the fuel body with the highest stress field, bodies 2 and 4, respectively.

[d] Body 3 of FTE-1 has a lower stress (4.66 MPa) but also a lower increase in elastic modulus because of lower fluence exposure, which results in a higher stress-strength ratio (0.196) than for body 2 (0.194).

[e] Element 297, body 1, and element 1, body 3.

[f] Element 349, body 1.

TABLE 7-7
PEAK SHUTDOWN STRESSES DURING LIFE FOR
PEACH BOTTOM TEST ELEMENTS

Test Element	Shutdown Stress (MPa)			Fuel Body Sequence
	Peak	Mean[a]	±RMS[a]	
Tensile Stress				
In-Plane				
FTE-1 (element 359)	18.27	17.48	±1.10	213
FTE-2 (element 359)	19.42	18.79	±0.64	23
FTE-3 (element 359)	11.91	8.85	±2.46	213
FTE-4 (element 359)	15.82	14.37	±1.41	123
FTE-5 (element 359)	14.70	13.20	±1.75	123
FTE-6 (element 359)	16.44	15.57	±1.17	213
FTE-14 (element 216)	5.82	4.50	±0.94	231
FTE-15 (element 216)	5.78	4.59	±0.85	213
PTE-2 (element 562)	5.88	--	--	2[b]
FTE-18 (element 33)	19.50	--	--	4[b]
Stress-Strength Ratio				
FTE-1	1.69	1.60	±0.12	213
FTE-2	1.77	1.71	±0.06	23
FTE-3	1.11	0.81	±0.25	213
FTE-4	1.42	1.27	±0.18	123
FTE-5	1.32	1.21	±0.16	123
FTE-6	1.53	1.43	±0.10	213
FTE-14	0.54	0.41	±0.09	231
FTE-15	0.54	0.42	±0.08	213
PTE-2	0.52	--	--	2[b]
FTE-18	4.28	--	--	4[b]
Axial				
FTE-1 (element 20)[c]	17.85	16.72	±1.51	123
FTE-2 (element 20)	19.22	18.59	±0.63	23
FTE-3 (element 10)[d]	11.44	7.78	±2.65	213[e]
FTE-4 (element 20)	15.69	14.46	±1.34	213
FTE-5 (element 20)	14.61	12.92	±1.35	213
FTE-6 (element 20	16.38	15.36	±0.82	213
FTE-14 (element 12)	10.55	8.40	±1.55	231
FTE-15 (element 12)	10.84	8.72	±1.50	213[e]
PTE-2 (element 72)	8.51	--	--	2[b]
FTE-18 (element 329)	11.93	8.94	±2.52	435261

TABLE 7-7 (Continued)

Test Element	Shutdown Stress (MPa)			Fuel Body Sequence
	Peak	Mean	±RMS	
	Stress-Strength Ratio			
FTE-1	0.78	0.72	±0.08	123
FTE-2	0.82	0.80	±0.03	23
FTE-3	0.51	0.34	±0.12	213
FTE-4	0.69	0.61	±0.08	213
FTE-5	0.65	0.56	±0.07	213
FTE-6	0.73	0.67	±0.04	213
FTE-14	0.47	0.36	±0.08	231
FTE-15	0.48	0.38	±0.07	213[e]
PTE-2	0.35	--	--	2[b]
FTE-18	3.38	2.03	±0.57	435261

[a] The mean and RMS are used to describe the variation of calculated peak stresses between the three fuel body positions and are not a representative statement for mean body stresses or of uncertainties in calculations.

[b] The stress analysis of PTE-2 and principal in-plane stresses in FTE-18 were determined only for the fuel body with the highest stress field, bodies 2 and 4, respectively.

[c] Element 10, body 3.

[d] Element 20, body 2.

[e] Body 3 of FTE-15 has a lower stress (7.53 MPa) but also a lower increase in elastic modulus because of lower fluence exposure, which results in a higher stress-strength ratio (0.33) than for body 1 (0.32).

TABLE 7-8
PEAK OPERATIONAL STRESS AT EOL FOR
PEACH BOTTOM TEST ELEMENTS

Test Element	Operational Stress (MPa)			Fuel Body Sequence
	Peak	Mean[a]	±RMS[a]	
Tensile Stress				
In-Plane				
FTE-1 (element 359)	3.90	2.23	±1.57	213
FTE-2 (element 359)	4.78	4.62	±0.16	23
FTE-3 (element 288)[b]	1.14	0.83	±0.42	123
FTE-4 (element 359)	5.18	4.16	±0.80	231
FTE-5 (element 359)	4.33	3.40	±1.21	321
FTE-6 (element 359)	5.42	4.37	±0.81	231
FTE-14 (element 216)[c]	1.04	0.68	±0.39	231
FTE-15 (element 216)	1.74	1.14	±0.57	231
PTE-2 (element 12)	0.51	--	--	2[d]
FTE-18 (element 33)	8.27	5.14	±2.14	435216
Stress-Strength Ratio				
FTE-1	0.34	0.19	±0.14	213
FTE-2	0.41	0.39	±0.01	23
FTE-3	0.10	0.07	±0.04	123
FTE-4	0.43	0.34	±0.07	231
FTE-5	0.36	0.28	±0.10	321
FTE-6	0.45	0.36	±0.07	231
FTE-14	0.09	0.06	±0.03	231
FTE-15	0.15	0.10	±0.05	231
PTE-2	0.04	--	--	2[d]
FTE-18	1.82	1.11	±0.46	435216
Axial				
FTE-1 (element 20)	4.97	3.61	±1.65	213
FTE-2 (element 20)	6.23	6.01	±0.22	23
FTE-3 (element 20)[e]	2.55	1.56	±0.81	213
FTE-4 (element 20)	7.10	5.89	±0.86	231
FTE-5 (element 20)	8.08	5.98	±1.97	231
FTE-6 (element 20)	7.69	6.20	±1.05	213
FTE-14 (element 12)	1.54	1.23	±0.38	231
FTE-15 (element 12)	3.41	2.51	±1.06	231
PTE-2 (element 72)	1.91	--	-	2[d]
FTE-18 (element 33)	2.79	1.85	±0.67	142531

TABLE 7-8 (Continued)

Test Element	Operational Stress (MPa)			Fuel Body Sequence
	Peak	Mean	±RMS	
	Stress-Strength Ratio			
FTE-1	0.19	0.14	±0.07	213
FTE-2	0.24	0.23	±0.01	23
FTE-3	0.10	0.06	±0.03	213
FTE-4	0.28	0.23	±0.03	231
FTE-5	0.33	0.24	±0.08	231
FTE-6	0.30	0.24	±0.04	213
FTE-14	0.06	0.04	±0.02	231
FTE-15	0.14	0.10	±0.04	231
PTE-2	0.07	--	--	2[d]
FTE-18	0.63	0.42	±0.15	142531

[a] The mean and RMS are used to describe the variation of calculated peak stresses between the three fuel body positions and are not a representative statement for mean body stresses or of uncertainties in calculations.

[b] Element 359, body 1.

[c] Element 445, body 1.

[d] Stress analysis was done for body 2 only of PTE-2, demonstrated by stress analyses of other fuel test elements as the position of maximum stress.

[e] Element 297, body 1, and element 1, body 3.

TABLE 7-9
PEAK SHUTDOWN STRESS AT EOL FOR
PEACH BOTTOM TEST ELEMENTS

Test Element	EOL Shutdown Stress (MPa)			
	Peak	Mean[a]	±RMS[a]	Fuel Body Sequence
Tensile Stress				
In-Plane				
FTE-1 (element 359)	18.27	17.48	±1.10	213
FTE-2 (element 359)	19.42	18.78	±0.64	23
FTE-3 (element 359)	11.91	8.85	±2.46	213
FTE-4 (element 359)	15.82	14.37	±1.41	123
FTE-5 (element 359)	8.77	7.53	±1.07	132
FTE-6 (element 359)	14.33	12.18	±1.52	132
FTE-14 (element 216)	5.82	4.50	±0.94	231
FTE-15 (element 216)	4.68	3.87	±0.60	231
PTE-2 (element 562)	5.88	--	--	2[b]
FTE-18 (element 33)	15.69	9.73	±4.99	435612
Stress-Strength Ratio				
FTE-1	1.69	1.60	±0.12	213
FTE-2	1.77	1.71	±0.06	23
FTE-3	1.11	0.81	±0.25	213
FTE-4	1.42	1.27	±0.18	123
FTE-5	0.78	0.68	±0.09	132
FTE-6	1.28	1.11	±0.12	132
FTE-14	0.54	0.41	±0.09	231
FTE-15	0.44	0.35	±0.06	231
PTE-2	0.52	--	--	2[b]
FTE-18	3.45	2.09	±1.07	435612
Axial				
FTE-1 (element 20)[c]	17.85	16.72	±1.51	123
FTE-2 (element 20)	19.22	18.59	±0.63	23
FTE-3 (element 10)[d]	11.44	7.78	±2.65	213
FTE-4 (element 20)	15.69	14.46	±1.34	213
FTE-5 (element 20)	10.10	9.38	±0.72	231
FTE-6 (element 20)	13.98	13.05	±0.86	123[e]
FTE-14 (element 12)	10.55	8.40	±1.55	231
FTE-15 (element 12)	8.62	7.15	±1.29	231
PTE-2 (element 72)	8.51	--	--	2[b]
FTE-18 (element 296)	10.07	7.45	±2.17	453261

TABLE 7-9 (Continued)

Test Element	EOL Shutdown Stress (MPa)			Fuel Body Sequence
	Peak	Mean	±RMS	
	Stress-Strength Ratio			
FTE-1	0.78	0.72	±0.08	123
FTE-2	0.82	0.80	±0.03	23
FTE-3	0.51	0.34	±0.12	213
FTE-4	0.69	0.61	±0.08	213
FTE-5	0.44	0.40	±0.04	231
FTE-6	0.58[e]	0.56	±0.03	213[e]
FTE-14	0.47	0.36	±0.08	231
FTE-15	0.38	0.31	±0.07	231
FTE-2	0.35	--	--	2[b]
FTE-18	2.85	1.69	±0.49	453261

[a] The mean and RMS are used to describe the variation of calculated peak stresses between the three fuel body positions and are not a representative statement for mean body stresses or of uncertainties in calculations.

[b] Stress analysis was done for body 2 only of PTE-2, demonstrated by stress analyses of other fuel test elements as the position of maximum stress.

[c] Element 10, body 3.

[d] Element 20, body 2.

[e] Body 2 of FTE-6 has a lower stress (13.26 MPa), but also a lower increase in elastic modulus because of higher irradiation temperature, which results in a higher stress-strength ratio (0.581) than for body 1 (0.578).

TABLE 7-10
RING-CUT, PRESSURE-BURST, AND DIAMETRAL-COMPRESSION TESTS
OF 20-mm-THICK FUEL BODY SLICES FROM PEACH BOTTOM TEST ELEMENTS

H-327 Test Specimens			Irradiation Conditions		Pressure Burst Test					Diametral Compression Test					In-Plane Strain Measurements							
																		Groove Change			Outer Diam. Change		
							Pressure ± 0.04 MPa (1σ)						Force ± 0.02 kN(1σ)					±0.01 mm (1σ)		Predicted	±0.002 mm (1σ)		Predicted
Element Type	Body I.D.	Graphite I.D. (psi)	Body Fast Fluence (10^{25} n/m^2)	Average Mean Temp. (°C)	Sample Fast Fluence (10^{25} n/m^2)	Time Avg. Temp. at Failure Loc. (°C)	No. of Samples	Mean (MPa)	±RMS (MPa)	Sample Fast Fluence (10^{25} n/m^2)	Time Avg. Temp. at Failure Loc. (°C)	No. of Samples	Mean (kN)	±RMS (kN)	Sample Fast Fluence (10^{25} n/m^2)	Time Avg. Temp. At Failure Loc. (°C)	No. of Samples	Mean (mm)	±RMS (mm)	Mean (mm)	Mean (mm)	±RMS (mm)	Mean (mm)
Unirradiated Control Tests																							
6-Hole	1	1390					69	3.41	0.39			9	1.35	0.16			3	-0.004	0.003		-0.007	0.006	
	2	1390	N/A	N/A	N/A	N/A	65	3.00	0.42	N/A	N/A	9	1.34	0.11			3	+0.025	0.004		-0.003	0.001	
	3	1390					138	3.33	0.38			21	1.32	0.13	N/A	N/A	7	-0.004	0.011	N/A	-0.002	0.003	N/A
	4	1390					163	3.22	0.48			22	1.45	0.12			7	-0.009	0.006		-0.003	0.004	
	Mean						435	3.25	0.44			61	1.38	0.14			20	-0.001	0.014		-0.004	0.004	
8-Hole	6	1390					98	3.57	0.33			7	0.50	0.02			3	-0.025	0.026		-0.001	0.001	
	7	1390	N/A	N/A	N/A	N/A	102	3.09	0.38	N/A	N/A	7	0.46	0.01			3	+0.029	0.013		-0.003	0.005	
	8	1390					223	3.15	0.46			17	0.49	0.04	N/A	N/A	7	+0.011	0.014	N/A	-0.003	0.002	N/A
	Mean						423	3.23	0.45			31	0.49	0.03			13	+0.007	0.026		-0.003	0.003	
8-Hole	RTE-3-2	2270	N/A	N/A	N/A	N/A	54	2.45	0.34	N/A	N/A	0	N/A	N/A	N/A	N/A	0	N/A	N/A	N/A	N/A	N/A	N/A
	RTE-ORNL	<1000					73	3.32	0.39			10	0.50	0.01			0						
8-Hole Teledial Irradiated Test																							
	1	1940	1.32	689	1.50	861	88	2.37	0.46	1.54	873	5	0.44	0.05	1.51	790	5	-0.150	0.082	-0.201	-0.036	0.017	-0.054
FTE-2	2	1740	1.69	903	1.77	946	22	2.30	0.25	1.77	946	2	0.52	0.10	1.77	856	2	-0.265	0.011	--	-0.069	0.010	--
	Mean						110	2.37	0.45			7	0.46	0.08			7	-0.207	0.073		-0.052	0.013	
FTE-3	1	2150	0.41	671	0.52	868	83	2.97	0.35	0.37	742	9	0.42	0.03	0.51	775	6	-0.305	0.068	-0.133	-0.053	0.018	-0.035
	2	2270	0.54	851	0.56	968	23	1.11	0.25	0.56	970	1	0.44	0	0.56	873	2	-0.262	0.013		-0.048	0.005	--
	3	1830	0.34	835	0.40	946	67	2.08	0.30	0.41	933	7	0.37	0.04	0.39	877	5	-0.240	0.030	-0.095	-0.044	0.010	-0.025
	Mean						173	2.64	0.55			17	0.40	0.04			13	-0.273	0.059		-0.049	0.014	
FTE-4	1	1880	1.40	707	1.40	850	142	2.71	0.45	1.45	865	9	0.47	0.04	1.40	758	9	-0.207	0.065	-0.182	-0.056	0.040	-0.049
	2	1830	1.94	924	1.88	1051	30	2.27	0.22	1.82	1024	6	0.44	0.08	1.88	913	2	-0.309	0.024	-0.239	-0.062	0.001	-0.063
	3	1830	1.26	923	1.26	1026	142	2.31	0.40	1.27	1020	11	0.41	0.04	1.26	944	10	-0.213	0.058	-0.181	-0.038	0.014	-0.048
	Mean						314	2.49	0.46			25	0.44	0.06			21	-0.219	0.066		-0.048	0.030	
FTE-5	2	1880	3.71	925	3.70	1057	55	3.46	0.58	3.67	1071	3	0.52	0.06	3.70	941	4	-0.110	0.057	-0.143	-0.043	0.009	-0.038
	3	1830	2.54	915	2.88	1053	56	3.80	0.42	2.67	1040	3	0.56	0.02	2.84	963	4	-0.071	0.071	-0.133	-0.023	0.007	-0.035
	Mean						111	3.63	0.53			6	0.54	0.05			8	-0.090	0.068		-0.033	0.013	
FTE-6	1	2150	1.93	743	1.46	769	68	2.85	0.56	1.75	835	3	0.51	0.06	1.32	660	6	-0.056	0.060	-0.178	-0.016	0.008	-0.047
	2	1830	2.77	979	2.74	1106	53	2.91	0.59	2.72	1094	2	0.50	0.07	2.75	976	5	-0.134	0.051	-0.233	-0.039	0.007	-0.061
	3	1830	1.97	960	2.12	1084	69	2.58	0.40	1.84	1048	3	0.43	0.07	2.21	992	6	-0.133	0.103	-0.177	-0.037	0.033	-0.049
	Mean						190	2.77	0.54			8	0.48	0.07			17	-0.106	0.085		-0.030	0.023	
6-Hole Teledial Irradiated Test																							
FTE-14	1	2040	1.05	725	1.05	752	98	3.91	0.62	1.06	750	9	1.75	0.12	1.07	813	9	-0.150	0.050	-0.152	-0.028	0.014	-0.033
	2	2040	1.42	1048	1.42	985	27	4.36	0.49	1.40	964	3	2.22	0.54	1.42	1051	3	-0.207	0.018	-0.268	-0.038	0.011	-0.057
	3	2590	0.97	1081	0.95	1078	109	3.71	0.63	0.96	1050	11	1.80	0.33	0.96	1122	11	-0.148	0.034	-0.180	-0.029	0.010	-0.038
	Mean						234	3.87	0.64			23	1.84	0.34			23	-0.157	0.044		-0.030	0.012	
FTE-15	1	2015	1.47	707	0.73	565	23	4.64	0.31	0.68	557	3	1.79	0.16	0.87	630	3	-0.072	0.036	-0.127	-0.009	0.005	-0.027
	2	2040	2.00	1031	2.00	975	27	5.07	0.64	1.97	951	4	2.05	0.07	2.00	1049	3	-0.109	0.013	-0.213	-0.036	0	-0.045
	3	2040	1.55	1045	1.43	987	34	3.76	0.86	1.86	1014	3	1.71	0.22	1.53	1068	4	-0.099	0.017	-0.172	-0.005	0.011	-0.037
	Mean						84	4.43	0.88			10	1.87	0.23			9	-0.092	0.028		-0.013	0.014	
Outer Ring Test																							
Unirrad.	6,7,8	1830										9	0.17	0.01									
FTE-3	3											1	0.19	0									
FTE-4	1,2,3	1880/1830										3	0.25	<0.01									

(a) All data are final.

TABLE 7-11
FOUR-POINT BEND TEST RESULTS FOR STRIPS CUT FROM PEACH BOTTOM TEST ELEMENTS

FTE Body I.D.	Single Tensile Test (MPa)	Moment of Inertia (mm^4)	Irradiation Conditions: Fast Fluence (10^{25}n/m)	Irradiation Conditions: Time Wt. Strip Avg. Irr. Temp. (°C)	No. of Samples	Modulus of Rupture: Mean (MPa)	Modulus of Rupture: ±RMS (MPa)	Modulus of Rupture: Irr./Unirr. Predicted	Modulus of Rupture: Irr./Unirr. Measured	Young's Modulus: Mean (10^3 MPa)	Young's Modulus: ±RMS (10^3 MPA)	Young's Modulus: Irr./Unirr. Predicted	Young's Modulus: Irr./Unirr. Measured
					Unirradiated Control Tests								
6-Hole													
1-Thin	9.58	14.2	NA	NA	14	22.62	2.36	NA	NA	5.97	0.67	NA	NA
1-Thick	9.58	9.80×10^3	NA	NA	11	14.75	1.54	NA	NA	4.82	0.51	NA	NA
8-Hole													
8-Thin	9.58	121	NA	NA	20	21.31	1.94	NA	NA	5.09	0.44	NA	NA
8-Thick	9.58	2.36×10^3	NA	NA	16	21.01	2.10	NA	NA	7.03	0.78	NA	NA
					Irradiated Tests								
Thin 8-Hole													
2-2	12.00	121	1.72	909	19	30.64	2.93	1.48	1.44	10.19	3.36	1.78	2.00
3-2	15.65	121	0.52	858	19	28.75	2.18	1.42	1.35	8.57	0.70	1.68	1.68
4-2	12.62	121	1.87	929	20	30.73	3.51	1.46	1.44	10.09	1.16	1.77	1.98
16-2T	17.86	121	2.23	993	14	27.25	2.64	1.45	1.28	7.75	0.81	1.74	1.52
16-3T	13.89	121	1.26	849	16	27.80	3.41	1.48	1.31	9.28	0.67	1.80	1.82
Mean										9.26		1.78	1.82
Thick 8-Hole													
2-2	12.00	2.36×10^3	1.72	959	8	18.39	3.23	1.44	0.88	10.69	2.60	1.72	1.52
3-2	15.65	2.36×10^3	0.52	917	8	20.60	1.64	1.41	0.98	9.75	0.96	1.66	1.39
4-2	12.62	2.36×10^3	1.87	1000	8	23.44	3.28	1.44	1.12	11.57	2.76	1.72	1.65
5-2	12.96	2.36×10^3	3.71	1027	8	18.38	3.47	1.45	0.88	11.29	2.82	1.75	1.61
5-3	12.62	2.36×10^3	2.39	966	8	24.94	3.11	1.46	1.19	13.36	1.93	1.76	1.90
6-1	14.82	2.36×10^3	2.28	866	8	25.02	2.91	1.50	1.19	13.02	0.79	1.82	1.85
6-2	12.62	2.36×10^3	2.79	1055	8	22.45	1.91	1.43	1.07	11.84	0.92	1.71	1.68
6-3	12.62	2.36×10^3	1.77	985	8	23.75	1.19	1.44	1.13	10.86	0.87	1.73	1.55
16-2	17.86	7.07×10^3	2.23	1010	16	22.29	2.51	1.44	(a)	9.42	0.84	1.71	(a)
16-3	13.89	7.07×10^3	1.60	915	16	19.70	4.25	1.47	(a)	9.20	1.09	1.77	(a)
Mean													
Thick 6-Hole													
14-2	14.07	1.67×10^4	1.42	1148	6	28.80	2.22	1.42	(a)	7.28	0.52	1.68	(a)
15-1	13.89	1.67×10^4	1.61	820	6	24.99	3.27	1.49	(a)	8.38	0.57	1.81	(a)
15-2	14.07	1.67×10^4	2.03	1132	6	29.61	2.49	1.40	(a)	8.70	0.48	1.65	(a)
15-3	14.07	1.67×10^4	1.36	1099	6	24.12	2.02	1.41	(a)	7.63	0.25	1.68	(a)
Mean													

(a) Different cross-section configuration than unirradiated control strips.

TABLE 7-12
ELONGATION AND BOW RESULTS FOR STRIPS CUT FROM PEACH BOTTOM TEST ELEMENTS

		Thin Strip												Thick Strip									
		Irradiation Conditions				Elongation[a]				Bow				Irradiation Conditions				Elongation[a]				Bow			
		Time Wt. Temp.		EOL Temp.			Measured		Predicted		Measured		Predicted	Time Wt. Temp.		EOL Temp.			Measured		Predicted		Measured		Predicted
FTE-Body	Strip Fast Fluence (10^{25} n/m^2)	Mean (°C)	ΔT (°C)	Mean (°C)	ΔT (°C)	No. of Samples	Mean (mm)	±RMS (mm)	Mean (mm)	No. of Samples	Mean (mm)	±RMS (mm)	Mean (mm)	Mean (°C)	ΔT (°C)	Mean (°C)	ΔT (°C)	No. of Samples	Mean (mm)	±RMS (mm)	Mean (mm)	No. of Samples	Mean (mm)	±RMS (mm)	Mean (mm)
Unirradiated Control Tests																							
6-Hole																							
1	NA	NA	NA	NA	NA	5	+0.04	0.06	NA	6	-0.55	1.03	NA	NA	NA	NA	NA	6	+0.09	0.08	NA	NA	NA	NA	NA
8-Hole																							
6	NA	NA	NA	NA	NA	7	+0.08	0.10	NA	8	+0.12	0.21	NA	NA	NA	NA	NA	8	+0.11	0.06	NA	7	+0.06	0.07	NA
Irradiated Tests																							
8-Hole																							
2-1	NA	NA	NA	NA	NA	NA	NA	NA	NA	NA	NA	NA	NA	NA	NA	NA	NA	NA	NA	NA	NA	NA	NA	NA	NA
2-2	1.72	909	28	950	35	8	+0.06	0.05	+0.17	7	+0.89	0.20	+3.01	959	129	1003	141	7	+0.06	0.08	+0.04	8	+0.99	0.13	+4.01
3-1	NA	NA	NA	NA	NA	NA	NA	NA	NA	NA	NA	NA	NA	NA	NA	NA	NA	NA	NA	NA	NA	NA	NA	NA	NA
3-2	0.52	858	24	923	36	8	+0.06	0.03	+0.11	8	+0.58	0.23	+1.96	917	141	994	177	8	+0.04	0.07	+0.03	8	+0.83	0.07	+2.63
3-3	NA	NA	NA	NA	NA	NA	NA	NA	NA	NA	NA	NA	NA	NA	NA	NA	NA	NA	NA	NA	NA	NA	NA	NA	NA
4-1	NA	NA	NA	NA	NA	NA	NA	NA	NA	NA	NA	NA	NA	NA	NA	NA	NA	NA	NA	NA	NA	NA	NA	NA	NA
4-2	1.87	929	35	956	44	8	+0.06	0.04	+0.16	8	-0.16	0.70	+2.49	1000	179	1035	202	7	-0.03	0.02	+0.04	8	+0.66	0.28	+2.90
4-3	NA	NA	NA	NA	NA	NA	NA	NA	NA	NA	NA	NA	NA	NA	NA	NA	NA	NA	NA	NA	NA	NA	NA	NA	NA
5-2	3.71	947	36	701	25	5	+0.06	0.04	+0.11	6	-3.17	1.20	+1.79	1027	195	753	130	8	-0.02	0.07	+0.03	8	-0.67	0.48	+2.16
5-3	2.39	917	21	730	16	7	+0.01	0.03	NA	7	+0.23	0.35	+1.48	966	120	773	103	8	+0.05	0.07	NA	8	+0.25	0.23	+1.85
6-1	2.28	791	34	771	41	8	+0.08	0.04	+0.10	8	+0.47	0.46	+1.69	866	184	843	185	8	+0.04	0.04	+0.03	8	+0.97	0.12	+2.49
6-2	2.79	976	39	971	45	7	+0.13	0.10	+0.16	7	-2.04	0.32	+3.21	1055	196	1048	198	6	+0.04	0.06	+0.04	8	+0.21	0.23	+3.84
6-3	1.77	936	22	973	27	8	+0.17	0.13	+0.11	8	-0.95	0.18	+2.15	985	119	1027	135	8	+0.03	0.06	+0.03	8	+0.36	0.11	+2.73
16-2B	2.23	942	25	942	30	8	+0.09	0.07	NA	8	-0.40	0.29	NA	985	111	985	117	8	+0.02	0.04	NA	8	+0.15	0.17	NA
16-2T	2.23	993	24	1017	30	8	+0.03	0.11	NA	8	-1.29	0.15	NA	1034	106	1059	116	8	+0.06	0.05	NA	8	+0.20	0.12	NA
16-3B	1.94	896	29	936	39	8	+0.02	0.04	NA	8	+0.05	0.14	NA	947	132	991	149	8	+0.01	0.02	NA	8	+0.25	0.05	NA
16-3T	1.26	849	18	894	26	8	+0.06	0.02	NA	8	+0.14	0.09	NA	883	87	934	106	8	0.00	0.01	NA	8	+0.23	0.05	NA
6-Hole																									
14-1	NA	NA	NA	NA	NA	NA	NA	NA	NA	NA	NA	NA	NA	NA	NA	NA	NA	NA	NA	NA	NA	NA	NA	NA	NA
14-2	1.42	1073	22	1160	28	5	+0.14	0.03	+0.22	5	-1.50	0.41	+3.72	1148	172	1248	205	6	+0.06	0.03	+0.02	6	+0.74	0.10	+2.64
14-3	NA	NA	NA	NA	NA	NA	NA	NA	NA	NA	NA	NA	NA	NA	NA	NA	NA	NA	NA	NA	NA	NA	NA	NA	NA
15-1	1.61	743	20	659	21	6	+0.03	0.06	+0.07	6	+0.56	0.18	+0.68	820	172	728	159	6	+0.03	0.10	0	6	+0.58	0.07	+1.09
15-2	2.03	1052	23	926	21	5	+0.07	0.02	+0.18	5	-2.19	0.35	+3.22	1132	184	994	157	6	-0.01	0.08	+0.02	6	+0.53	0.14	+2.19
15-3	1.36	1049	13	956	14	5	+0.07	0.04	+0.15	5	-2.82	0.42	+2.44	1099	112	1004	108	5	0	0.06	+0.01	6	+0.32	0.09	+1.79

[a] Irradiated strip elongations were corrected by a bias from the mean elongation of all unirradiated strips, except for FTE-16 strips.

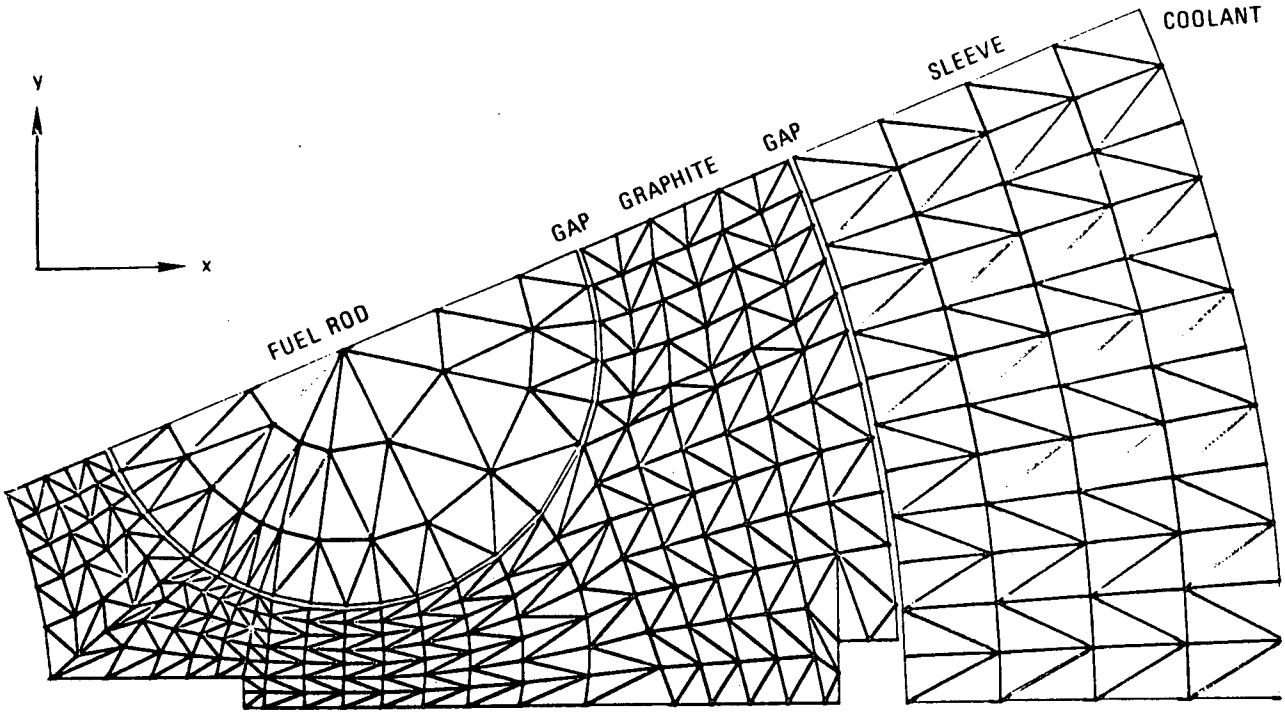

(a)

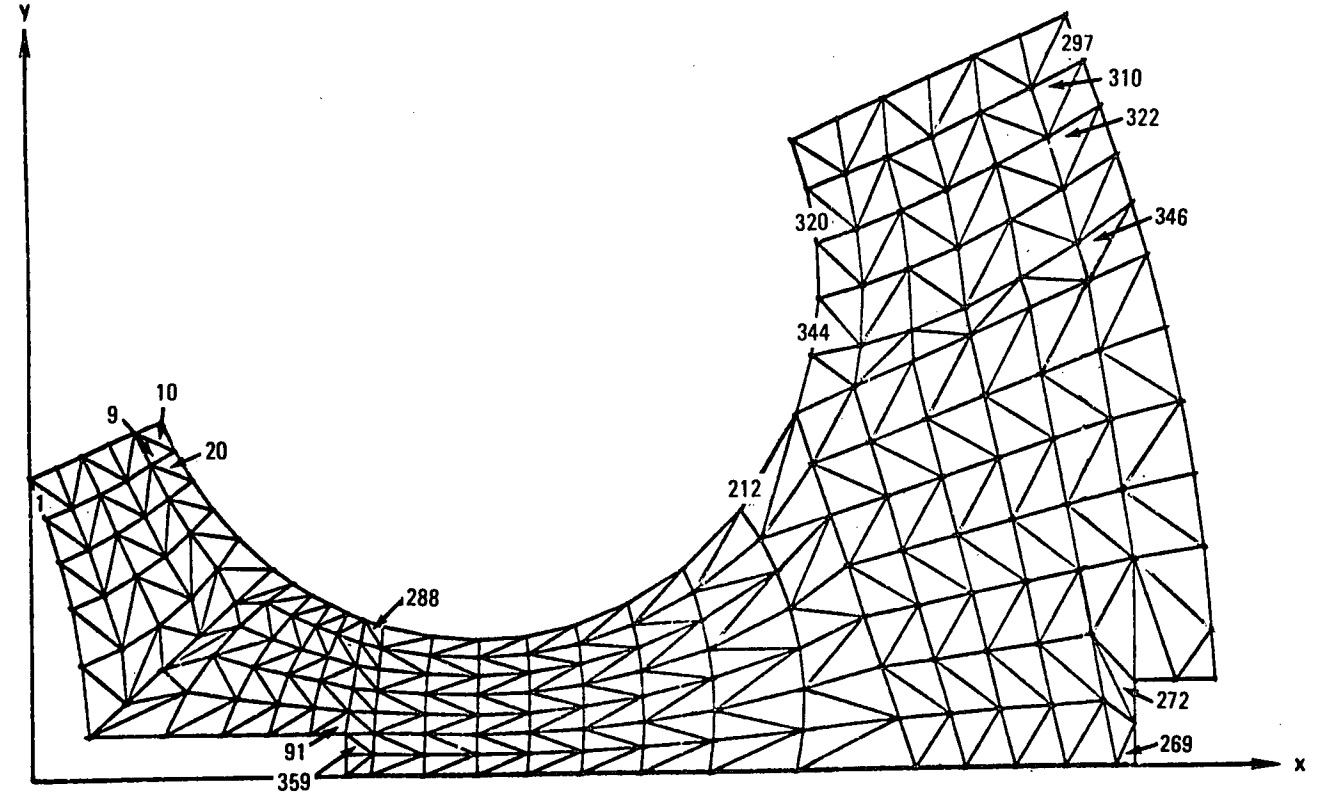

(b)

Fig. 7-1. Finite element model for eight-hole teledial configuration: (a) for thermal analysis; (b) for residual stress analysis (FTE-1, -2, -3, -4, -5, -6)

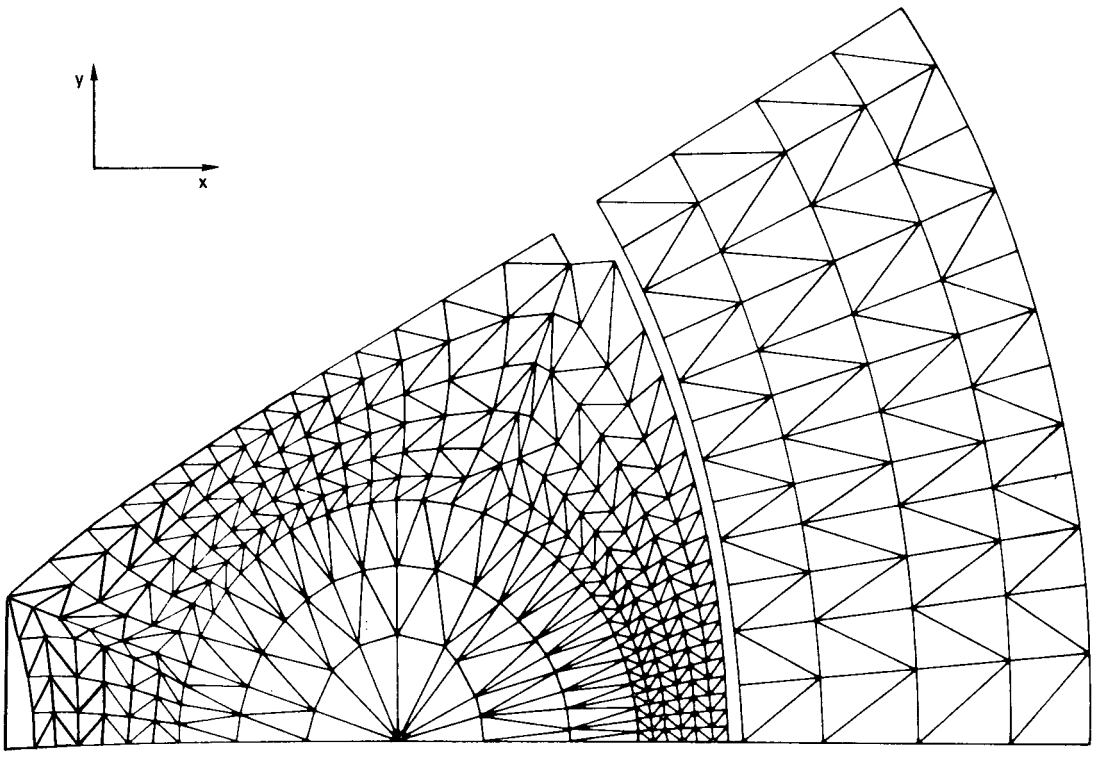

Fig. 7-2(a). Finite element model for thermal analysis of six-hole teledial configuration (FTE-14, -15)

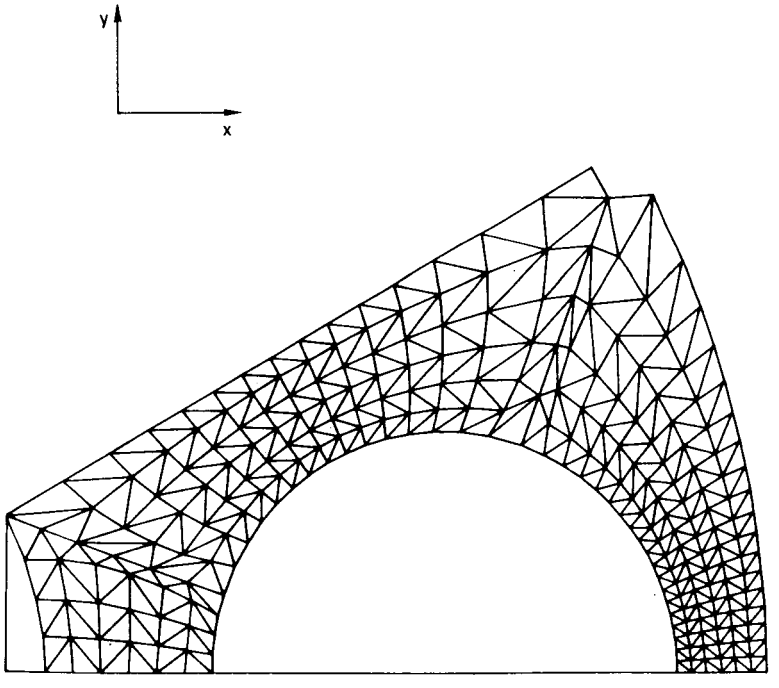

Fig. 7-2(b). Finite element model for residual stress analysis of six-hole teledial configuration (FTE-14, -15)

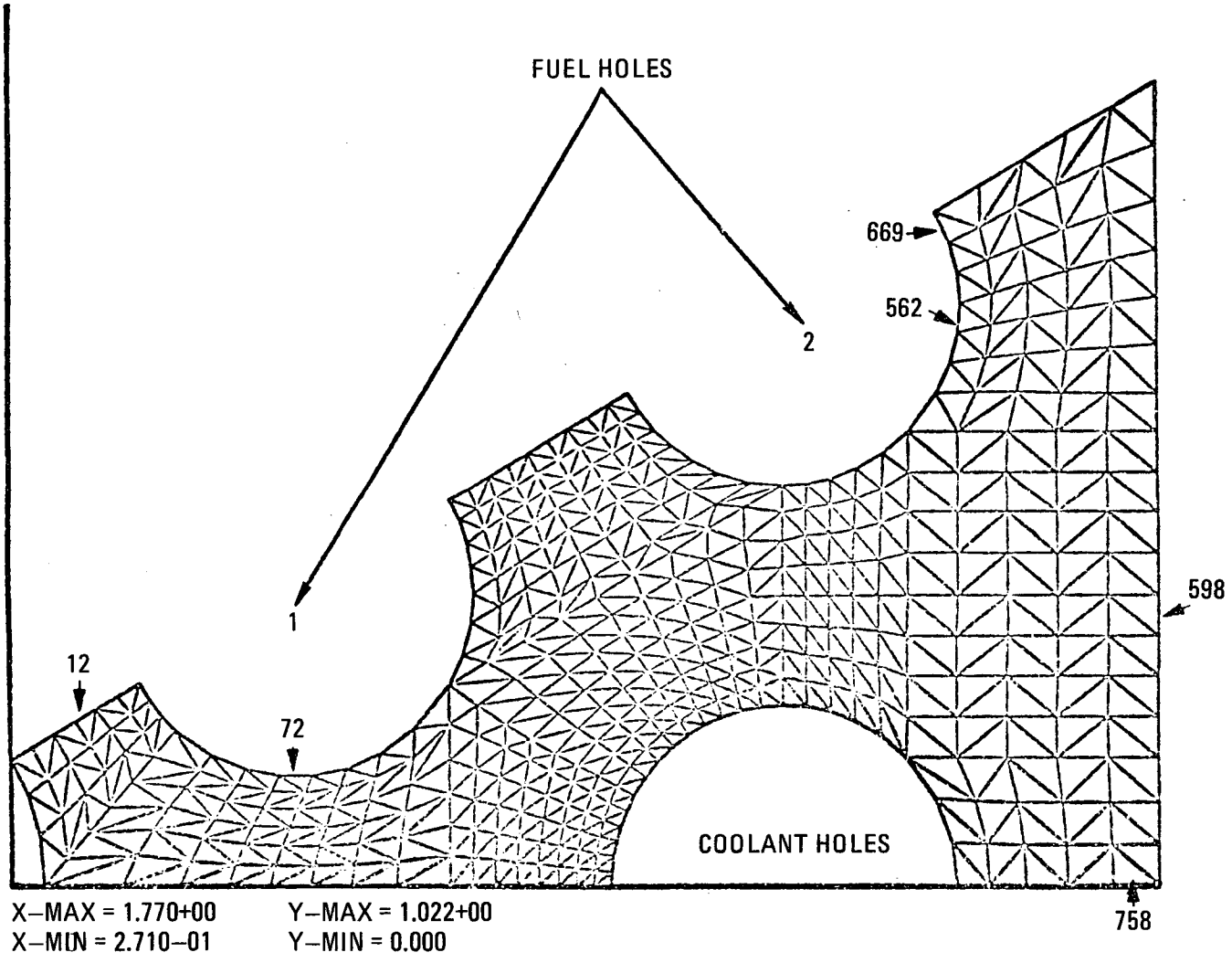

Fig. 7-3. Finite element model for 12-fuel-hole hexagonal fuel element configuration (PTE-2)

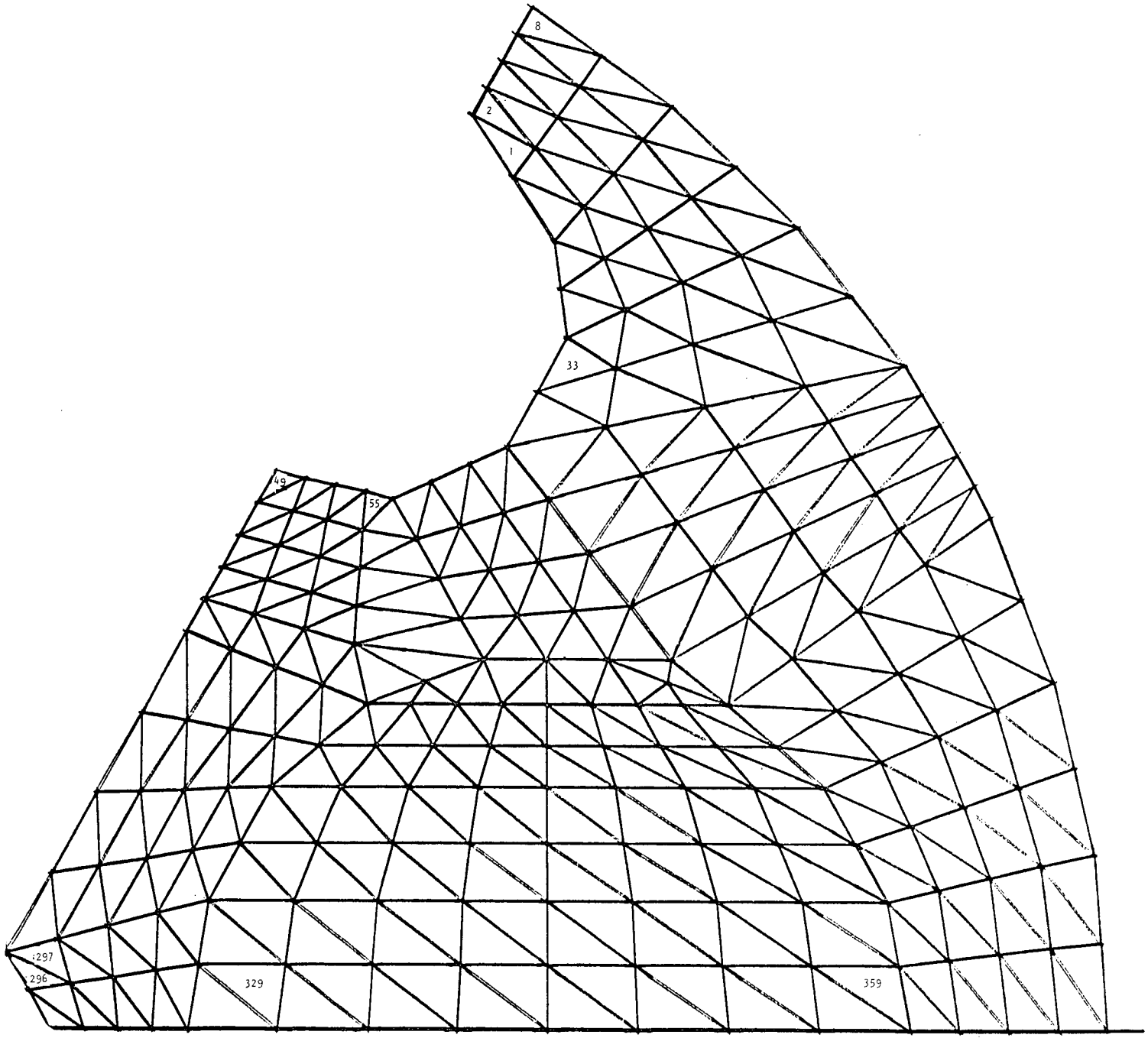

Fig. 7-4. Finite element model for molded block configuration (FTE-18)

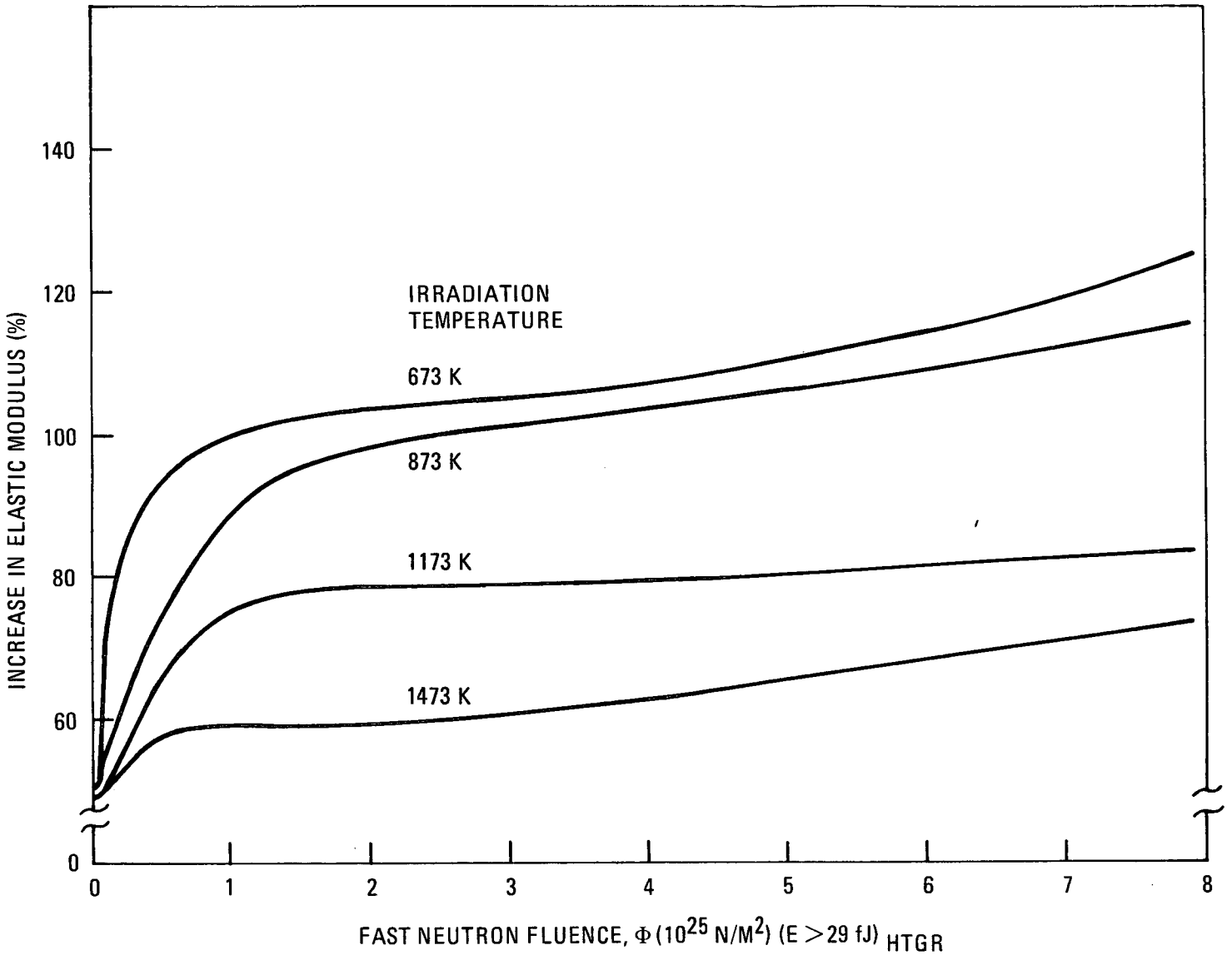

Fig. 7-5. Design curves for change in elastic modulus of H-327 graphite as a function of irradiation conditions

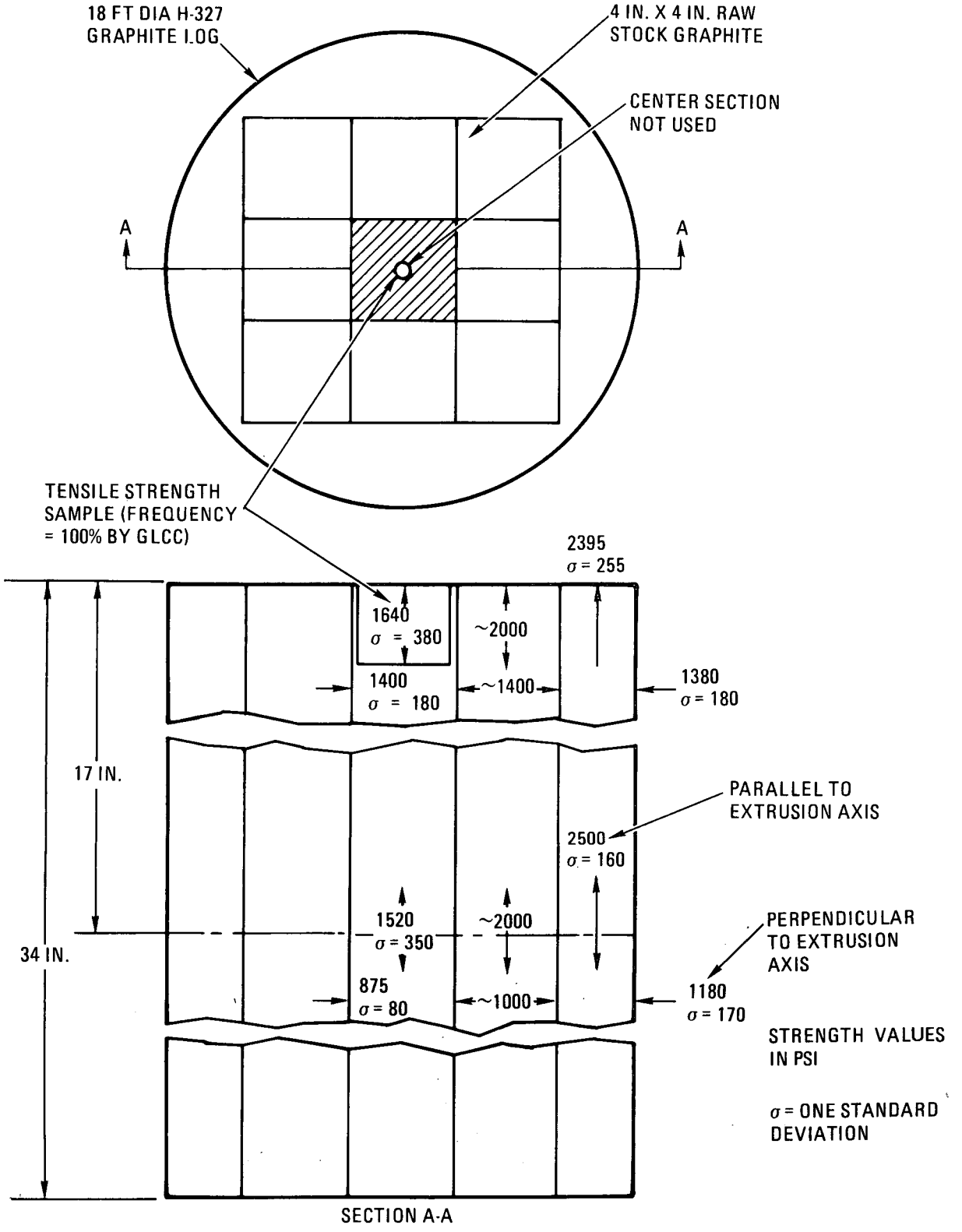

Fig. 7-6. Tensile strength of H-327 graphite (psi)

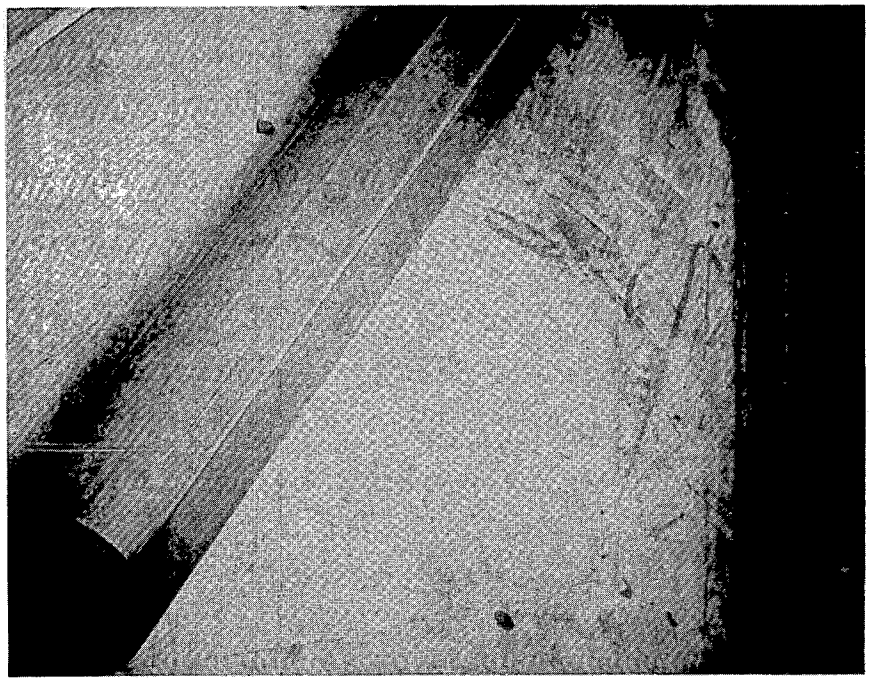

Fig. 7-7. External crack in fuel body 2 of FTE-2; evidence that crack propagated through bottom of body

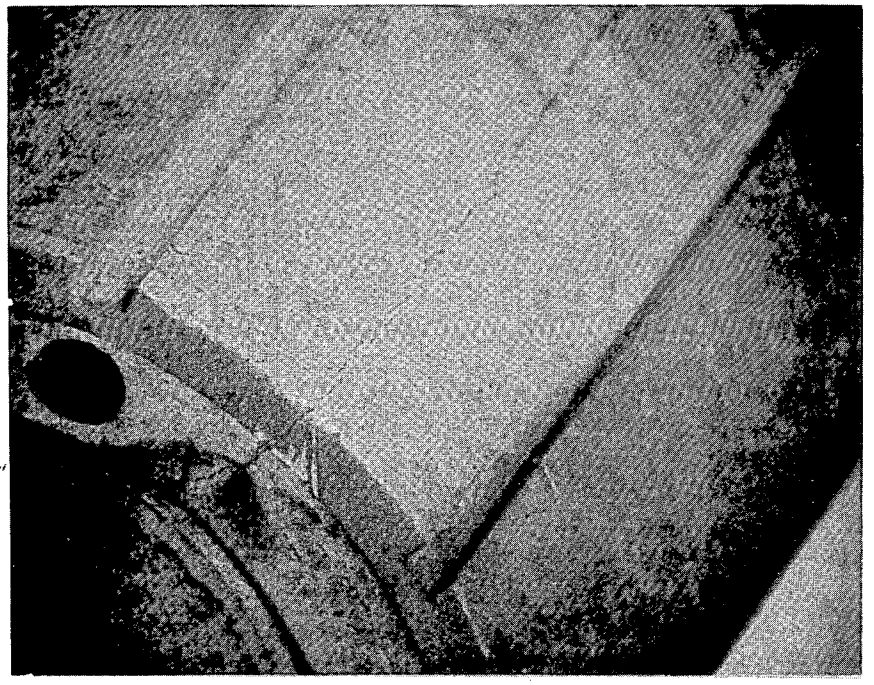

Fig. 7-8. Close-up of external crack shown in Fig. 7-7

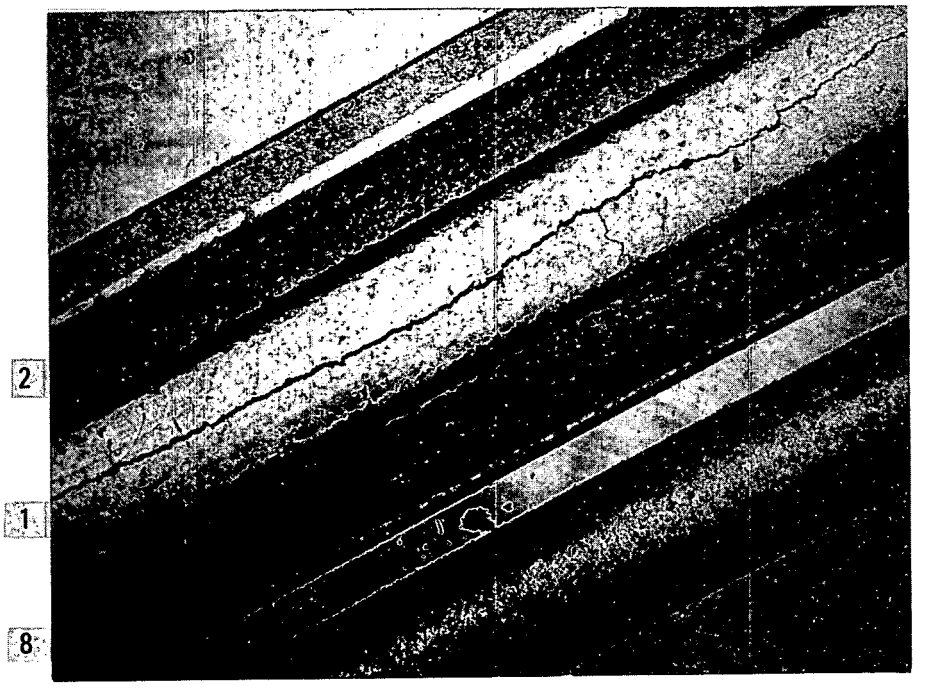

Fig. 7-9. Internal cracks in fuel body 2 of FTE-2. Crack in hole 1 (center face) is clearly evident, while cracks in holes 2 and 8 are somewhat obscure.

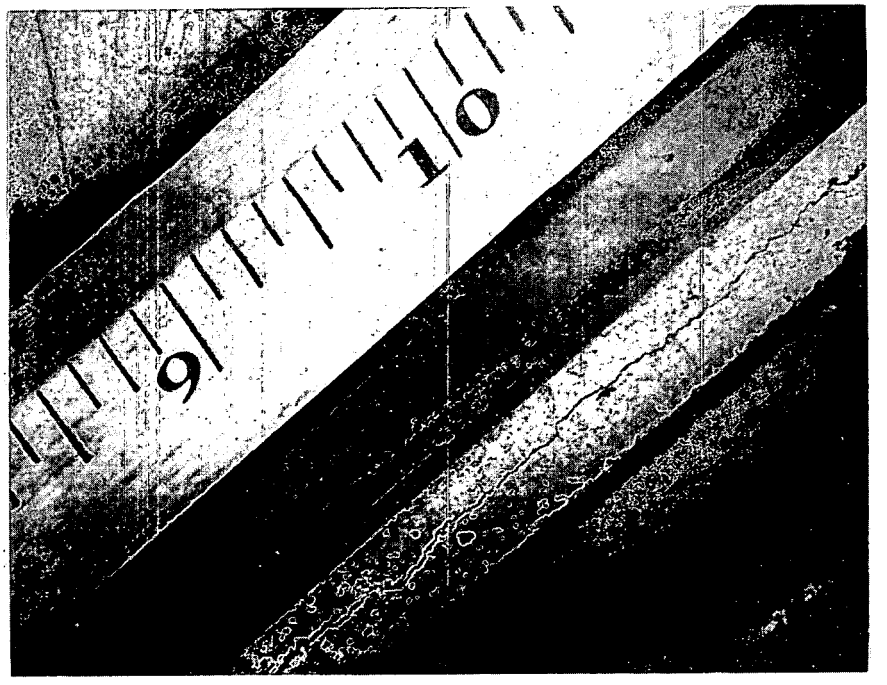

Fig. 7-10. Internal crack in hole 8 of FTE-2 fuel body 2 (center face)

Fig. 7-11. Internal crack in hole 1 of FTE-2 fuel body 2 (center face)

Fig. 7-12. Internal crack in hole 2 of FTE-2 fuel body 2 (center face)

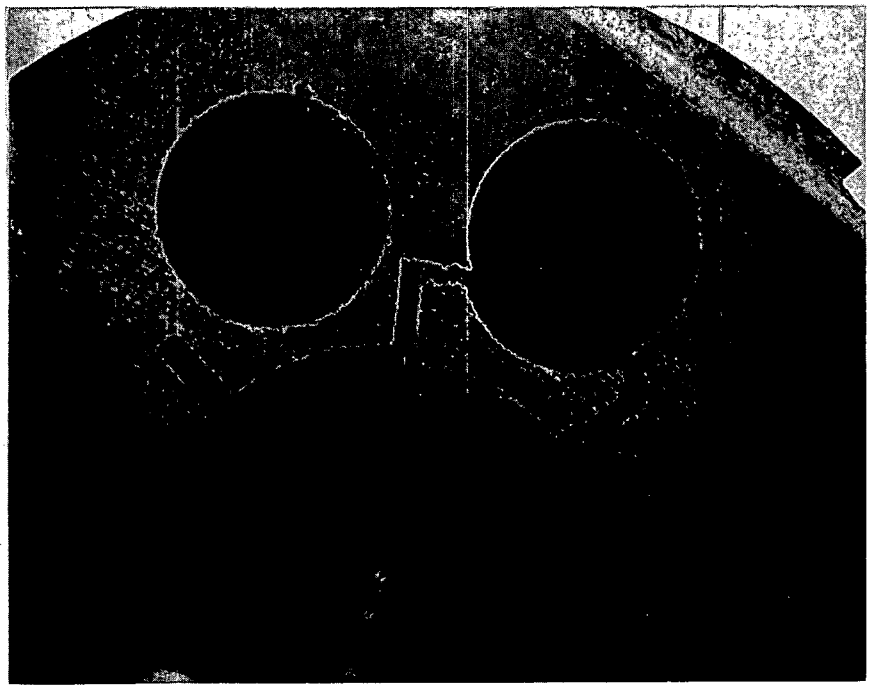

Fig. 7-13. Transverse section showing "fail-safe" cracks in hole 5 of FTE-2 fuel body 2 at 6 in. from bottom

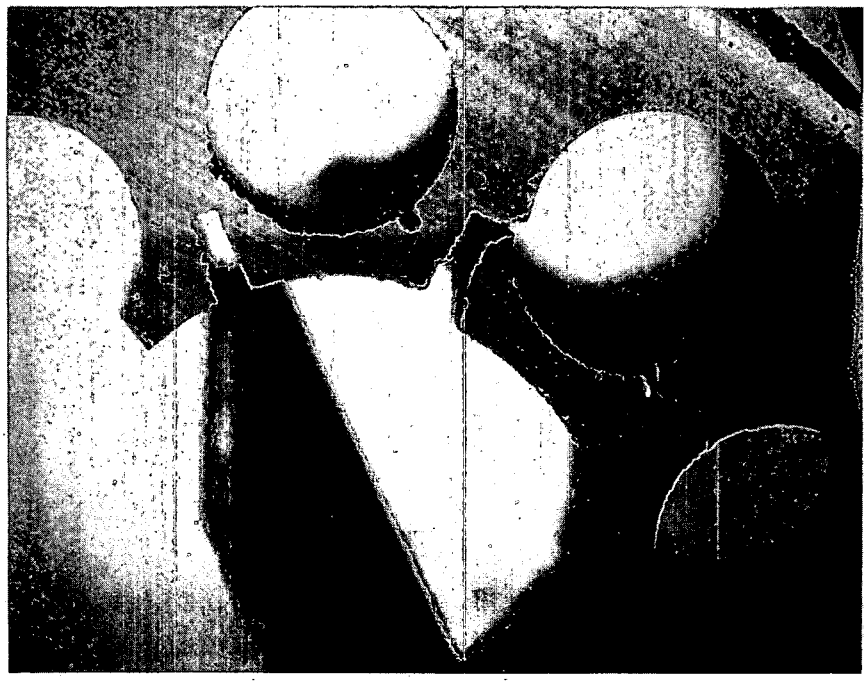

Fig. 7-14. Different view of cracks shown in Fig. 7-13 demonstrating size of cracks

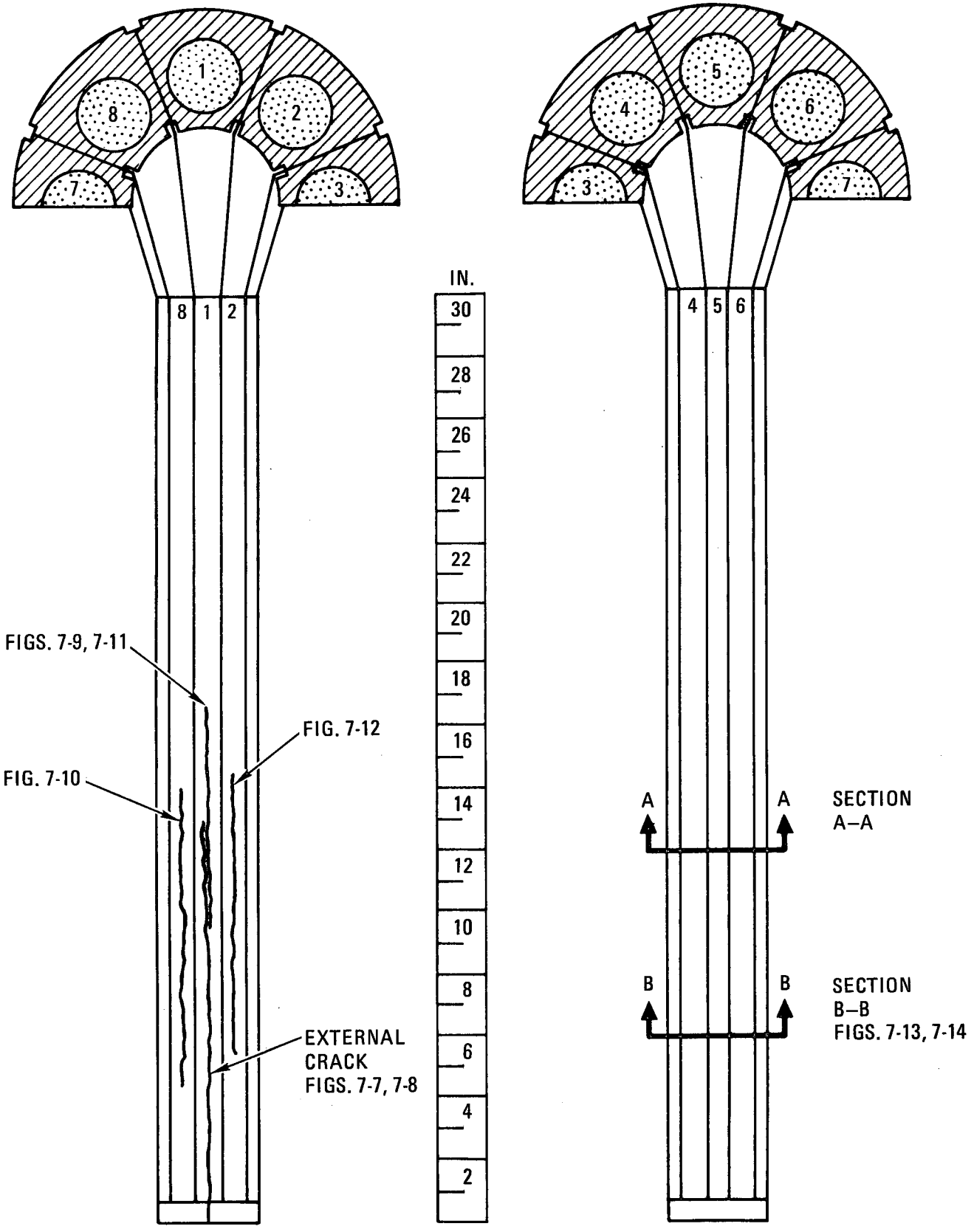

Fig. 7-15. Location of internal cracks in FTE-2 center body

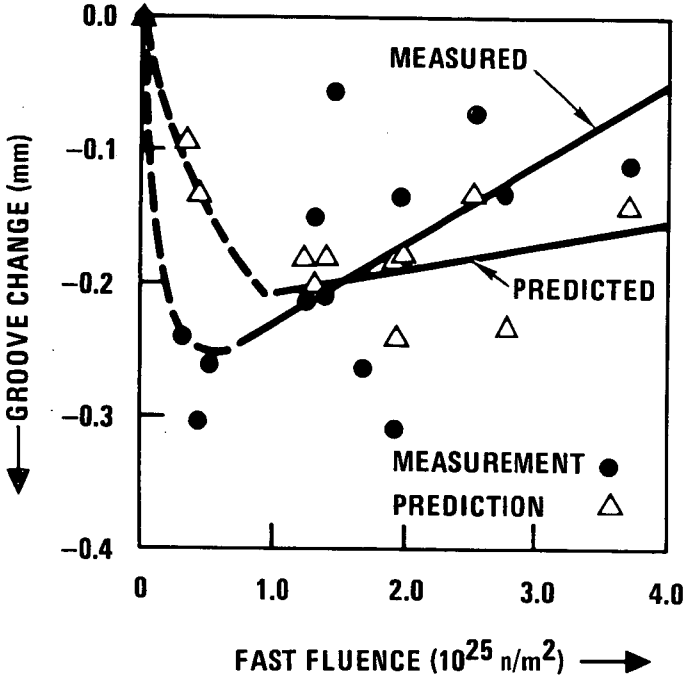

Fig. 7-16. In-plane stress determined from change in groove distance after cutting (eight-hole-element slices)

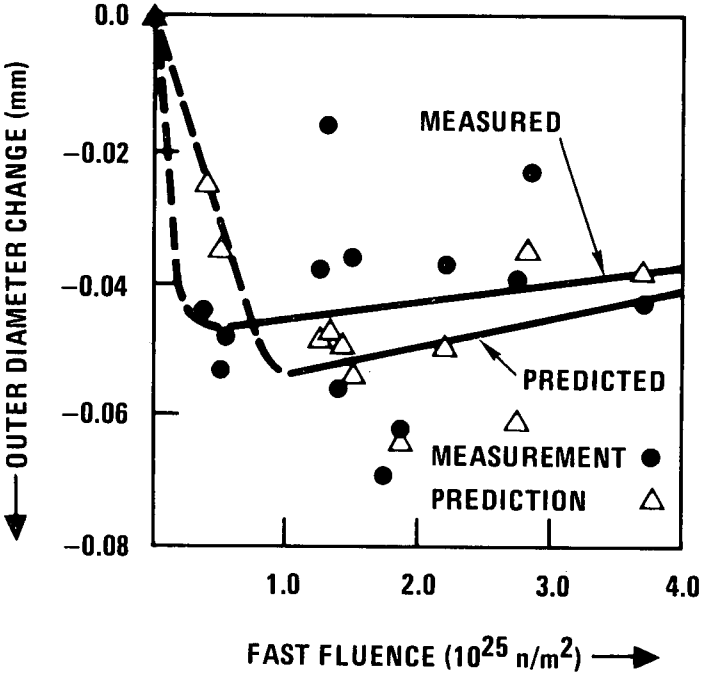

Fig. 7-17. In-plane stress determined from change in ring outer diameter after cutting (eight-hole-element slices)

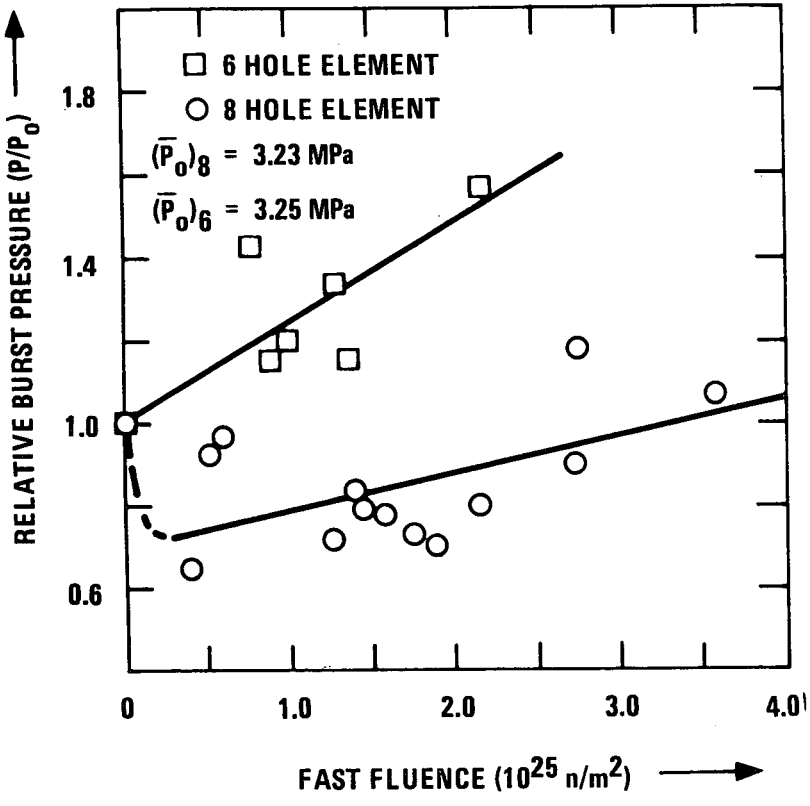

Fig. 7-18. In-plane strength test versus fast fluence as determined from pressure-burst tests

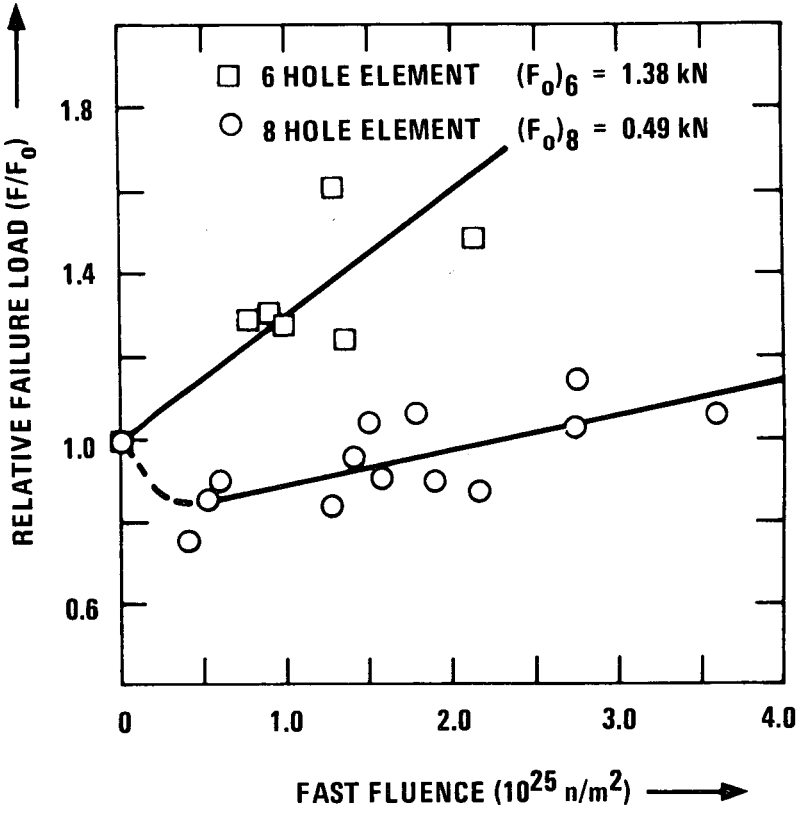

Fig. 7-19. In-plane strength test versus fast fluence as determined from diametral-compression tests

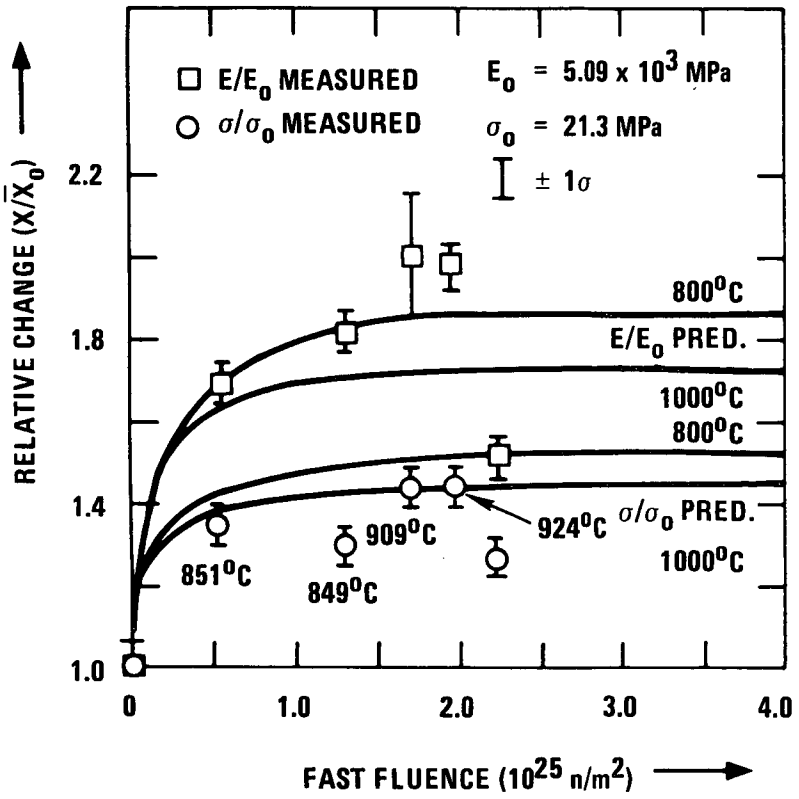

Fig. 7-20. Increase in Young's modulus (E/E_0) and rupture modulus (σ/σ_0) with irradiation as determined from four-point bend tests of thin strips from eight-hole elements

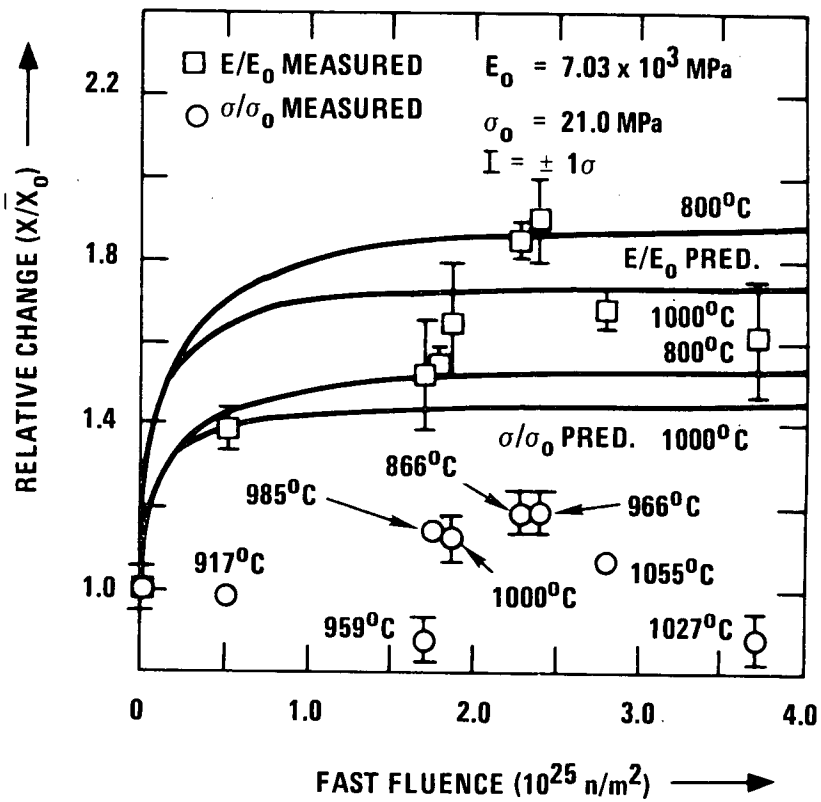

Fig. 7-21. Increase in Young's modulus (E/E_0) and rupture modulus (σ/σ_0) with irradiation as determined from four-point bend tests of thick strips from eight-hole elements

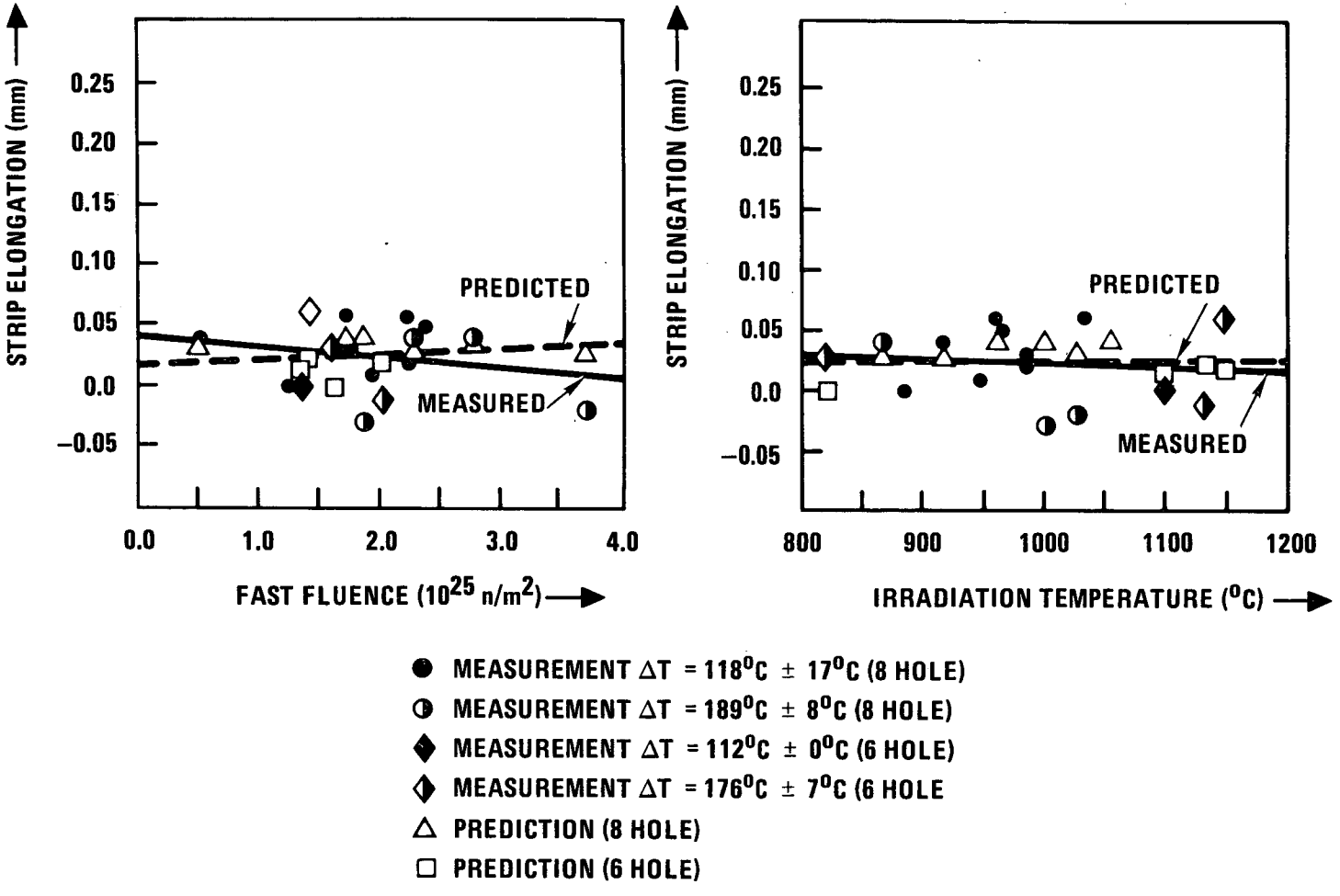

Fig. 7-22. Thick strip elongation versus fast fluence

Fig. 7-23. Thick strip elongation versus temperature

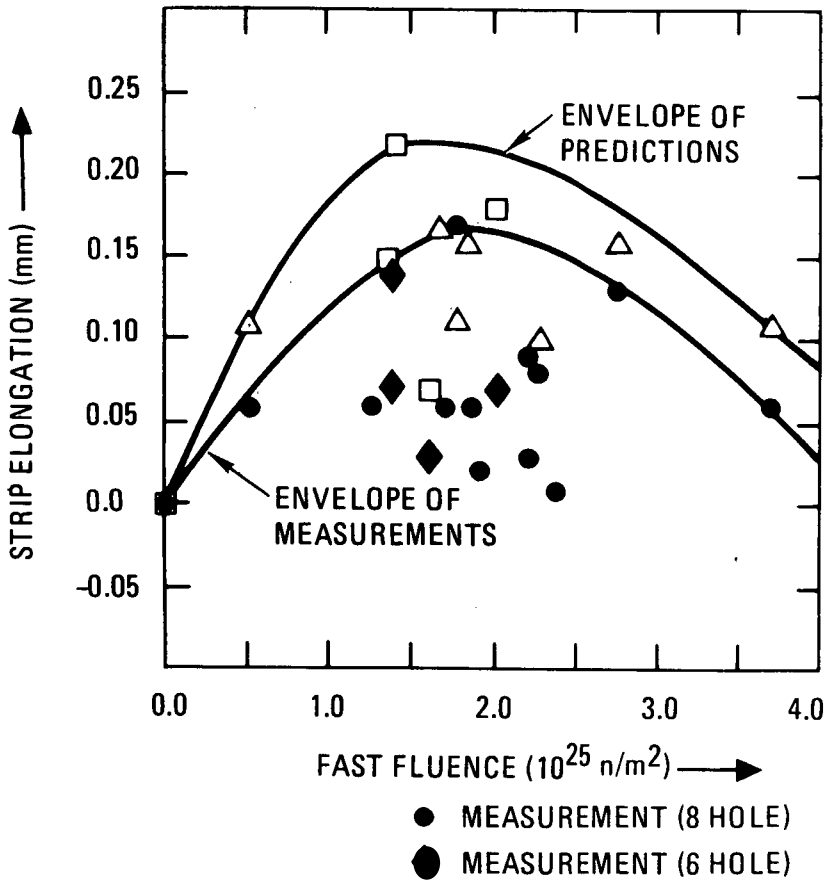

Fig. 7-24. Thin strip elongation versus fast fluence

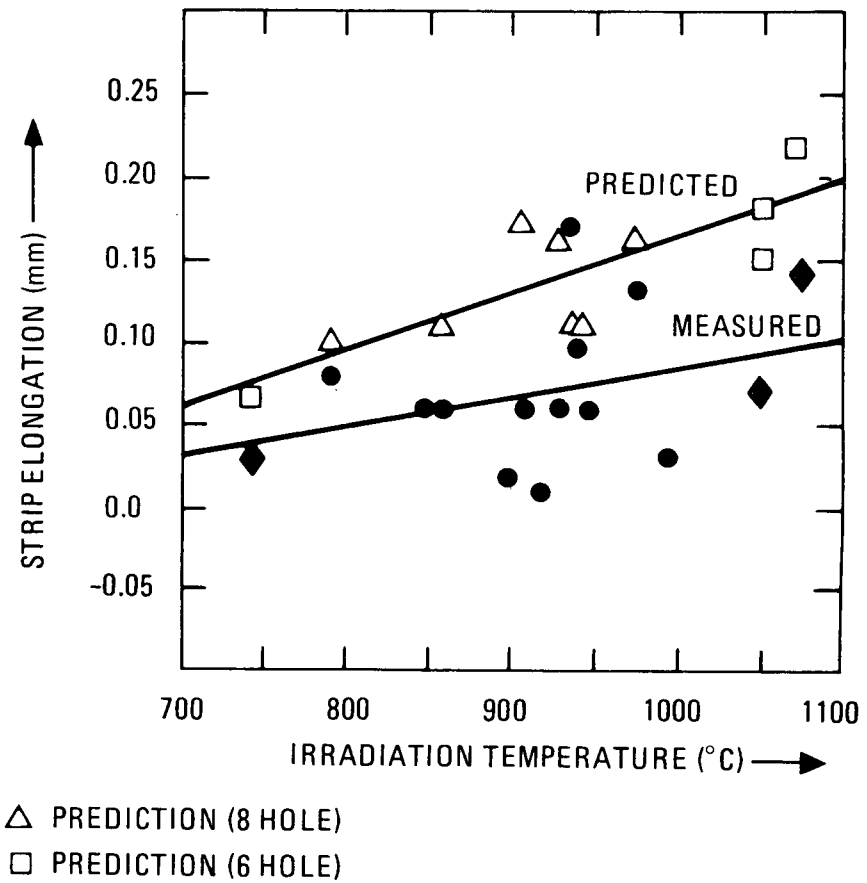

Fig. 7-25. Thin strip elongation versus temperature

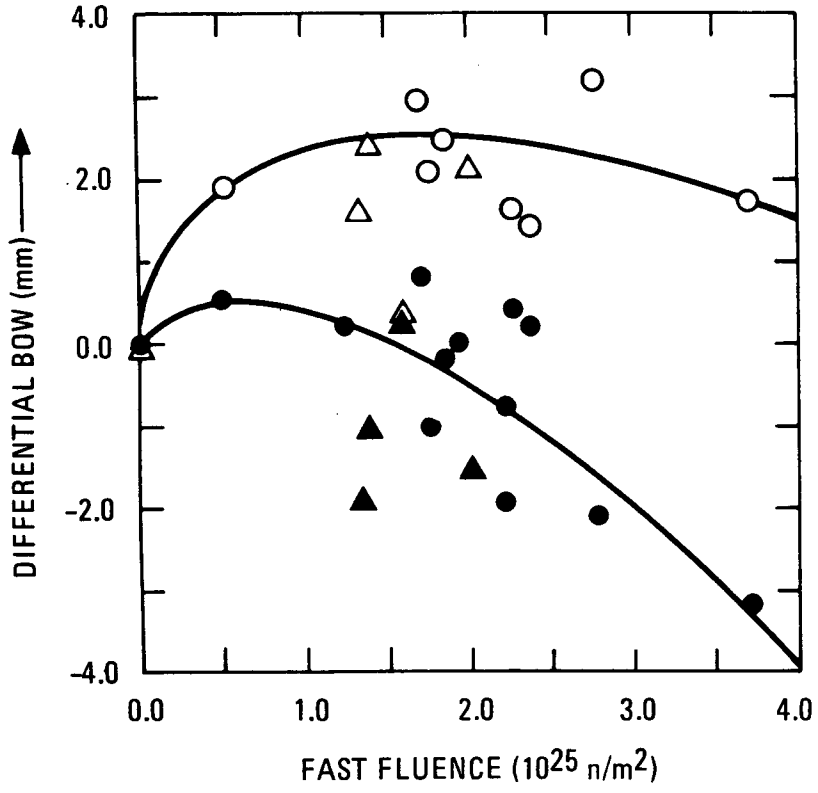

Fig. 7-26. Thin strip differential bow versus fast fluence

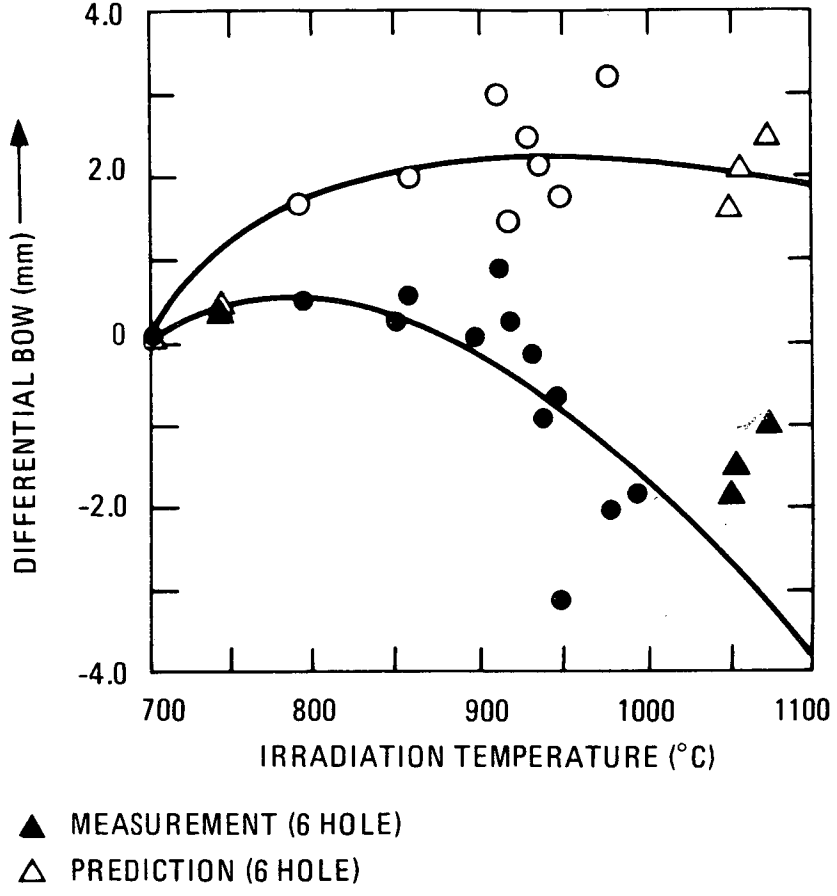

Fig. 7-27. Thin strip differential bow versus temperature

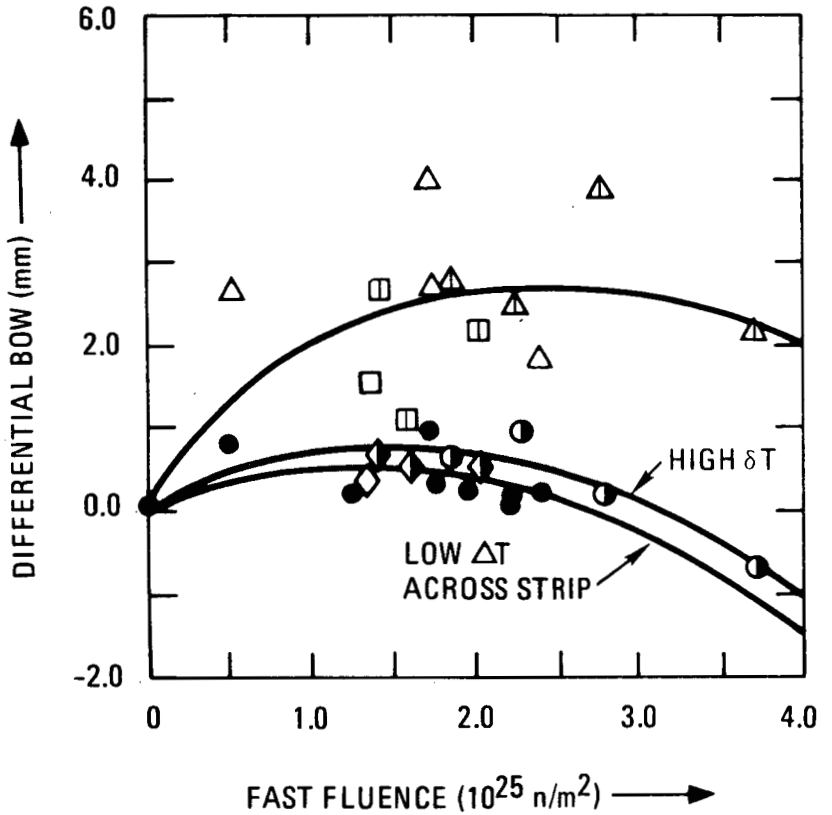

Fig. 7-28. Thick strip differential bow versus fast fluence

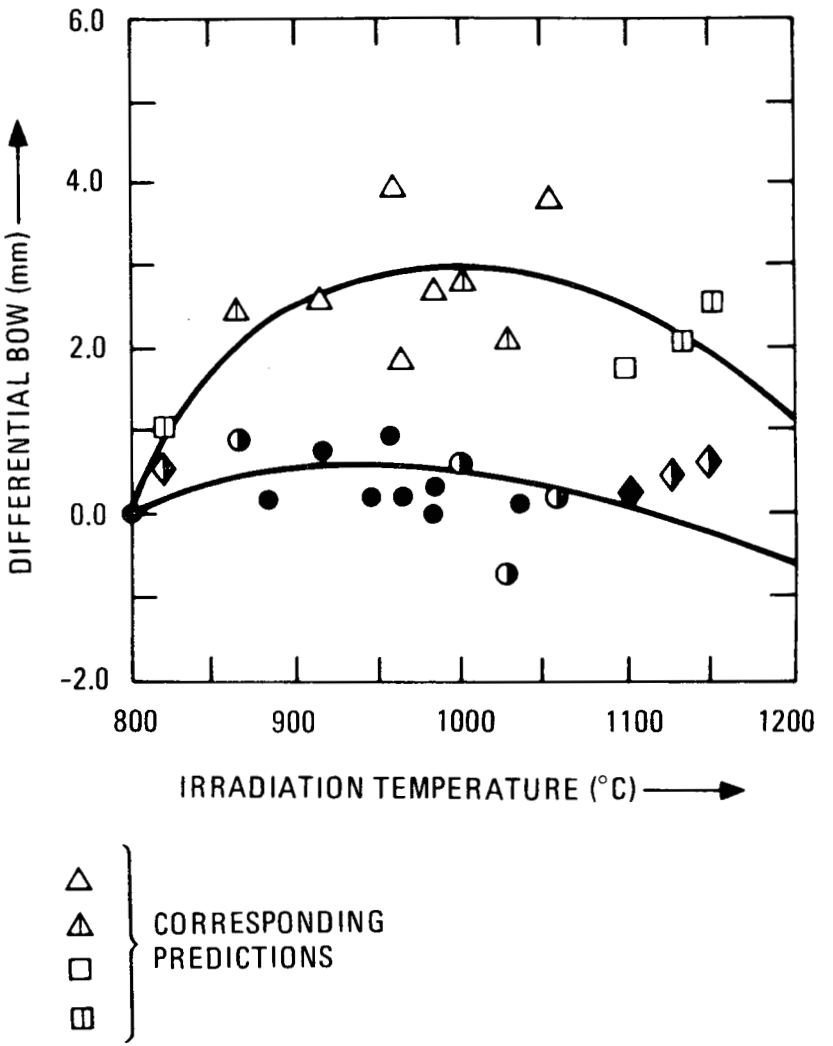

Fig. 7-29. Thick strip differential bow versus temperature

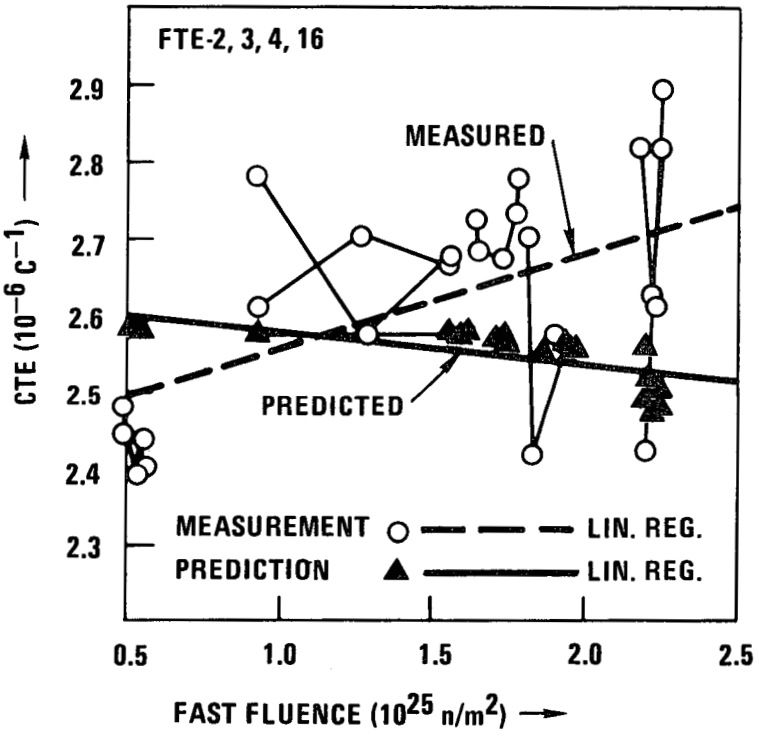

Fig. 7-30. Coefficient of thermal expansion versus fast fluence over 500° to 900°C range for thin strips of eight-hole elements

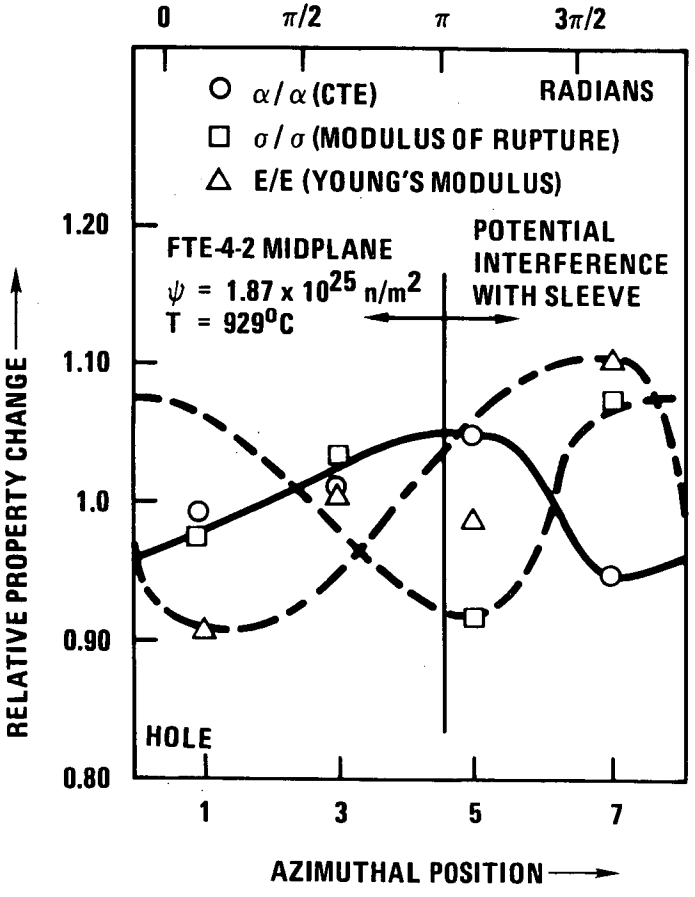

Fig. 7-31. Normalized azimuthal variation for CTE, modulus of rupture, and Young's modulus for FTE-4

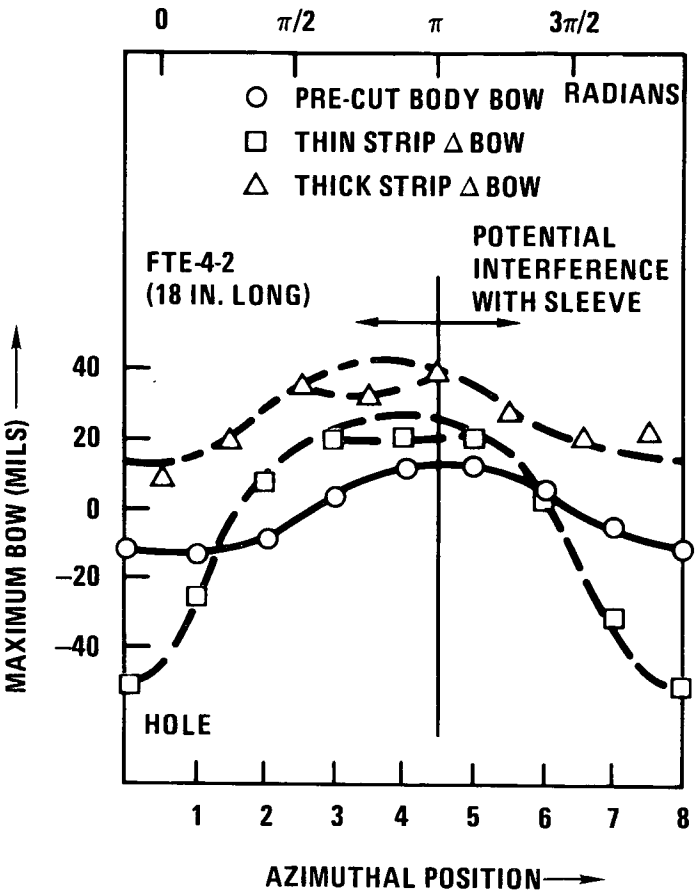

Fig. 7-32. Azimuthal variation of maximum bow for FTE-4

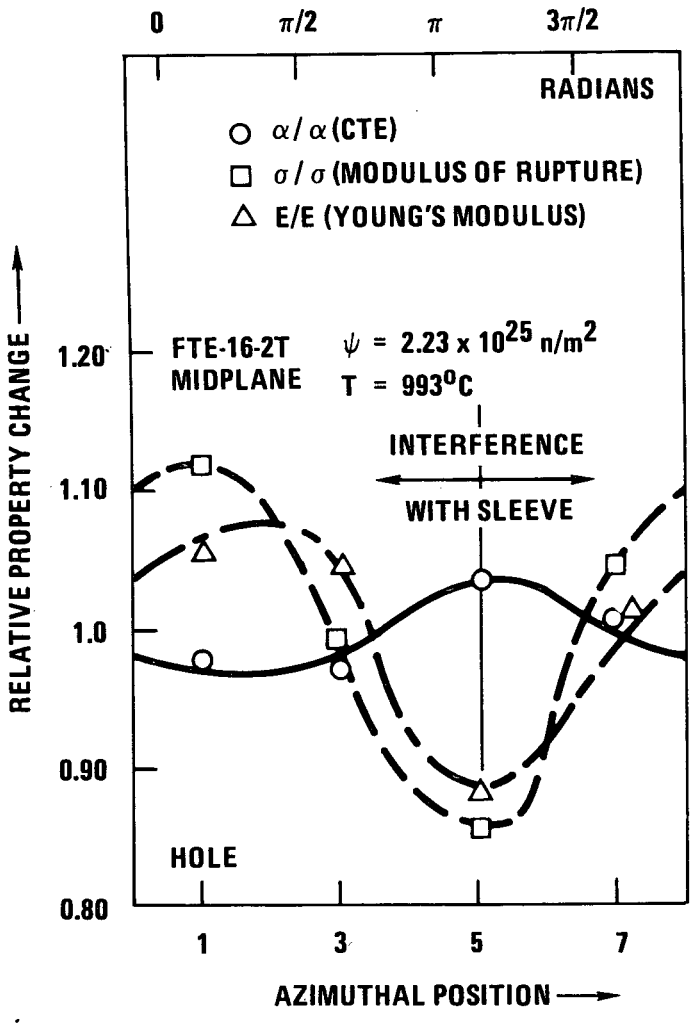

Fig. 7-33. Normalized azimuthal variation for CTE, modulus of rupture, and Young's modulus for FTE-16

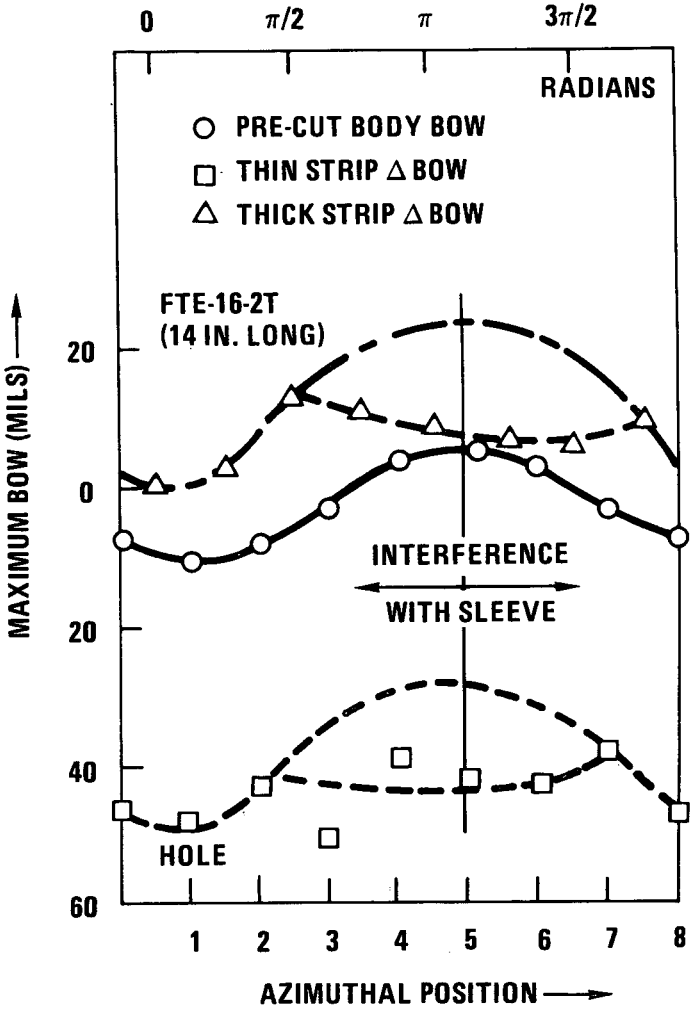

Fig. 7-34. Azimuthal variation of maximum bow for FTE-16

8. FUEL EXAMINATION

Fuel testing in the Peach Bottom reactor was an important part of the irradiation testing program for candidate HTGR fuels. Accelerated irradiation experiments (irradiation capsules) (Ref. 8-1) have extended the fuel performance data base to peak HTGR irradiation conditions but have not verified fuel performance under real-time HTGR operating conditions. The Peach Bottom test elements provided real-time fuel performance data at fast fluences up to 4.2×10^{25} n/m^2 [$(E > 29 \text{ fJ})_{HTGR}$] and time-averaged temperatures between 600° and 1600°C. Table 8-1 lists the test elements that were destructively examined at GA and ORNL. The fuel performance data obtained from these examinations are discussed below.

8.1. PYROLYTIC CARBON PERFORMANCE ON COATED FUEL PARTICLES

Dense outer pyrolytic carbon (OPyC) coatings are deposited on TRISO and BISO fuel particles to retain fission products and to protect and support the SiC layer (on TRISO particles). Harmon and Scott (Ref. 8-1) have summarized the performance of PyC coatings irradiated in capsule experiments conducted by GA and in other experiments. They concluded that the structural characteristics that affect OPyC failure are crystalline anisotropy and size, microporosity, and coating volume:

1. High OPyC anisotropy causes stress concentrations from differential shrinkage of the coating.

2.* Large crystal sizes increase the probability of failure because of high local anisotropy. [All OPyC coatings examined in the Peach

*These attributes are related to the bulk density and intrinsic strength of the coating.

Bottom test elements were low-temperature isotropic (LTI) coatings which had small crystal sizes.]

3.* Microporosity allows the matrix to impregnate and adhere to the OPyC coating. The coating is pulled or ripped off when the coating and matrix shrink away from each other during irradiation.

4. The volume of OPyC coating under stress is directly related to the probability of a critical flaw that will cause failure. This is defined in Weibull failure statistics (Ref. 8-2).

The effects of anisotropy, microporosity, and Weibull statistics on OPyC performance in the Peach Bottom test elements were consistent with results from the accelerated irradiation tests (Ref. 8-1).

8.1.1. OPyC Performance on BISO Particles

The OPyC coatings on BISO particles from 120 Peach Bottom fuel rods and loose particle batches had low irradiation-induced failure (<1%), as summarized in Tables 8-2 and 8-3. No BISO particles from the capsule tests or Peach Bottom tests had significant OPyC coating failure below a fast fluence of 5×10^{25} n/m^2 [$(E > 29 \text{ fJ})_{HTGR}$] and a temperature of 1600° C.

8.1.2. OPyC Performance on TRISO Particles

8.1.2.1. OPyC Anisotropy. Harmon and Scott (Ref. 8-1) identified an anisotropy value (BAF_o** = 1.03) above which OPyC coating failure on TRISO particles increased rapidly with increasing anisotropy. This trend was also observed in the Peach Bottom test elements. TRISO particle batches with OPyC BAF_o values below 1.03 had little or no OPyC coating failure (see Fig. 8-1 and

*These attributes are related to the bulk density and intrinsic strength of the coating.

**BAF = Bacon anisotropy factor.

Tables 8-4 and 8-5), except batch 4000-307 (see Section 8.1.2.2). TRISO particle batches with OPyC BAF_0 values above 1.05 frequently exhibited high OPyC coating failure.

The coating failure was more strongly correlated with BAF_0 than with fast fluence. Figure 8-2 shows that significant failure occurred at fast fluences as low as 1 x 10^{25} n/m^2 [E > 29 fJ)$_{HTGR}$]. Harmon and Scott (Ref. 8-1) had suggested that failure began above 3 x 10^{25} n/m^2. There was no observable failure of OPyC coatings below a fast fluence of 1 x 10^{25} n/m^2 even for TRISO particle batches with OPyC BAF_0 values greater than 1.03.

There did not appear to be any correlation between OPyC performance and irradiation temperature (see Figs. 8-1 and 8-2).

8.1.2.2. Microporosity. Matrix-coating interaction due to high OPyC microporosity was a source of OPyC coating failure in the Peach Bottom test elements and in irradiation capsules (Ref. 8-1). The effect of high microporosity on OPyC coating performance was obvious in batch 4000-302, which was irradiated in several test elements. From preirradiation metallography of batch 4000-302, it was evident that the microporosity was very high (Ref. 8-3). Blended batch 4000-307* also contained batch 4000-302. Matrix-coating interactions were obvious in both of these batches (Fig. 8-3). Figure 8-4 shows the coating failure fraction versus fast fluence for these two batches, which were irradiated in both fuel rods and loose particle beds. No OPyC failure occurred in the loose particle beds because there was no matrix to interact with the coatings. The coating failure in the fuel rods had an obvious fast fluence dependence. The failure began at 1.5 x 10^{25} n/m^2 [(E > 29 fJ)$_{HTGR}$] and increased with increasing fluence. Twenty to thirty percent of the coatings failed completely at fast fluences of >2 x 10^{25} n/m^2. The cracks propagated slowly as the stresses caused by differential matrix-coating shrinkage increased. The cracks in some coatings propagated radially through the coatings and circumferentially around the particles (Ref. 8-4).

*Blend of batches 4000-302, 4000-303, 4000-305, and 4000-306. BAF_0 = 1.02 to 1.05 and density = 1.68 to 1.79 kg/m^3.

The circumferential cracks were associated with low-density bands seen in the preirradiation metallography (Ref. 8-3).

8.1.2.3. Coating Volume. Several authors have discussed Weibull statistics in relation to OPyC failure (Refs. 8-1, 8-2). The basis of Weibull statistics is that the probability of finding a critical flaw that will cause failure in a brittle material is proportional to the volume of material under stress. The mathematical formulation is

$$F = 1 - \exp\left[-\int_V \left(\frac{\sigma}{\sigma_o}\right)^M dV\right] \quad , \tag{8-1}$$

where F = failure probability,
V = volume under stress,
σ = uniaxial stress,
σ_o = normalizing material property parameter,
M = Weibull modulus.

Fuel batch OR1694, irradiated as loose particles in FTE-14 and FTE-15, was an excellent example of the effect of fuel particle size on failure. This batch was unique in that it had a wide range of particle diameters (450 to 850 μm). If it is assumed that the material properties and stresses in the coatings are the same regardless of particle size because of similar coating conditions and irradiation exposures, Eq. 8-1 can be reduced to Eq. 8-2:

$$\log (1 - F) = C_1 \left[d^3 - (d - 2t)^3\right] + C_2 \quad , \tag{8-2}$$

where C_1 and C_2 = constants,
d = particle diameter,
$1 - F$ = survival fraction,
t = OPyC coating thickness = 40 μm.

The survival fraction, log (1 - F), and the term proportional to the volume, $d^3 - (d - 2t)^3$, are plotted in Fig. 8-5 at particle diameter increments of 25 μm. Equation 8-2 indicates that this plot should be a straight line. A linear least-squares fit of the data where failure occurred indicated a strong correlation between OPyC and failed particle size.

8.2. SiC PERFORMANCE ON COATED FUEL PARTICLES

Silicon carbide coating failure observed during metallography of fuel rods and loose particles is always suspect because of polishing damage. The SiC failure fraction from metallography was therefore assumed to be significant only when it was coupled with a high fission gas release (as measured in TRIGA at 1100°C).

Only three of the examined samples from the Peach Bottom test elements had high SiC failure and high fission gas release. Two of the samples were UO_2 particles from FTE-6 (Ref. 8-5), in which the SiC was attacked by migrating kernels. The other was fuel rod 2-2-5 from FTE-15 (Ref. 8-6), in which the ThC_2 particles had 44.9% OPyC failure and 23.9% SiC failure. The release of fission products from these cases is discussed in Section 8.6.

8.3. CHEMICAL ATTACK OF COATINGS

8.3.1. Fission Product - SiC Reactions

Degradation of the SiC coating as a result of fission product - SiC reactions is a potential failure mechanism in irradiated fuel particles. Postirradiation optical metallography and electron microprobe data show that palladium and rare earth fission products are among the species that react with the SiC layer. Smith (Refs. 8-7 and 8-8) has studied the kinetics of fission product - SiC reactions in out-of-pile experiments. The Peach Bottom test elements are the largest source of in-pile data on this phenomenon.

Thirty-three cases of palladium attack on SiC coatings were found during the microprobe examination of FTE-13 (the plutonium test element) at ORNL (Ref. 8-9). The high incidence of palladium attack in this element is attributed to the high yield of palladium from fissioning of Pu-239 (13 times higher than from fissioning of U-235). Two examples of this attack are shown in Fig. 8-6. The attack zones were randomly oriented in the particles and were generally associated with large white phases at the IPyC-SiC boundary. This large white phase was also observed in a denatured uranium particle from FTE-5 (see Fig. 8-7). Concentrations of a palladium-rich phase at, or near, reaction zones were also observed in an HEU UC_2 TRISO particle irradiated in capsule P13Q (Ref. 8-10).

In addition to the palladium attack in FTE-13, 24 cases of fission product attack on SiC coatings were found in 11 other Peach Bottom test elements. Cerium, praseodymium, neodymium, and lanthanum were identified in several cases as being the fission products in the reaction zones (Ref. 8-4). These zones were located on the cold side of the particles and were accompanied by graphitization of the IPyC and buffer coatings (Fig. 8-8).

The SiC attack data for FTE-13 and for the other Peach Bottom test elements are presented in Tables 8-6 and 8-7.

8.3.2. Kernel Attack

Migrating UO_2 and PuO_x kernels were observed to have attacked the SiC coating in FTE-6 and FTE-13 (Figs. 8-6, 8-9, and 8-10). $(Th,U)C_2$ that had been dispersed during manufacturing also mildly attacked the SiC coating in FTE-16 (Fig. 8-9). The dispersed kernels attacked the inner SiC layer uniformly, but the reaction zone never penetrated more than a few microns into the SiC.

8.3.3. Contamination

Contamination in fuel rods attacked both SiC and OPyC layers in several isolated cases. Microprobe work done at ORNL identified iron as a reactive contaminant in one case from RTE-2 (Ref. 8-4). Figure 8-11 shows examples of contamination attack observed in FTE-5. This type of attack was most prevalent in Phase I* test element fuel rods. These rods were not cleaned with an acid leach.

8.4. KERNEL MIGRATION

Kernel migration is another potential fuel failure mechanism. All particle coatings that come into contact with a migrating kernel are chemically degraded (see Section 8.3.2). Extensive out-of-pile and in-pile data have been collected on the migration of fuel kernels. Carbide fuels [UC_2, ThC_2, and $(Th,U)C_2$] migrate by the diffusion of carbon through the kernel (Refs. 8-11, 8-12). The rate of migration is expressed as a kernel migration coefficient (KMC):

$$KMC = \frac{T^2}{dT/dx}\frac{dx}{dt} = \beta \exp\left(-\frac{\Delta H}{RT}\right), \qquad (8\text{-}3)$$

where T = absolute temperature (K),

dT/dx = linear temperature gradient across the coated particle (K/cm),

dx/dt = kernel migration rate (cm/s),

dx = kernel migration distance, cm,

β = preexponential constant (cm^2-K/s),

R = gas constant,

ΔH = activation energy for the self-diffusion of carbon in the fuel phase (kcal/mol).

*Phase I = PTE-2; all FBTES; FTE-1, FTE-2, FTE-5; and all RTEs except RTE-1 (FTE-11).

Migration of UO_2 and $(Th,U)O_2$ fuel kernels has also been observed. The mechanism for oxide kernels is not well understood. It has been suggested that the migration is due to gas phase transport (Ref. 8-13). In the absence of an accepted theoretical model, UO_2 and $(Th,U)O_2$ migration is also characterized in the literature in terms of KMC values (Eq. 8-3).

The kernal migration data obtained from the Peach Bottom test elements are provided in Tables 8-8 and 8-9. (The kernel migration data for the plutonium fuel irradiated in FTE-13 are presented and discussed in Ref. 8-9.) The predicted migration distances given in these tables were calculated with the TREVER code using the KMCs listed in Table 8-10. These KMCs are based on kernel migration data from out-of-pile and capsule (accelerated) experiments. The kernel migration in all fuel types except $(Th,U)C_2$ was generally overpredicted. The kernel migration in $(Th,U)C_2$ particles was underpredicted in a few instances. These results indicate that kernel migration distances calculated using data from out-of-pile and capsule experiments are conservative.

8.4.1. UC_2

No UC_2 kernel migration was observed in the Peach Bottom test elements.*

8.4.2. UO_2

Widespread migration of UO_2 kernels was observed in fuel rods irradiated in FTE-4, FTE-6, and several of the RTEs. The observed kernel migration was always accompanied by large gas bubbles** that deformed and dispersed the kernels (Fig. 8-10). Occasionally there were deposits of carbon behind the kernel, which is typical of diffusion of carbon in carbide kernels. Contrary to predictions, no kernel migration was observed in UO_2 particles irradiated

*Only measured migration distances greater than 5 μm were considered to be significant (5 μm is considered to be the minimum resolution for metallographic measurements).

**The formation and swelling of fission gas bubbles is not a new phenomenon. It has been discussed in detail in the literature (Refs. 8-14 through 8-20).

in FTE-14 and FTE-15, even though the irradiation temperatures in three of the six examined fuel rods were close to 1400°C. The kernels in these particles had smaller gas bubbles than those in the FTE-4, FTE-6, and RTE samples and were not deformed (Fig. 8-12). The reason for this is not known.

8.4.3. $(Th,U)C_2$

Kernel migration in $(Th,U)C_2$ particles was observed in FTE-5, FTE-6, and FTE-16. In some cases, the observed migration was characterized by movement in several directions. Figure 8-13 shows two such cases. Nodules formed on the kernels, and rejected carbon collected between nodules. This behavior is not well understood. One possible explanation is that the temperature gradients shifted during irradiation. Such shifts could have been caused by changes in particle morphology or by shifts in the intra-rod power distributions. Particle morphology changes that could have shifted the temperature gradients were the development of voids at the IPyC-SiC and IPyC-buffer boundaries (see Fig. 8-13). Shifts in the intra-rod power distributions may have occurred during irradiation if the fissile and the fertile particles were non-homogeneously distributed within the rods.

$(Th,U)C_2$ kernel movement from swelling, cracking, and dispersion was also observed. Swelling and extrusion of the kernel into buffer cracks were observed in several cases (see Fig. 8-14). This is consistent with the testing of $(Th,U)C_2$ in capsule F-30 (Ref. 8-21). Cracking of the kernels was widespread in fuel rods from FTE-5. The cracks were initiated in the buffer and slowly propagated into the kernels (see Fig. 8-14). $(Th,U)C_2$ kernels from FTE-16 were dispersed owing to improper heat treatment during manufacturing (see Fig. 8-14).

Migration of $(Th,U)C_2$ kernels was also observed in Peach Bottom driver elements and is discussed in Refs. 8-22 and 8-23. Quantitative comparisons of predicted and measured migration distances were not made. All the migrating kernels had rejected carbon behind them, which is characteristic of the carbon diffusion discussed in Refs. 8-12 and 8-13.

8.4.4. $(Th,U)O_2$

Kernel migration in $(Th,U)O_2$ particles was observed in fuel rods from FTE-14 and some of the RTEs. In all cases the migration was less than 15 μm. The migration in each case was characterized by migration up the temperature gradient and by graphite deposits on the cool side of the kernel (see Fig. 8-15).

8.4.5. ThO_2

No ThO_2 kernel migration was observed in the Peach Bottom test elements.

8.4.6. ThC_2

ThC_2 kernel migration was observed in fuel rod 2-1-5 from FTE-15. The migration was accompanied by deposits of carbon behind the kernel (Fig. 8-15). No ThC_2 kernel migration was observed in any of the other 64 fuel rods (from 14 fuel elements) that were examined.

8.5. KERNEL MORPHOLOGY

The ThO_2 and ThC_2 kernels irradiated in the Peach Bottom test elements underwent little structural change because of their low burnups. Fission gas bubbles were observed in all of the fissile kernel types. UO_2 and UC_2 kernels irradiated at relatively low temperatures tended to have larger fission gas bubbles than UO_2 and UC_2 kernels irradiated at higher temperatures (Figs. 8-10, 8-12, and 8-16). UC_2 and $(Th,U)O_2$ kernels retained their shapes (Figs. 8-15 and 8-16), while UO_2 and $(Th,U)C_2$ kernels were observed to have undergone extensive deformation in some cases (Figs. 8-10 and 8-14). Some cracking was also observed in $(Th,U)C_2$ kernels (Fig. 8-14).

8.6. FISSION PRODUCT RELEASE

Fission gases and metallic fission products are released from fuel particles upon failure of the retentive coatings or by diffusive release through the coatings. Diffusive release from intact BISO fuel was evident in some of the Peach Bottom test elements and in the regular Peach Bottom fuel elements (Ref. 8-23).

Myers, et al. (Refs. 8-24 and 8-25), have done extensive work to establish the fractional release of fission gases from failed fuel particles. Only three of the examined fuel rods from the Peach Bottom test elements had high enough coating failure to allow the fractional release of Kr-85m to be determined: a rod from FTE-15 with high ThC_2 failure and two rods from FTE-6 with high UO_2 failure due to kernel migration. The fractional releases calculated for these three fuel rods are given in Table 8-11. The fractional release value for the fuel rod geometry given in Ref. 8-25 is 0.0053 ± 0.0027 (1σ). The values in Table 8-11 and the literature value are in good agreement.

An estimate of the loss of Cs-137 from failed TRISO particles was determined from the measured failure fractions and missing Cs-137 data (as determined using the method described in Section 4.1.4) for the two fuel rods from FTE-6 which had high UO_2 failure. The average Cs-137 loss per failure was 81%. This is consistent with the high Cs-137 loss per failure measured in fuel samples from P13R and P13S (Ref. 8-26). Diffusive release of Cs-137 from BISO particles is discussed in the report on the results of the Peach Bottom gamma scanning (Ref. 8-23).

8.7. FUEL ROD PERFORMANCE

The fuel rod performance was satisfactory in all of the Peach Bottom test elements. Some matrix cracking and particle debonding were observed, but these were minor. Figures 8-17 and 8-18 show representative

examples of fuel rods irradiated in the Peach Bottom test elements. Fuel rod dimensional changes are discussed in Section 6.

Isolated cases of unusual fuel rod performance are listed below:

1. Fuel rods from stacks 4 and 5 in FTE-15 had high fuel rod cracking because of low fuel rod matrix loadings (Ref. 8-6).

2. Gross fuel particle inhomogeneity in FTE-6 fuel rods caused the rods to bow. The disproportionate concentration of TRISO and BISO particles in different parts of the fuel rods caused regional differences in irradiation shrinkage (see Ref. 8-5).

3. The cured-in-place fuel rods in each of the eight fuel holes in body 3 of FTE-5 were found to be bonded together.

4. High OPyC failure of TRISO ThC_2 particles in FTE-15 fuel rods caused the fuel rod shrinkage to be less anisotropic than in companion fuel rods that had no OPyC failure.

8.8. FUEL PERFORMANCE SUMMARY

The examinations of 115 fuel rods and 59 loose particle samples from 17 Peach Bottom test elements increased the data base for OPyC and SiC coating performance, chemical attack of SiC coatings, kernel migration, kernel morphology, fission product release from failed fuel particles, and fuel rod performance. The results of the examinations are summarized below:

1. OPyC coatings on TRISO particles with preirradiation BAF values above 1.03 failed rapidly at fast fluences $>1.0 \times 10^{25}$ n/m^2 $[(E > 29 \text{ fJ})_{HTGR}]$ and time-averaged temperatures between 640° and

1530°C. OPyC coatings with BAF values below 1.03 were stable to fast fluences of approximately 3.0×10^{25} n/m^2 [$(E > 29\ fJ)_{HTGR}$].

2. OPyC coatings with high microporosity failed through interaction with the matrix phase. Crack initiation began at 1.5×10^{25} n/m^2 [$(E > 29\ fJ)_{HTGR}$], and 20% to 30% of the coatings failed completely at fast fluences $>2 \times 10^{25}$ n/m^2.

3. OPyC coatings on BISO particles performed well over the entire range of fast fluences experienced by the elements [$<4.2 \times 10^{25}$ n/m^2, $(E > 29\ fJ)_{HTGR}$].

4. UC_xO_y (WAR) particle batch OR1694 showed increasing OPyC coating failure with increasing coating volume, as is predicted by Weibull statistics.

5. Palladium and rare earth fission product attack on SiC coatings was observed in fuel from several of the test elements. Palladium attack, which was observed primarily in the PuO_2 fuel particles irradiated in FTE-13, was randomly oriented around the particles. Rare earth fission products attacked the SiC on the cooler side of the particles. Rare earth attack was observed primarily in UC_2 and UO_2 particles.

6. Iron contamination attacked both the OPyC and SiC coatings in some fuel particles. These particles were from fuel rods that did not undergo chlorine leach prior to irradiation.

7. No kernel migration was observed in any UC_2 or ThO_2 particles irradiated in the Peach Bottom test elements. Kernel migration distances up to 15 μm were observed in some ThC_2 and $(Th,U)O_2$ particles irradiated at time-averaged temperatures above ∿1250°C. Widespread kernel migration (or kernel dispersion) was observed in UO_2 and $(Th,U)C_2$ particles.

8. Kernel migration was generally overpredicted for UO_2, UC_2, $(Th,U)O_2$, ThO_2, and ThC_2 particles. The kernel migration in $(Th,U)C_2$ particles was underpredicted in a few cases.

9. Extensive kernel deformation accompanied by fission gas bubble formation was observed in UO_2 particles. The kernel deformation and fission gas bubble formation tended to be more severe in UO_2 particles irradiated at temperatures below $\sim$1250°C than at temperatures above $\sim$1250°C. Kernel deformation and cracking were observed in $(Th,U)C_2$ particles. No structural changes (other than fission gas bubble formation) were observed in UC_2, $(Th,U)O_2$, ThO_2, and ThC_2 particles.

10. The fractional release of Kr-85m from failed fuel in three test element fuel rods was measured and found to be in good agreement with the fractional release determined from previous experiments: 0.0053 ± 0.0027 (1σ). The Cs-137 release from failed UO_2 particles was also measured. The fractional release per failed particle was approximately 0.8.

11. The irradiation performance of the examined fuel rods was satisfactory.

REFERENCES

8-1. Harmon, D. P., and C. B. Scott, "Development and Irradiation Performance of LHTGR Fuel," ERDA Report GA-A13173, October 31, 1975.

8-2. Kaae, J. L., "Application of Weibull Statistics to the Strength of Pyrolytic Carbon," Report GA-A13869, March 1976.

8-3. Morissette, R. P., and K. P. Steward, "Recycle Test Element Program Design, Fabrication, and Assembly," Report GA-10109, September 1971.

8-4. Tiegs, T. L., and E. L. Long, Jr., "Postirradiation Examination of Recycle Test Elements from the Peach Bottom Reactor," Oak Ridge National Laboratory Report ORNL-5422, December 1978.

8-5. Wallroth, C. F., J. F. Holzgraf, and D. D. Jensen, "Postirradiation Examination and Evaluation of Peach Bottom Fuel Test Element FTE-6," ERDA Report GA-A13943, September 1977.

8-6. Holzgraf, J. E., et al., "Postirradiation Examination and Evaluation of Peach Bottom Fuel Test Elements FTE-14 and FTE-15," DOE Report GA-A13944, February 1979.

8-7. Smith, C. L., "SiC - Fission Product Reactions in TRISO UC_2 and WAR UC_xO_y Fissile Fuel," Report GA-A15313, September 1977.

8-8. "FSV MEU Program - Final Report," Report GA-A15216, July 1979.

8-9. Tiegs, T. N., "Postirradiation Examination of Plutonium-Containing Coated Particle Fuel in Peach Bottom Test Element FTE-13," Oak Ridge National Laboratory, unpublished data, September 15, 1978.

8-10. Young, C. A., and C. B. Scott, "Postirradiation Examination of Capsule P13Q," ERDA Report GA-A14174, September 1977.

8-11. Gulden, T. D., "Carbon Thermal Diffusion in the UC_2-C System," J. Am. Ceram. Soc. 55, 14 (1972).

8-12. Stansfield, O. M., C. B. Scott, and J. Chin, "Kernel Migration in Coated Carbide Fuel Particles," Nucl. Tech. 25, 517 (1975).

8-13. Lindemer, T. B., and R. L. Pearson, "Kernel Migration for LHTGR Fuels from the Th-U-C-O-N System," Oak Ridge National Laboratory Report TM-5207, April 1976.

8-14. Buescher, B. J., and R. D. Meyer, "Thermal Gradient Migration of Helium Bubbles in Uranium Dioxide," J. Nucl. Mater. 48, 143-156 (1973).

8-15. Turnbull, J. A., "The Distribution of Intragranular Fission Gas Bubbles in UO_2 during Irradiation," J. Nucl. Mater. 38, 203-212 (1971).

8-16. Baker, C., "The Migration of Intragranular Fission Gas Bubbles in Irradiated Uranium Dioxide," J. Nucl. Mater. 71, 117-123 (1977).

8-17. Speight, M. V., "A Calculation on the Size Distribution of Intragranular Bubbles in Irradiated UO_2," J. Nucl. Mater. 38, 236-238 (1971).

8-18. Turnbull, J. A., "The Mobility of Intragranular Bubbles in Uranium Dioxide during Irradiation," J. Nucl. Mater. 62, 325-328 (1976).

8-19. Dollins, C. C., "On Fission Gas Swelling Below ∿1200°C," J. Nucl. Mater. 60, 107-110 (1976).

8-20. Fulrath, R. M., and J. A. Pask, Ceramic Microstructures, John Wiley & Sons, New York, 1968.

8-21. Scott, C. B., and D. P. Harmon, "Postirradiation Examination of Capsule F-30," Report GA-13208, April 1, 1975.

8-22. Wichner, R. P., et al., "Distribution of Fission Products in Peach Bottom HTGR Fuel Element E11-07," Oak Ridge National Laboratory Report 5214, to be published.

8-23. Holzgraf, J. F., F. McCord, and C. F. Wallroth, "Gamma Spectroscopic Examination of Peach Bottom HTGR Core Components," DOE Report GA-A13453, April 1978.

8-24. Myers, B. F., et al., "The Behavior of Fission Product Gases in HTGR Fuel Material," DOE Report GA-A13723, October 1977.

8-25. Myers, B. F., and R. E. Morrissey, "The Measurement and Modeling of Postirradiation Fission Product Release from HTGR Fuel Particles Under Accident Conditions," DOE Report GA-A15018, December 1978.

8-26. Scott, C. B., D. P. Harmon, and J. F. Holzgraf, "Postirradiation Examination of Capsules P13R and P13S," ERDA Report GA-A13827, October 8, 1976.

TABLE 8-1
SUMMARY OF THE PIE PROGRAM FOR THE PEACH BOTTOM TEST ELEMENTS

Test Element	Irradiation Conditions: Time (EFPD)[a]	Time Avg. Max. Fuel Temp. (°C)	Max. Fissile FIMA (%)	Max. Fast Fluence, E > 29 fJ ($\times 10^{25}$ n/m^2)	Samples: Fuel Rod: Fission Gas Release[b]	Fuel Rod: Metallography	Loose Particles[c]	Test Purpose	Companion Accelerated Test
Fuel Test Elements									
FTE-1	252.4	1277	20.4	1.2	0	8[d]	9	BISO vs TRISO, OPyC properties	
FTE-2	385.4	1143	28.3	1.8	0	6[d]	6	BISO vs TRISO, OPyC properties	
FTE-3	133.1	1057	10.3	0.6	11	4	11	Demonstrate TRISO UC_2 and UO_2 fissile particles	P13L,P13M
FTE-4	448.8	1187	36.0	2.0	12	5	1	Demonstrate TRISO UC_2 and UO_2 fissile particles	P13L,P13M
FTE-5	897.3	1263	56.3	3.8	9	10	4	Demonstrate BISO and TRISO U fissile particles, cure-in-place vs cure-in-bed	P13K
FTE-6	644.9	1232	45.6	2.9	8	5	2	Demonstrate TRISO UC_2 and UO_2 fissile particles	P13L,P13M
FTE-13[e]					0	20	10	Demonstrate plutonium fuel	None
FTE-14	315.8	1414	24.6	1.5	10	5	8	Demonstration test of UC_2 (VSM), UC_xO_y (WAR), and ThO_2 BISO, Large HTGR fuel rods	P13N,P13P
FTE-15	511.9	1401	37.4	2.0	14	7	8		P13N,P13P
FTE-16	511.9	1236	40.0	2.3	23	5	0	Demonstration of FSV production fuel	F-30
Recycle Test Elements									
RTE-1[c]	644.9	1495	49.6	3.0	0	6	0	Reprocessing fuel source	
RTE-2[e,f]	701.2	1282	45.6	3.1	2	7	0		
RTE-4[e,f]	385.4	1303	32.2	1.9	2	3	0		
RTE-5[c]	897.3	1291	58.7	4.1	0	9	0		
RTE-6[c]	897.3	1259	59.8	4.2	0	7	0		
RTE-7[c]	252.4	1230	20.0	1.2	0	2	0		
RTE-8[c]	897.3	1297	60.1	4.2	0	6	0	Reprocessing fuel source	
Total					101	115	59		

(a) EFPD: effective full power days.
(b) Kr-85m at 1100°C in TRIGA.
(c) Spine samples.
(d) Loose bed.
(e) Examined at ORNL.
(f) Two fuel rods examined at GA.

TABLE 8-2
OPyC FAILURE IN BISO PARTICLES IRRADIATED IN PEACH BOTTOM FUEL TEST ELEMENTS

Fuel Rod/ Spine Sample Ident.(a)	Particle Ident.			OPyC Characteristics				Irradiation Conditions			OPyC Failure (% ± 2σ)	Remarks	Reference
	Batch No.	Particle Type	Diameter (μm)	Density (g/cm^3)	BAF	Coating Rate (μm/min)	Thickness (μm)	Fast Fluence, E > 29 fJ ($10^{25} n/m^2$)	Time Avg. Max Fuel Temp. (^oC)	Burnup FIMA (%)			
3-TS-5-1	4000-246	UC_2	315	1.84	NA(b)	NA	66	0.32	925	5.94	0 < 0 < 0.15		GA-A13004 or FTE-3
3-TS-5-2	4000-300	UC_2	346	1.85	NA	NA	74	0.32	925	5.94	0 < 0 < 0.11		Data Package
3-TS-5-6	4503-59	UO_2	472	1.83	NA	NA	70	0.32	925	5.94	0 < 0 < 0.20		
3-TS-11-6	4503-53	$(Th,U)O_2$	788	1.64	NA	NA	124	0.31	915	2.87	0 < 0 < 0.99		
3-TS-17-6	4493-149	ThO_2	607	1.85	NA	NA	70	0.37	952	0.02	0 < 0 < 0.35		
3-TS-23-1	4423-33	$(Th,U)C_2$	NA	NA	NA	NA	NA	0.36	944	3.19	0 < 0 < 0.69		GA-A13004 or FTE-3
3-TS-23-2	4423-35	$(Th,U)C_2$	NA	NA	NA	NA	NA	0.36	944	3.19	0 < 0 < 0.90		Data Package
4-2-1-7	4000-339	ThO_2	690	1.78	1.027	NA	81	1.97	1174	0.69	0 < 0 < 9.2		GA-A13452 and FTE-4
4-2-2-7	4000-339	ThO_2	690	1.78	1.027	NA	81	1.97	1174	0.69	0 < 0 < 2.0		Data Package
4-2-3-8	4000-345	ThO_2	629	1.81	1.043	NA	69	1.96	1169	0.68	0 < 0 < 2.2		GA-A13452 and FTE-4
4-2-8-7	4000-345	ThO_2	629	1.81	1.043	NA	69	1.97	1163	0.69	0.4 < 1.2 < 3.5	Production failures	Data Package
6-2-1-7	4000-339	ThO_2	690	1.78	1.027	NA	81	2.88	1210	1.54	0.1 < 0.4 < 2.1		FTE-6 Data Package
6-2-2-7	4000-339	ThO_2	690	1.78	1.027	NA	81	2.88	1210	1.54	0.0 < 0.0 < 1.8		
6-2-3-7	4000-345	ThC_2	629	1.81	1.043	NA	69	2.88	1191	1.54	0.0 < 0.0 < 5.7		
6-2-8-7	4000-345	ThC_2	629	1.81	1.043	NA	69	2.88	1195	1.54	0.0 < 0.0 < 2.2		FTE-6 Data Package
5-1-5-3	4000-225-009	ThC_2	580	1.88	1.025	NA	66	1.66	699	0.59	0.1 < 0.5 < 2.8		FTE-5 Data Package
5-2-1-7	4000-225-009	ThC_2	580	1.88	1.025	NA	66	3.78	1195	2.27	0.0 < 0.0 < 0.9		
5-2-1-2	4000-225-009	ThC_2	580	1.88	1.025	NA	66	3.74	1111	2.25	0.2 < 0.7 < 2.7	Production failures	
5-2-3-7	4000-225-009	ThC_2	580	1.88	1.025	NA	66	3.78	1299	2.27	0.0 < 0.0 < 1.9		
5-2-5-7	4000-225-009	ThC_2	580	1.88	1.025	NA	66	3.78	1165	2.27	0.2 < 0.8 < 2.8	Production failures	
5-3-1-2	4000-225-009	ThC_2	580	1.88	1.025	NA	66	3.27	1154	1.70	0.1 < 0.4 < 2.0	Production failures	
5-3-3-2	4000-225-009	ThC_2	580	1.88	1.025	NA	66	3.27	1192	1.70	0.2 < 0.9 < 3.2	Production failures	
5-3-5-2	4000-225-009	ThC_2	580	1.88	1.025	NA	66	3.27	1150	1.70	0.3 < 2.1 < 8.9	Production failures	FTE-5 Data Package
14-TS-6-1	4252-01-070	ThO_2	765	2.02	1.046	1.58	72.0	1.42	1325	0.25	0.0 < 0.0 < 9.0		FTE-14 Data Package
14-2-1-7	4251-00-031	ThC_2	711	2.00	1.041	2.49	93.0	1.44	1347	0.35	0.0 < 0.0 < 1.8		
14-2-3-6	4252-00-011	ThO_2	714	2.00	1.041	2.40	70.0	1.45	1383	0.36	0.0 < 0.0 < 1.4		
14-2-4-7	4251-01-021	ThC_2	721	1.96	1.038	3.20	64.0	1.44	1323	0.35	0.0 < 0.0 < 3.1		FTE-14 Data Package
15-TS-6-1	4252-01-070	ThO_2	765	2.02	1.046	1.58	72.0	2.02	1303	0.86	0.0 < 0.0 < 10.7		FTE-15 Data Package
15-2-1-5	4251-00-031	ThO_2	711	2.00	1.041	2.49	93.0	2.01	1386	1.02	0.0 < 0.0 < 1.6		
15-2-3-9	4252-00-011	ThO_2	714	2.00	1.041	2.40	70.0	2.02	1264	0.93	0.0 < 0.0 < 1.6		
15-2-4-3	4251-01-021	ThC_2	721	1.96	1.038	3.20	64.0	1.98	1239	1.01	4.7 < 8.3 < 14.2	Carbide hydrolysis during examination	
15-2-5-2	4251-01-021	ThC_2	721	1.96	1.038	3.20	64.0	1.96	1253	1.00	0.5 < 1.6 < 4.4	Production failures	FTE-15 Data Package

(a) 4-2-1-7: FTE-4 - body 2 - hole 1 - rod 7.
3-TS-5-1: FTE-3 - thermal stability - type 5 - location 1.

(b) NA: not available.

TABLE 8-3

OPyC FAILURE IN BISO PARTICLES IRRADIATED IN PEACH BOTTOM RECYCLE AND FUEL TEST ELEMENTS

Fuel Rod/ Spine Sample Ident.[a]	Particle Ident.			OPyC Characteristics				Irradiation Conditions[b]			OPyC Failure (% ± 2σ)	Irradiation Configuration
	Batch No.	Particle Type	Particle Diameter (μm)	Density (g/cm^3)	BAE_0	Coating Rate (μm/min)	Thickness (μm)	Fast Fluence, E > 29 fJ (10^{25} n/m²)	Time Avg. Max Fuel Temp. (°C)	Burnup FIMA (%)		
Recycle Test Elements												
4-4-1-3	4000-226	ThC_2	614	1.88	1.019	NA[c]	71.0	1.802	1303	0.49	0	Fuel rod
4-1-1-3	4000-309	UC_2	340	1.84	1.008	NA	74.0	1.024	789	16.72	0	↓
4-1-1-3	4000-226	ThC_2	614	1.88	1.019	NA	71.0	1.024	789	0.11	0	
4-5-1-3	PR-61	$(2Th,U)O_2$	754.2	1.91	NA	6.983	122.2	1.471	1267	8.43	0	
4-5-1-3	4000-225	ThC_2	580	1.88	1.025	NA	66.0	1.471	1267	0.30	0	
2-2-1-2	PR-66	$(2Th,U)O_2$	793.5	1.86	NA	7.349	128.6	2.688	1098	14.70	0	
2-2-1-6	PR-66	$(2Th,U)O_2$	793.5	1.86	NA	7.349	128.6	3.029	1145	15.92	0	
2-2-1-2	9T-980-BL	ThC_2	NA	NA	NA	NA	NA	2.688	1098	1.27	0	
2-2-1-6	9T-980-BL	ThC_2	NA	NA	NA	NA	NA	3.029	1145	1.62	0	
2-4-1-1	4000-309	UC_2	340	1.84	1.008	NA	74.0	3.065	1223	44.45	0	
2-4-1-1	4000-226	ThC_2	614	1.88	1.019	NA	71.0	3.065	1223	1.63	0	
2-6-1-1	4000-226	ThC_2	614	1.88	1.019	NA	71.0	1.980	1077	0.63	0	
2-2-5-1	PR-66	$(2Th,U)O_2$	793.5	1.86	NA	7.349	128.6	2.545	1021	8.92	0	
2-2-5-1	9T-980-BL	ThC_2	NA	NA	NA	NA	NA	2.545	1021	1.12	0	
2-2-1-1	PR-66	$(2Th,U)O_2$	793.5	1.86	NA	7.349	128.6	2.545	1021	8.92	0	
2-2-1-1	9T-980-BL	ThC_2	NA	NA	NA	NA	NA	2.545	1021	1.12	0	
2-3-1-1	4000-225	ThC_2	580	1.88	1.025	NA	66.0	3.071	1069	1.67	0	
5-3-1-6	PR-57-1	$(4Th,U)O_2$	783.5	1.92	NA	7.736	134.6	4.125	1117	13.81	0	
5-3-1-6	4000-226	ThC_2	614	1.88	1.019	NA	71.0	4.125	1117	2.70	0	
5-3-3-6	PR-61	$(2Th,U)O_2$	754.2	1.91	NA	6.983	122.2	4.125	1164	21.22	0	
5-3-3-6	PR-51	ThO_2	633.3	1.91	NA	7.505	69.8	4.125	1164	2.70	0	
5-3-5-6	4000-226	ThC_2	614	1.88	1.019	NA	71.0	4.125	1085	2.70	0	
5-3-7-6	Mixed 1	UO_2	213	1.89	NA	35.294	60.0	4.125	1171	58.26	0	
5-3-7-6	PR-48	ThO_2	645.2	1.94	NA	6.688	62.2	4.125	1171	2.70	0	
5-5-1-1	4000-274	UO_2	371.0	NA	<1.027	NA	60.0	3.720	1146	53.72	0	
5-5-1-1	4000-225	ThC_2	580	1.88	1.025	NA	66.0	3.720	1146	2.14	0	
5-5-3-1	4000-309	UC_2	340	1.84	1.008	NA	74.0	3.720	1128	53.72	0	
5-5-3-1	4000-226	ThC_2	614	1.88	1.019	NA	71.0	3.720	1128	2.14	0	
5-5-5-1	4000-309	UC_2	340	1.84	1.008	NA	74.0	3.720	1137	53.72	0	
5-5-5-1	4000-273 (PR-47)	ThO_2	670.0	1.94	<1.027	7.867	75.0	3.720	1137	2.14	0	
5-5-7-1	PR-60	$(2Th,U)O_2$	751.0	1.91	NA	7.247	123.2	3.720	1177	19.33	0	
5-5-7-1	4000-225	ThC_2	580	1.88	1.025	NA	66.0	3.720	1177	2.14	0	
6-1-1-5	4000-309	UC_2	340	1.84	1.008	NA	74.0	2.965	866	46.84	0	
6-1-1-6	4000-309	UC_2	340	1.84	1.008	NA	74.0	3.222	883	50.76	0	
6-2-7-6	4000-226	ThC_2	614	1.88	1.019	NA	71.0	4.043	1054	2.85	0	
6-4-1-1	4000-226	ThC_2	614	1.88	1.019	NA	71.0	4.134	1145	2.96	0	
6-5-5-2	4000-226	ThC_2	614	1.88	1.019	NA	71.0	3.829	1177	2.23	0	
4-3-BB	PR-54	$(4Th,U)O_2$	656.3	1.94	NA	7.176	73.2	1.909	1185	11.01	0	
4-3-BB	9T-980-BL	ThC_2	NA	NA	NA	NA	NA	1.909	1185	0.58	0	
6-6-1-1	Mixed 1	UO_2	213	1.89	NA	35.294	60	2.912	1114	43.94	0	
6-6-1-1	PR-48	ThO_2	645.2	1.94	NA	6.688	62.2	2.912	1114	1.31	0	
8-6-7-1	4000-226	ThC_2	614	1.88	1.019	NA	71.0	2.959	1073	1.34	0	
8-3-1-6	4000-309	UC_2	340	1.84	1.008	NA	74.0	4.217	1127	59.63	0	
8-3-1-6	4000-226	ThC_2	614	1.88	1.019	NA	71.0	4.217	1127	3.08	0	
8-4-1-6	PR-60	$(2Th,U)O_2$	751.0	1.91	NA	7.247	123.2	3.904	1221	20.39	0	
8-4-1-5	4000-225	ThC_2	580	1.88	1.025	NA	66.0	3.976	1276	2.68	0	
1-4-1-6	PR-56	$(4Th,U)O_2$	772.5	1.91	NA	7.420	129.1	2.875	1237	10.46	0	
1-4-1-6	4000-226	ThC_2	614	1.88	1.019	NA	71.0	2.875	1237	1.50	0	
1-3-6-6	4000-323	ThC_2	597	1.85	1.030	67.0	NA	3.031	1337	1.78	0	
1-4-3-6	PR-67	$(2Th,U)O_2$	805.8	1.85	NA	10.065	141.1	2.875	1327	10.46	0	
1-4-3-6	Mixed A	ThO_2	NA	1.99	NA	NA	60-74	2.875	1327	1.50	0	
1-4-8-6	Mixed 1	UO_2	213	1.89	NA	35.294	60	2.875	1378	46.29	0	
1-4-8-6	Mixed A	ThO_2	NA	1.99	NA	NA	60-74	2.875	1378	1.50	0	
1-5-8-1	4000-355	UO_2	481	1.80	1.22	NA	37.0	2.812	1331	45.47	0	
1-5-3-1	4000-340	UC_2	331	1.78	1.041	NA	73.0	2.812	1292	45.47	0	
1-5-3-1	4000-339	ThO_2	696	1.78	1.027	NA	81.0	2.812	1292	1.42	0	Fuel rod
Fuel Test Elements												
1-1-1-BB	4000-244	$(2Th,U)C_2$	435	1.79	NA	NA	72.0	0.863	950	5.18	0 < 0 < 0.84	Loose bed
1-1-1-BB	4000-225	ThC_2	580	1.88	1.025	NA	66.0	0.863	950	0.09	0 < 0 < 1.6	↓
1-2-1-BB	4000-246	UC_2	315	1.84	NA	NA	66.0	1.105	1239	19.48	0 < 0 < 0.2	
1-2-1-BB	4000-237	ThC_2	626	1.79	NA	NA	72.0	1.105	1239	0.15	0 < 0 < 0.44	
1-2-2-BB	4000-246	UC_2	315	1.84	NA	NA	66.0	1.105	1239	19.48	0 < 0 < 0.2	
1-2-2-BB	4000-237	ThC_2	626	1.79	NA	NA	72.0	1.105	1239	0.15	0 < 0 < 0.44	
1-2-5-BB	4000-247	UC_2	303	1.60	NA	NA	60.0	1.105	1244	19.48	0.01 < 0.07 < 0.29	
1-2-5-BB	4000-308	ThC_2	668	1.57	NA	NA	88.0	1.105	1244	0.15	0.0 < 0.0 < 0.58	
1-2-5-BB	4000-247	UC_2	303	1.60	NA	NA	60.0	1.105	1244	19.48	0.0 < 0.0 < 0.27	
1-2-5-BB	4000-308	ThC_2	668	1.57	NA	NA	88.0	1.105	1244	0.15	0.0 < 0.0 < 0.58	
1-3-1-BB	4000-229	$(2Th,U)C_2$	428	1.84	NA	NA	66.0	0.679	1130	4.37	0.0 < 0.0 < 0.71	
1-3-1-BB	4000-237	ThC_2	626	1.79	NA	NA	72.0	0.679	1130	0.05	0.0 < 0.0 < 0.36	
1-3-5-BB	4000-239	$(2Th,U)C_2$	401	1.58	NA	NA	59.0	0.679	1131	4.37	0.0 < 0.0 < 0.71	↓
1-3-5-BB	4000-308	ThC_2	668	1.57	NA	NA	88.0	0.679	1131	0.05	0.0 < 0.0 < 0.36	Loose bed
1-TS-2-6	4503-59E	UO_2	472	1.83	NA	NA	70.0	1.050	1262	18.54	0.0 < 0.0 < 0.24	Spine sample
1-TS-14-1	4000-238	ThC_2	618	1.84	NA	NA	70.0	1.093	1270	0.14	0.0 < 0.0 < 0.33	↓
1-TS-14-2	4000-225	ThC_2	580	1.88	1.025	NA	66.0	1.093	1270	0.14	0.0 < 0.0 < 0.29	
1-TS-14-6	4493-149	ThO_2	607	1.85	NA	NA	70.0	1.093	1270	0.14	0.0 < 0.0 < 0.35	
1-TS-20-1	4423-33	$(4Th,U)C_2$	NA	NA	NA	NA	NA	1.079	1269	3.91	0.0 < 0.0 < 0.74	↓
1-TS-20-2	4423-35	$(4Th,U)C_2$	NA	NA	NA	NA	NA	1.079	1269	3.91	0.0 < 0.0 < 0.73	Spine sample
2-1-1-BB	4000-244	$(2Th,U)C_2$	435	1.79	NA	NA	72.0	1.318	853	7.28	0.0 < 0.0 < 0.31	Loose bed
2-1-1-BB	4000-225	ThC_2	580	1.88	1.025	NA	66.0	1.318	853	0.23	0.0 < 0.0 < 0.22	↓
2-2-1-BB	4000-246	UC_2	315	1.84	NA	NA	66.0	1.691	1102	26.89	0.0 < 0.0 < 0.80	
2-2-1-BB	4000-237	ThC_2	626	1.79	NA	NA	72.0	1.691	1102	0.37	0.0 < 0.0 < 0.24	
2-2-5-BB	4000-247	UC_2	303	1.60	NA	NA	60.0	1.691	1104	26.89	0.0 < 0.0 < 0.80	
2-2-5-BB	4000-308	ThC_2	668	1.57	NA	NA	88.0	1.691	1104	0.37	0.0 < 0.0 < 0.24	
2-3-1-BB	4000-229	$(2Th,U)C_2$	428	1.84	NA	NA	66.0	1.039	1021	6.03	0.0 < 0.0 < 0.41	
2-3-1-BB	4000-327	ThC_2	630	1.80	1.22	NA	70.0	1.039	1021	0.12	0.0 < 0.0 < 0.29	
2-3-5-BB	4000-230	$(2Th,U)C_2$	418	1.60	NA	NA	63.0	1.039	1023	6.03		↓
2-3-5-BB	4000-330	ThC_2	624	1.84	1.027	NA	69.0	1.039	1023	0.12		Loose bed
2-TS-19-1	4423-33	$(4Th,U)C_2$	NA	NA	NA	NA	NA	1.654	1136	5.51	0.0 < 0.0 < 0.74	Spine sample
2-TS-19-2	4423-35	$(4Th,U)C_2$	NA	NA	NA	NA	NA	1.654	1136	5.51	0.0 < 0.0 < 0.68	Spine sample

(a) 4-4-1-3: FTE(RTE)-4 - body 4 - hole 1 - rod 3.
1-TS-2-6: FTE-1 - thermal stability - type 2 - location 6.
2-1-1-BB: FTE-2 - body 1 - hole 1 - blended bed.

(b) Only three digits are significant.

(c) NA = not available.

TABLE 8-4

OPyC FAILURE OF TRISO PARTICLES FROM LOOSE PARTICLE SAMPLES IRRADIATED IN PEACH BOTTOM TEST ELEMENTS

Spine Sample Ident.(a)	Particle Ident.			OPyC Properties				Irradiation Conditions			OPyC Failure	
	Batch No.	Particle Type (μm)	Particle Diameter (μm)	Density (kg/m^3)	BAF_o	Coating Rate (μm/min)	Thickness (μm)	Fast Fluence, E > 29 fJ (10^{25} n/m^2)	Time Avg. Max. Fuel Temp. (°C)	Burnup FIMA (%)	Stereo $C_{0.05} < \bar{x} < C_{0.95}$ (%)	Metallography $C_{0.05} < \bar{x} < C_{0.95}$ (%)
3-TS-5-1	4000-302	UC_2	344	1.71	1.014	NA(b)	36	0.32	925	5.94	0 < 0 < 0.15	NA
3-TS-11-6	4505-53	$(Th,U)O_2$	NA	NA	NA	NA	NA	0.31	915	2.87	0 < 0 < 0.99	NA
3-TS-23-3	4423-41	$(Th,U)C_2$	NA	NA	NA	5.5	33	0.36	944	3.19	0 < 0 < 1.04	NA
3-TS-23-4	4423-53	$(Th,U)C_2$	NA	NA	NA	9.33	28	0.36	944	3.19	0 < 0 < 0.7	NA
3-TS-29-6	4413-67	UO_2	344	1.75	1.011	6.77	22	0.34	935	6.14	0 < 0 < 0.54	NA
4-TS-4-5	4000-302	UC_2	344	1.71	1.016	NA	36	1.19	1051	22.55	0	NA
6-TS-18-3	4000-242	ThC_2	650	1.71	1.014	NA	42	2.08	1152	0.73	0	0 < 0 < 5.7
6-TS-6-5	4000-302	UC_2	344	1.71	1.016	NA	36	1.87	1115	31.42	0	0 < 0 < 2.0
5-TS-15-3	4000-242	ThC_2	650	1.71	1.014	NA	42	3.70	∿1100	2.13	0	0 < 2.5 < 9.1
5-TS-3-5	4000-302	UC_2	344	1.71	1.016	NA	36	3.63	∿1219	53.42	0.1	0 < 0 < 5.5
5-TS-27-4	4423-3	UC_2	NA	NA	NA	NA	NA	3.66	∿1100	53.89	6.6	5.4 < 9.2 < 15.4
5-TS-27-5	4413-137	UC_2	NA	NA	NA	NA	NA	3.66	∿1100	53.89	0	0 < 0 < 3.3
14-TS-1-4	4161-01-020	UC_2	524	1.80	1.033	3.53	38	1.26	1282	21.76		0 < 0 < 4.2
14-TS-3-6	4161-01-030	UC_2	↓	↓	↓	↓	↓	1.31	1095	22.43	0	0 < 0 < 4.5
14-TS-5-6	4161-01-030	UC_2	↓	↓	↓	↓	↓	1.44	1418	24.13	0	0 < 0 < 4.2
14-TS-4-6	4161-01-030	UC_2	↓	↓	↓	↓	↓	1.45	1364	24.59	0	0 < 0 < 22
14-TS-8-3	4161-01-030	UC_2	524	1.80	1.033	3.53	38	1.20	1534	19.82	0	0 < 0 < 4.5
15-TS-1-4	4161-01-020	UC_2	524	1.80	1.033	3.53	38	1.73	1294	33.55	0	0 < 0 < 4.0
15-TS-8-2	4161-01-020	UC_2	↓	↓	↓	↓	↓	1.87	1468	31.88	0	0 < 0 < 4.7
15-TS-3-6	4161-01-030	UC_2	↓	↓	↓	↓	↓	1.80	1086	34.54	0	1.0 < 5.7 < 16.0
15-TS-4-6	4161-01-030	UC_2	↓	↓	↓	↓	↓	1.99	1355	37.34	0	0.3 < 4.8 < 16.6
15-TS-5-6	4161-01-030	UC_2	524	1.80	1.033	3.53	38	2.02	1338	36.96	0	0 < 0 < 7.9
1-1-8-BB	4000-245	$(2Th,U)C_2$	459	1.74	1.016	NA	39	0.5	639	2.88	0 < 0 < 0.46	NA
1-1-8-BB	4000-306	ThC_2	656	1.78	1.016	NA	42	0.5	639	0.02	0 < 0 < 0.54	NA
1-TS-14-3	4000-242	ThC_2	662	1.70	1.014	NA	42	1.1	∿1100	0.17	0.0 < 0.0 < 0.38	NA
1-TS-14-5	4503-25	ThC_2	632	1.84	NA	NA	39	1.1	∿1100	0.17	0.0 < 0.0 < 0.34	NA
1-TS-26-6	4413-67	UO_2	340	1.75	1.006	NA	22	1.1	∿1100	20.0	0.0 < 0.0 < 0.7	NA
2-1-5-BB	4000-245	$(2Th,U)C_2$	459	1.74	1.016	NA	39	0.8	591	4.06	0.0 < 0.0 < 0.26	NA
2-1-5-BB	4000-306	ThC_2	656	1.78	1.016	NA	42	0.8	591	0.05	0.0 < 0.0 < 0.25	NA
2-TS-19-5	4000-211	$(1.8Th,U)C_2$	485	1.77	1.011	NA	39	1.7	∿1030	10.11	0.0 < 0.0 < 0.98	NA
2-TS-19-6	4000-220	$(3Th,U)C_2$	456	1.86	1.035	NA	39	1.7	∿1030	7.20	0.0 < 0.0 < 0.40	NA
2-TS-25-3	3592-35	$(2Th,U)C_2$	310	2.00	NA	NA	10	1.7	∿1030	9.46	0.1 < 0.2 < 0.8	NA
2-TS-25-4	4423-3	UC_2	NA	1.92	1.006	NA	NA	1.7	∿1030	22.61	0.7 < 1.5 < 3.32	NA

(a) 3-TS-5-1: FTE-3 - thermal stability - type 5 - location 1
2-1-5-BB: FTE-2 - body 1 - hole 5 - blended bed

(b) NA = not available.

TABLE 8-5

OPyC FAILURE OF TRISO PARTICLES FROM PEACH BOTTOM FUEL RODS

Fuel Rod Ident.(a)	Particle Ident.			OPyC Characteristics				Irradiation Conditions			OPyC Failure $C_{0.05} < \bar{x} < C_{0.95}$ (%)	Comments
	Batch No.	Particle Type	Particle Diameter (μm)	Density (kg/m³)	BAF_o	Coating Rate (μm/min)	Thickness (μm)	Fast Fluence, E > 29 fJ (10^{25} n/m²)	Time Avg. Max Fuel Temp. (°C)	Burnup FIMA (%)		
Fuel Test Elements												
3-2-2-7	4000-355	UO_2	481	1.8	1.022	13.04	37	0.56	1054	10.1	- < 0.0 < -	
4-2-1-7	4000-355	UO_2	481	1.8	1.022	13.04	37	1.97	1174	35.7	0.0 < 0.0 < 8.3	
4-2-2-7	4000-355	UO_2	481	1.8	1.022	13.04	37	1.97	1174	35.7	0.1 < 0.6 < 4.1	
4-2-3-8	4000-357	$(Th,U)C_2$	509	1.8	1.019	NA(b)	44	1.96	1163	18.0	0.0 < 0.1 < 0.9	
4-2-5-7	4000-357	$(Th,U)C_2$	509	1.8	1.019	NA	44	1.97	1150	18.2	2.4 < 5.0 < 10.0	
4-2-5-7	4000-335	ThC_2	663	1.79	1.038	NA	41	1.97	1150	0.7	2.0 < 4.0 < 8.0	
4-2-8-7	4000-358	UC_2	382	1.79	1.033	NA	33	1.97	1163	35.7	0.1 < 0.7 < 1.6	
6-2-1-7	4000-355	UO_2	481	1.8	1.022	13.04	37	2.88	1210	45.4	16.1 < 22.8 < 3.3	UO_2 amoeba failure
6-2-2-7	4000-355	UO_2	481	1.8	1.022	13.04	37	2.88	1210	45.4	8.5 < 13.2 < 20.0	UO_2 amoeba failure
6-2-3-7	4000-357	$(Th,U)C_2$	509	1.8	1.019	NA	44	2.88	1192	10.1	0.3 < 0.7 < 1.7	
6-2-6-7	4000-357	$(Th,U)C_2$	509	1.8	1.019	NA	44	2.88	1186	10.1	0.7 < 1.4 < 2.7	
6-2-6-7	4000-335	ThC_2	663	1.79	1.038	NA	41	2.88	1186	1.5	2.5 < 8.7 < 21.0	
6-2-8-7	4000-358	UC_2	382	1.79	1.033	NA	33	2.88	1195	45.4	0.8 < 1.7 < 2.2	
5-1-5-3	4000-307	UC_2	347	1.73	1.011	NA	32	1.90	699	30.0	2.1 < 3.8 < 6.8	
5-2-5-7	4000-307	UC_2	347	1.73	1.011	NA	32	3.74	1165	55.7	19.0 < 23.6 < 28.9	
5-2-7-7	4000-245	$(Th,U)C_2$	450	1.69-1.82	1.041	NA	38-44	3.74	1174	29.0	12.9 < 18.0 < 24.7	Composite batch
5-2-7-7	4000-306	ThC_2	644	1.71-1.83	1.046	NA	38-44	3.74	1174	55.7	12.0 < 15.2 < 19.2	Composite batch
5-3-5-2	4000-307	UC_2	347	1.73	1.027	NA	32	3.68	1050	50.5	32.0 < 34.7 < 36	
5-3-7-2	4000-247	$(Th,U)C_2$	450	1.69-1.82	1.041	NA	38-44	3.68	1147	26.1	12.5 < 16.2 < 20.8	Composite batch
5-3-7-2	4000-306	ThC_2	644	1.71-1.83	1.046	NA	38-44	3.68	1147	1.7	8.2 < 12.8 < 19.3	Composite batch
14-2-1-7	4161-01-031	UC_2	524	1.80	1.033	3.53	38	1.44	1347	24.0	0.0 < 1.4 < 7.5	
14-2-2-6	4161-01-031	UC_2	524	1.80	1.033	3.53	38	1.45	1354	24.3	0.8 < 2.4 < 6.7	
14-2-3-6	4162-00-031	UO_2	550	1.83	1.022	3.89	37	1.45	1383	24.3	0.7 < 2.0 < 6.1	
14-2-4-7	4163-00-011	$(Th,U)O_2$	686	1.79	1.027	4.11	72	1.44	1323	12.2	1.0 < 3.0 < 8.4	
14-2-6-7	4162-00-031	UO_2	550	1.83	1.022	3.89	37	1.44	1340	24.0	0.5 < 2.0 < 6.9	
14-2-6-7	4262-00-051	ThO_2	676	1.81	1.025	7.69	25	1.44	1340	0.4	0.0 < 0.0 < 4.1	
15-2-1-5	4161-01-031	UC_2	524	1.80	1.033	3.53	38	2.01	1386	37.4	0.0 < 1.6 < 8.6	
15-2-2-5	4161-01-031	UC_2	524	1.80	1.033	3.53	38	2.01	1367	37.4	0.1 < 4.4 < 12.1	
15-2-2-5	4261-00-011	ThC_2	628	1.81	1.041	2.87	38	2.01	1367	1.0	32.0 < 47.9 < 68.0	
15-2-3-9	4162-01-031	UO_2	550	1.83	1.022	3.89	37	2.02	1264	36.2	0.0 < 1.8 < 10.1	
15-2-4-3	4163-00-011	$(Th,U)O_2$	686	1.79	1.027	4.11	72	1.98	1239	19.1	0.4 < 1.6 < 5.6	
15-2-5-2	4162-01-021	UO_2	396	1.86	1.027	2.98	25	1.96	1253	37.0	21.3 < 27.9 < 35.6	Unloading damage
15-2-6-5	4162-01-031	UO_2	550	1.83	1.022	3.89	37	2.01	1366	37.4	0.0 < 0.0 < 4.3	
15-2-6-5	4262-00-051	ThO_2	676	1.81	1.025	7.69	25	2.01	1366	1.0	0.4 < 1.3 < 3.8	
15-3-6-10		UO_2	550	1.83	1.022	3.89	37	1.04	1118	21.7	10.0 < 20 < 34.5	Unloading damage
15-3-6-10	4261-01-011	ThC_2	628	1.81	1.041	2.87	38	1.04	1118	0.2	5.9 < 9.9 < 16.2	
16-3-5-4	FT-1378-BILSL-1W	$(Th,U)C_2$	489	1.79	1.022	NA	45	2.60	1098	17.5	0 < 0 < 5	
16-3-5-4	CT6A-2399	ThC_2	373	1.80	1.054	NA	43	2.00	1098	0.7	38 < 44.6 < 60.0	
Recycle Test Elements												
7-3-7-3	4000-307	UC_2	347	1.73	1.011	NA	32	1.2	1168	20.9	ND(c)	Cracks in OPyC from matrix interaction
7-5-5-5	4000-307	UC_2	347	1.73	1.011	NA	32	0.8	1097	13.7	0	
7-3-7-3	4000-306	ThC_2	644	1.71-1.83	1.046	NA	38-44	1.2	1179	0.2	ND	Cracks in OPyC from matrix interaction
7-5-5-5	4000-306	ThC_2	644	1.71-1.83	1.046	NA	38-34	0.8	1097	0.1	0	
4-4-7-3	4000-307	UC_2	347	1.73	1.011	NA	32	1.8	1303	29.8	0 < 0 < 2.0	
4-4-1-3	4000-307	UC_2	347	1.73	1.011	NA	32	1.8	1303	29.8	0.4 < 1.0 < 2.2	10% particles had matrix interactions
2-6-1-3	4000-307	UC_2	347	1.73	1.011	NA	32	1.6	1078	28.0	1.4 < 2.7 < 5.0	
2-6-1-1	4000-307	UC_2	347	1.73	1.011	NA	32	2.0	1077	31.4	1.9 < 3.2 < 5.4	25% coatings had matrix interaction
2-3-1-1	4000-307	UC_2	347	1.73	1.011	NA	32	3.0	1069	45.0	0	Blended bed, no matrix
5-3-5-7	4000-307	UC_2	347	1.73	1.011	NA	32	4.1	1085	58.2	~5%	
5-6-7-1	4000-307	UC_2	347	1.73	1.011	NA	32	2.8	1064	43.3	~20%	
5-6-7-1	4000-306	ThC_2	644	1.71-1.83	1.046	NA	38-44	2.8	1064	1.2	~25%	
8-2-7-7	4000-306	ThC_2	644	1.71-1.83	1.046	NA	38-44	4.0	1020	2.9	~50%	
1-3-6-6	4000-325	UC_2	331	1.71	1.033	NA	27	3.0	1337	49.4	0	
1-5-8-1	4000-355	UO_2	481	1.8	1.022	13.04	37	2.8	1331	45.5	0	

(a) 3-2-2-7: FTE(RTF)-3 - body 2 - hole 2 - rod 7.
(b) NA = not available.
(c) ND = not determined.

TABLE 8-6
SUMMARY OF SiC ATTACK BY PALLADIUM IN FTE-13

Fuel Rod Ident.[a]	Photo Ident.	Total Particle Photo Ident.	Particle Identification		Distance from Rod Center (μm)	Mean Core Height (mm)	Max. SiC Attack (μm)	Fast Fluence, E > 29 fJ (10^{25} n/m^2)	Linear[b] Time Average Temperature		Burnup FIMA (%)	SiC Thinning Rate (x 10^{-4} μm/h)
			Type	Item					K	± RMS (K)		
2-2-2	R71649	R71647	PuO_2	6	2800	1528	2.0	2.22	1414	98	(c)	1.6
2-2-6	R71656	R71654	PuO_2	6	1200	1725	3.0	2.26	1533	107		2.4
2-2-6	R71659	R71657	PuO_2	6	Rod center	1725	23.0	2.26	1579	121		18.7
2-2-9	R71639	R71637	PuO_2	6	950	1873	10.5	2.26	1391	92		8.5
2-2-12	R71624	R71622	PuO_2	6	1800	2021	3.0	2.22	1322	82		2.4
2-2-12	R71620	Same	PuO_2	6	On o.d.	2021	18.0	2.22	1322	82		14.7
2-2-12	R71631	R71628	PuO_2	6	1000	2021	23.5	2.22	1322	82		19.1
2-5-3	R71677	Same	PuO_{2-x}	1	900	1577	2.0	2.24	1408	102		1.6
2-5-3	R71675	Same	PuO_{2-x}	1	1500	1577	4.0	2.24	1408	102		3.3
2-5-6	R71707	Same	PuO_{2-x}	1	On o.d.	1725	2.0	2.26	1506	110		1.6
2-5-6	R71703	Same	PuO_{2-x}	1	3000	1725	6.0	2.26	1506	110		4.9
2-5-9	R71715	Same	PuO_{2-x}	1	2300	1873	2.0	2.26	1366	92		1.6
2-5-9	R71713	Same	PuO_{2-x}	1	2100	1873	2.0	2.26	1366	92		1.6
2-5-9	R71711	Same	PuO_{2-x}	1	Rod center	1873	4.0	2.26	1408	103		3.3
2-5-12	R71690	Same	PuO_{2-x}	1	1200	2021	2.0	2.22	1300	81		1.6
2-5-12	R71685	Same	PuO_{2-x}	1	1700	2021	2.0	2.22	1300	81		1.6
2-5-12	R71682	Same	PuO_{2-x}	1	Location unknown	2021	2.0	2.22	1300	81		1.6
2-5-12	R71681	Same	PuO_{2-x}	1	Location unknown	2021	3.0	2.22	1300	81		2.4
2-5-12	R71683	Same	PuO_{2-x}	1	800	2021	2.0	2.22	1300	81		1.6
2-6-2	R71585	R71585	PuO_{2-x}	4	Rod center	1528	4.0	2.22	1459	111		3.3
2-6-6	R71573	R71571	PuO_{2-x}	4	Rod center	1725	14.0	2.26	1579	121		11.4
2-6-6	R71567	R71565	PuO_{2-x}	4	650	1725	12.0	2.26	1533	107		9.8
2-6-9	R71562	R71560	PuO_{2-x}	4	Rod center	1873	6.0	2.26	1435	103		4.9
2-6-12	R71580	R71578	PuO_{2-x}	4	On o.d.	2021	4.5	2.22	1322	82		3.7
2-7-6	R71594	R71592	$3ThO_2$-PuO_{2-x}	2	Rod center	1725	4.5	2.26	1552	127		3.7
2-7-9	R71599	R71597	$3ThO_2$-PuO_{2-x}	2	3800	1873	4.5	2.26	1367	93		3.7
2-7-9	R71602	R71603	$3ThO_2$-PuO_{2-x}	2	1150	1873	3.5	2.26	1367	93		2.8
2-7-9	R71605	Same	$3ThO_2$-PuO_{2-x}	2	On o.d.	1873	3.0	2.26	1367	93		2.4
2-8-6	R71754	R71752	$3ThO_2$-PuO_{2-x}	5	On o.d.	1725	2.0	2.26	1508	112		1.6
2-8-6	R71746	Same	$3ThO_2$-PuO_{2-x}	5	900	1725	2.0	2.26	1508	112		1.6
2-8-9	R71739	R71737	$3ThO_2$-PuO_{2-x}	5	Rod center	1873	3.0	2.26	1410	104		2.4

[a] 2-2-2: body 2 - hole 2 - rod 2.

[b] Volume-averaged fuel temperatures are provided for all samples except those located at the center of the rod. Maximum fuel temperatures are given for these samples.

[c] The burnup is estimated to be 43% FIMA for PuO_2 and 10% FIMA for $3ThO_2$-PuO_{2-x}.

TABLE 8-7
SUMMARY OF SiC THINNING RATES IN PEACH BOTTOM TEST ELEMENTS

Test Element	Fuel Rod/ Spine Sample Ident.[a]	FMB Batch Ident.	Mean Core Height (mm)	Irradiation Conditions[b]			Max. SiC Attack (μm)	Real Time Operation (h)	SiC Thinning Rate ($\times 10^{-4}$ μm/h)	
				Fast Fluence, E > 29 fJ (n/m^2)	Linear[b] Time Weighted Temp. (°C)	Burnup FIMA (%)			Meas.	Calc.
FTE-5	TS 3-5	4000-302	2028	3.63	NA[c]	53.4	4.0	24,832	1.6	NA
FTE-5	2-5-7	4000-307	1776	3.78	1110	55.7	1.7	24,832	0.7	1.14
FTE-5	3-5-2	4000-307	2318	3.27	1101	50.5	1.8	24,832	0.7	0.75
FTE-6	TS 6-5	4000-302	2684	1.87	1105	31.4	4.0	18,358	2.2	NA
FTE-14	TS 4-6	4161-01-030	1636	1.45	1364	24.6	4.5	8,712	5.2	44.83
FTE-14	TS 5-6	4161-01-030	1844	1.44	1418	24.1	10.0	8,712	11.1	93.63
FTE-14	TS 8-3	4161-01-030	2423	1.20	1534	19.8	10.0	8,712	11.1	305.93
FTE-14	2-1-7	4161-01-031	1865	1.44	1275	24.0	5.0	8,712	5.7	39.73
FTE-15	TS 4-6	4161-01-030	1645	1.99	1355	37.3	5.0	14,901	3.4	63.10
FTE-15	TS 5-6	4161-01-030	1845	2.02	1338	36.9	15.0	14,901	10.1	87.90
FTE-15	TS 8-3	4161-01-030	2424	1.87	1468	31.9	2.0	14,901	1.3	170.00
FTE-15	2-1-5	4161-01-031	1733	2.01	1319	37.4	9.0	14,901	6.0	92.46
FTE-15	2-2-5	4161-01-031	1733	2.01	1299	37.4	12.0	14,901	8.0	70.86
FTE-15	2-1-9	4161-01-031	1987	2.02	1185	36.2	4.0	14,901	2.7	17.68
RTE-2	6-1-3	4000-307	2772	1.64	1041	28.0	2.5	18,641	1.3	0.84
RTE-4	4-7-3	4000-307	1982	1.80	1237	29.8	5.0	9,931	5.0	6.20
ORNL PIE Data										
RTE-1	3-6-6	4000-325	1752	3.03	1267	49.4	5.0	18,358	2.7	33.76
RTE-2	6-1-1	4000-307	2664	1.98	1036	31.4	1.0	18,641	0.5	0.81
RTE-2	(d)	4000-307	1460	3.06	1044	44.9	5.0	18,641	2.7	0.22
RTE-4	4-1-3	4000-309	1982	1.80	1237	29.8	5.0	9,931	5.0	6.20
RTE-5	3-5-6	4000-307	1747	4.12	1034	58.3	5.0	24,832	2.0	0.22
RTE-6	4-1-1	4000-307	1875	4.13	1072	58.8	5.0	24,832	2.0	0.95
RTE-7	5-5-5	4000-307	2483	0.78	1056	13.7	1.5	6,474	2.3	0.17
RTE-8	5-7-1	4000-307	2267	3.93	1072	54.9	5.0	24,832	2.0	0.55

(a) TS-3-5: Thermal stability - type 3 - location 5. 2-5-7: Body 2 - hole 5 - rod 7.

(b) Temperatures are volume averaged.

(c) NA = not available.

(d) Body 3, 100 SF, 2329.

TABLE 8-8

SUMMARY OF FISSILE KERNEL MIGRATION IN PEACH BOTTOM FUEL AND RECYCLE TEST ELEMENTS

Coating Type	Fuel Rod Ident.[a]	Irradiation Conditions: Fast Fluence,[b] E > 29 fJ (10^{25}n/m^2)	Irradiation Conditions: Time Avg. Max. Fuel Temp. (°C)	Irradiation Conditions: Burnup FIMA (%)	Irradiation Conditions: Time At Temp. (h)	Kernel Migration (μm): Measured[c]	Kernel Migration (μm): Predicted[d] $C_{0.05} < \bar{x} < C_{0.95}$
Fuel Test Elements, UC_2 Kernel							
TRISO	3-2-8-7	0.559	1057	10.1	3816	<5	0.0 < 0.1 < 0.4
TRISO	4-2-6-7	1.958	1163	35.7	12858		ND[e]
TRISO	6-2-6-7	2.825	1195	45.4	18358		0.7 < 2.9 < 11.4
TRISO	5-1-5-3	1.662	699	30.1	24832		0
BISO	5-2-1-2	3.735	1111	55.8	24832		0.4 < 1.6 < 6.3
BISO	5-2-1-7	3.785	1195	55.7	24832		1.5 < 6.1 < 24.0
TRISO	5-2-5-7	3.785	1165	55.7	24832		1.0 < 3.9 < 15.4
BISO	5-3-1-2	3.266	1154	50.5	24832		0.5 < 1.8 < 7.1
TRISO	5-3-5-2	3.266	1150	50.5	24832		0.5 < 1.8 < 7.1
TRISO	14-2-1-7	1.438	1347	24.0	8721		3.4 < 13.3 < 52.4
TRISO	14-2-2-6	1.447	1321	24.3	8721		10.1 < 39.8 < 156.8
TRISO	15-2-1-5	2.009	1386	37.4	14901		11.1 < 44 < 173.4
TRISO	15-2-1-9	2.022	1251	36.2	14901		2.0 < 8.1 < 31.9
TRISO	15-2-2-5	2.009	1367	37.4	14901	<5	8.8 < 34.5 < 135.3
Recycle Test Elements, UC_2 Kernel							
TRISO	7-3-7-3	1.160	1168	20.0	6473	<5	0.1 < 0.4 < 1.6
TRISO	7-5-5-5	0.785	1097	13.7	6473		0.0 < 0.1 < 0.3
TRISO	4-4-1-3	1.802	1303	29.8	9930		1.5 < 4.2 < 12.0
BISO	4-1-1-3	1.024	789	16.7	9930		0.0
BISO	2-4-1-1	3.065	1223	44.5	18641		1.5 < 4.7 < 13.4
TRISO	2-6-1-4	1.436	1077	26.3	18641		0.0 < 0.1 < 0.3
BISO	2-2-1-1	2.545	1021	40.1	18641		2.8 < 8.1 < 23.1
TRISO	2-3-1-BB	3.099	1059	45.0	18641		2.0 < 5.7 < 16.2
TRISO	5-3-5-6	4.125	1085	58.3	24832		0.2 < 0.7 < 2.0
BISO	5-5-3-1	3.720	1128	53.7	24832		0.4 < 1.1 < 3.1
BISO	5-5-5-1	3.720	1073	53.7	24832		0.5 < 1.3 < 3.7
TRISO	5-6-7-1	2.824	1064	43.3	24832		0.1 < 0.3 < 0.9
BISO	6-1-1-5	2.955	866	46.8	24832		0.0
BISO	6-1-1-6	3.222	883	50.8	24832		0.0
TRISO	6-2-7-6	4.043	1054	58.5	24832		0.1 < 0.4 < 1.6
TRISO	6-4-1-1	4.134	1145	58.8	24832		0.7 < 2.0 < 7.9
TRISO	6-5-5-2	3.829	1177	53.4	24832		0.8 < 2.4 < 9.5
TRISO	8-2-7-6	4.093	1020	58.8	24832		0.1 < 0.2 < 0.8
TRISO	8-5-7-1	3.935	1120	54.9	24832		0.4 < 1.0 < 3.9
TRISO	8-6-7-1	2.959	1063	44.2	24832		0.1 < 0.3 < 1.2
BISO	8-3-1-6	4.217	1127	59.6	24832		0.6 < 1.6 < 6.3
TRISO	1-5-6-6	3.031	1355	49.4	18358		12.7 < 36.2 < 142.6
BISO	1-5-3-1	2.812	1292	45.5	18358	<5	4.1 < 11.7 < 46.1
Fuel Test Elements, UO_2 Kernel							
TRISO	3-2-2-7	0.559	1054	10.1	3816	<5	3.4 < 13.5 < 43.7
TRISO	4-2-1-7	1.968	1174	35.7	3816	To SiC, plastic deformation	15.7 < 61.9 < 200.6
TRISO	4-2-2-7	1.968	1174	35.7	12858	To SiC, plastic deformation	15.7 < 61.9 < 200.6
TRISO	6-2-1-7	2.825	1210	45.4	18358	To SiC, plastic deformation	41.9 < 165.0 < 535.0
TRISO	6-2-2-7	2.825	1210	45.4	18358	To SiC, plastic deformation	41.9 < 165.0 < 535.0
TRISO	14-2-3-6	1.447	1383	24.3	8721	<5	19.3 < 76.0 < 245.2
TRISO	14-2-6-7	1.438	1373	24.0	8721		14.3 < 56.3 < 182.4
TRISO	15-2-3-9	2.022	1264	36.2	14901		20.2 < 79.4 < 257.3
TRISO	15-2-5-2	1.962	1252	37.0	14901		24.2 < 95.1 < 308.1
TRISO	15-2-6-5	2.009	1397	37.4	14901		30.7 < 121.0 < 392.0
TRISO	15-3-6-10	1.037	1135	21.7	14901	<5	11.3 < 44.3 < 143.5
Recycle Test Elements, UO_2 Kernel							
BISO	5-3-7-6	4.125	1191	58.3	24832	To OPyC, plastic deformation	17.7 < 69.7 < 225.8
BISO	5-5-1-1	3.720	1146	53.7	24832	To OPyC, plastic deformation	13.9 < 54.9 < 177.9
BISO	6-6-1-1	2.912	1059	43.9	24832	25 μm, plastic deformation	
BISO	1-4-8-6	2.875	1455	46.3	18358	To OPyC, plastic deformation	25.4 < 100 < 324.0
TRISO	1-5-8-1	2.812	1331	45.5	18358	To OPyC, plastic deformation	25.2 < 99.1 < 321.1
Fuel Test Elements, $(Th,U)C_2$ Kernel							
TRISO[f]	3-2-3-7	0.559	1030	2.8	3816	<5	0.0 < 0.1 < 0.3
TRISO[f]	3-2-5-7	0.559	1049	2.8	3816	<5	0.0 < 0.1 < 0.3
TRISO[f]	4-2-3-8	1.958	1169	10.1	12858	<5	0.5 < 1.5 < 5.0
TRISO[f]	4-2-5-7	1.968	1150	10.1	12858	<5	0.4 < 1.2 < 4.0
TRISO[f]	6-2-3-7	2.825	1191	13.4	18358	5	1.3 < 4.3 < 14.3
TRISO[f]	6-2-6-7	2.825	1186	13.4	18358	Hydrolysis prevents measurement	1.4 < 4.7 < 15.6
BISO[g]	5-2-3-7	3.785	1249	29.1	24832	~20	3.8 < 12.5 < 41.5
TRISO[g]	5-2-7-7	3.785	1174	29.1	24832	5 μm with extrusion into buffer cracks	1.7 < 5.6 < 18.6
BISO[g]	5-3-3-2	3.266	1193	26.1	24832	~50	1.4 < 4.6 < 15.3
TRISO[g]	5-3-7-2	3.266	1147	26.1	24832	~50 μm with extrusion into buffer cracks	1.1 < 3.6 < 12.0
TRISO[h]	16-2-2-11	2.235	1146	8.3	14901	Kernel dispersion	0.5 < 1.6 < 5.3
TRISO[h]	16-2-7-10	2.244	1185	8.3	14901	<5	1.2 < 3.9 < 12.9
TRISO[h]	16-2-8-6	2.259	1036	8.5	14901	Kernel dispersion	0.1 < 0.3 < 1.0
TRISO[h]	16-2-8-10	2.244	1141	8.4	14901	Kernel dispersion	0.5 < 1.5 < 5.0
TRISO[i]	16-3-5-4	1.966	1093	10.3	14901	Extrusion into buffer cracks	0.3 < 1.0 < 3.3
Fuel Test Elements, $(Th,U)O_2$ Kernel							
TRISO	14-2-4-7	1.438	1323	13.2	8721	14	11 < 36 < 274.4
TRISO	15-2-4-3	1.984	1239	19.2	14901	<5	8 < 39 < 191.1
Recycle Test Elements, $(Th,U)O_2$ Kernel							
BISO[g]	4-5-1-3	1.471	1267	8.4	9930	<5	5.8 < 28.4 < 139.2
BISO[g]	2-2-1-2	2.668	1098	14.8	18641		3.6 < 17.8 < 87.2
BISO[g]	2-2-1-6	3.029	1155	15.8	18641		5.0 < 24.5 < 120.1
BISO[g]	2-2-5-1	2.545	1021	14.1	18541		1.7 < 8.1 < 39.7
BISO[h]	5-3-1-6	4.125	1136	13.9	24832	<5	4.1 < 20.3 < 99.5
BISO[g]	5-3-3-6	4.125	1153	21.2	24832	5	7.8 < 38.1 < 186.7
BISO[g]	5-5-7-1	3.720	1177	19.1	24832	<5	8.1 < 39.6 < 194.0
BISO[g]	6-3-1-6	4.157	1162	21.6	24832	<5	11.6 < 57.0 < 279.3
BISO[g]	8-4-1-6	3.904	1221	20.2	24832	5	12.0 < 58.6 < 287.1
BISO[h]	1-4-1-6	2.875	1299	10.5	18358	<5	10.2 < 49.9 < 244.5
BISO[g]	1-4-3-6	2.875	1398	16.3	18358	<5	20.0 < 97.9 < 479.7
BISO[g]	8-4-5-1	4.193	1229	21.5	24832	5	13.5 < 66.4 < 325.4

[a] 3-2-8-7: FTE(RTE)-3 - body 2 - hole 8 - rod 7. 2-3-1-BB: RTE-3 - body 3 - hole 1 - blended bed.

[b] Three digits significant.

[c] Migration <5 μm cannot be resolved with metallography.

[d] Calculated with modified TRIGER and KMC values from TABLE 8-10

[e] ND = not determined.

[f] 2.7%Th,U.

[g] 2%Th,U.

[h] 4%Th,U.

[i] 2.52%Th,U.

TABLE 8-9

SUMMARY OF FERTILE KERNEL MIGRATION IN PEACH BOTTOM FUEL AND RECYCLE TEST ELEMENTS

Coating Type	Fuel Rod Ident.[a]	Irradiation Conditions: Fast Fluence,[b] E > 29 fJ (10^{21}n/m^2)	Irradiation Conditions: Time Avg. Max Fuel Temp. (°C)	Irradiation Conditions: Burnup FIMA (%)	Irradiation Conditions: Time At Temp. (h)	Kernel Migration (μm): Measured[c]	Kernel Migration (μm): Predicted[d] $C_{0.05} < \bar{x} < C_{0.95}$
Fuel Test Elements, ThO_2 Kernel							
BISO	3-2-2-7	0.559	1054	0.4	3816	<5	0.0 < 0.1 < 0.4
BISO	4-2-1-7	1.968	1174	0.7	12858		0.2 < 1.0 < 4.2
BISO	4-2-2-7	1.968	1174	0.7	12859		0.2 < 1.0 < 4.2
BISO	6-2-1-7	2.825	1210	1.5	18358		3.5 < 14.6 < 61.6
BISO	6-2-2-7	2.825	1210	1.5	18358		3.5 < 14.6 < 61.6
BISO	14-2-3-6	1.447	1383	0.4	8721		6.9 < 28.7 < 121.1
TRISO	14-2-6-7	1.438	1373	0.4	8721		3.4 < 14.0 < 59.1
BISO	15-2-3-9	2.022	1264	1.0	14901		2.0 < 8.4 < 354
TRISO	15-2-6-5	2.009	1397	1.0	14901	<5	11.6 < 48.4 < 204.2
Recycle Test Elements, ThO_2 Kernel							
BISO	5-3-3-6	4.125	1183	2.7	24832	<5	1.1 < 4.4 < 18.6
BISO	5-3-7-6	4.125	1191	2.7	24832		1.2 < 5.0 < 21.1
BISO	5-5-5-1	3.720	1073	2.1	24832		0.6 < 2.5 < 10.6
BISO	6-6-1-1	2.912	1059	1.3	24832		0.4 < 1.6 < 6.8
BISO	1-4-3-6	2.875	1399	1.5	18358		6.6 < 27.4 < 115.6
BISO	1-5-8-1	2.812	1331	1.4	18358		5.9 < 24.4 < 102.9
BISO	1-5-3-1	2.812	1292	1.4	18358		3.6 < 14.9 < 62.9
BISO	1-4-8-6	2.875	1455	1.5	18358	<5	11.8 < 49.4 < 208.5
Fuel Test Elements, ThC_2 Kernel							
BISO	3-2-3-7	0.559	1053	0.4	3816	<5	0.0 < 0.1 < 0.4
TRISO	3-2-5-7	0.559	1052	0.4	3816		0.0 < 0.1 < 0.4
BISO	3-2-8-7	0.559	1057	0.4	3816		0.0 < 0.1 < 0.4
BISO	4-2-3-8	1.958	1169	0.7	12858		0.6 < 2.0 < 7.1
TRISO	4-2-5-7	1.967	1150	0.7	12858		0.4 < 1.5 < 5.4
BISO	4-2-8-7	1.967	1163	0.7	12858		ND[e]
BISO	6-2-3-7	2.825	1191	1.5	18358		1.8 < 6.4 < 23.0
TRISO	6-2-6-7	2.825	1186	1.5	18358		2.0 < 7.2 < 25.8
BISO	6-2-8-7	2.825	1195	1.5	18358		1.9 < 6.7 < 24.1
BISO	5-1-5-3	1.662	755	0.6	24832		0
BISO	5-2-1-2	3.735	1111	2.2	24832		1.0 < 3.6 < 12.9
BISO	5-2-1-7	3.785	1195	2.3	24832		3.9 < 14.1 < 50.6
BISO	5-2-3-7	3.785	1249	2.3	24832		6.5 < 23.1 < 82.9
BISO	5-2-5-7	3.785	1165	2.3	24832		2.5 < 9.0 < 32.3
TRISO	5-2-7-7	3.785	1174	2.3	24832		2.5 < 8.8 < 31.5
BISO	5-3-1-2	3.266	1154	1.7	24832		1.1 < 4.1 < 14.7
BISO	5-3-3-2	3.266	1193	1.7	24832		1.9 < 6.8 < 24.4
BISO	5-3-5-2	3.266	1150	1.7	24832		1.1 < 4.1 < 14.7
TRISO	5-3-7-2	3.266	1147	1.7	24832		1.0 < 3.6 < 12.9
BISO	14-2-1-7	1.438	1347	0.4	8721		8.9 < 31.8 < 114.2
TRISO	14-2-2-6	1.447	1321	0.4	8721		5.9 < 21.2 < 76.1
BISO	14-2-4-7	1.438	1322	0.4	8721	<5	6.6 < 23.4 < 84.0
BISO	15-2-1-5	2.009	1386	1.0	14901	15	28 < 100 < 359.0
BISO	15-2-1-9	2.022	1251	1.0	14901	<5	5.3 < 19 < 68.2
TRISO	15-2-2-5	2.009	1367	1.0	14901		23.3 < 83.3 < 299.0
BISO	15-2-4-3	1.984	1239	1.0	14901		4.5 < 16.1 < 57.7
BISO	15-2-5-2	1.962	1253	1.0	14901		8.5 < 30.2 < 108.4
BISO	15-3-6-10	1.037	1135	0.2	14901		0.3 < 1.0 < 3.6
TRISO	16-2-2-11	2.235	1146	0.9	14901		0.6 < 2.3 < 8.3
TRISO	16-2-7-10	2.244	1185	0.9	14901		1.8 < 6.5 < 23.3
TRISO	16-2-8-6	2.259	1036	1.0	14901		0.1 < 0.3 < 1.1
TRISO	16-2-8-10	2.244	1141	0.9	14901		0.6 < 2.1 < 7.5
TRISO	16-3-5-4	1.966	1083	0.7	14901	<5	0.3 < 1.1 < 3.9
Recycle Test Elements, ThC_2 Kernel							
BISO	7-3-7-3	1.160	1168	0.2	6473	<5	0.3 < 1.0 < 3.6
BISO	7-5-5-5	0.785	1097	0.1	6473		0.1 < 0.3 < 1.1
BISO	4-4-1-3	1.802	1303	0.5	9930		2.7 < 9.8 < 35.2
BISO	4-1-1-3	1.024	789	0.1	9930		0
BISO	4-5-1-3	1.471	1267	0.3	9930		2.1 < 7.5 < 26.9
BISO	2-2-1-2	2.688	1098	1.3	18641		0.4 < 1.5 < 5.4
BISO	2-2-1-6	3.029	1145	1.6	18641		0.7 < 2.5 < 8.9
BISO	2-4-1-1	3.065	1223	1.6	18641		3.0 < 10.8 < 38.8
BISO	2-6-1-4	1.436	1077	0.3	18641		0.1 < 0.3 < 1.1
BISO	2-2-5-1	2.545	1021	1.1	18641		0.1 < 0.3 < 1.1
BISO	2-2-1-1	2.545	1021	1.1	18641		0.1 < 0.3 < 1.1
BISO	2-3-1-BB	3.099	1069	1.7	18641		0.3 < 1.2 < 4.3
BISO	5-3-1-6	4.125	1136	2.7	24832		0
BISO	5-3-5-6	4.125	1085	2.7	24832		0.4 < 1.6 < 5.7
BISO	5-5-1-1	3.720	1146	2.1	24832		1.0 < 3.4 < 12.2
BISO	5-5-3-1	3.720	1128	2.1	24832		0.7 < 2.4 < 8.6
BISO	5-5-7-1	3.720	1177	2.1	24832		2.0 < 6.9 < 24.8
TRISO	5-6-7-1	2.824	1064	1.2	24832		0.2 < 0.6 < 2.2
BISO	6-1-1-5	2.965	866	1.5	24832		0
BISO	6-1-1-6	3.222	883	1.7	24832		0
BISO	6-2-7-6	4.043	1054	2.9	24832		0.2 < 0.8 < 2.9
BISO	6-4-1-1	4.134	1145	3.0	24832		1.3 < 4.6 < 16.5
BISO	6-5-5-2	3.829	1177	2.2	24832		1.9 < 5.3 < 19.0
BISO	6-3-1-6	4.157	1162	2.9	24832		3.7 < 13.3 < 47.72
TRISO	8-2-7-6	4.093	1020	4.1	24832		0.2 < 0.6 < 2.2
TRISO	8-5-7-1	3.935	1120	2.4	24832		0.7 < 2.5 < 8.9
BISO	8-6-7-1	2.959	1063	1.3	24832		0.2 < 0.7 < 2.5
BISO	8-3-1-6	4.217	1127	3.1	24832		1.0 < 3.6 < 12.9
BISO	8-4-1-6	3.904	1221	2.6	24832		3.8 < 13.7 < 49.2
BISO	8-4-5-1	4.193	1228	3.0	24832		5.1 < 18.2 < 65.3
BISO	1-4-1-6	2.875	1299	1.5	18358		ND
BISO	1-3-6-6	3.031	1355	1.8	18358	<5	24.2 < 86.6 < 310.9

[a] 3-2-2-7: FTE(RTE)-3 - body 2 - hole 2 - rod 7. 2-3-1-BB: FTE-2 - body 3 - hole 1 - blended bed.

[b] Three digits significant.

[c] Migration <5 μm cannot be resolved with metallography.

[d] Calculated with modified TREVER and KMC values from Table 8-10

[e] ND = not determined.

TABLE 8-10
KERNEL MIGRATION COEFFICIENTS
USED IN CALCULATIONS

Kernel	KMC ($m^2 \cdot k/s$)[a]	Correlation Coefficient	
		C_5	C_{95}
UO_2	$0.265 \times 10^{-7} \exp\left(\frac{-6.78 \times 10^4}{8.313T}\right)$	0.254	3.94
UC_2	$0.62 \exp\left(\frac{-3.11 \times 10^5}{8.313T}\right)$	0.351	2.85
$(4Th,U)O_2$	$0.172 \times 10^{-4} \exp\left(\frac{-1.55 \times 10^5}{8.313T}\right)$	0.204	4.9
$(4Th,U)C_2$	$1.6 \times 10^{-2} \exp\left(\frac{-2.61 \times 10^5}{8.313T}\right)$	0.30	3.32
ThC_2	$2.2 \exp\left(\frac{-3.17 \times 10^5}{8.313T}\right)$	0.28	3.59
ThO_2	$0.39 \exp\left(\frac{-2.96 \times 10^5}{8.313T}\right)$	0.24	4.22

(a) Multiply by 10^4 to get $cm^2 \cdot k/s$.

TABLE 8-11
FRACTIONAL RELEASE OF Kr-85m FROM PEACH BOTTOM
TEST ELEMENT FAILED FUEL RODS

FTE/Rod	Failure Metallography		$(R/B)_{corr}$ [a]	$(R/B)_f$ [b]
	P (%)	$2\sigma < P < 2\sigma$ (%)	$1\sigma < P < 1\sigma$ ($\times 10^{-3}$)	Range
6/2-1-7	21.1	$14.6 < P < 29.4$	$0.71 < P < 6.34$	0.0024 - 0.0434
6/2-2-7	8.1	$4.6 < P < 13.9$	$0.77 < P < 6.91$	0.0055 - 0.1502
15/2-2-5	19.7	$10.6 < P < 29.8$	$0.20 < P < 1.78$	0.0007 - 0.0168

[a] Represents R/B for ThC_2 particles only in FTE-15 and UO_2 particles only in FTE-6.

[b] $(R/B)_f$ = fractional fission gas release from failed particle: calculated using upper and lower bounds on failure and R/B.

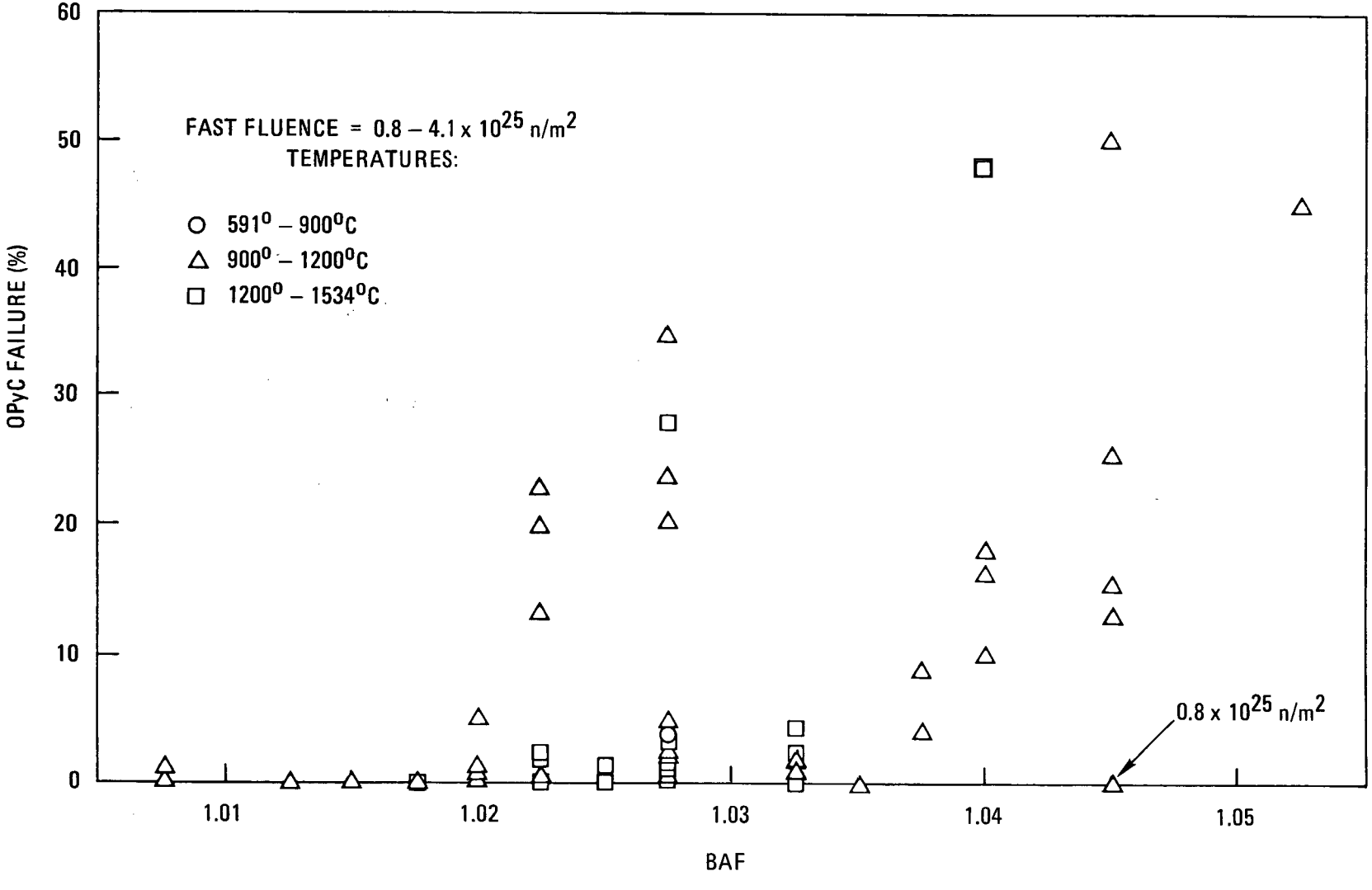

Fig. 8-1. TRISO particle OPyC coating failure versus BAF

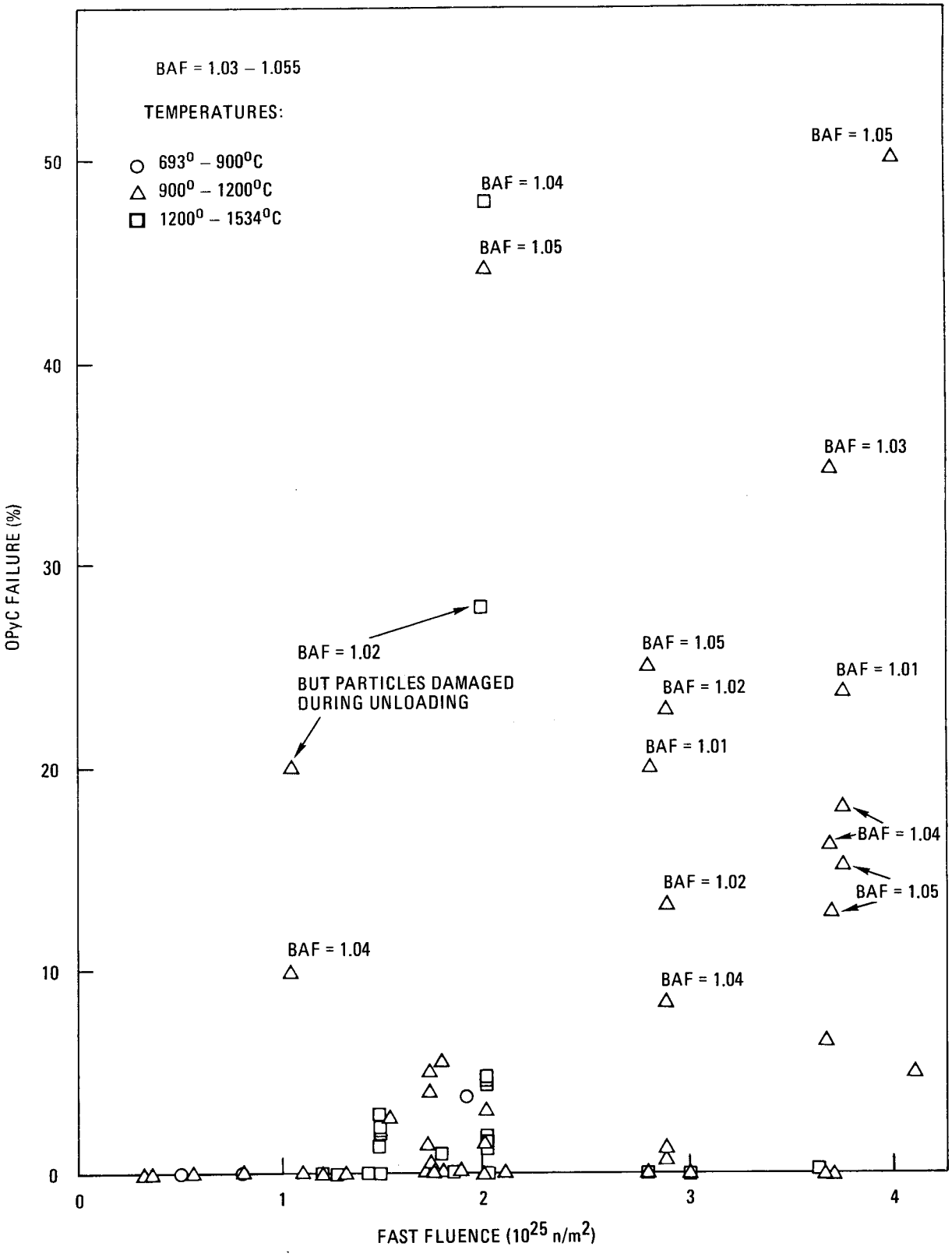

Fig. 8-2. TRISO particle OPyC coating failure versus fast fluence

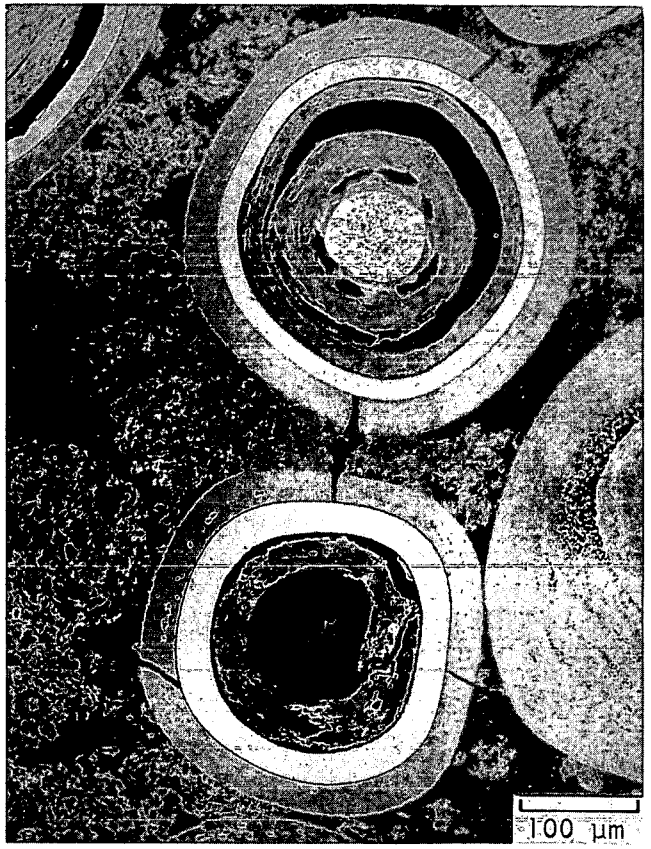

L7537–280

(a)

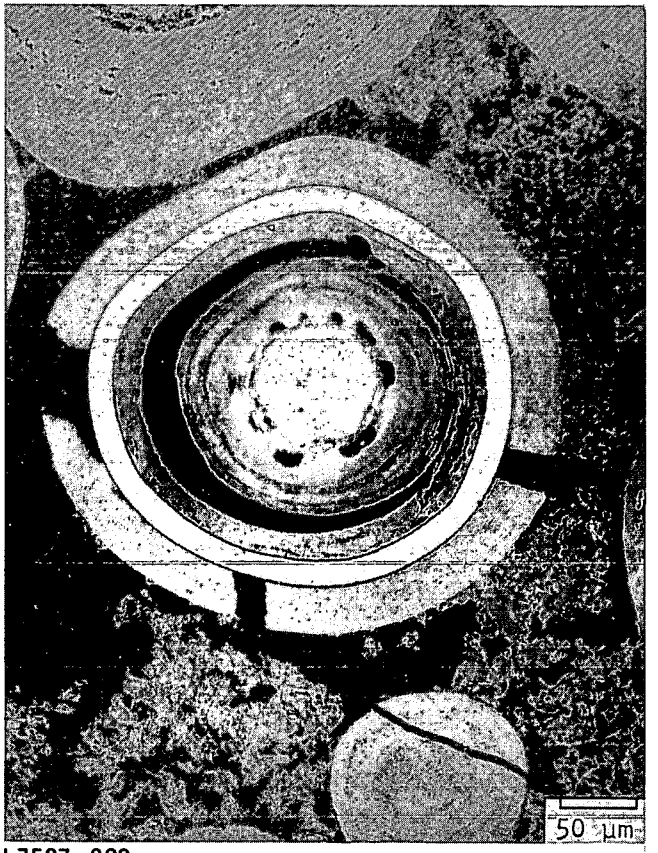

L7537–262

(b)

Fig. 8-3. OPyC failure caused by matrix-coating interactions in FTE-5 fuel rod 3-5-2. Irradiation conditions: 3.7×10^{25} n/m^2 $[(E > 29 \text{ fJ})_{HTGR}]$ at 1085°C.

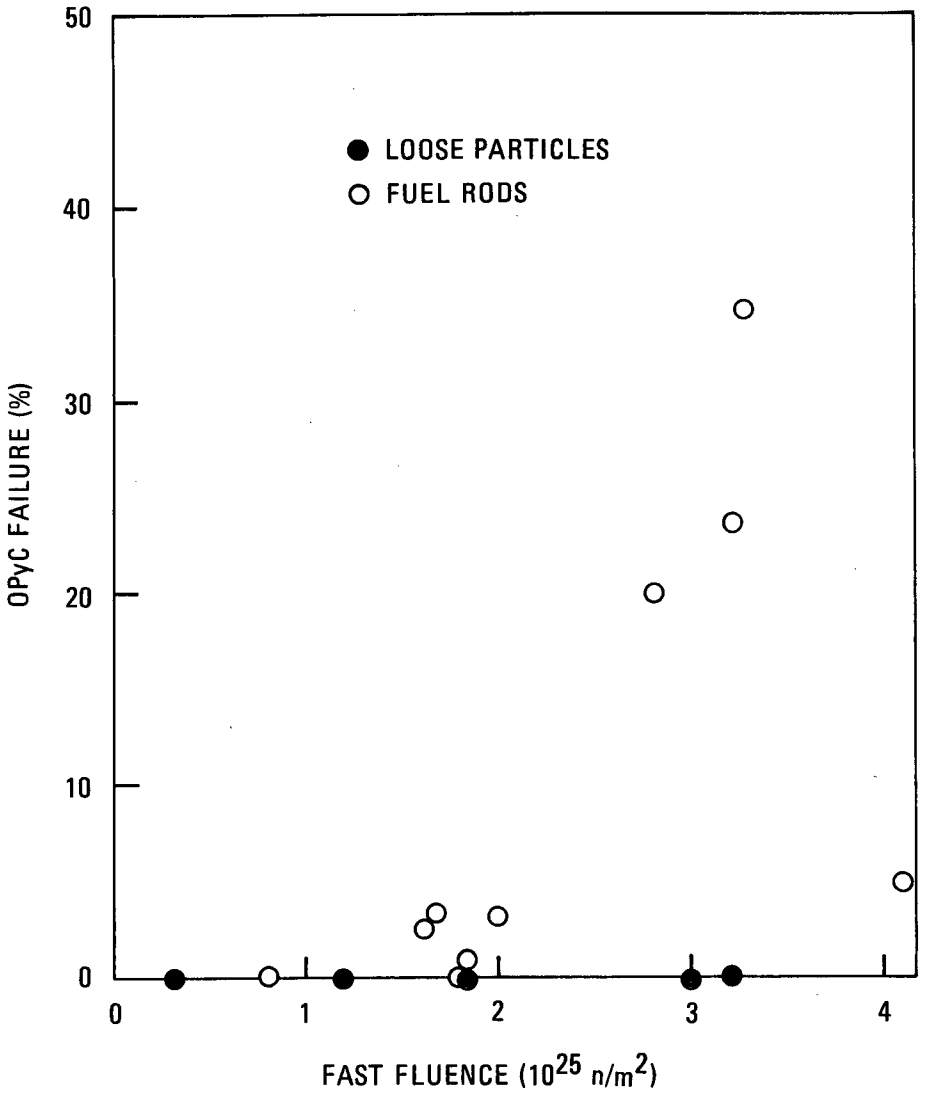

Fig. 8-4. OPyC failure of batches 4000-302 and 4000-307 versus fast fluence

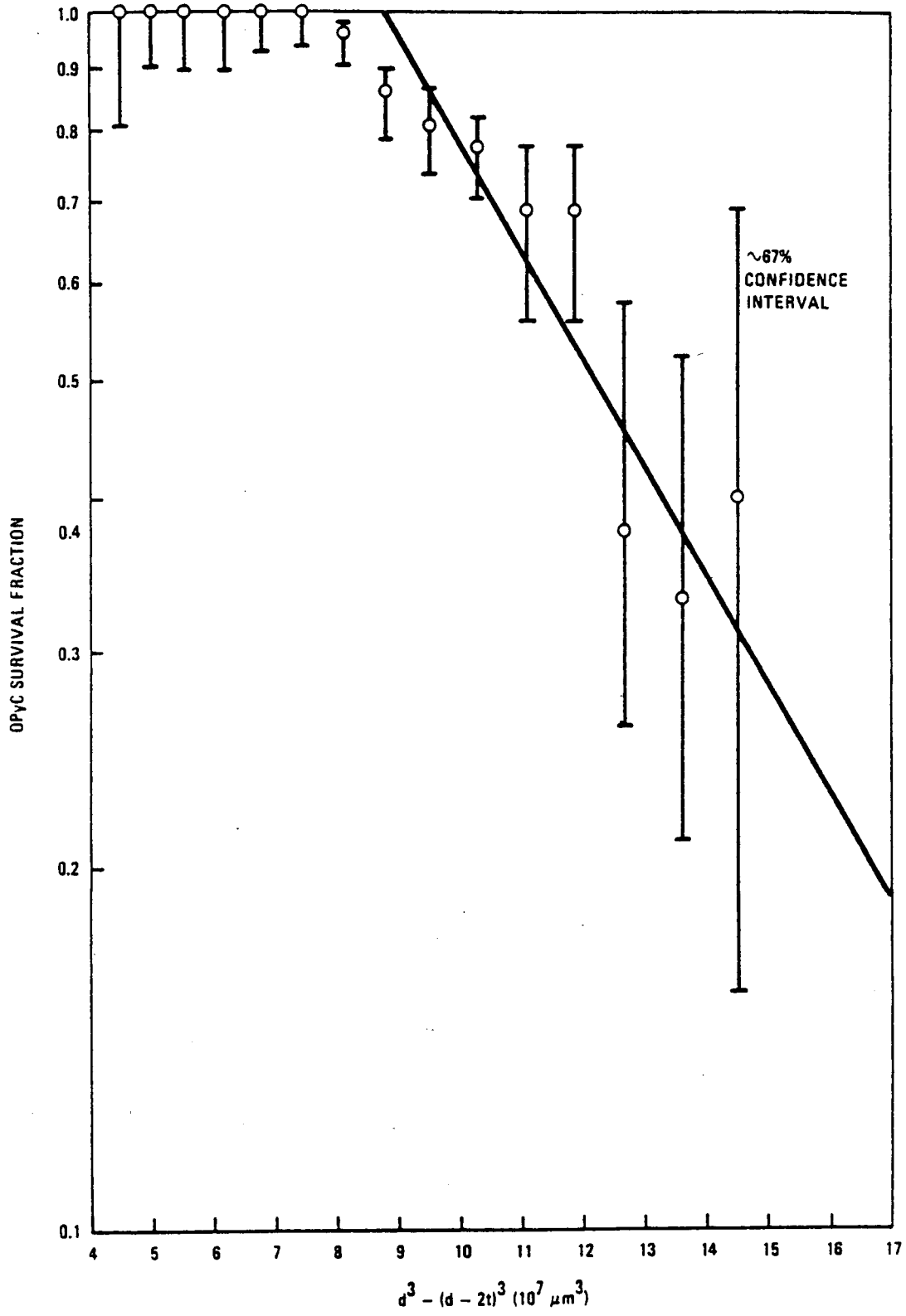

Fig. 8-5. Coating volume effect on OPyC survival

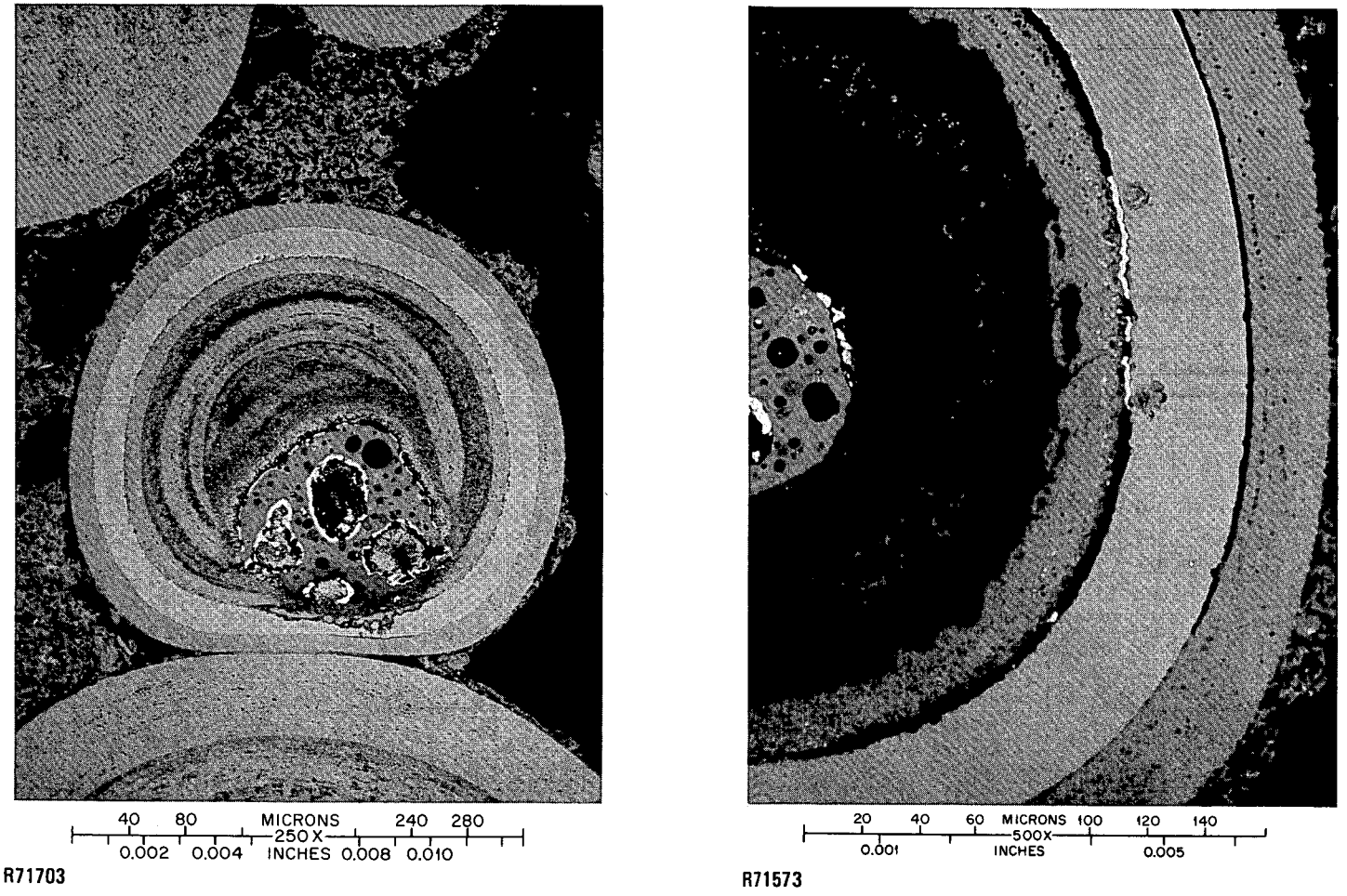

Fig. 8-6. Palladium attack of SiC in FTE-13 PuO_x particles: (a) $PuO_{1.8}$ particle from rod 2-5-6 with palladium attack on entire inner surface of SiC coating, and (b) $PuO_{1.65}$ particle from fuel rod 2-6-6 with localized palladium attack

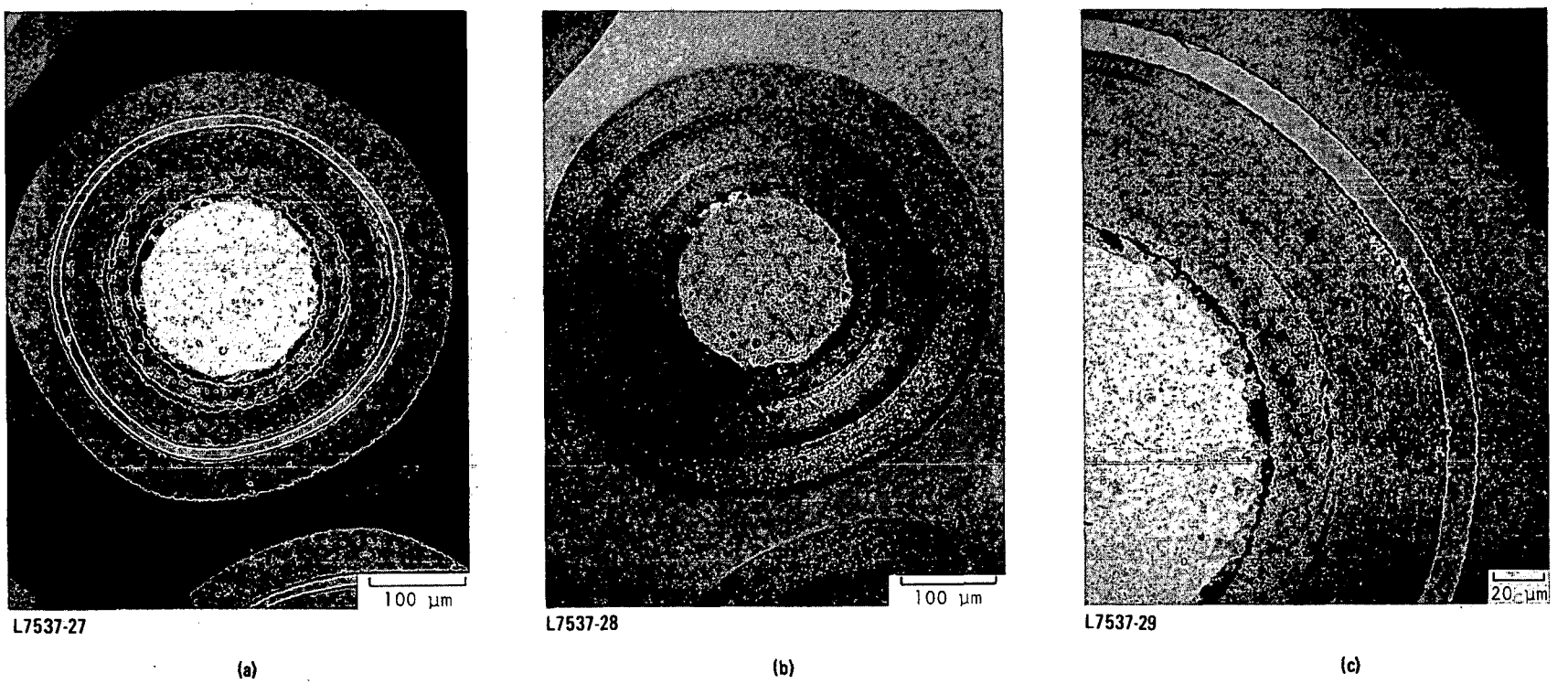

Fig. 8-7. Palladium attack of SiC in denatured fuel particle batch 4423-3; irradiated in FTE-5 spine sample TS27-4 to 3.6 x 10^{25} n/m^2 [$(E > 29\ fJ)_{HTGR}$] at 1180°C: (a) bright field, (b) dark field, and (c) high magnification of fission products at SiC interface

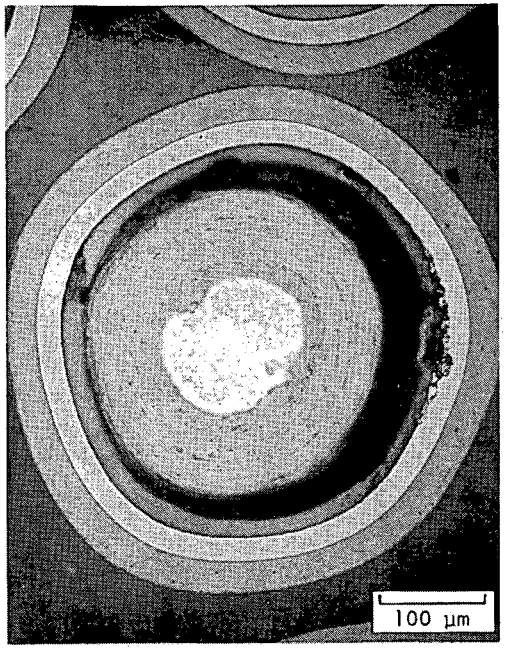

L7437-63 (a)

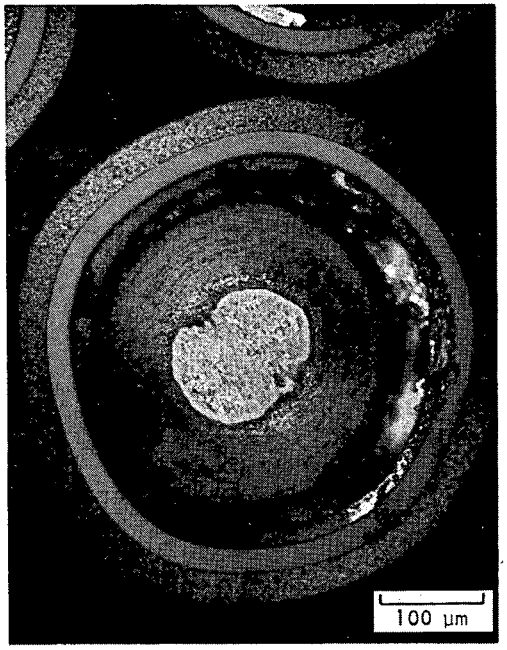

L7437-64 (b)

L7437-22 (c)

Fig. 8-8. Lanthanide attack of SiC in dense UC_2 particle; FTE-15 UC_2 (VSM) TRISO fissile particle batch 4161-01-030 from spine sample TS5-6. Irradiation conditions: 2.0×10^{25} n/m^2 $[(E > 29 \text{ fJ})_{HTGR}]$ at 1340°C; (a) bright field, (b) dark field, and (c) high magnification of SiC attack.

L7708-1

(a)

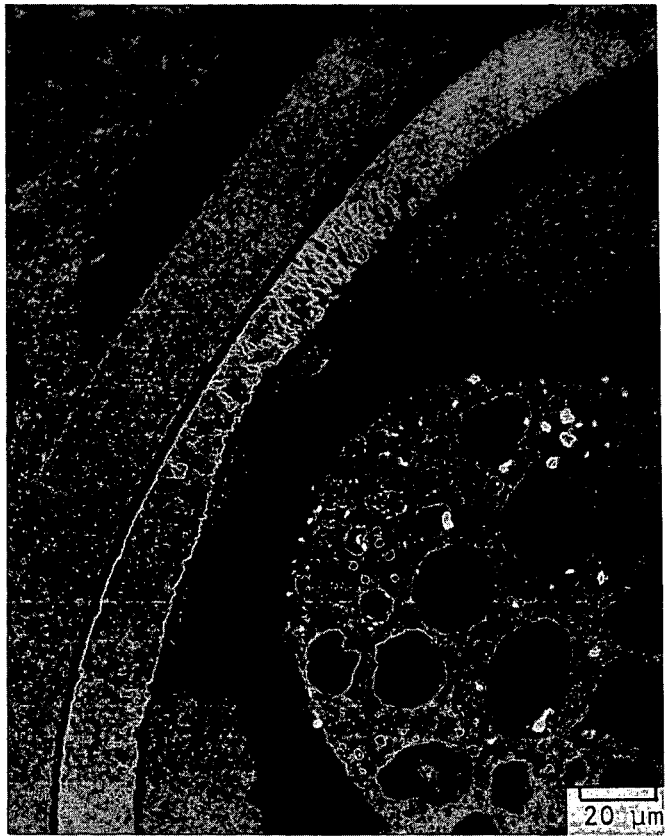

L7519-56

(b)

Fig. 8-9. Kernel attack of SiC coating: (a) dispersed $(Th,U)C_2$ kernel from FTE-16 fuel rod 2-3-10 with minor attack on entire inner SiC surface, and (b) UO_2 kernel attack in FTE-6 fuel rod 2-1-7

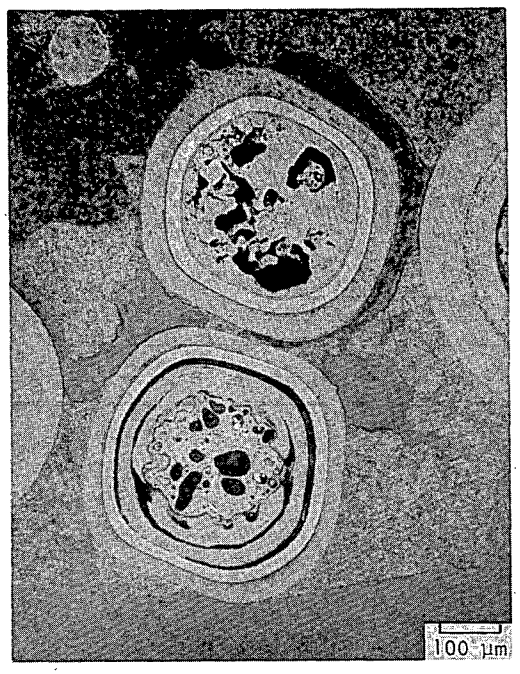

L7519-117

(a)

L7519-127

(b)

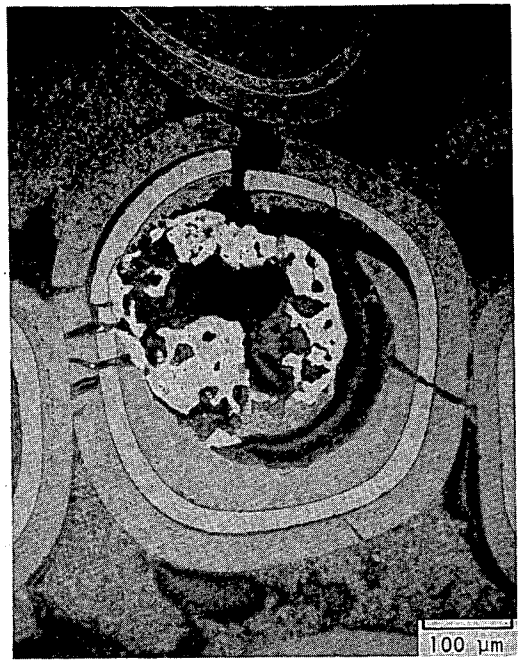

L7519-133

(c)

Fig. 8-10. UO_2 kernel migration in fuel rod 2-2-6 from FTE-6. Irradiation conditions: 2.9×10^{25} n/m^2 $[(E > 29 \text{ fJ})_{HTGR}]$ at 1210° C.

(a)

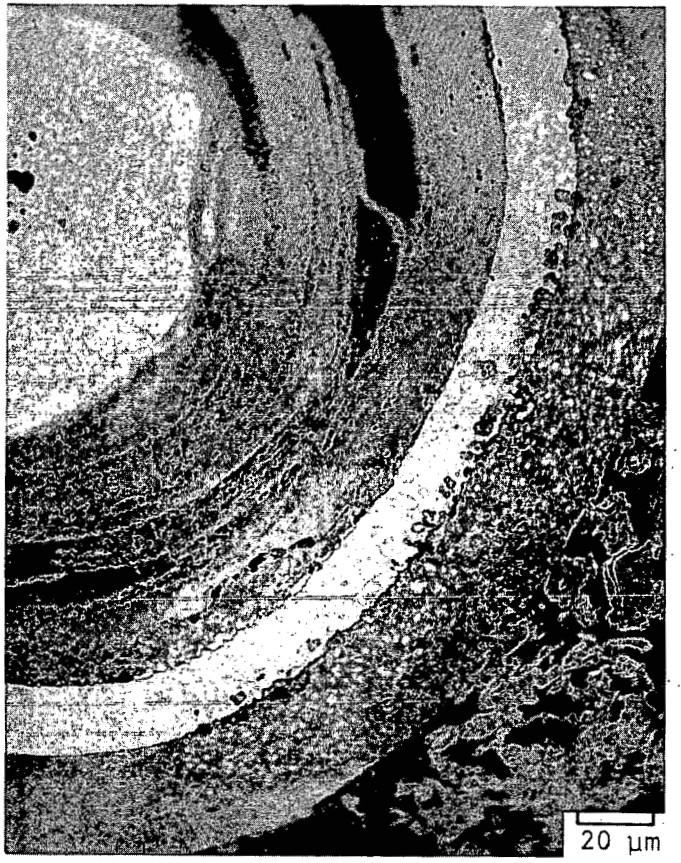

(b)

Fig. 8-11. Contamination attack of SiC and OPyC coatings in FTE-5 fuel rod 3-5-2: (a) BISO attack and (b) TRISO attack

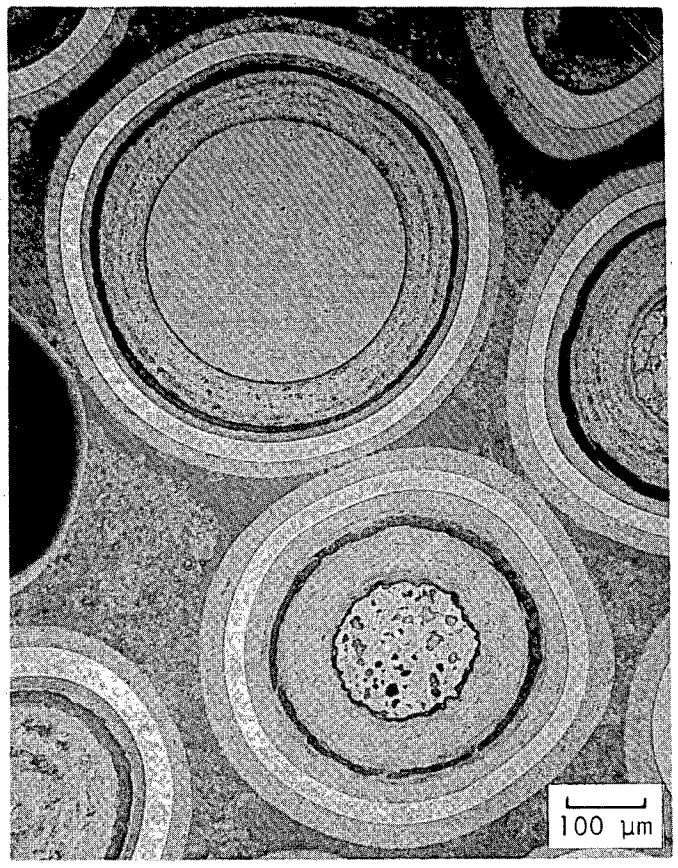

L7437-135 (a)

L7437-136 (b)

Fig. 8-12. UO_2 TRISO fuel particles from FTE-15 fuel rod 2-6-5. Irradiation conditions: 2.0×10^{25} n/m^2 $[(E > fJ)_{HTGR}]$ at 1397°C: (a) light field and (b) dark field.

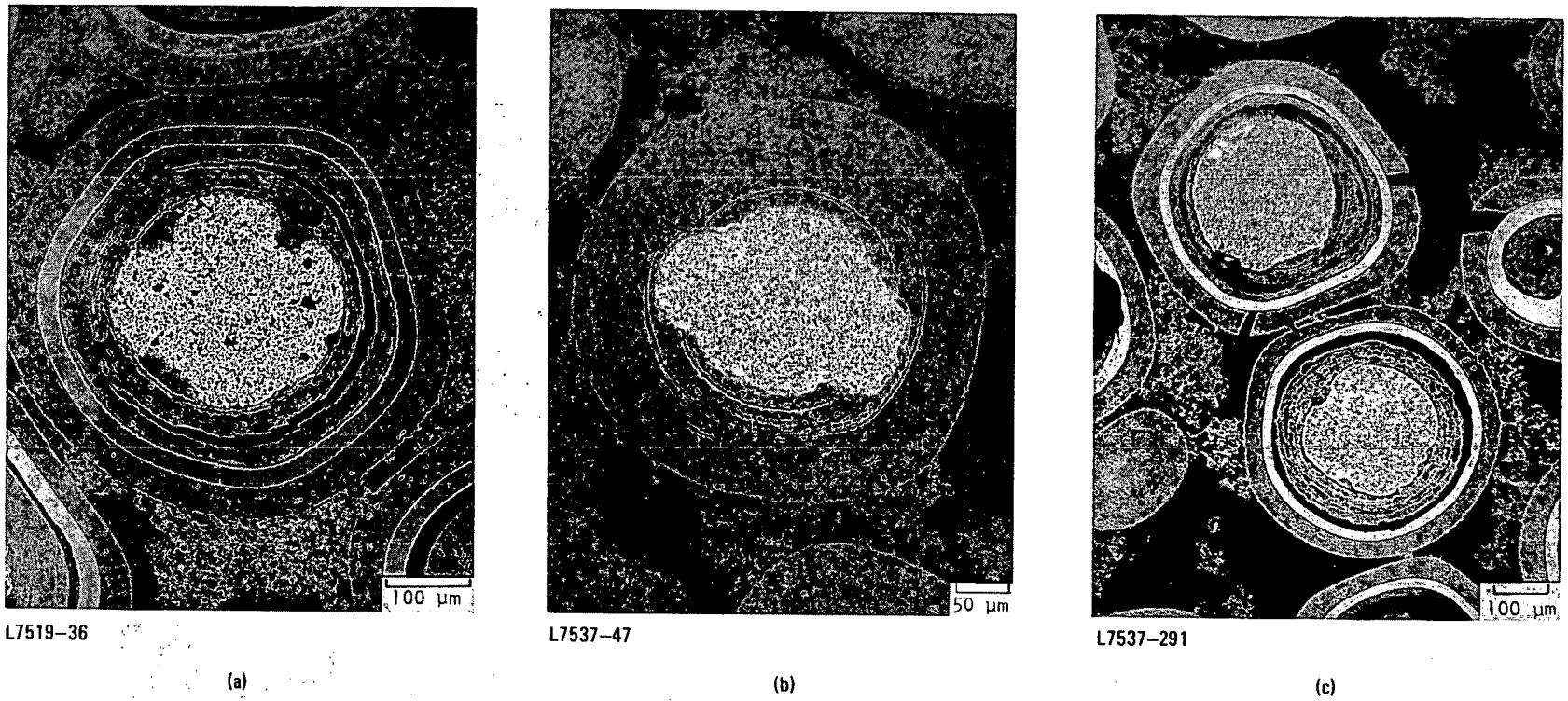

Fig. 8-13. $(Th,U)C_2$ kernel migration: (a) FTE-6 fuel rod 2-3-7, irradiation conditions 2.9×10^{25} n/m^2 [$(E > 29\ fJ)_{HTGR}$] at 1191°C; (b) FTE-5 fuel rod 2-3-7, irradiation conditions 3.8×10^{25} n/m^2 [$(E > 29\ fJ)_{HTGR}$] at 1249°C; and (c) FTE-5 fuel rod 3-7-2, irradiation conditions 3.3×10^{25} n/m^2 [$(E > fJ)_{HTGR}$] at 1147°C

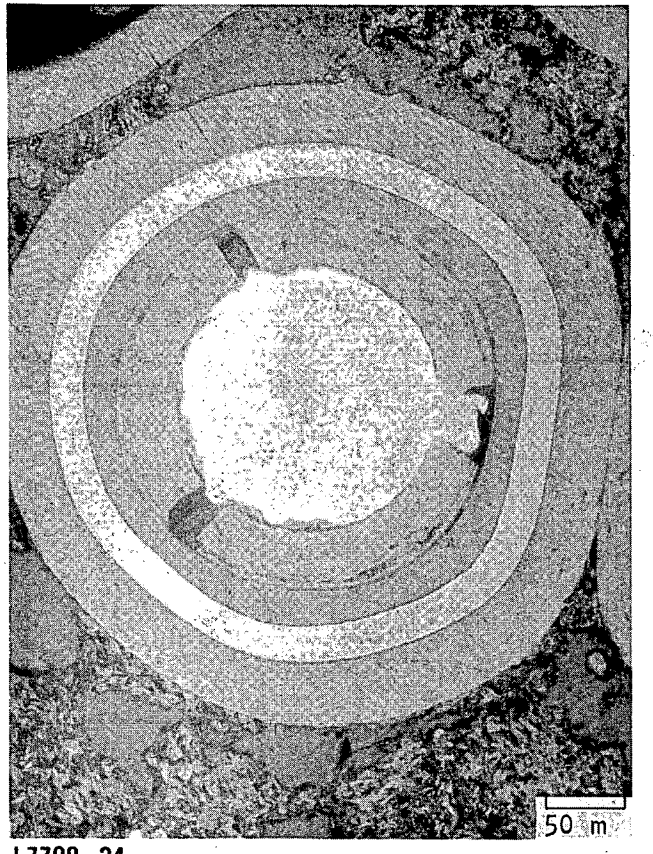

Fig. 8-14. $(Th,U)C_2$ kernel deformation and cracking: (a) fuel rod 3-7-2 from FTE-5, irradiation conditions 3.3×10^{25} n/m^2 [E > 29 fJ)$_{HTGR}$] at 1147°C; and (b) fuel rod 3-5-4 from FTE-16, irradiation conditions 2.0×10^{25} n/m^2 [E > 29 fJ$_{HTGR}$] at 1093°C

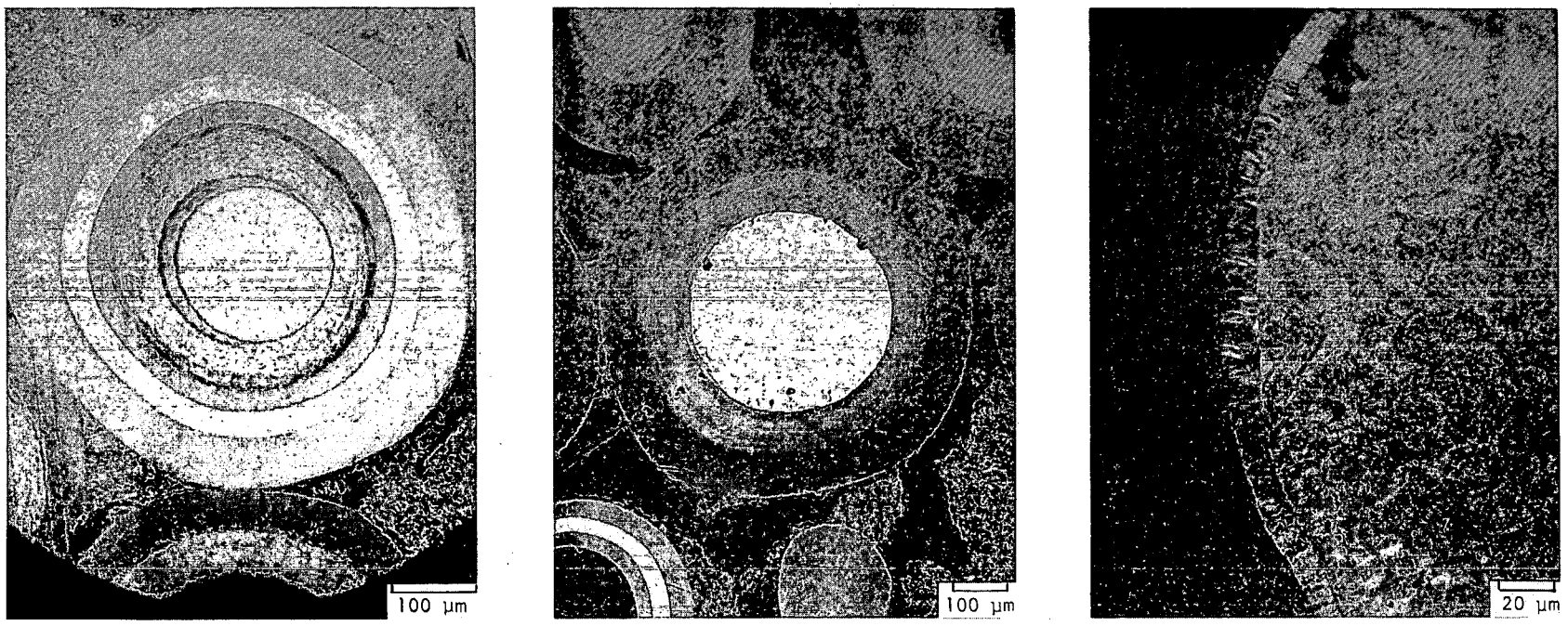

Fig. 8-15. $(Th,U)O_2$ and ThC_2 kernel migration: (a) $(Th,U)O_2$ kernel from fuel rod 2-4-7 in FTE-14, irradiation conditions 1.4×10^{25} n/m^2 $[(E > 29\ fJ)_{HTGR}]$ at 1244°C; (b) ThC_2 kernel from fuel rod 2-1-5 in FTE-15, irradiation condition 2.0×10^{25} n/m^2 $[(E > 29\ fJ)_{HTGR}]$ at 1386°C; and (c) high-magnification dark field of rejected carbon in ThC_2 particle

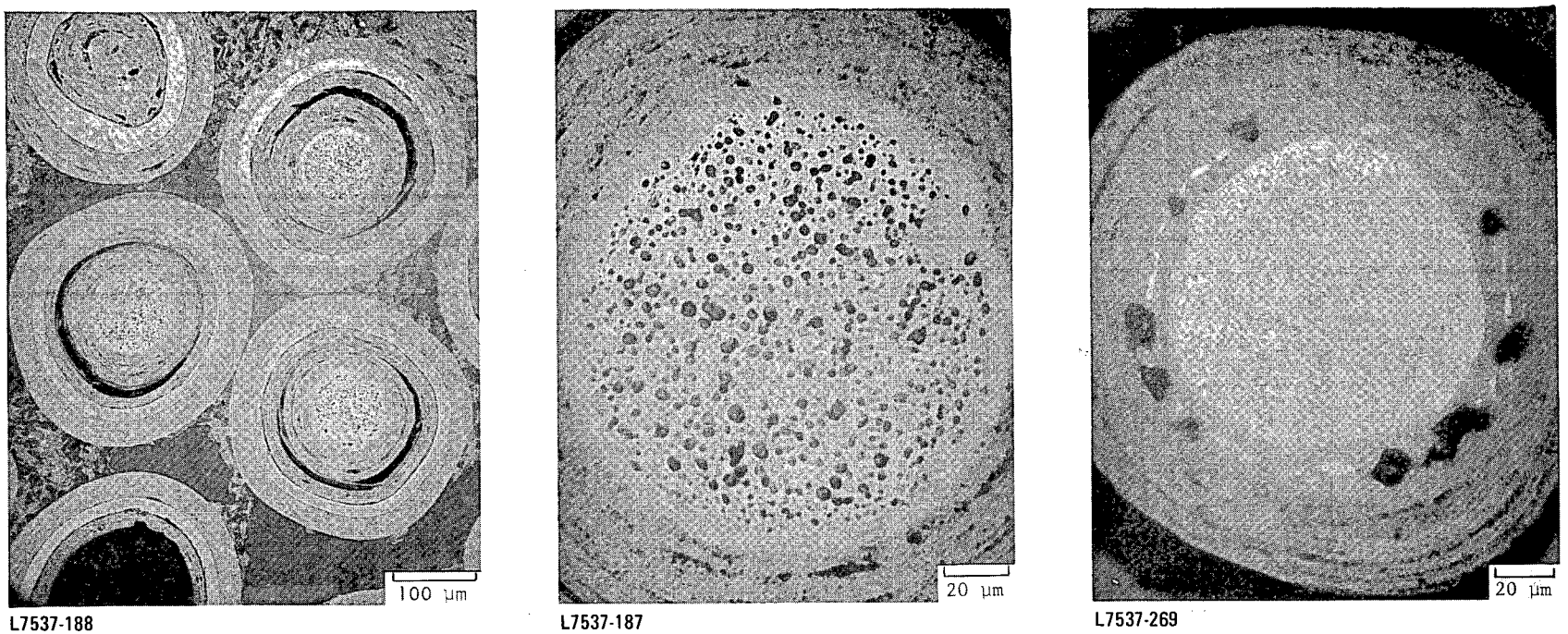

Fig. 8-16. UC_2 kernel morphology of TRISO particles from FTE-5 fuel rod 1-5-3 and comparison of UC_2 kernel structure with particles from rod 3-5-2. Irradiation conditions: rod 1-5-3, 1.9×10^{25} n/m^2 [$(E > 29\ fJ)_{HTGR}$] at 755°C and rod 3-5-2, 3.3×10^{25} n/m^2 [$(E > 29\ fJ)_{HTGR}$] at 1150°C: (a) bright field of three typical UC_2 particles in rod 1-5-3, (b) high magnification of UC_2 kernel in fuel rod 1-5-3, and (c) high magnification of UC_2 kernel in fuel rod 3-5-2.

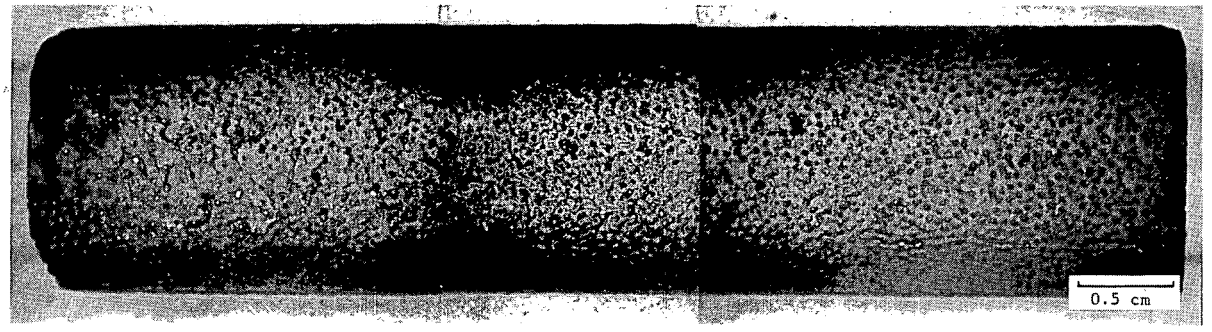

S7437 (123-125)

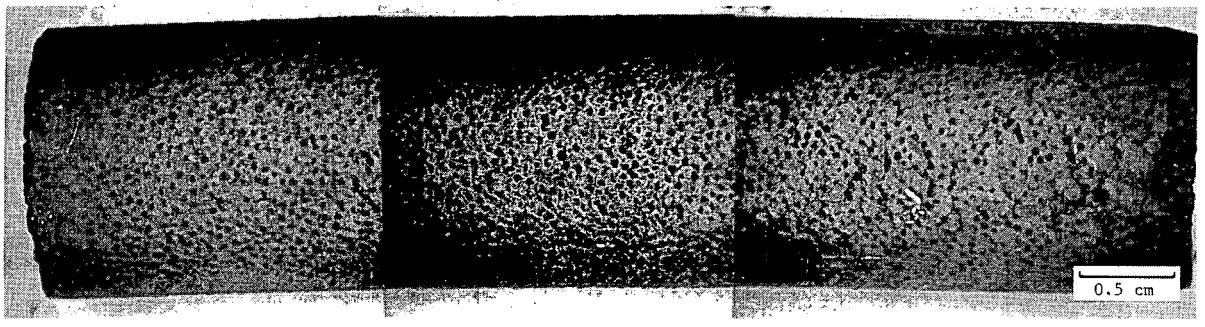

S7437 (127-129)

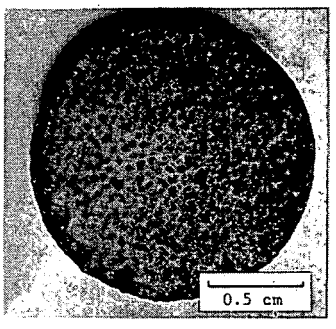

S7437-122

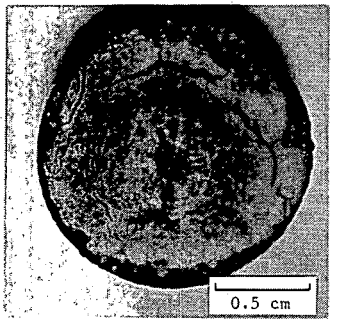

S7437-121

Fig. 8-17. Visual examination of FTE-6 fuel rod 2-6-7. Irradiation conditions: ~2.8 x 10^{25} n/m^2 [(E > 29 fJ)$_{HTGR}$] at 1186°C

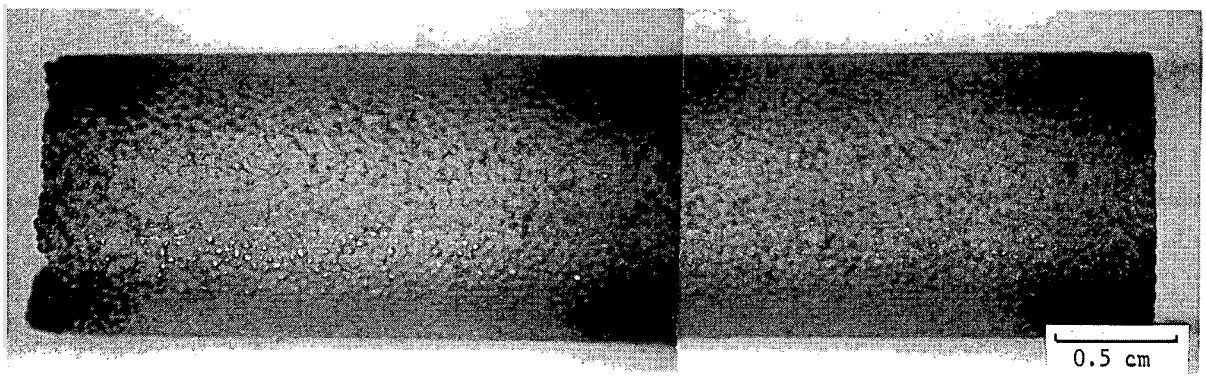

S7519 (33-34)

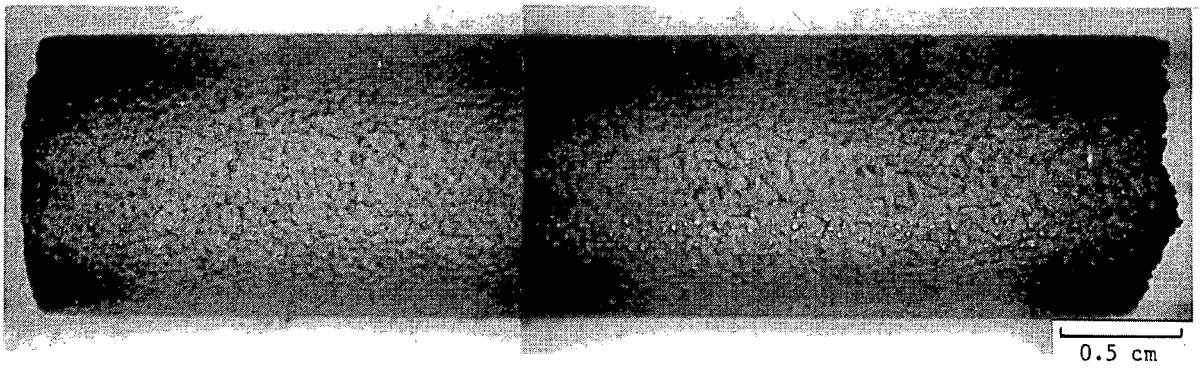

S7519 (35-36)

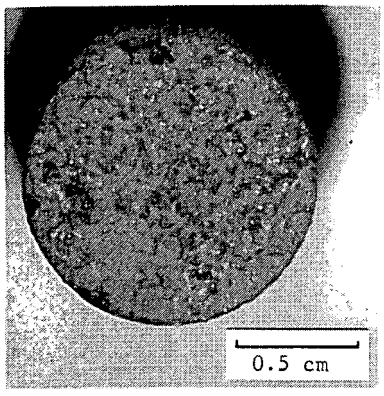

S7519-32

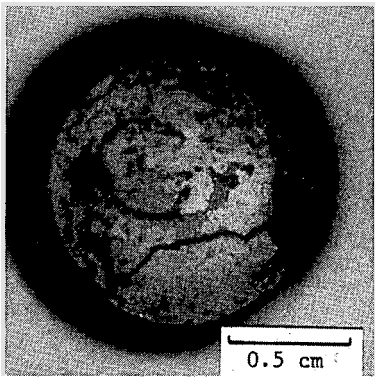

S7519-31

Fig. 8-18. Visual examination of FTE-15 fuel rod 2-1-4. Irradiation conditions: ~2.0 x 1025 n/m2 [(E > 29 fJ)HTGR] at 1380°C

9. METALLIC FISSION PRODUCT TRANSPORT

This section is a review of and commentary on the results from the metallic diffusion spine samples in the test elements. Results and analyses have been presented in previous reports, as indicated below, and some further analyses are presented here.

The major conclusions deduced from the diffusion experiments on the test elements are:

1. Cesium diffusion in H-327 graphite occurs by a non-Fickian diffusion process under irradiation conditions.
2. The diffusion coefficients for cesium and strontium decrease strongly with increasing fast neutron fluence.

The latter conclusion is deduced from the analyses presented here.

9.1. METALLIC DIFFUSION SPINE SAMPLES

9.1.1. Test Description

Sixty-four fission metal diffusion samples were irradiated in the center spines of test elements FTE-1, FTE-2, FTE-3, FTE-4, FTE-5, and FTE-6. These diffusion samples were designed to provide data on:

1. The transport properties of selected metal fission products in H-327 graphite under HTGR irradiation conditions as a function of temperature, fast neutron exposure, and metal concentration.
2. The distribution of metal fission products between matrix material and H-327 graphite (partition coefficient).

3. The effect of different matrix materials on metal migration.
4. The effect of certain getter materials on metal migration.
5. The effect of the presence of fission product metals on the migration rate of individual metals (especially strontium).

The samples contained isotopes of barium, strontium, samarium, and cesium, or mixtures of these isotopes, in varying concentrations. Several of the mixed isotope samples contained the potential getter material, magnesium fluoride. Two types of matrix material, furfuryl alcohol resin coke and calcined petroleum coke, were used. The latter material is of particular interest since it closely resembles the current HTGR reference matrix material.

An overview of the metallic diffusion spine sample program is given in Table 9-1.

9.1.2. Experimental Procedure

The spine sample in which diffusion occurred consisted of an H-327 graphite cylinder with an annular well for the source material. A cross-sectional view of the spine sample is shown in Fig. 9-1. The graphite which is interior to the annular well is termed the center post and that exterior to the annular well is termed the crucible wall. The annular well held the matrix material which contained the metal diffusants.

The metallic source materials were initially loaded as carbides into previously outgassed H-327 graphite cylinders (Fig. 9-1) in a glove box with an inert atmosphere. The carbides were formed by sorbing the metal isotopes on matrix material and converting to the carbide at 1673 K in a vacuum furnace. The conversion was accomplished by heating the loaded matrix material in a tantalum crucible lined with graphite foil to minimize contamination of the matrix with tantalum. After loading, the graphite cylinders were sealed with screw-top lids and coated with polystyrene to protect the metals from exposure to moist air, thereby preventing hydrolysis or oxidation prior to insertion into the reactor.

After irradiation and a suitable cooling period, selected cylinders were removed from the test elements, the matrix materials were separated from the cylinders and gamma-counted, and the samples were sectioned by turning the crucible walls and center posts in a glove-box-enclosed lathe, uniformly removing a layer of graphite with each section. The sections of known weight were gamma-counted using a Ge(Li) detector and a 4096-channel pulse height analyzer. Fission product concentration profiles of Cs-134, Sr-85, Ba-133, and Eu-154 in both the crucible center posts and outer walls were obtained from the gamma scanning of these radial sections. Thirty-nine of the 64 irradiated samples were subjected to analysis. The concentration profiles for diffusion spine samples irradiated in FTE-3, FTE-4, and FTE-6 are presented in Refs. 9-1, 9-2, and 9-3, respectively.

9.1.3. Analysis

The concentration profiles and matrix concentration data were analyzed to obtain diffusion coefficients, permeation coefficients, and partition coefficients.

9.1.3.1. Diffusion Coefficients. Diffusion coefficients were deduced by analysis of the concentration profiles of Cs-134, Sr-85, Ba-133, and Eu-154.

Examination of the profiles indicated that many of them were more complex than was to be expected from a single diffusing component that obeys Fick's law. Specifically, all the cesium profiles showed a component which did not correspond to a Fick's law diffusion behavior. On the other hand, the strontium and barium profiles were of the classical (Fick's law) type. The europium profiles were predominantly of the classical type, but showed in some cases an indication of a non-Fickian behavior similar to that of cesium. In a few cases, a minor non-Fickian component for strontium and barium was evident.

9.1.3.1.1. Fickian Diffusion

The analysis of the profiles which were in accordance with Fick's law was performed with the following equations. In the center post of the graphite cylinder, the concentration of diffusant, C_s, is given by

$$\frac{C_s}{C_s^o} = \left(\frac{a}{r}\right)^{1/2} \operatorname{erfc} \frac{a - r}{2\sqrt{Dt}} + \frac{(a - r)\,(Dta)^{1/2}}{4ar^{3/2}} \operatorname{ierfc} \frac{a - r}{2\sqrt{Dt}}$$

$$+ \frac{(9a^2 - 7r^2 - 2ar)Dt}{32a^{3/2}r^{5/2}} \; i^2\operatorname{erfc} \frac{a - r}{2\sqrt{Dt}} \quad , \tag{9-1}$$

where r = radial distance measured from the center line of the graphite spine sample (m),

a = radius of center post (m) (see Fig. 9-1),

C_s^o = concentration of diffusant at r = a,

D = diffusion coefficient (m^2/s),

t = time (s).

Equation 9-1 is a good approximation provided r/a is not too small and the time is small. Since the period of test element runs is short relative to the charateristic Fickian diffusion time, t_D ($t_D = a^2/4D$), diffusion equation solutions for short times are the most appropriate (Ref. 9-4).

In the case of the crucible wall, two approximate solutions apply:

1. For depths of penetration (r - b) near the inner radius b where C_s^o = concentration of the diffusant at r = b,

$$\frac{C_s}{C_s^o} = \operatorname{erfc} \frac{r - b}{2\sqrt{Dt}} \quad . \tag{9-2}$$

2. For depths of penetration (c - r) near the outer wall,

$$\frac{C_s}{C_s^L} = \text{erfc}\ \frac{c - r}{2\sqrt{Dt}} \quad , \tag{9-3}$$

where C_s^L = concentration of the diffusant at r = c.

9.1.3.1.2. Non-Fickian Diffusion

The analysis of the cesium profiles, which were not in accord with Fick's law, was performed by using a model in which the diffusant is considered to migrate on surfaces in the graphite and to undergo sorption on or in the graphite. This model could be descriptively termed the diffusion-trapping model.

The model is represented by the following equations:

$$\frac{\partial C}{\partial t} = D_s \nabla^2 C - KC \quad , \tag{9-4}$$

$$\frac{\partial S}{\partial t} = KC \quad , \tag{9-5}$$

where C = concentration of diffusant on surfaces (m^{-3}),
S = concentration of diffusant sorbed or trapped (m^{-3}),
K = frequency of sorption or trapping (1/s) (assumed constant),
D_s = surface diffusion coefficient (m^2/s).

The solutions to Eqs. 9-4 and 9-5 are as follows. For the center post,

$$C_f = (1 + Kt)\ C_f^o\ \frac{I_o\ (\theta r)}{I_o\ (\theta a)} \quad , \tag{9-6}$$

and for the crucible wall,

$$C_f = (1 + Kt) \left[C_f^o \frac{K_o(\theta c) I_o(\theta r) - I_o(\theta c) K_o(\theta r)}{K_o(\theta c) I_o(\theta b) - I_o(\theta c) K_o(\theta b)} + C_f^L \frac{I_o(\theta b) K_o(\theta r) - K_o(\theta b) I_o(\theta r)}{K_o(\theta c) I_o(\theta b) - I_o(\theta c) K_o(\theta b)} \right] , \quad (9\text{-}7)$$

where $C_f = C + S$,

C_f^o = concentration of diffusant at r = a and r = b,

C_f^L = concentration of diffusant at r = c,

$\theta = K/D_s$,

$I_o(y)$, $K_o(y)$ = modified Bessel functions of order zero.

The values of θ were treated as follows. The flux of atoms, J, due to surface diffusion is a function of position r; it is independent of time once the quasi-steady state is reached. With cylindrical geometry, it is given by

$$J = -D_s \frac{dC}{dr} . \quad (9\text{-}8)$$

In terms of the total concentration (which is determined by analysis of the experimental data), D_{eff} is defined so that

$$J = -D_{eff} \left(\frac{dC_f}{dr} \right) . \quad (9\text{-}9)$$

Then from Eqs. 9-8 and 9-9 and the relation $C_f = C + S = C(1 + Kt)$,

$$D_{eff} = \frac{D_s}{1 + Kt} , \quad (9\text{-}10)$$

which, for Kt >> 1, becomes

$$D_{eff} = 1/\theta t \ . \qquad (9\text{-}11)$$

There is an uncertainty associated with selecting the proper value of time to be used in Eq. 9-11 since the power level of the reactor varied in time. Several definitions and the corresponding values of time are given in Table 9-2 along with the choices made in the previous analyses (Refs. 9-1 through 9-3). Further analysis in this matter is desirable, but in any event, the error introduced by the referenced choices will be less than about 20%.

9.1.3.1.3. Ingress Analysis

In some FTE diffusion spine samples, fission product metals from fuel rods adjacent to the spine samples entered the spine sample, migrating as far into the sample as the center post. In these cases, estimates of the diffusion coefficient, made only for cesium, were derived from the apparent time-integrated flux of cesium through the crucible wall into the matrix material. Since the matrix is highly sorptive, it acts as a sink for diffusant permeating the crucible wall. Therefore, the cesium loading in the matrix was assumed to be a measure of the integrated flux through the crucible wall (assuming insignificant cesium loss to the center post graphite). The diffusion coefficient of cesium in graphite was derived from the matrix loading using the following analysis. The linear matrix density was calculated using

$$\sigma_{m_1} = (b^2 - a^2)(\pi)\ (\sigma_{m_s}) \ , \qquad (9\text{-}12)$$

where σ_{m_1} = mass of matrix per millimeter of crucible length (mg/mm),

b = radius at crucible wall liner surface (7.6 mm),

a = radius at center post outer surface (5.6 mm),

σ_{m_s} = matrix density (~0.82 mg/mm^3).

Using these values, a linear matrix density of 68.0 mg/mm was calculated. The flux of cesium into the matrix was computed using

$$\bar{J} = \frac{(C_m)(\sigma_{m_1})}{(t)(\pi)(2b)} \quad , \tag{9-13}$$

where $\bar{J}$ = mean flux ($\mu g/mm^2$ x s),

C_m = Cs-134 concentration in the matrix material ($\mu g/mg$),

t = real time.

The computer value of $\bar{J}$ is used to calculate D_{eff} for the case of a hollow cylinder as follows (Ref. 9-3):

$$D_{eff} = \frac{(\bar{J})(2)(b)\ell n(c/b)(10^{-6})}{(C_\ell)(\sigma_g)} \quad , \tag{9-14}$$

where D_{eff} = effective diffusion coefficient (m^2/s),

C_ℓ = extrapolated concentration of cesium at the outer crucible wall boundary ($\mu g/mg$),

c = outer radius of crucible (12.7 mm),

σ_g = graphite density (1.75 mg/mm^3).

9.1.3.1.4. Calculations

Diffusion coefficients for the fission metals in the various spine samples were obtained by using the CPROFIT (Concentration Profile Fit) computer code.* CPROFIT employs a nonlinear least-squares fitting technique similar to that suggested by Bevington (Ref. 9-5). It is designed so that concentration profiles are divided into two or more regions and components are sequentially analyzed so that least-squares fits are obtained with the concentration equations deemed appropriate. The optional functions used by the CPROFIT code for curve-fitting are discussed in detail in Ref. 9-1.

*The CPROFIT code was devised by L. R. Zumwalt; see Ref. 9-1.

Spine sample temperatures were obtained from TREVER thermal analyses and have been weighted by the activation energy factor

$$W_i = \frac{\Delta t_i \exp(-Q/RT_i)}{\Sigma_i \Delta t_i \exp(-Q/RT_i)} \quad , \tag{9-15}$$

where T_i = temperature (K),
Δt_i = time at temperature T_i,
Q = activation energy (J/mol),
R = gas constant (8.3147 J/K·mol).

This factor was used because changing temperatures bring about dissimilar changes in the rate of diffusion of metals having different activation energies. For strontium, barium, and europium, Q = 267 J/mol (Ref. 9-6) was used, and for cesium, Q = 144 kJ/mol (Ref. 9-7) was used.

9.1.3.2. Permeation Coefficients. From the results of the diffusion spine sample analyses, a permeation coefficient can be derived. The permeability coefficient was defined as

$$K_m = D_{eff}(C_f^o/C_m) \quad , \tag{9-16}$$

where C_m is the diffusant concentration in the matrix. The quantity $C_f^o/C_m \equiv \phi_f$ is thus needed to obtain K_m from the diffusion coefficients derived via Eq. 9-11 or 9-14.

9.1.3.3. Partition Coefficients. The partition coefficient can be calculated from the concentration data obtained in the metallic diffusion spine samples. The partition coefficient, ϕ, is defined as follows:

$$\phi = \frac{C_m}{C_g} = \frac{\text{concentration of metal in matrix material}}{\text{concentration of metal in graphite}} \tag{9-17}$$

at equilibrium in a system consisting of a matrix material specimen, a graphite specimen, and a quantity of metal. Such a system is approximated by the region of the diffusion spine samples on both sides of the boundary between the matrix material source (contained in the annular well as shown in Fig. 9-1) and the graphite. In deriving the partition coefficient from the metal concentrations in the source and graphite at their boundary, the assumption of equilibrium has to be made. This assumption is generally acceptable in analyzing the metallic diffusion spine samples, as is substantiated by comparing the so-derived partition coefficients with those obtained under known equilibrium conditions.

In the analysis of the metallic diffusion spine samples, Section 9.1.3.2., a different partition coefficient was defined as

$$\phi_f = \frac{\text{concentration of metal in matrix material}}{\text{surface-diffusion-dependent concentration of metal in graphite}} \quad (9\text{-}18)$$

The denominator of ϕ_f represents the concentration of metal at the boundary of the graphite next to the matrix material that would have resulted from only surface diffusion and the accompanying sorption on the graphite. Thus, ϕ_f depends on the adoption of a particular transport model and does not take into account the actual (total) concentration of metal in the graphite at the boundary next to the matrix material. ϕ_f is useful for defining a permeation coefficient for transport of metal through the graphite by the mechanism of surface diffusion with accompanying sorption.

The failure in subsequent analyses (Refs. 9-2, 9-3) to maintain the distinction between ϕ and ϕ_f has led to erroneous conclusions (Ref. 9-2). This will be rectified below.

9.1.4. Results

9.1.4.1. Cesium.

9.1.4.1.1. Diffusion Coefficients

A representative profile for Cs-134 for the center post is shown in Fig. 9-2. The profile is seen to consist of two regions.

The first region consists of a sharp decline in cesium concentration beginning at a boundary concentration of about 0.003 mg Cs/g graphite at $a - r \tilde{\sim} 0.0$. The latter concentration represents the concentration of cesium in the graphite in equilibrium with the concentration of cesium in the adjacent matrix material, as will be discussed in Section 9.1.4.1.2. If the diffusion were Fickian, then the predicted profile would be the dashed line in Fig. 9-2. Clearly, this accounts only for the region of sharp decline. Therefore, the main mechanism for transport of cesium in H-327 graphite is non-Fickian.

The second region, consisting of the bulk of the profile data in Fig. 9-2, can, however, be fit according to the diffusion-trapping model. This is shown by the solid line in Fig. 9-2.

In past analyses (Refs. 9-1, 9-2, 9-3), the first region has been attributed to Fickian diffusion of cesium. However, the first region is not always prominent, and there is some indication that the temperature dependence of the diffusion coefficients derived by assuming Fickian diffusion in this region is weak in contrast to that for normal bulk diffusion processes.

Another possible interpretation of the first region could involve the equilibration between the concentration of cesium in the matrix material adjacent to the graphite boundary and the concentration of cesium vapor over the matrix material. The area of the graphite surfaces directly accessible to cesium vapor would be expected to decline rapidly with depth of penetration into the graphite.

The interpretation of the first region as a diffusion phenomenon is not certain. In the present summary and analysis, diffusion coefficients

derived from the data of this region for cesium as well as other elements will not be treated further. However, since attribution of diffusion to the first region has been made in prior analyses (Refs. 9-1, 9-2, 9-3), the results of these analyses are presented in the tables of this report. In these prior analyses of the cesium data, the first region has been termed the "slow component" and the second region has been termed the "fast component" of diffusion.

An example of the cesium profiles observed in spine samples which were dominated by cesium ingress from the adjacent fuel rods is shown in Fig. 9-3. Besides the moderately steep profile in the crucible wall, as shown in Fig. 9-3, a much flatter profile was found in the center post. This kind of data was analyzed by the method of Section 9.1.3.1.3.

The results of the analyses of the Cs-134 concentration profiles in the diffusion spine samples are summarized in Tables 9-3 and 9-4. The data in these tables are taken from Refs. 9-1 through 9-3. The effective diffusion coefficients, D_{eff}, from Table 9-3 are plotted versus reciprocal temperature in Fig. 9-4. Also, the reference curve (Ref. 9-6) and the associated 95% confidence bands are shown in Fig. 9-4.

The values of D_{eff} in Fig. 9-4 show a very large scatter. There are two factors which significantly contribute to this scatter. As will now be demonstrated, these are the effect of neutron fluence and the effect of source concentration. The data to be used in demonstrating these effects will include those from out-of-pile tests on H-327 graphite and from the FTE-3 and FTE-6 experiments. At present, the data from FTE-4 and FTE-5 have not been analyzed for these effects.

The least-squares fits to the values of D_{eff} as a function of the source concentration, C_m, for the data of Ref. 9-8 and of Table 9-3 for FTE-3 and FTE-6, are shown in Fig. 9-5. This figure clearly illustrates that:

1. The D_{eff} values decrease with decreasing source concentration, C_m.

2. The D_{eff} values decrease with increasing fast neutron fluence, at a fixed source concentration.
3. The functional dependence of D_{eff} on C_m is independent of fast neutron fluence, at least up to 2.2×10^{25} n/m^2.

For Fig. 9-5, all data used in the least-squares analysis were normalized to a temperature of 1233 K by use of the factor exp[14.525 (1233/T - 1)]. This factor corresponds to an activation energy of 148.9 kJ/mol, which is the value deduced in Ref. 9-7.

A clear portrayal of the effect of neutron fluence is given in Fig. 9-6, where the ratio D_o/D_f is plotted versus fast fluence. Here D_o is the diffusion coefficient at zero fast fluence and D_f is the diffusion coefficient at fast fluence, f. The ratio D_o/D_f is the factor by which the transport coefficient is reduced. In addition to the data on H-327 graphite from out-of-pile, FTE-3, and FTE-6 experiments, Fig. 9-6 includes a datum based on experiments with H-451 graphite at a fast fluence of about 4.5×10^{25} n/m^2. The combination of all the data in Fig. 9-6 indicates that the dependence of D_o/D_f on fast fluence is roughly linear.

9.1.4.1.2. Partition Coefficients

A reanalysis of the cesium data from the diffusion spine samples in FTE-3, FTE-4, and FTE-6 to determine the partition coefficient, ϕ (see Eq. 9-17) has been performed. The results are presented in Table 9-5. The values of C_m were taken from Table 9-3, and the values of C_g were obtained by extrapolating near-surface cesium concentration data, such as those shown in Fig. 9-2, to the graphite boundary (equivalent to zero penetration depth).

From the data of Table 9-5, the following conclusions can be drawn:

1. The partition coefficients, ϕ, from the FTE-3 data have values of the order of 200 for those cases in which the matrix material

is resin based. These values are consistent with those previously found for tests involving unirradiated, resin-based matrix materials (Ref. 9-9).

2. The partition coefficients, Φ, for the FTE-3 data for those cases in which the matrix is based on petroleum coke have values in the range 7 to 20, which is consistent with results previously found (Ref. 9-7) in tests involving petroleum-coke-based matrix material.
3. The partition coefficients for the resin-based matrix material decrease with increasing fast fluence experienced by the diffusion spine samples. This behavior is consistent with the observations (Ref. 9-7) that the sorptivity of the graphite increases while that of the matrix material remains unchanged as the fast fluence increases.
4. There is only a slight temperature dependence for ϕ in those cases involving resin-based matrix material. As the temperature increases, ϕ decreases.

The values of the ratio ϕ_f (see Eq. 9-18) have been previously calculated and are given in Table 9-3. These ratios show the same relationship between resin-based and petroleum-coke-based matrix materials as the values of ϕ discussed above. Otherwise, the interpretation of ϕ_f is not simple and will not be treated further here. (See discussion in Section 9.1.3.3.)

Finally, the presence of the getter material, MgF_2, in the matrix material of crucible 55 in FTE-3 apparently had no significant effect on the sorptivity of cesium in the matrix.

9.1.4.2. Strontium.

9.1.4.2.1. Diffusion Coefficients

An example of a profile for Sr-85 for the center post is presented in Fig. 9-7. As shown, the bulk of these data can be resonably fit with

a model based on Fickian diffusion. This is found to be true for all strontium profiles. However, some profiles from FTE-3 experiments with higher concentrations give, in addition, a hint of a non-Fickian contribution to the diffusion; most profiles give no such indication.

The profile in Fig. 9-7 exhibits the effect of a "depletion" of strontium near the matrix boundary. This has been attributed (Ref. 9-1) to a lowering of the temperature during the latter part of the irradiation. Since the partition coefficient (Eq. 9-17) for strontium is inversely proportional to the temperature (Ref. 9-6), a lower temperature results in a smaller strontium graphite concentration relative to the approximately constant strontium matrix material concentration.

The results for all data on strontium are given in Table 9-6 and plotted in Fig. 9-8. The reference curve (Ref. 9-6) is also shown.

As in the case of the cesium diffusion coefficients, the data for the strontium diffusion coefficients in Fig. 9-8 show a large scatter. The factor that significantly contributes to this is the effect of neutron fluence. The effect of source concentration, which was important in the case of cesium, is not important for the strontium data because C_m values for strontium in the FTE-3, -4, and -6 experiments were low. To demonstrate the effect of neutron fluence on strontium diffusion coefficients, the data of Table 9-5 will be used with one exception, as discussed below.

The effect of neutron fluence is shown in Fig. 9-9, where the ratio D_o/D_f is plotted versus the fast fluence. As in Fig. 9-6, the ratio D_o/D_f is the factor by which the transport coefficient is reduced. The ratios plotted in Fig. 9-9 represent out-of-pile data (Ref. 9-6) and data from FTE-3, -4, and -6 experiments. Included in Fig. 9-9 is the curve for the corresponding data for cesium from Fig. 9-6. Based on Fig. 9-9, the following conclusions are evident:

1. The dependence of D_o/D_f on fast neutron fluence is roughly linear.

2. The dependence of D_o/D_f on fast neutron fluence for strontium is essentially the same as that for cesium, at least for fast fluences up to 2.2×10^{25} n/m^2.

For Fig. 9-9, all data used were normalized to a temperature of 1233 K by use of the factor exp[26.143(1233/T - 1)]. This factor corresponds to an activation energy of 268 kJ/mol, which is the value deduced in Ref. 9-6.

The data from crucible 55 of FTE-3 were excluded from the analysis because of the unusually high, total-metal source loading, which apparently increased the diffusion rate.

9.1.4.2.2. Partition Coefficients

The partition coefficients obtained from the analyses of the strontium-loaded samples in FTE-3 are quite small (≈2.0) and independent of temperature. They are smaller than the reference design data. The partition coefficients for sample 55, which contained the getter material MgF2, were much larger than for other samples. However, the unusually high, total-metal matrix loading of this sample may have had an influence on the partition coefficient. Thus, the interpretation of the large Φ values is not clear. Determination of partition coefficients for the strontium samples in FTE-4 and FTE-6 was precluded by the inability to establish the Sr-85 concentration in the matrix.

There are no other data with which the partition coefficients for strontium given in Table 9-6 may be directly compared. The data from Table 9-6 show an increase of ϕ with increase in the matrix concentration of strontium. This dependence is not found for the cesium partition coefficients.

9.1.4.3. Barium. The Ba-133 concentration profiles in the diffusion spine samples can be analyzed in terms of diffusion according to Fick's law. As with strontium, the higher-concentration profiles suggest a

minor contribution from a non-Fickian diffusion process, and there is evidence in many samples of a depletion effect near the matrix boundary.

The results of the analyses of Ba-133 concentration profiles in the diffusion spine samples are summarized in Table 9-7. It should be noted that the diffusion coefficients for crucible 55 of FTE-3 are high because of a high, total metal loading of the matrix, and the diffusion coefficient from the center post of crucible 45 of FTE-3 is high because of a back-diffusion contribution to the profile (Ref. 9-1). The diffusion coefficient results from FTE-4 amd FTE-5 are suspect, since only data near the graphite-matrix boundary were used in deriving them (see Section 9.1.4.1.1). Because of these irregularities, the barium diffusion coefficients have not been further analyzed.

9.1.4.4. Europium. The Eu-154 concentration profiles in the diffusion spine samples exhibited predominantly Fickian diffusion, but a number of them had well-developed profiles which resulted from a non-Fickian diffusion process similar to that for cesium. An example of this behavior is shown in Fig. 9-10. As in the case of strontium and cesium, a depletion effect in the graphite near the source matrix was observed. Evidence of europium ingress through the outer wall of the diffusion spine crucibles is provided by a number of the profiles.

The results of the analysis of Eu-154 concentration profiles in the diffusion samples is summarized in Table 9-8. Again, as in the case of barium, the data from crucible 55 of FTE-3 are considered to be high, and the data from FTE-4, -5, and -6 are difficult to evaluate since the concentration data used in deriving the diffusion coefficients in Table 9-8 are from graphite locations near the graphite-matrix boundary. In addition, the crucible wall data from crucible 24 of FTE-3 yield a partition coefficient which is 10^2 to 10^3 times larger than the partition coefficients obtained from other europium data. In view of these irregularities, further analysis of the europium data is not presented here.

9.1.5. Summary

The results from the analyses of the Cs-134, Sr-85, Ba-133, and Eu-154 concentration profiles on the metallic diffusion spine samples irradiated in Peach Bottom fuel test elements are summarized below. Included are the results presented above and in previous reports (Refs. 9-1 through 9-3).

1. Cesium diffusion in H-327 graphite occurs by a non-Fickian diffusion process. The cesium concentration profiles can be reasonably described by a model, first applied to these data by Zumwalt (Ref. 9-1), in which cesium is considered to migrate on surfaces in the graphite and to undergo sorption on the graphite. The validity of this model for predicting release of cesium from the graphite has yet to be established.

2. The diffusion of strontium, barium, and europium through H-327 graphite proceeds primarily according to Fick's law, although indications of a minor non-Fickian contribution were seen in a few strontium and barium profiles and were more strongly indicated in a number of europium profiles.

3. The diffusion coefficients for cesium and strontium decrease strongly with increasing fast neutron fluence. For both cesium and strontium, the effective diffusion coefficient was reduced by a factor of 20 for each increase of 10^{25} n/m^2 $[(E > 29 \text{ fJ})_{HTGR}]$ in fast fluence. The data for barium and europium were too uncertain to permit a similar conclusion.

4. The diffusion coefficient for cesium increases with increasing cesium concentration in the matrix material. The relationship between the diffusion coefficient and the cesium matrix concentration is independent of fast neutron fluence. This effect was not observed for strontium, barium, and europium. However,

this may be more indicative of a lack of data than an absence of the effect.

5. The interpretation of concentration profile data in the graphite near the graphite-matrix material boundary is ambiguous. They were variously interpreted as evidence of bulk diffusion, surface effects, sectioning technique, or equilibration of diffusant between matrix material and graphite.

6. In many of the strontium, barium, and europium profiles, the concentration profile passed through a maximum as the depth of penetration increased. The initial rise was termed a depletion effect and was attributed to back-diffusion resulting from a decrease in temperature in the latter part of the irradiation period.

7. The partition coefficients derived from the cesium data are consistent with values previously found for both resin-based and petroleum-coke-based matrix materials. The partition coefficients for the resin-based matrix material decrease with increasing fast neutron fluence as expected. Data on the petroleum-coke-based matrix material were too few to analyze in this way.

8. Partition coefficients for strontium, barium, and europium involving resin-based matrix materials were derived.

9. The getter material, MgF_2, had apparently no effect on the behavior of cesium, barium, and europium. In the case of strontium, no deduction could be made.

10. No indication that the presence of other fission product metals affects the migration of a particular fission metal was found.

REFERENCES

9-1. Wallroth, C. F., et al., "Postirradiation Examination of Peach Bottom Fuel Test Element FTE-3," USAEC Report GA-A13004, August 15, 1974.

9-2. Wallroth, C. F., et al., "Postirradiation Examination of Peach Bottom Fuel Test Element FTE-4," ERDA Report GA-A13452, July 1977.

9-3. Wallroth, C. F., J. F. Holzgraf, and D. D. Jensen, "Postirradiation Examination and Evaluation of Peach Bottom Fuel Test Element FTE-6," ERDA Report GA-A13943, September 1977.

9-4. Crank, J., Mathematics of Diffusion, Oxford University Press, Oxford, England, 1957, p. 66.

9-5. Bevington, P. R., Data Reduction and Error Analysis for the Physical Sciences, McGraw-Hill Book Company, New York, 1969.

9-6. Myers, B. F., and W. E. Bell, "Strontium Transport Data for HTGR Systems," USAEC Report GA-A13168, December 6, 1974.

9-7. Myers, B. F., and W. E. Bell, "Cesium Transport Data for HTGR Systems," DOE Report GA-A13990, September 1979.

9-8. Chandra, D., and J. H. Norman, "Diffusion of Cesium Through Graphite," J. Nucl. Mater. 62, 293 (1976).

9-9. "Public Service Company of Colorado 330-MW(e) High-Temperature Gas-Cooled Reactor Research and Development Program, Quarterly Progress Report for the Period Ending June 30, 1968," USAEC Report GA-8725, July 29, 1968.

TABLE 9-1
OVERVIEW OF PEACH BOTTOM TEST ELEMENT DIFFUSION SPINE SAMPLES

Element(s)	Matrix Material	Approximate Metal Conc.[b]	Crucible Identification Numbers					
			Phase 1			Phase 2		
			FTE-1	FTE-2	FTE-5	FTE-3	FTE-4	FTE-6
Cs	RC[a]	Low		2	1			
		Medium				3,5		
		High					4,6	
Sr	RC	Low	15	8,14,20	9			
		Medium				11,16	10,21	17
		High					12,18,22	13,19
Sm	RC	Low		25				
		Medium						23
		High				24	27,28	26
Ba	RC	Low	36	32	29			
		Medium				30	34	33
		High				31,35,37		
Cs, Sr, Sm, Ba	RC	Low	39,43	47	38,44			
		Medium				45	41	40
		High				42	46,49	
Cs, Sr, Sm, Ba + 1% MgF	RC	Low	56	50	53			
		Medium					54	51
		High				55	52,58	
Cs, Sr, Sm, Ba + 0.5% S	CPC[c]	Low		59,62	65			
		Medium				63,66		60
		High					61,64,67	

[a] Furfuryl alcohol/resin coke matrix.

[b] Concentrations are of the order of 0.1, 1, and 10 mg/g for low, medium, and high, respectively.

[c] Calcined petroleum coke matrix.

TABLE 9-2
FTE IRRADIATION TIMES

Element	Real Time[a] (days)	Time at Significant Power[b] (days)	Effective Full Power Days[c]	t[d] Eq. (9-11) (days)
FTE-3	159	144	133	133
FTE-4	536	507	449	536
FTE-5	1068	1035	897	1034
FTE-6	792	765	645	792

[a] Real time is the time reactor power was non-zero.

[b] Time at significant power is the real time minus the time at very low power.

[c] Effective full power day (EFPD) is a reactor day equivalent to a day at 115.0 MW(t).

[d] t is the time used in evaluating Eq. 9-11 in Refs. 9-1 through 9-3.

TABLE 9-3
RESULTS OF ANALYSES OF CESIUM CONCENTRATION PROFILES (FAST COMPONENT) IN PEACH BOTTOM DIFFUSION SPINE SAMPLES

Crucible No.[a]	Test Element	Activation Energy Weighted Temp.		Neutron Fluence ($\times 10^{25}$ n/m^2)		C_m[d] (μg/mg)	$\bar{J}$[e] (μg/mm^2-s)	C_l[f] (μg/mg)	D_{eff} (m^2/s)	C_g[g] (μg/mg)	ϕ_f[h] (C_m/C_g)
		K	10^4/T(K)	Thermal[b]	Fast[c]						
3(P)	FTE-3	1039	9.62	0.35	0.40	9.5-2[i]	--	--	9.2-13	8.3-6	11,400
3(w)		1039	9.62	0.35	0.40	9.5-2	--	--	1.3-13	3.2-5	3,000
16(w)		1209	8.27	0.33	0.28	4.0-3	5.0-10		1.5-13	5.0-6	800
42(P)		1155	8.66	0.45	0.48	5.3-1	--	--	2.3-12	3.9-4	1,360
42(w)		1155	8.66	0.45	0.48	5.3-1	--	--	2.2-12	4.1-4	1,290
45(P)		1198	8.35	0.32	0.26	2.8-2	--	--	4.2-12	3.3-5	850
45(w)		1198	8.35	0.32	0.26	2.8-2	--	--	6.7-13	4.0-5[j]	700
55(P)		1175	8.51	0.30	0.22	4.0-1	--	--	2.8-12	1.2-3	350
55(w)		1175	8.51	0.30	0.22	4.0-1	--	--	1.1-12	1.3-3	310
63(P)		1187	8.42	0.31	0.24	1.2-2	--	--	2.7-12	3.2-4	38
63(w)		1187	8.42	0.31	0.24	1.2-2	--	--	N.D.	3.0-4[j]	40
66(P)		1330	7.52	0.65	0.60	1.3-2	--	--	1.3-12	9.2-4	14
10(P)	FTE-4	1200	8.33	1.95	1.48	1.86-2	--	--	4.5-13	3.0-5	620
10(w)		1200	8.33	1.95	1.48	1.86-2	6.83-10	5.0-4	3.6-12		
12(P)		1180	8.47	1.85	1.42	1.14-2	--	--	5.3-13	6.8-6	1,670
12(w)		1180	8.47	1.85	1.42	1.14-2	4.18-10	7.0-4	1.6-12		
18(P)		1305	7.66	2.55	1.80	1.52-2	--	--	7.3-13	5.0-5	304
18(w)		1305	7.66	2.55	1.80	1.52-2	5.78-10	3.0-4	5.0-12		
22(P)		1415	7.07	2.79	1.94	5.01-4			1.4-12	9.0-6	56
22(w)		1415	7.07	2.79	1.94	5.01-4	1.84-11	2.0-4	2.4-13		
31(P)		1159	8.63	1.74	1.36	1.19-2			4.7-13	7.5-6	1,590
31(w)		1159	8.63	1.74	1.36	1.19-2	4.37-10	4.0-4	2.9-12		
41(P)		1136	8.80	1.64	1.30	6.68-2	--	--	3.3-13	1.7-5	3,930
13(w)	FTE-6	1208	8.28	2.37	2.04	3.32-3	6.9-11	4.0-4	7.6-13	1.5-5	221
17(w)		1367	7.32	3.46	2.63	1.31-3	2.7-11	5.6-4	2.1-13	3.0-5	44
19(w)		1367	7.32	3.59	2.70	1.78-3	3.7-11	4.2-4	3.9-13	3.0-5	59
33(w)		1380	7.25	3.54	2.67	1.22-3	2.5-11	4.2-4	2.6-13	3.0-5	41
40(P)		1122	8.91	1.90	1.70	6.85-2	--	--	2.7-13	3.0-4	228
40(w)		1122	8.91	1.90	1.70	6.85-2	--	--	5.8-14		
60(P)		1184	8.45	2.22	1.95	3.99-2	--	--	3.8-13	1.0-3	40
60(w)		1184	8.45	2.22	1.95	3.99-2	--	--	3.7-13		
1(P)	FTE-5	1088	9.20	2.85	2.35				4.4-13	3.4-6	
1(w)		1088	9.20	2.85	2.35				6.0-14	1.9-3?	
9(P)		1123	8.90	3.08	2.50				1.0-13	1.8-6	
9(w)		1123	8.90	3.08	2.50						
29(P)		1151	8.69	3.34	2.66				2.7-13	1.7-7	
29(w)		1151	8.69	3.34	2.66						
38(P)		1178	8.49	3.51	2.75				7.6-13	6.5-6	
38(w)		1178	8.49	3.51	2.75				7.5-13	1.8-4?	

[a] P = center post; w = crucible wall.

[b] Thermal fluence: $0 < E < 0.35$ fJ.

[c] Fast fluence: $E > 29$ fJ.

[d] Matrix concentration of cesium.

[e] Time-averaged cesium flux at outer boundary of crucible wall.

[f] Extrapolated cesium concentration at outer boundary of crucible wall.

[g] Extrapolated cesium concentration in graphite crucible wall adjacent to matrix.

[h] Calculated according to Eq. 9-18.

[i] 9.5-2 = 9.5×10^{-2}.

[j] Established from graph rather than CPROFIT code fit.

TABLE 9-4
RESULTS OF ANALYSES OF CESIUM CONCENTRATION PROFILES (SLOW COMPONENT)
IN PEACH BOTTOM DIFFUSION SPINE SAMPLES

Crucible No.(a)	Test Element	Activation Energy Weighted Temp.		Neutron Fluence (x 10^{25} n/m^2)		C_m(d) (μg/mg)	Diffusion Coefficient, D (m^2/s)	C_g(e) (μg/mg)	Partition Factor, ϕ (C_m/C_g)
		K	10^4/T(K)	Thermal(b)	Fast(c)				
3(P)	FTE-3	1039	9.62	0.35	0.40	9.5-2	9.4-16	2.8-4	340
16(P)		1209	8.27	0.33	0.28	--	9.3-16	3.0-5	--
42(P)		1155	8.66	0.45	0.48	5.3-1	3.0-16	7.0-3	76
45(P)		1198	8.35	0.32	0.26	2.8-2	4.6-16	2.1-4	133
63(P)		1187	8.42	0.31	0.24	1.2-2	4.8-16	7.5-4	16
10(P)	FTE-4	1200	8.33	1.95	1.48	186.2	4.9-16	--	--
12(P)		1180	8.47	1.85	1.42	1.14-2	6.5-16	--	--
31(P)		1159	8.63	1.74	1.36	1.19-2	2.8-16	--	--
41(P)		1136	8.80	1.64	1.30	6.68-2	1.8-16	--	--
1(P)	FTE-5	1088	9.20	2.85	2.35	--	2.8-17	6.6-4	--
1(w)		1088	9.20	2.85	2.35	--	6.0-17	1.7-3	--
9(P)		1123	8.90	3.08	2.50	--	2.1-17	9.9-4	--
29(P)		1151	8.69	3.34	2.66	--	1.2-16	2.1-6	--
38(P)		1178	8.49	3.51	2.75	--	7.3-17	1.3-3	
38(w)		1178	8.49	3.51	2.75	--	5.8-17	8.3-4	--

(a) P = center post; w = crucible wall.

(b) Thermal fluence: $0 < E < 0.35$ fJ.

(c) Fast fluence: $E > 29$ fJ.

(d) Matrix concentration of cesium.

(e) Extrapolated cesium concentration in graphite crucible wall adjacent to matrix (from CPROFIT code fit of cesium profile).

TABLE 9-5
REANALYSIS OF PARTITION COEFFICIENTS, ϕ, FROM CESIUM DATA

Crucible No.[a]	Test Element	Activation Energy Weighted Temp. (K)	Mean Fast Neutron Fluence[b] ($\times 10^{25}$ n/m^2)	C_m[c] (μg/mg)	C_g[d] (μg/mg)	ϕ[e]
3(w)	FTE-3	1039	0.34	9.5(-2)	4.0(-4)	238
3(P)		1039		9.5(-2)	3.0(-4)	317
16(w)		1209		4.0(-3)	2.0(-5)	200
16(P)		1209		4.0(-3)	2.0(-5)	200
42(w)		1155		5.3(-1)	2.0(-3)	265
42(P)		1155		5.3(-1)	3.0(-3)	177
45(w)		1198		2.8(-2)	1.2(-4)	233
45(P)		1198		2.8(-2)	2.0(-4)	140
55(w)		1175		4.0(-1)	2.0(-3)	200
55(P)		1175		4.0(-1)	5.0(-3)	80
63(w)		1187		1.2(-2)	6.0(-4)	20
63(P)		1187		1.2(-2)	8.0(-4)	15
66(P)		1330		1.3(-2)	2.0(-3)	7
10(P)	FTE-4	1200	1.57	1.9(-2)	2.0(-4)	93
10(w)		1200		1.9(-2)	1.0(-4)	186
12(P)		1180		1.1(-2)	6.0(-5)	190
18B(P)		1305		1.5(-2)	2.0(-4)	76
22B(P)		1415		5.0(-4)	1.5(-5)	33
31(P)		1159		1.2(-2)	7.0(-5)	170
31(w)		1159		1.2(-2)	7.0(-5)	170
41(P)		1136		6.7(-2)	~1.0(-3)	67
41(w)		1136		6.7(-2)	~6.0(-4)	111
13(P)	FTE-6	1208	2.17	3.3(-3)	4.0(-5)	83
13(w)		1208		3.3(-3)	8.0(-5)	41
17(P)		1367		1.3(-3)	5.0(-5)	26
17(w)		1367		1.3(-3)	4.0(-5)	33
19(P)		1367		1.8(-3)	2.0(-4)	89
19(w)		1367		1.8(-3)	1.5(-4)	118

TABLE 9-5 (Continued)

Crucible No.[a]	Test Element	Activation Energy Weighted Temp. (K)	Mean Fast Neutron Fluence[b] (x 10^{25} n/m^2)	C_m[c] (μg/mg)	C_g[d] (μg/mg)	ϕ[e]
33(P)	FTE-6	1380	2.17	1.2(-3)	2.0(-4)	61
33(w)	FTE-6	1380	2.17	1.2(-3)	8.0(-5)	153
40(P)	FTE-6	1122	2.17	6.9(-2)	2.0(-3)	34
40(w)	FTE-6	1122	2.17	6.9(-2)	8.0(-4)	86
60(P)	FTE-6	1184	2.17	4.0(-2)	2.0(-3)	20
60(w)	FTE-6	1184	2.17	4.0(-2)	1.0(-3)	40

[a] P = center post; w = crucible wall.

[b] Fast fluence: E > 29 fJ.

[c] Matrix concentration of cesium.

[d] Cesium concentration in graphite at graphite-matrix boundary.

[e] Calculated according to Eq. 9-17.

TABLE 9-6
RESULTS OF ANALYSES OF STRONTIUM CONCENTRATION PROFILES IN
PEACH BOTTOM DIFFUSION SPINE SAMPLES

Crucible No.[a]	Test Element	Activation Energy Weighted Temp.		Neutron Fluence ($\times 10^{25}$ n/m^2)		C_m[d] (μg/mg)		Diffusion Coefficient, D (m^2/s)	C_g[e] (μg/mg)	Partition Factor, ϕ (C_m/C_g)
		K	10^4/T(K)	Thermal[b]	Fast[c]	Metal	Isotope			
11(P)	FTE-3	1086	9.21	0.37	0.43	0.83	3.4-4	4.6-16	1.53-4	2.2
16(P)		1218	8.21	0.33	0.28	0.83	1.5-4	8.2-14	7.4-5	2.0
16(w)		1218	8.21	0.33	0.28	0.83	1.5-4	1.1-13	6.5-5	2.3
42(P)		1166	8.58	0.45	0.48	6.55	2.1-3	8.1-15	4.0-4	5.3
42(w)		1166	8.58	0.45	0.48	6.55	2.1-3	6.3-15	3.9-4	5.4
45(P)		1207	8.29	0.32	0.26	0.46	6.7-5	2.9-14	8.0-5	0.84
45(w)		1207	8.29	0.32	0.26	0.46	6.7-5	2.5-14	1.0-4	0.66
55(P)		1183	8.45	0.30	0.22	5.48	1.3-3	4.1-13	1.4-5	92
55(w)		1183	8.45	0.30	0.22	5.48	1.3-3	1.6-13	1.9-5	70
10	FTE-4	1211	8.26	1.95	1.48	0.83	(f)	5.8-16	--	--
10		1211	8.26	1.95	1.48	0.83	(f)	2.6-16	--	--
12		1190	8.40	1.85	1.42	1.59	(f)	1.1-15	--	--
18		1316	7.60	2.55	1.80	1.59	(f)	2.1-14	--	--
18		1316	7.60	2.55	1.80	1.59	(f)	1.3-14	--	--
22		1427	7.01	2.79	1.94	1.59	(f)	1.9-13	--	--
22		1427	7.01	2.79	1.94	1.59	(f)	1.0-13	--	--
13(P)	FTE-6	1226	8.16	2.37	2.04	1.59	(f)	7.9-16	1.5-4	--
13(w)		1226	8.16	2.37	2.04	1.59	(f)	8.8-16	1.9-4	--
17(P)		1385	7.22	3.46	2.63	0.83	(f)	6.3-15	1.9-4	--
17(w)		1385	7.22	3.46	2.63	0.83	(f)	5.0-15	1.9-4	--
19(P)		1385	7.22	3.59	2.70	1.59	(f)	4.7-14	7.5-5	--
19(w)		1385	7.22	3.59	2.70	1.59	(f)	6.1-14	7.1-5	--

[a] P = center post; w = crucible wall.

[b] Thermal fluence: $0 < E < 0.35$ fJ.

[c] Fast fluence: $E > 29$ fJ.

[d] Matrix concentration of strontium.

[e] Extrapolated strontium concentration in graphite crucible wall adjacent to matrix.

[f] Undetectable above background.

TABLE 9-7
RESULTS OF ANALYSES OF BARIUM CONCENTRATION PROFILES IN
PEACH BOTTOM DIFFUSION SPINE SAMPLES

Crucible No.[a,b]	Test Element	Activation Energy Weighted Temp.		Neutron Fluence ($\times 10^{25}$ n/m^2)		C_m[e] (μg/mg)	Diffusion Coefficient, D (m^2/s)	C_g[f] (μg/mg)	Partition Factor, ϕ (C_m/C_g)
		K	$10^4/T(K)$	Thermal[c]	Fast[d]				
42(P)	FTE-3	1166	8.58	0.45	0.48	6.0-4	4.2-15	9.2-6	65
42(w)		1166	8.58	0.45	0.48	6.0-4	4.5-15	7.1-6	85
45(P)		1207	8.29	0.32	0.26	3.0-4	1.3-13	1.3-5	23
45(w)		1207	8.29	0.32	0.26	3.0-4	2.6-14	1.6-5	19
55(P)		1183	8.45	0.30	0.22	5.0-4	2.1-13	5.8-6	86
55(w)		1183	8.45	0.30	0.22	5.0-4	7.6-14	1.0-5	50
31(P)	FTE-4	1170	8.55	1.74	1.36	6.9-4	3.2-16	--	--
31(w)	FTE-4	1170	8.55	1.74	1.36	6.9-4	5.7-16	--	--
29(P)	FTE-5	1159	8.63	3.34	2.66	--	1.3-16	1.9-5	--
29(w)		1159	8.63	3.34	2.66	--	3.9-17	4.9-5	--
38(P)		1186	8.43	3.51	2.75	--	6.6-17	9.0-5	--
38(w)		1186	8.43	3.51	2.75	--	1.8-16	2.1-5	--

[a] P = center post; w = crucible wall.

[b] No barium was detected in the matrix or graphite of samples 33, 40, and 60. This was probably due to the high background activity of other isotopes present in the sample.

[c] Thermal fluence: $0 < E < 0.35$ fJ.

[d] Fast fluence: $E > 29$ fJ.

[e] Barium concentration in matrix.

[f] Extrapolated barium concentration in graphite crucible adjacent to matrix (from CPROFIT code fit of concentration profile).

TABLE 9-8
RESULTS OF ANALYSES OF EUROPIUM CONCENTRATION PROFILES IN
PEACH BOTTOM DIFFUSION SPINE SAMPLES

Crucible No.[a]	Test Element	Activation Energy Weighted Temp.		Neutron Fluence ($\times 10^{25}$ n/m^2)		C_m[d] (μg/mg)	Diffusion Coefficient, D (m^2/s)	C_g[e] (μg/mg)	Partition Factor, ϕ (C_m/C_g)
		K	10^4/T(K)	Thermal[b]	Fast[c]				
24(P)	FTE-3	1114	8.98	0.40	0.45	1.2-1	1.2-15	1.3-2	9.5
24(w)		1114	8.98	0.40	0.45	1.2-1	3.8-15	8.3-5	1500
42(P)		1166	8.58	0.45	0.48	1.1-1	1.8-15	9.6-2	1.2
42(w)		1166	8.58	0.45	0.48	1.1-1	1.9-15	6.1-2	1.8
45(P)		1207	8.29	0.32	0.26	2.6-3	1.2-14	3.1-3	0.8
45(w)		1207	8.29	0.32	0.26	2.6-3	1.2-14	2.6-3	1.0
55(P)		1183	8.45	0.30	0.22	1.8-2	1.1-13	1.7-3	10.6
55(w)		1183	8.45	0.30	0.22	1.8-2	7.6-14	1.9-3	9.3
41(P)	FTE-4	1136	8.80	1.64	1.30	2.4-2	1.5-16	--	--
41(w)	FTE-4	1136	8.80	1.64	1.30	2.4-2	1.3-16	--	--
40(P)	FTE-6	1140	8.77	1.90	1.70	2.3-2	5.7-17	1.7-2	1.4
40(w)		1140	8.77	1.90	1.70	2.3-2	4.4-17	1.1-2	2.1
60(P)		1202	8.32	2.22	1.95	1.2-1	--	--	--
60(w)		1202	8.32	2.22	1.95	1.2-1	--	--	--
38(P)	FTE-5	1186	8.43	3.51	2.75	--	8.5-17	1.5-3	--
38(w)	FTE-5	1186	8.43	3.51	2.75	--	5.4-17	1.0-3	--

[a] P = center post; w = crucible wall.

[b] Thermal fluence: $0 < E < 0.35$ fJ.

[c] Fast fluence: $E > 29$ fJ.

[d] Europium concentration in matrix.

[e] Extrapolated europium concentration in graphite crucible adjacent to matrix (from CPROFIT code fit of concentration profile).

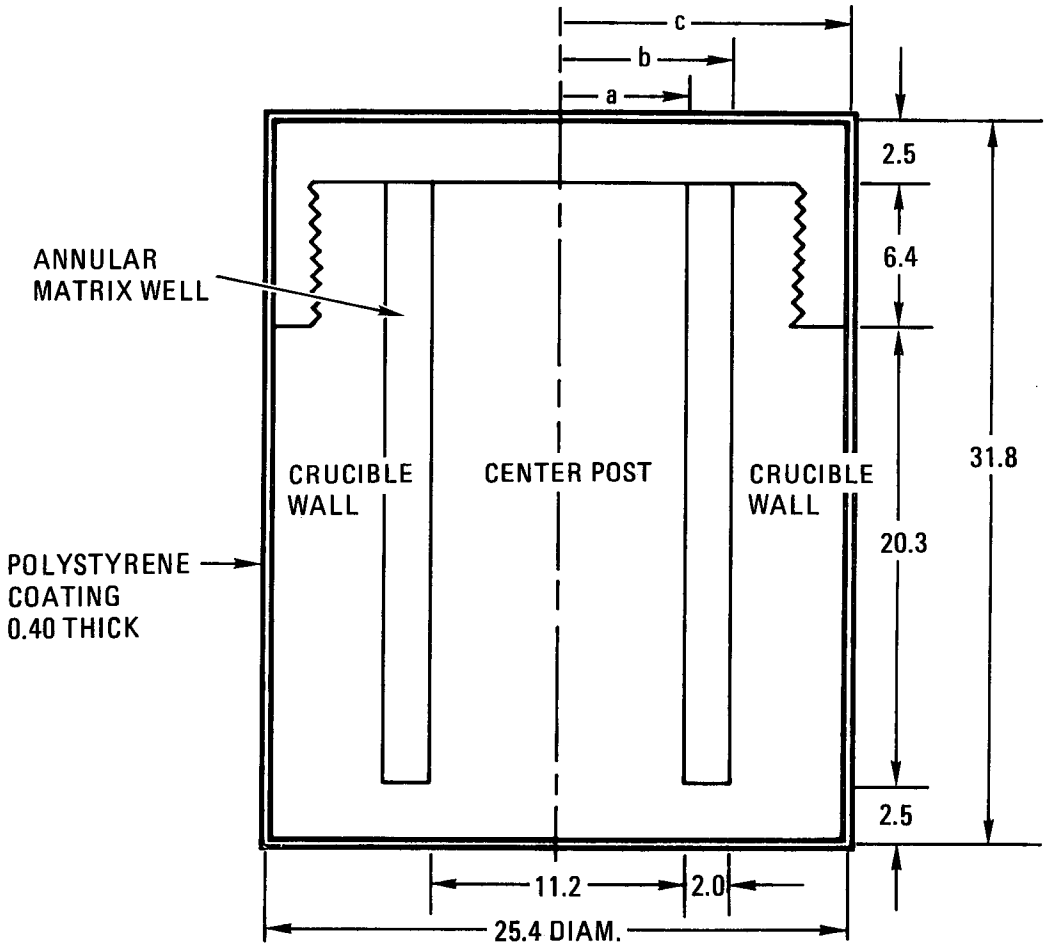

Fig. 9-1. Cross section of diffusion spine sample

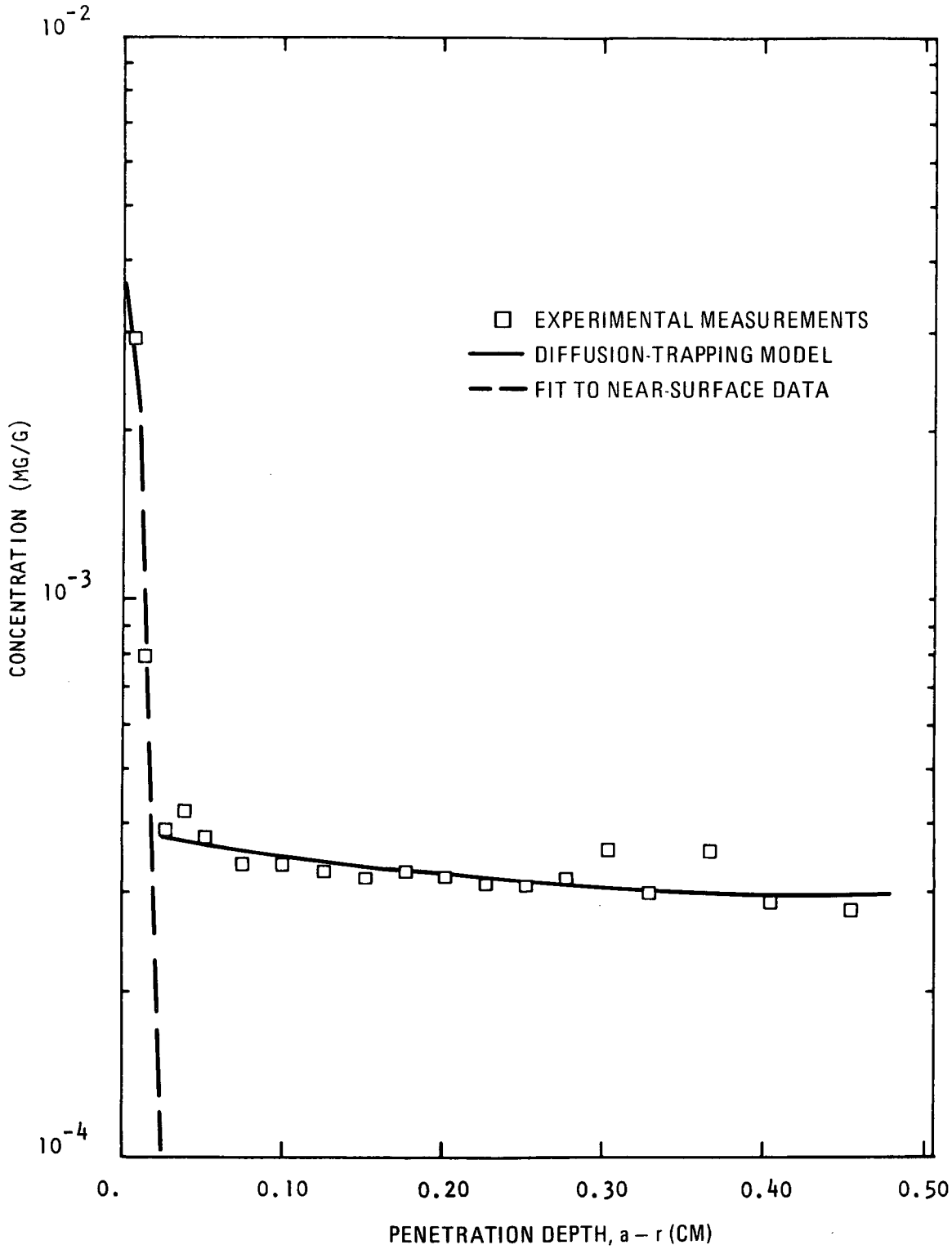

Fig. 9-2. Cs-134 profile for center post of diffusion spine sample FTE-3-42

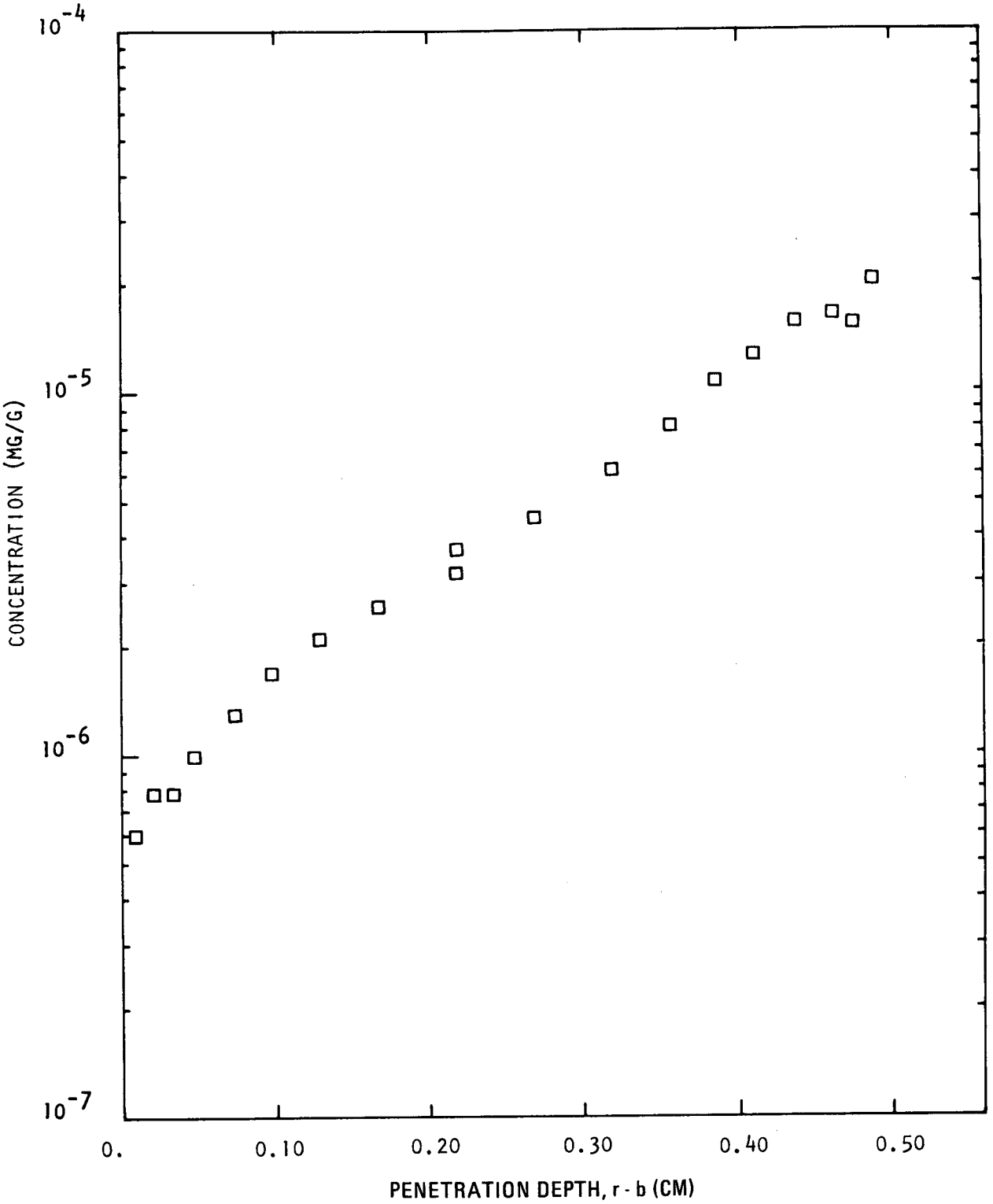

Fig. 9-3. Cs-134 profile for crucible wall of diffusion spine sample FTE-3-11

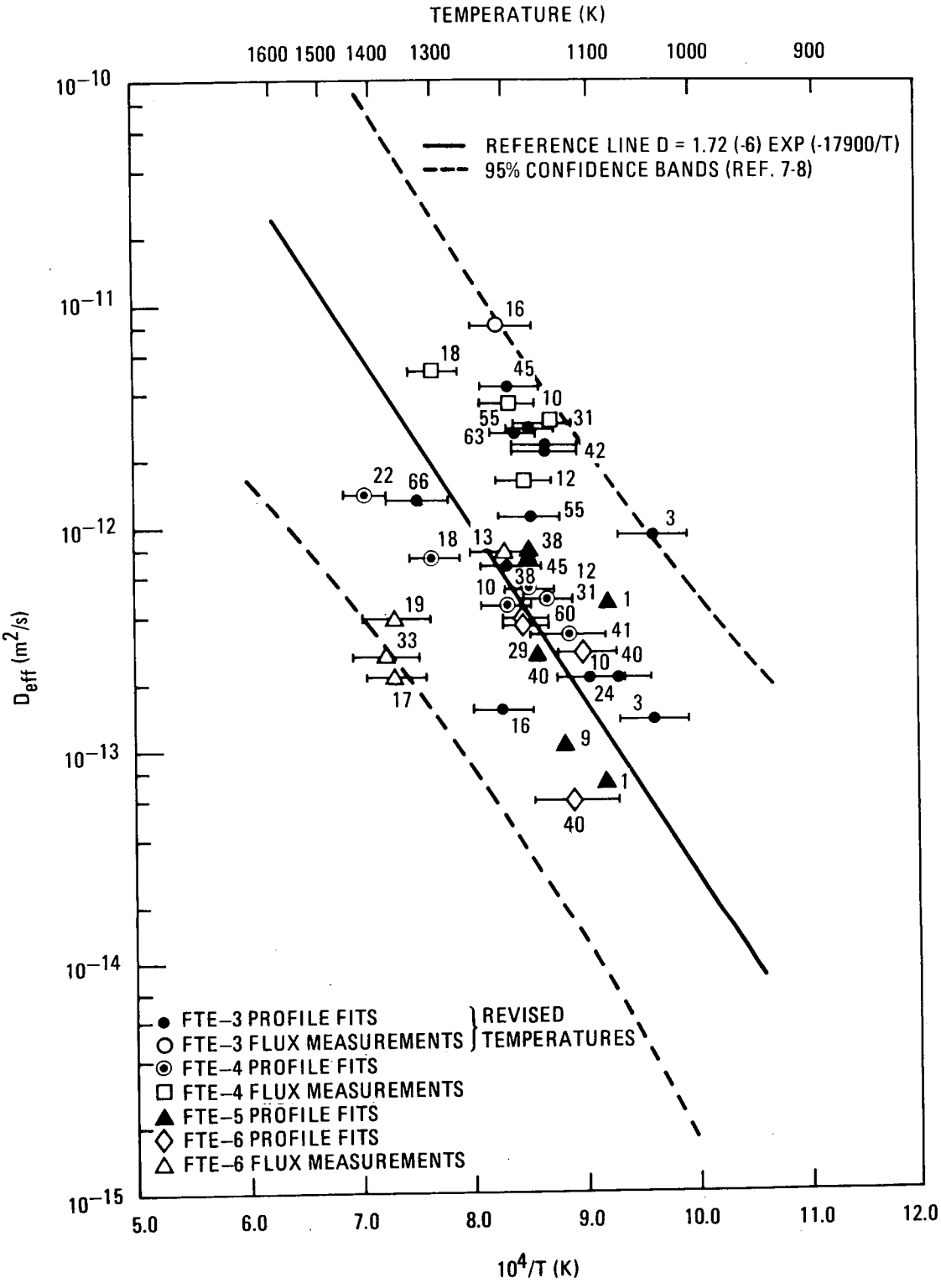

Fig. 9-4. Spine sample cesium diffusion coefficients (D_{eff}) as a function of activation-energy-weighted irradiation temperature

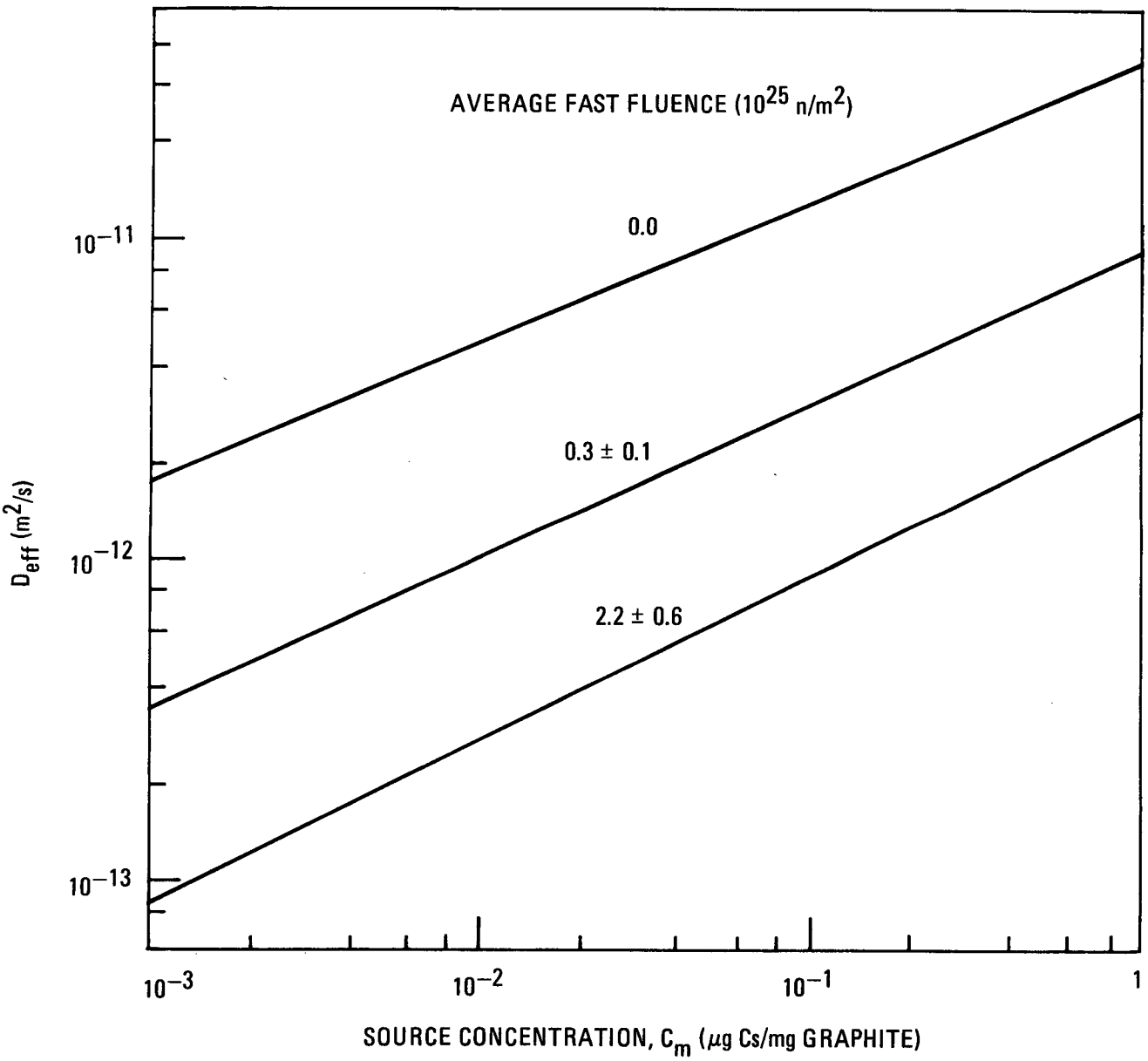

Fig. 9-5. Dependence of transport coefficient on source concentration at T = 1233 K for selected fluence values experienced by H-327 graphite samples

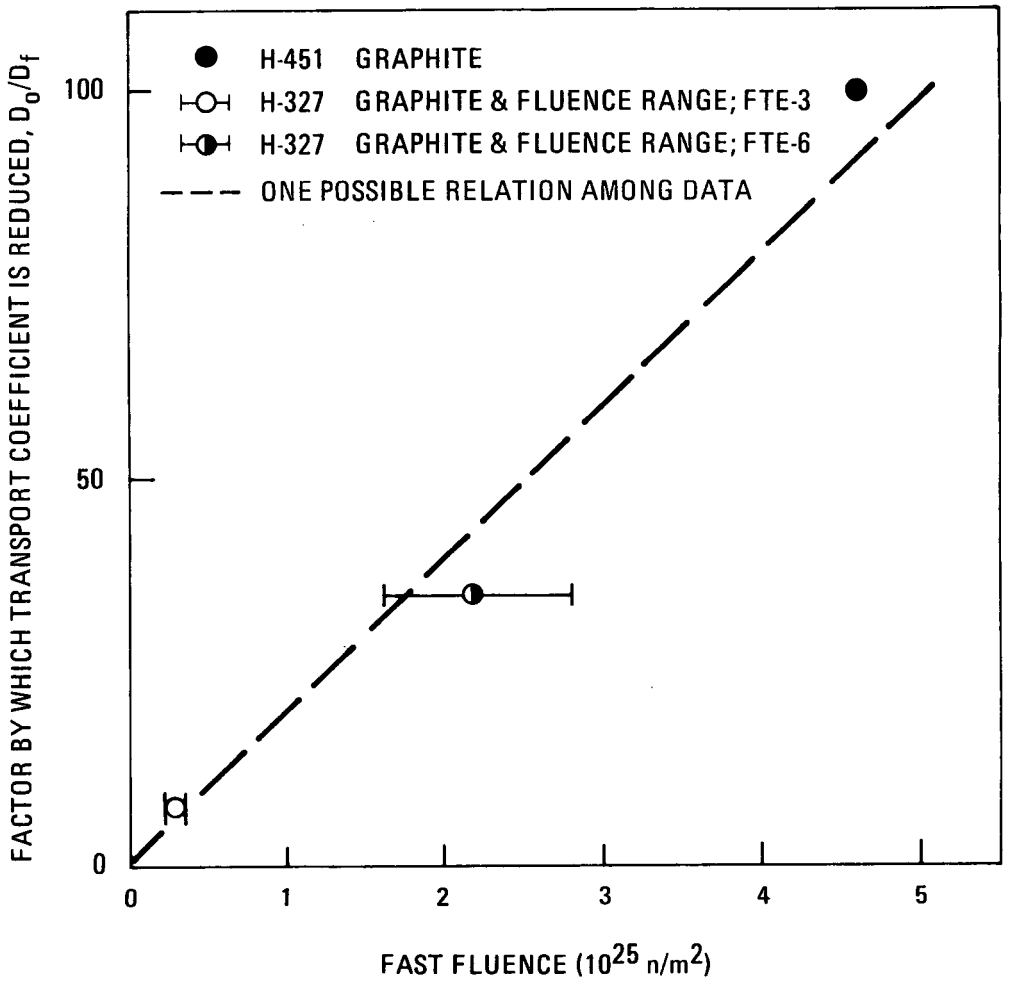

Fig. 9-6. Reduction in transport coefficients for cesium as a function of fast fluence at T = 1233 K for a source concentration of 5.48×10^{-5} mg cesium/kg graphite

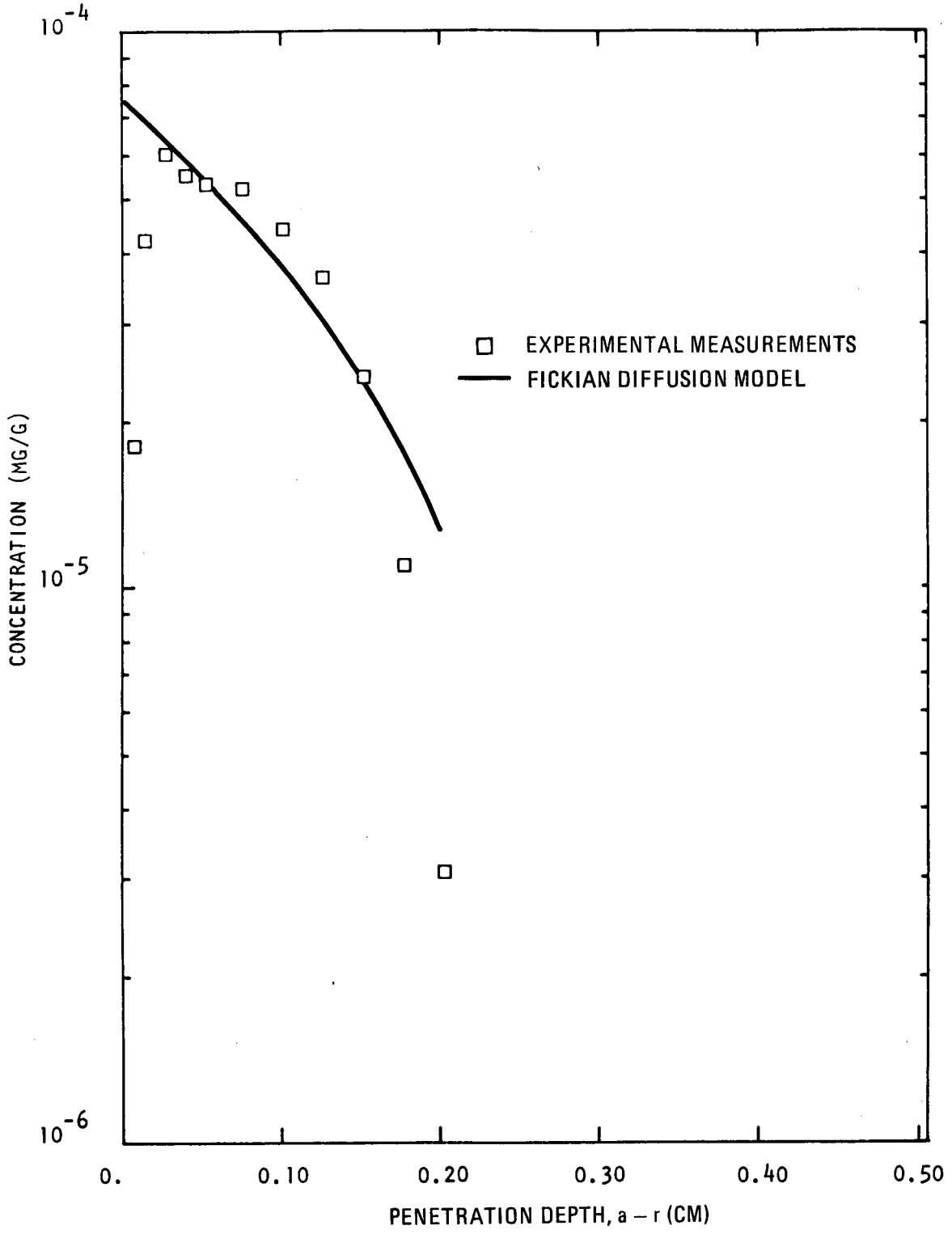

Fig. 9-7. Sr-85 profile for center post of diffusion spine sample FTE-3-16

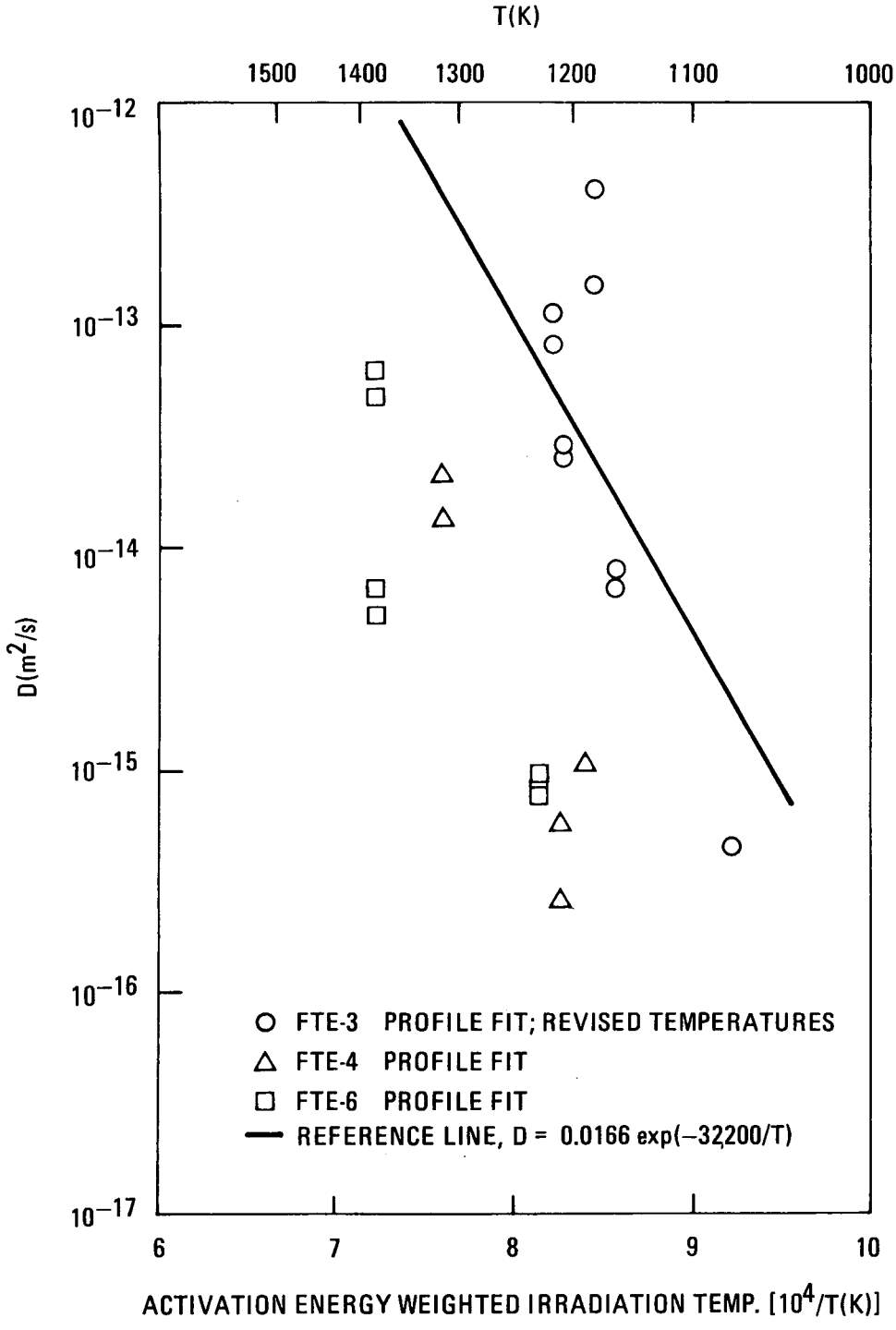

Fig. 9-8. Spine sample strontium diffusion coefficients as a function of activation-energy-weighted irradiation temperature

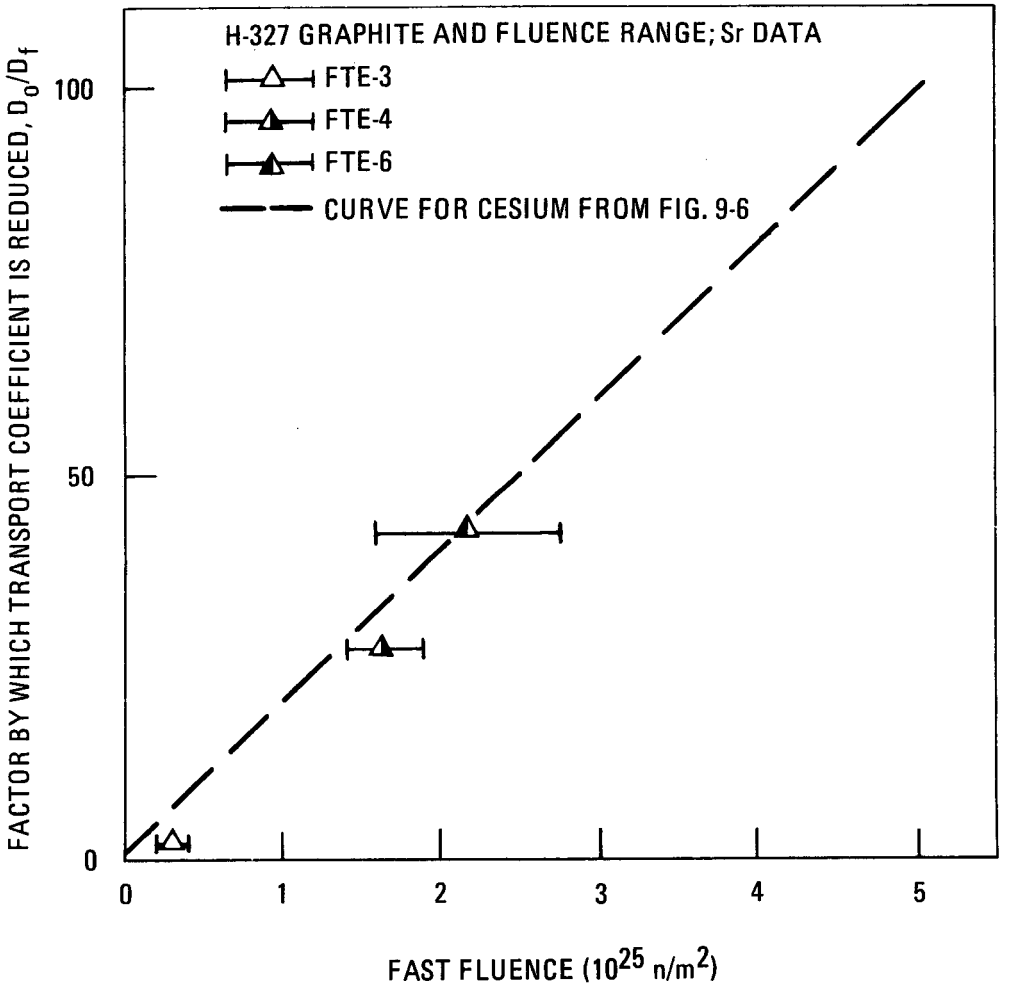

Fig. 9-9. Reduction in transport coefficients for strontium as a function of fast neutron fluence at T = 1233 K

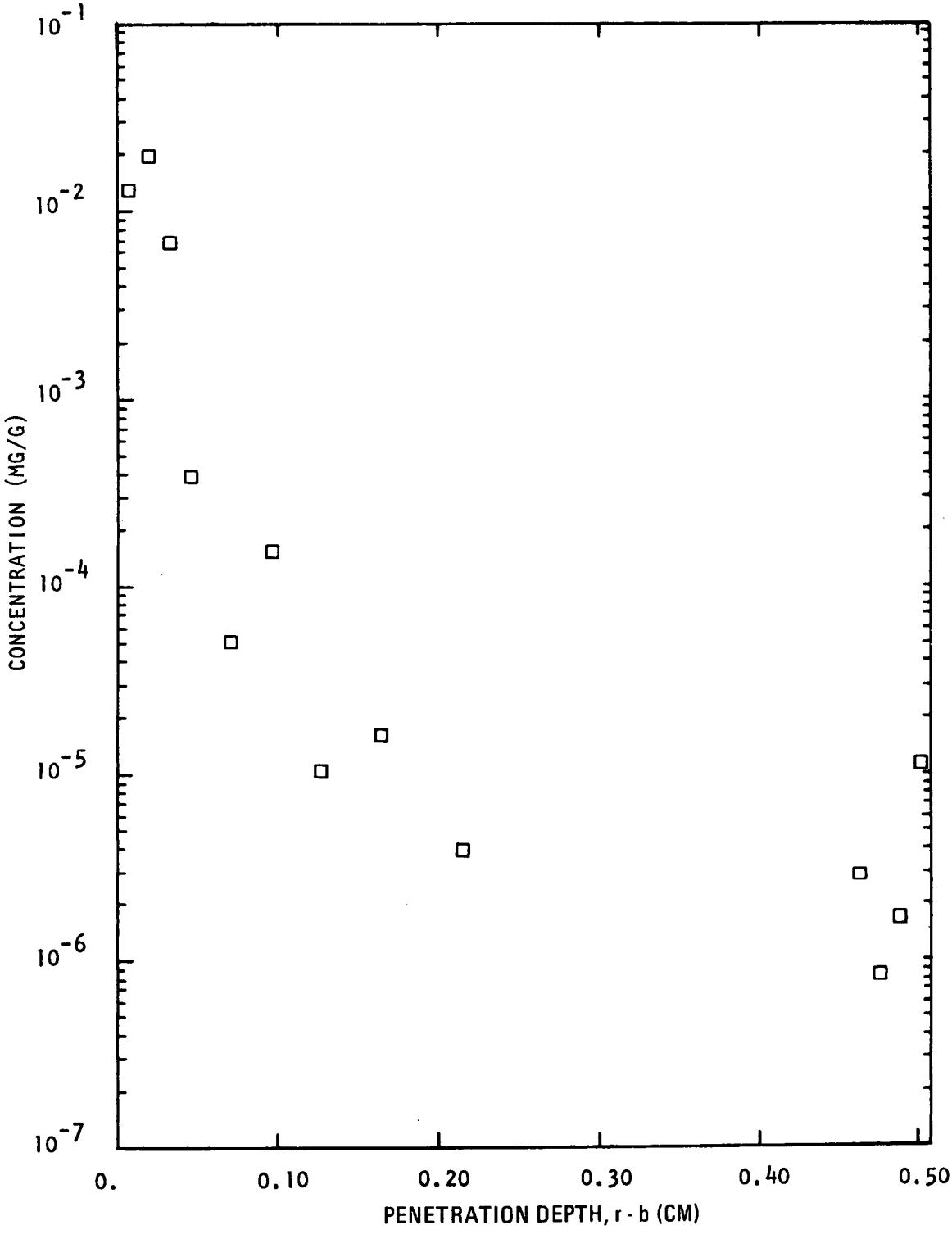

Fig. 9-10. Eu-154 profile for crucible wall of diffusion spine sample FTE-3-42

10. ACKNOWLEDGEMENTS

The authors wish to thank all those who participated in the Peach Bottom test element program, the list of whom is far too long to present here. In particular, Frances McCord is acknowledged for her assistance in compiling the temperature, fluence, and burnup data presented in this report.

APPENDIX A

RE-EVALUATION OF TEMPERATURES FOR FTE-18

Gamma spectrometric measurements performed by KFA (Ref. A-1) for Peach Bottom test element FTE-18 confirm the conclusion of Ref. A-2 that the power for FTE-18 was underpredicted. A comparison of measured and calculated burnup indicates the element average power was 14.3% higher than predicted. The time-averaged axial power profile was also established from the gamma spectrometric measurements. Temperatures for FTE-18 have been recalculated based on the measured element average power and time-averaged axial power profile.

The measured and calculated burnup profiles for FTE-18 are shown in Fig. A-1. The measured profile is a least-squares fit of the data provided in Table 4 of Ref. A-1. The burnups reported in Ref. A-1 were increased by a factor of 1.044 to account for the 7-mm decrease (from 9.7 to 2.7 mm) in the reported (Ref. A-3) fuel free zone at the ends of each fuel body. A comparison of measured and calculated burnups is shown in Table A-1. The normalized Cs-134/Cs-137 profile measured by KFA is shown in Fig. A-2. This profile is representative of the time-averaged axial power distribution. The calculated time-averaged axial power distribution is also shown in Fig. A-2.

Time-averaged irradiation temperatures calculated for FTE-18 based on KFA gamma spectrometric measurements are presented in Table A-2 and Fig. A-3. Envelope temperatures are provided in Table A-3 and Fig. A-4. The temperature history for the element is provided in Fig. A-5 through Fig. A-15.

FTE-18 contained two thermocouples of the W/Re type. These thermocouples were located in the center hole at a total core height of 1918 mm.

However, only one of the thermocouples produced a signal in-pile. When corrected for decalibration due to the effects of neutron bombardment (Section 5.2), the thermocouple readings represent actual irradiation temperatures and can be compared with calculated temperatures to provide an indication of the validity of the thermal analysis. A comparison of calculated and measured temperatures is provided in Fig. A-16 and Table A-4. The accuracy of the calculated temperatures at the location of the thermocouple was found to be ±48.9° C (1σ) with a bias (Calc. - Meas.) of 28.6° C. This is a considerable improvement over the temperatures previously calculated for the element and reported in Ref. A-2. The accuracy for these temperatures was ±64.5° C (1σ) with a bias (Calc. - Meas.) of -78.0° C.

REFERENCES

A-1. Schröder, R., et al., "PBR-B1 Gammaspektrometrische Nachunterguchungen," Kernforschungsanlage Jülich, Institut für Reaktorwerkstoffe, IRW-TN-23/79, February 13, 1979.

A-2. Wallroth, C. F., et al., "Postirradiation Examination and Evaluation of Peach Bottom Molded Fuel Test Element FTE-18," ERDA Report GA-A13699, June 1, 1976.

A-3. Holzgraf, J. F., et al., "Gamma Spectroscopic Examination of Peach Bottom HTGR Core Components," DOE Report GA-A13453, April 1978.

TABLE A-1
COMPARISON OF MEASURED AND CALCULATED FIMA FOR FTE-18

Total Core Height (mm)	Measured FIMA[a] (KFA) (%)	Calculated FIMA (GA) (%)	Measured/ Calculated
792	5.04	4.59	1.10
860	5.72	5.27	1.09
928	6.33	5.95	1.06
996	6.87	6.40	1.07
1065	7.36	6.88	1.07
1142	7.85	7.22	1.09
1210	8.22	7.49	1.10
1278	8.53	7.69	1.11
1346	8.78	7.87	1.12
1415	9.00	8.00	1.12
1492	9.18	8.15	1.13
1560	9.28	8.24	1.13
1628	9.35	8.31	1.13
1696	9.39	8.31	1.13
1765	9.38	8.30	1.13
1842	9.32	8.23	1.13
1910[b]	9.24	8.16	1.13
1978	9.12	8.04	1.13
2046	8.99	7.95	1.13
2115	8.82	7.80	1.13
2193	8.60	7.60	1.13
2260	8.39	7.35	1.14
2328	8.16	7.09	1.15
2396	7.92	6.90	1.15
2465	7.60	6.52	1.17
2543	7.35	6.13	1.20
2610	7.08	5.84	1.21
2678	6.79	5.37	1.26
2746	6.49	5.01	1.30
2815	6.20	4.59	1.35
Element Average			1.14

[a] Obtained from least-squares fit of KFA data. KFA data increased by a factor of 1.044 to account for decrease (from 9.7 to 2.7 mm) in the reported (Ref. A-3) fuel-free zones at the ends of each fuel body.

[b] Axial location of thermocouple hot junction.

TABLE A-2

FTE-18 TIME-WEIGHTED IRRADIATION TEMPERATURES

G= G. CAL/MOLE	CORE HT(MM)	FUEL MAX(C)	RMS (C)	FUEL AVG(C)	RMS (C)	FUEL MIN(C)	RMS (C)	BODY MED(C)	RMS (C)	BODY AVG(C)	RMS (C)	BODY MIN(C)	RMS (C)	SLV MAX(C)	RMS (C)	SLV AVG(C)	RMS (C)	SLV MIN(C)	RMS (C)	COOLANT (C)	RMS (C)
	790.	829.	73.	772.	61.	716.	50.	716.	50.	693.	45.	670.	40.	501.	24.	481.	18.	462.	11.	355.	7.
	859.	914.	97.	847.	82.	780.	68.	780.	68.	752.	61.	724.	54.	536.	34.	516.	23.	495.	13.	383.	7.
	928.	984.	109.	908.	92.	832.	76.	832.	76.	801.	69.	769.	61.	566.	38.	537.	26.	505.	15.	374.	6.
	997.	1045.	112.	963.	96.	880.	80.	880.	80.	845.	72.	811.	64.	593.	41.	562.	28.	531.	17.	386.	7.
	1066.	1100.	116.	1011.	99.	923.	83.	923.	83.	885.	75.	848.	67.	620.	43.	587.	30.	555.	19.	400.	7.
X,RMS(T)	928.	974.	103.	900.	87.	826.	72.	826.	72.	795.	65.	765.	58.	563.	37.	536.	25.	508.	15.	376.	7.
RNG,RMS(X) ,CRMS	345.	96.	140.	84.	121.	73.	103.	73.	103.	68.	94.	63.	86.	42.	56.	37.	45.	33.	36.	16.	17.
	1140.	1153.	119.	1059.	103.	966.	87.	966.	87.	926.	79.	887.	71.	647.	45.	613.	32.	579.	22.	414.	8.
	1209.	1195.	123.	1098.	107.	1001.	91.	1001.	91.	960.	83.	919.	75.	671.	47.	636.	34.	602.	24.	430.	9.
	1278.	1234.	126.	1134.	110.	1033.	94.	1033.	94.	991.	86.	948.	79.	694.	49.	657.	37.	624.	26.	446.	10.
	1347.	1266.	130.	1164.	114.	1062.	98.	1062.	98.	1018.	90.	975.	82.	715.	51.	680.	39.	645.	29.	462.	12.
	1416.	1296.	134.	1192.	118.	1088.	103.	1088.	103.	1044.	95.	1001.	87.	736.	54.	701.	42.	666.	31.	479.	13.
X,RMS(T)	1278.	1229.	126.	1129.	110.	1030.	95.	1030.	95.	988.	87.	946.	79.	692.	49.	658.	37.	623.	26.	446.	10.
RNG,RMS(X) ,CRMS	345.	51.	136.	47.	120.	43.	104.	43.	104.	42.	96.	40.	89.	32.	56.	31.	48.	31.	41.	23.	25.
	1491.	1322.	137.	1217.	121.	1112.	106.	1112.	106.	1067.	98.	1023.	90.	756.	56.	721.	44.	686.	33.	497.	15.
	1560.	1343.	140.	1237.	124.	1131.	109.	1131.	109.	1087.	101.	1042.	93.	774.	58.	740.	46.	705.	36.	514.	17.
	1629.	1360.	142.	1254.	127.	1148.	112.	1148.	112.	1103.	104.	1058.	96.	792.	60.	758.	48.	723.	38.	531.	18.
	1698.	1374.	143.	1269.	128.	1163.	113.	1163.	113.	1119.	106.	1074.	98.	809.	62.	775.	51.	741.	40.	549.	20.
	1767.	1385.	145.	1280.	130.	1175.	115.	1175.	115.	1131.	108.	1086.	100.	824.	63.	791.	53.	758.	42.	567.	22.
X,RMS(T)	1629.	1357.	141.	1251.	126.	1146.	111.	1146.	111.	1101.	103.	1057.	96.	791.	60.	757.	48.	723.	38.	532.	19.
RNG,RMS(X) ,CRMS	345.	23.	143.	23.	128.	23.	113.	23.	113.	23.	106.	23.	98.	24.	64.	25.	54.	25.	46.	25.	51.
	1841.	1392.	146.	1288.	131.	1184.	116.	1184.	116.	1140.	109.	1096.	101.	839.	65.	806.	54.	773.	44.	584.	24.
	1910.	1397.	148.	1294.	133.	1192.	118.	1192.	118.	1148.	110.	1105.	103.	852.	67.	820.	56.	789.	47.	601.	26.
	1978.	1398.	149.	1297.	134.	1196.	119.	1196.	119.	1153.	111.	1111.	104.	864.	68.	833.	58.	802.	49.	618.	28.
	2047.	1399.	149.	1299.	134.	1200.	119.	1200.	119.	1158.	112.	1116.	105.	876.	70.	845.	60.	816.	51.	635.	30.
	2116.	1396.	150.	1298.	135.	1201.	120.	1201.	120.	1160.	113.	1119.	106.	886.	71.	857.	62.	828.	53.	651.	32.
X,RMS(T)	1978.	1396.	148.	1295.	133.	1195.	119.	1195.	119.	1152.	111.	1109.	104.	863.	66.	833.	56.	802.	49.	618.	28.
RNG,RMS(X) ,CRMS	344.	2.	148.	4.	134.	6.	119.	5.	119.	7.	111.	8.	104.	17.	70.	16.	61.	19.	52.	24.	37.
	2190.	1388.	151.	1293.	136.	1199.	121.	1199.	121.	1159.	114.	1119.	107.	895.	73.	867.	64.	839.	55.	667.	34.
	2259.	1381.	150.	1289.	135.	1197.	120.	1197.	120.	1158.	113.	1119.	106.	903.	74.	876.	65.	849.	57.	682.	36.
	2327.	1373.	151.	1283.	136.	1193.	121.	1193.	121.	1155.	114.	1118.	107.	910.	75.	885.	67.	859.	59.	697.	38.
	2396.	1362.	152.	1275.	137.	1188.	122.	1188.	122.	1152.	115.	1115.	107.	916.	77.	892.	69.	868.	61.	710.	40.
	2465.	1346.	150.	1262.	135.	1179.	120.	1179.	120.	1144.	113.	1109.	106.	920.	77.	897.	70.	874.	63.	723.	42.
X,RMS(T)	2327.	1370.	151.	1280.	136.	1191.	121.	1191.	121.	1153.	114.	1116.	106.	909.	75.	883.	67.	858.	59.	696.	38.
RNG,RMS(X) ,CRMS	344.	15.	152.	11.	136.	7.	121.	7.	121.	5.	114.	4.	107.	9.	76.	11.	68.	13.	60.	26.	43.
	2539.	1333.	150.	1252.	135.	1172.	120.	1172.	120.	1138.	113.	1105.	106.	924.	79.	902.	72.	881.	65.	735.	44.
	2608.	1318.	149.	1241.	134.	1163.	119.	1163.	119.	1131.	112.	1099.	105.	927.	79.	906.	73.	886.	66.	747.	45.
	2676.	1301.	144.	1227.	130.	1153.	115.	1153.	115.	1122.	109.	1091.	102.	926.	78.	909.	73.	890.	67.	756.	47.
	2745.	1280.	139.	1210.	125.	1139.	111.	1139.	111.	1110.	105.	1081.	99.	927.	78.	910.	73.	893.	68.	765.	48.
	2814.	1258.	123.	1191.	111.	1125.	99.	1125.	99.	1097.	94.	1070.	89.	927.	74.	912.	70.	897.	66.	775.	50.
X,RMS(T)	2676.	1298.	141.	1224.	127.	1150.	113.	1150.	113.	1120.	107.	1089.	100.	927.	78.	908.	72.	889.	66.	756.	47.
RNG,RMS(X) ,CRMS	344.	27.	144.	22.	129.	17.	114.	17.	114.	15.	108.	12.	101.	1.	78.	3.	72.	6.	67.	14.	49.
X,RMS(T)	1803.	1271.	136.	1180.	121.	1090.	106.	1090.	106.	1052.	99.	1013.	92.	791.	63.	762.	54.	734.	46.	570.	29.
RNG,RMS(x) ,CRMS	2093.	151.	202.	142.	187.	135.	172.	135.	172.	132.	165.	129.	159.	131.	145.	133.	144.	136.	143.	135.	138.

TABLE

TABLE A-3
FTE-18 ENVELOPE OF IRRADIATION TEMPERATURES

	CORE HEIGHT (MM)	MAXIMUM FUEL (C)	MINIMUM FUEL (C)	MEDIAN BODY (C)	MINIMUM BODY (C)	MAXIMUM SLEEVE (C)	MINIMUM SLEEVE (C)
	790.	916.	644.	777.	615.	535.	433.
	859.	1035.	677.	866.	644.	581.	459.
	928.	1102.	716.	917.	678.	614.	479.
	997.	1169.	759.	969.	716.	647.	498.
	1066.	1229.	798.	1017.	751.	678.	516.
MEAN	928.	1090.	719.	909.	681.	611.	477.
RANGE/RMS	345.	109.	55.	83.	49.	50.	29.
	1140.	1288.	837.	1065.	785.	709.	535.
	1209.	1334.	867.	1105.	812.	736.	554.
	1278.	1377.	895.	1142.	837.	765.	572.
	1347.	1414.	918.	1177.	858.	792.	589.
	1416.	1448.	938.	1210.	876.	818.	608.
MEAN	1278.	1372.	891.	1140.	834.	764.	572.
RANGE/RMS	345.	57.	36.	51.	32.	38.	26.
	1491.	1477.	957.	1239.	894.	842.	627.
	1560.	1500.	972.	1262.	908.	865.	644.
	1629.	1518.	984.	1283.	921.	886.	662.
	1698.	1534.	997.	1301.	933.	907.	679.
	1767.	1546.	1006.	1316.	943.	926.	696.
MEAN	1629.	1515.	983.	1280.	920.	885.	662.
RANGE/RMS	345.	24.	18.	27.	17.	29.	25.
	1841.	1553.	1013.	1326.	951.	942.	712.
	1910.	1559.	1018.	1334.	957.	959.	729.
	1978.	1561.	1021.	1339.	961.	973.	745.
	2047.	1561.	1024.	1343.	966.	987.	758.
	2116.	1562.	1024.	1344.	967.	999.	766.
MEAN	1978.	1559.	1020.	1337.	960.	972.	742.
RANGE/RMS	344.	3.	4.	7.	6.	20.	19.
	2190.	1567.	1021.	1346.	966.	1008.	773.
	2259.	1567.	1021.	1348.	968.	1017.	780.
	2327.	1571.	1017.	1354.	967.	1026.	786.
	2396.	1568.	1012.	1354.	964.	1033.	790.
	2465.	1561.	1006.	1352.	960.	1036.	794.
MEAN	2327.	1567.	1015.	1351.	965.	1024.	784.
RANGE/RMS	344.	3.	6.	3.	3.	10.	7.
	2539.	1558.	1001.	1352.	957.	1040.	797.
	2608.	1543.	995.	1343.	953.	1043.	800.
	2676.	1526.	991.	1331.	951.	1043.	803.
	2745.	1504.	984.	1316.	946.	1042.	804.
	2814.	1441.	989.	1270.	951.	1041.	811.
MEAN	2676.	1514.	992.	1322.	952.	1042.	803.
RANGE/RMS	344.	41.	5.	29.	4.	1.	5.
MEAN	1803.	1436.	937.	1223.	885.	883.	673.
RANGE/RMS	2093.	176.	110.	363.	105.	156.	119.

TABLE A-4
FTE-18 THERMOCOUPLE DATA

TREVER SIMULATION								W/RE MEASURED TEMP.		W/RE CORRECTED TEMP.		RECAL	COMPARISON OF TREVER AND CORRECTED THERMOCOUPLE TEMP.			
REAL DAYS FROM	TO	ΔTIME W	EFPD FROM	TO	TEMP. TA	ERROR EA*	N	MEAN TB	TRANS. SB	MEAN TC	TRANS SC	ERROR EC*	DIFF TA-TC	ERROR ED*	REL. CHANGE TA/TC-1	ERROR ER*
413.75	555.68	141.93	385.44	499.59	1170.0	.0	20	1152.4	72.1	1173.5	77.7	.23	-3.5	.23	-.30	.00
555.68	628.37	72.69	499.59	564.07	1304.0	.0	10	1262.5	44.2	1332.0	56.3	.84	-28.0	.84	-2.10	.00
628.37	678.00	49.63	564.07	610.25	1457.0	.0	8	1276.4	9.5	1379.6	11.5	1.49	77.4	1.49	5.61	.00
678.00	776.73	98.73	610.25	701.23	1515.0	.0	13	1285.8	47.5	1449.5	60.9	1.84	65.5	1.84	4.52	.00
776.73	776.73	.00	701.23	701.23	1547.0	.0	1	1332.2	.0	1525.5	.0	.00	21.5	.00	1.41	.00
776.73	827.47	50.74	701.23	748.00	1549.0	.0	7	1311.0	19.1	1517.7	21.6	3.01	31.3	3.01	2.06	.00
827.47	877.47	50.00	748.00	788.00	1554.0	.0	7	1236.2	9.5	1457.3	19.9	3.28	96.7	3.28	6.64	.00
877.47	916.67	39.20	788.00	818.00	1526.0	.0	6	1240.8	11.8	1492.8	18.0	4.26	33.2	4.26	2.23	.00
916.67	946.67	30.00	818.00	835.00	1287.0	.0	4	1019.2	39.5	1213.9	52.4	4.16	73.1	4.16	6.03	.00
946.67	975.67	29.00	835.00	858.00	1525.0	.0	3	1153.6	91.2	1418.2	133.5	6.51	106.8	6.51	7.53	.00
975.67	1022.67	47.00	858.00	889.70	1416.0	.0	14	1171.6	91.7	1467.9	130.2	5.01	-51.9	5.01	-3.54	.00
1022.67	1034.67	12.00	889.70	897.30	1336.0	.0	2	1103.1	21.3	1387.3	28.7	7.96	-51.3	7.96	-3.69	.01
GRAND TOTAL W,N,TW,SW,EW		620.92			1391.9	.0	94	1215.8	91.9	1363.4	141.5	123.80	28.6	48.9	2.00	3.48
SW (1 SIGMA)					147.1			74.2		123.8			48.9		3.5	

NOTE: TREVER SIMULATION USED--> TREVER NODE 17, KFA MEASURED CS134/CS137 PROFILE, BURNUP DETERMINED ELEMENT POWER BIAS OF 14.3%. T/C CALCULATED, TA = (TMAX-TMIN)*.976 + TMIN.

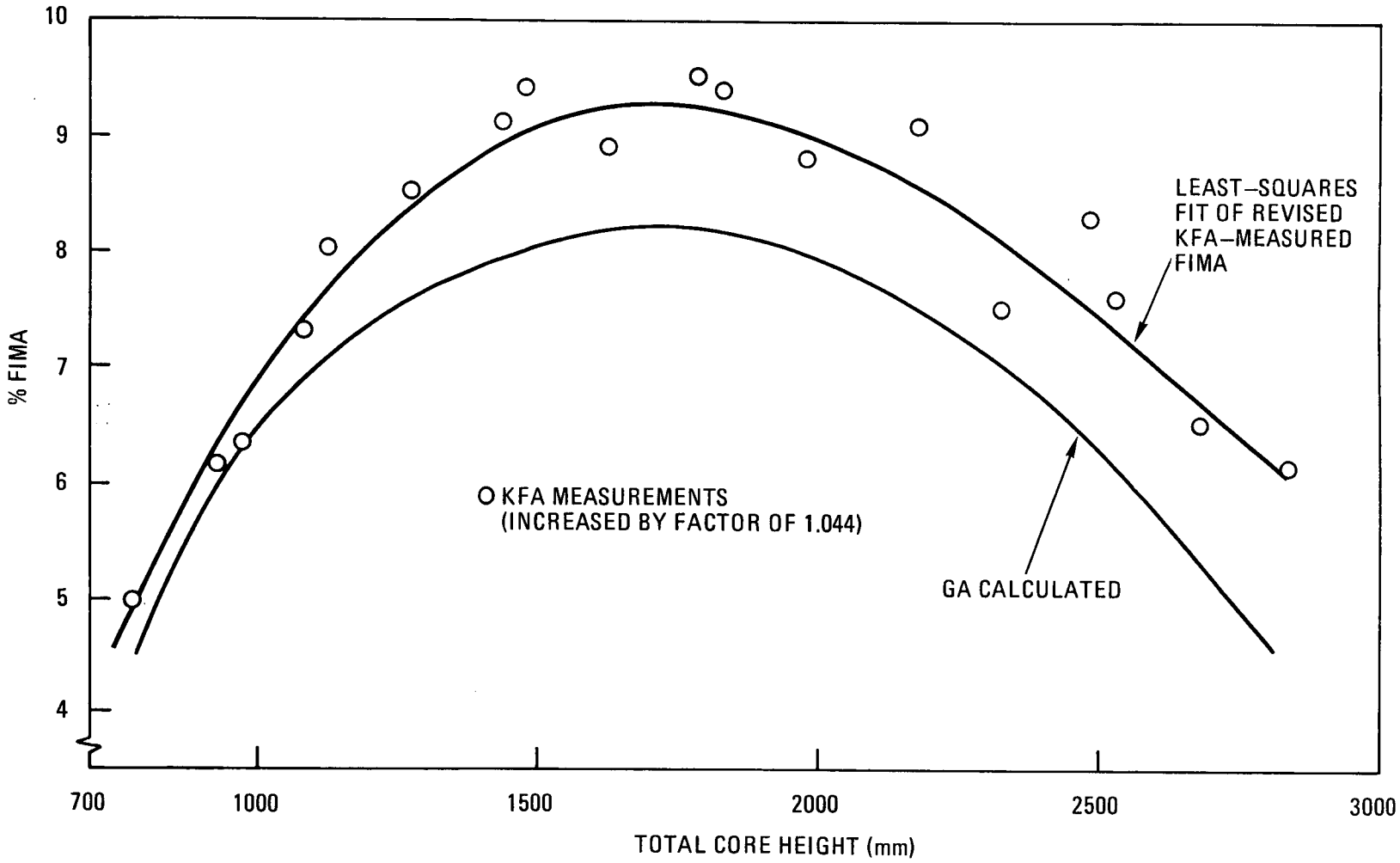

Fig. A-1. Comparison of measured and calculated FIMA for FTE-18

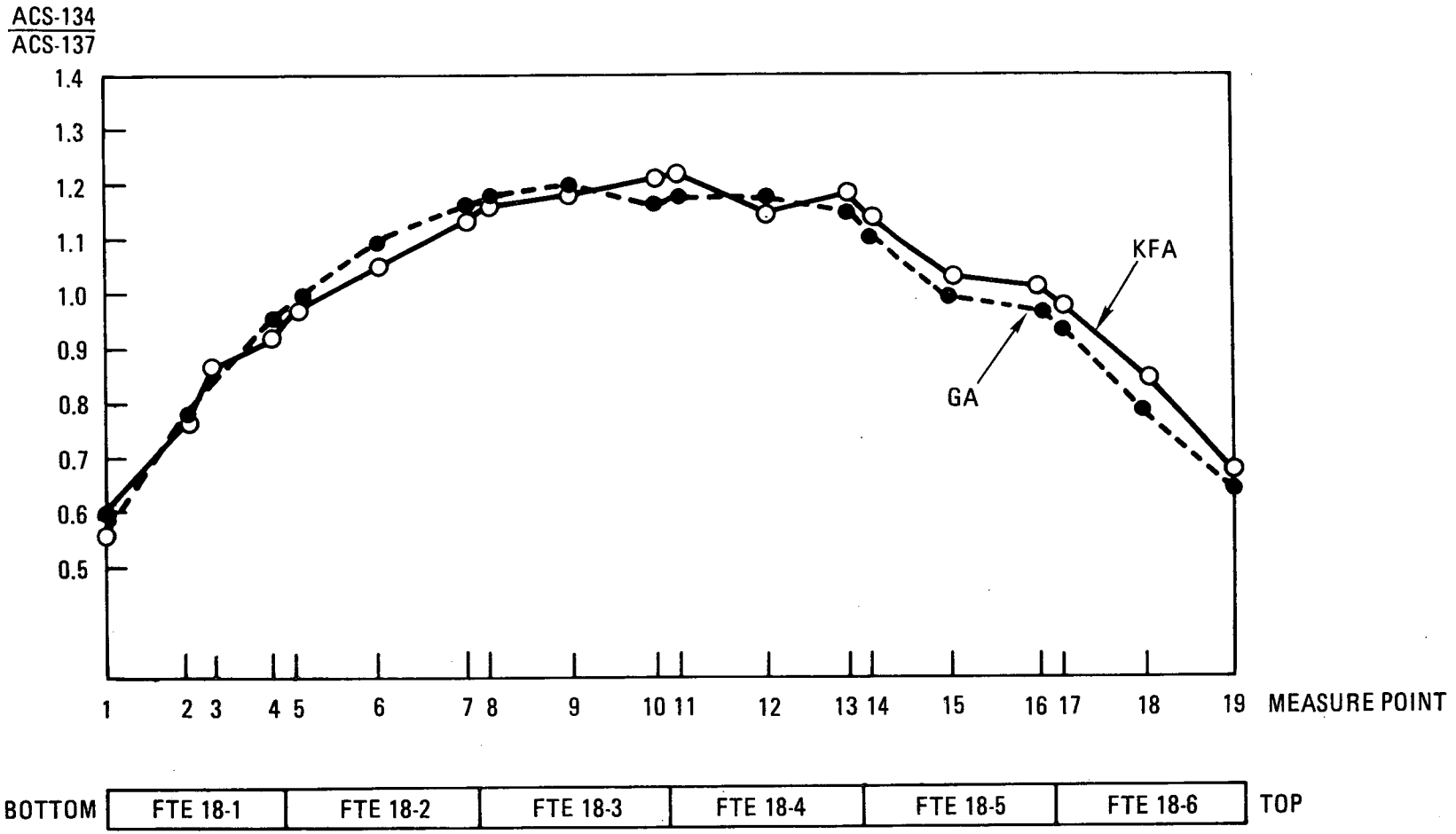

Fig. A-2. Measured Cs-134/Cs-137 profiles for FTE-18

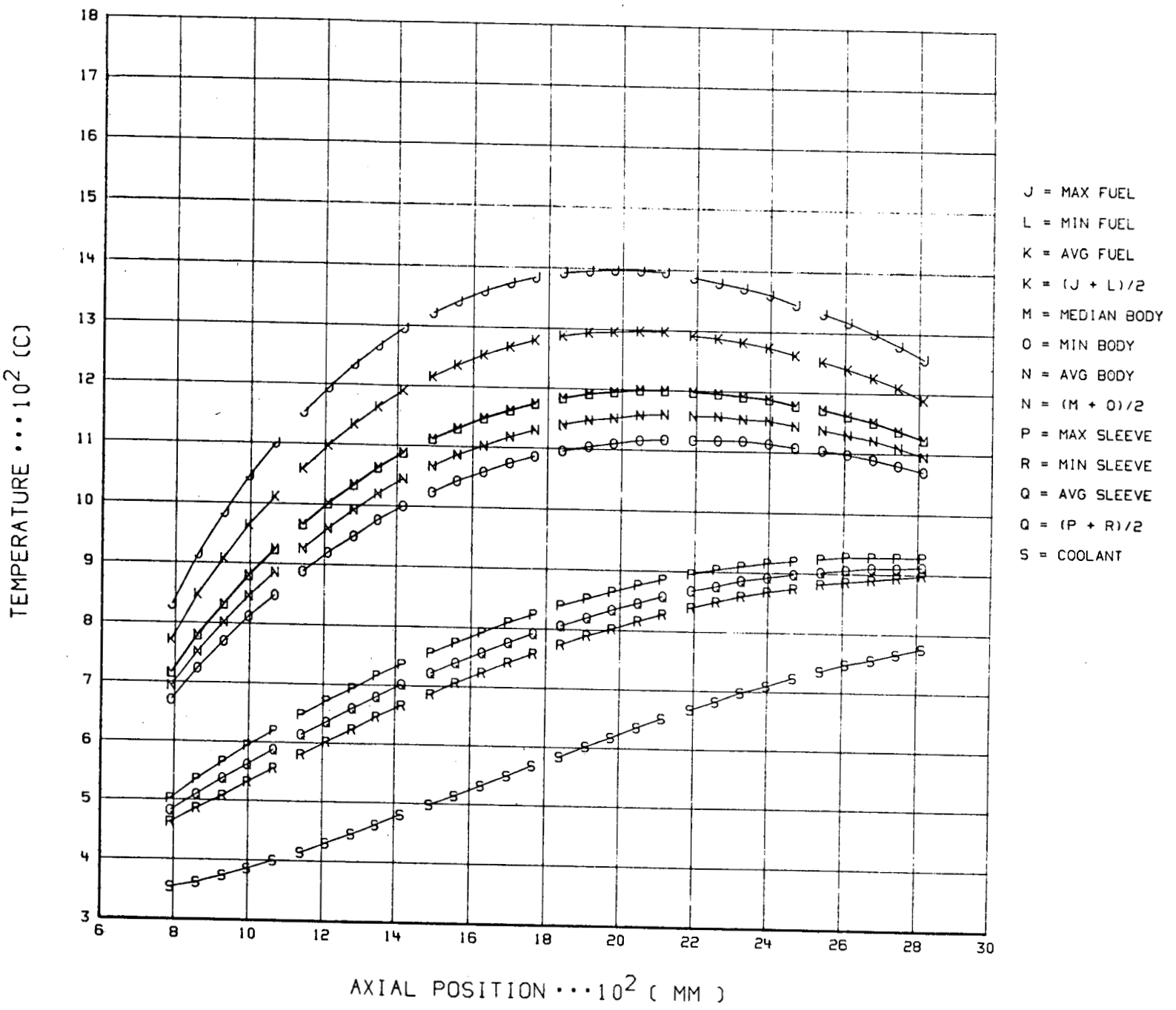
FTE-18 TIME AVERAGED TEMPERATURE
TEMPERATURE • • • 10^2 (C)
AXIAL POSITION • • • 10^2 (MM)
J = MAX FUEL
L = MIN FUEL
K = AVG FUEL
K = (J + L)/2
M = MEDIAN BODY
O = MIN BODY
N = AVG BODY
N = (M + O)/2
P = MAX SLEEVE
R = MIN SLEEVE
Q = AVG SLEEVE
Q = (P + R)/2
S = COOLANT

Fig. A-3

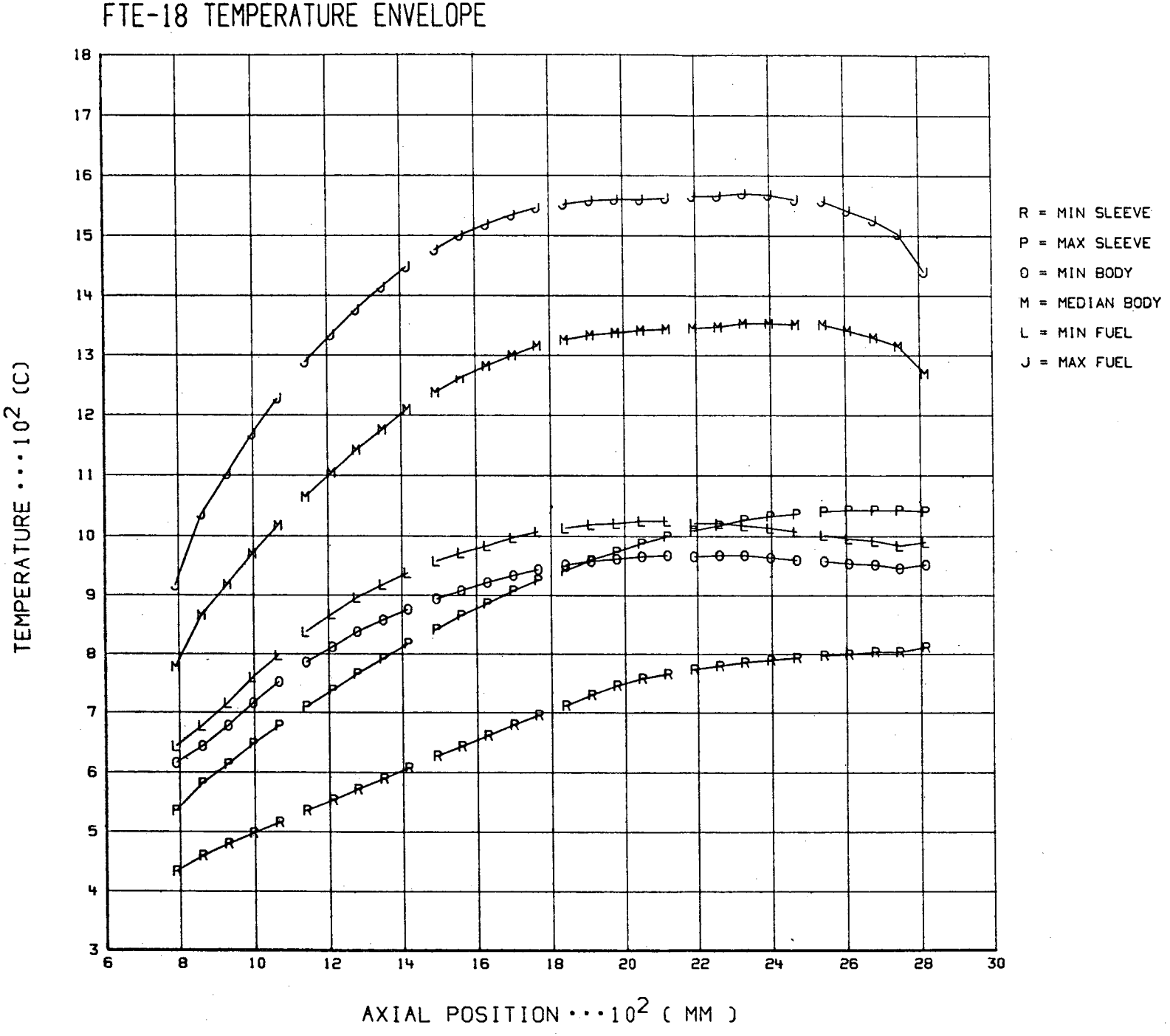
FTE-18 TEMPERATURE ENVELOPE
TEMPERATURE ···10² (C)
AXIAL POSITION ···10² (MM)
R = MIN SLEEVE
P = MAX SLEEVE
O = MIN BODY
M = MEDIAN BODY
L = MIN FUEL
J = MAX FUEL

Fig. A-4

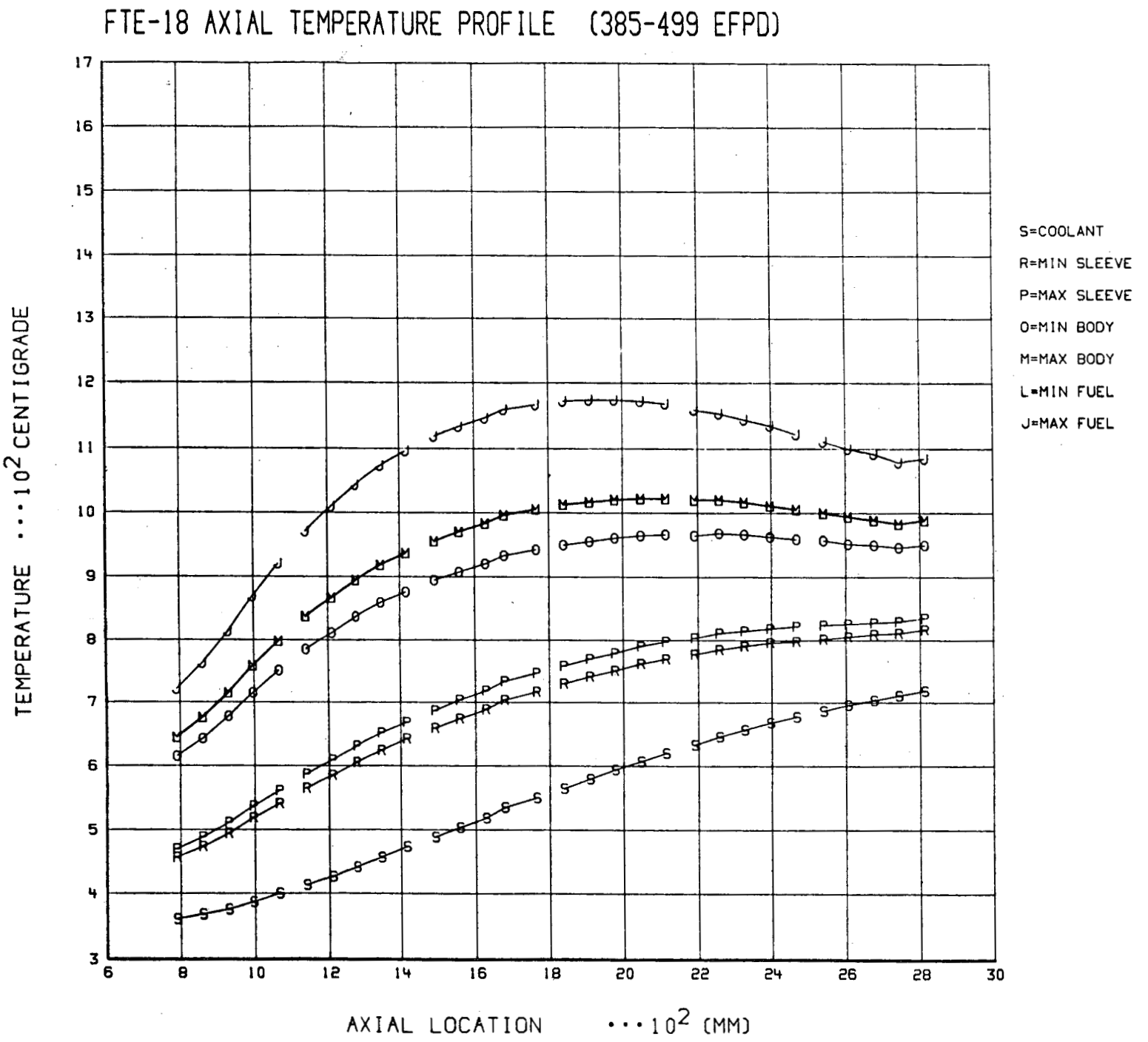
FTE-18 AXIAL TEMPERATURE PROFILE (385-499 EFPD)
TEMPERATURE ...10² CENTIGRADE
AXIAL LOCATION ...10² (MM)
S=COOLANT
R=MIN SLEEVE
P=MAX SLEEVE
O=MIN BODY
M=MAX BODY
L=MIN FUEL
J=MAX FUEL

Fig. A-5

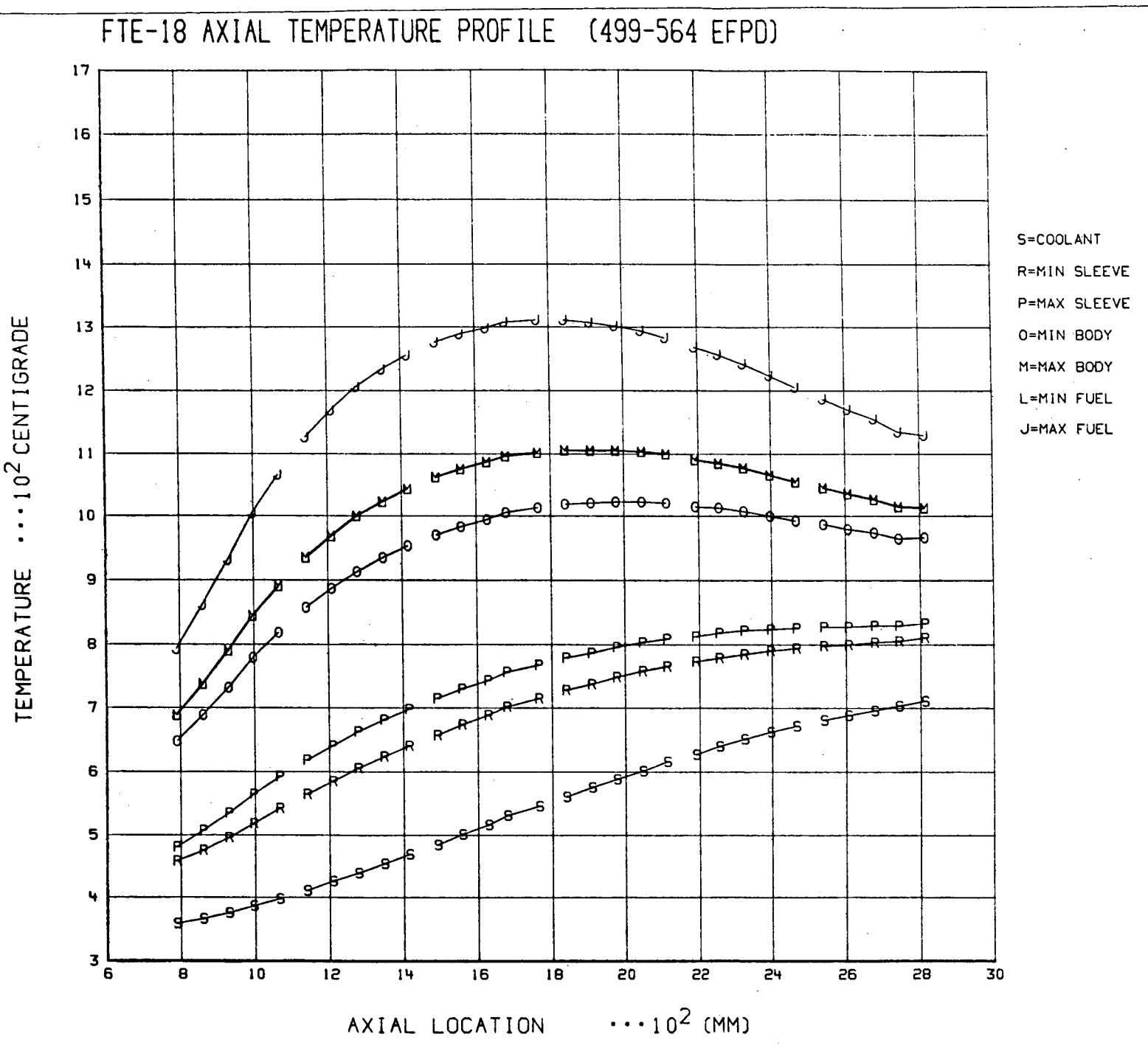
FTE-18 AXIAL TEMPERATURE PROFILE (499-564 EFPD)
TEMPERATURE ···10² CENTIGRADE
AXIAL LOCATION ···10² (MM)
S=COOLANT
R=MIN SLEEVE
P=MAX SLEEVE
O=MIN BODY
M=MAX BODY
L=MIN FUEL
J=MAX FUEL

Fig. A-6

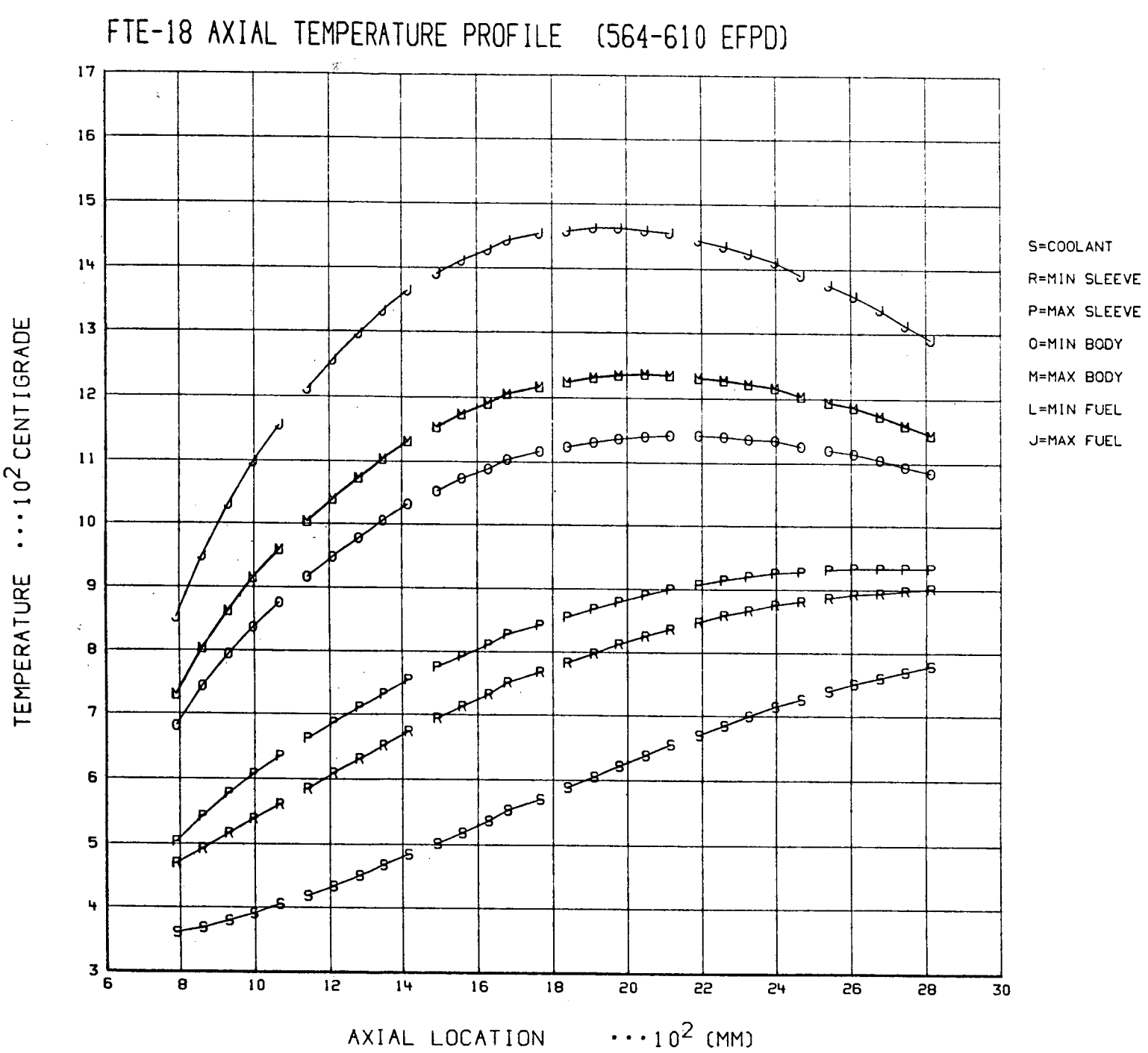
FTE-18 AXIAL TEMPERATURE PROFILE (564-610 EFPD)
TEMPERATURE ...10^2 CENTIGRADE
AXIAL LOCATION ...10^2 (MM)
S=COOLANT
R=MIN SLEEVE
P=MAX SLEEVE
O=MIN BODY
M=MAX BODY
L=MIN FUEL
J=MAX FUEL

Fig. A-7

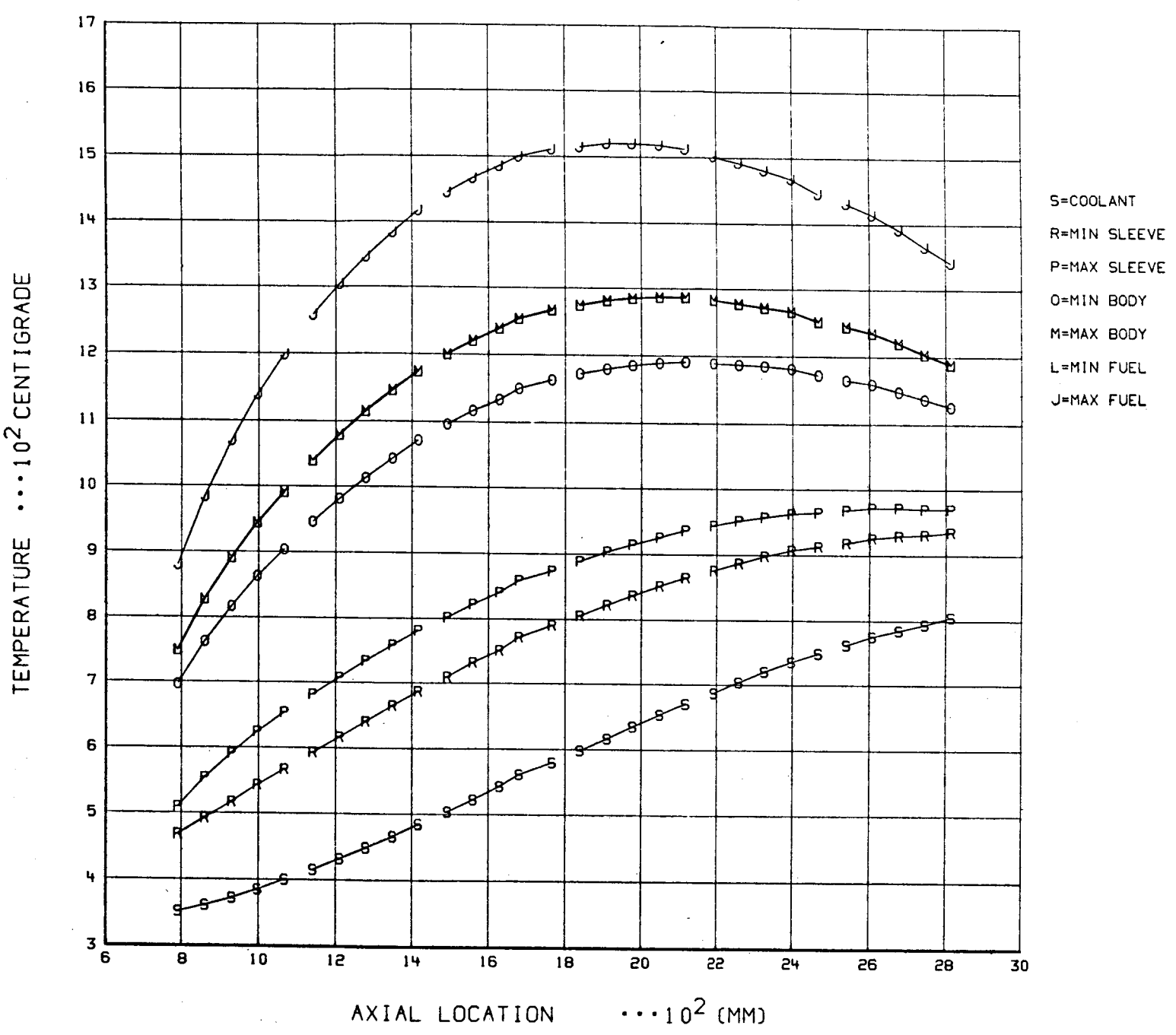
FTE-18 AXIAL TEMPERATURE PROFILE (610-701 EFPD)
TEMPERATURE ···10² CENTIGRADE
AXIAL LOCATION ···10² (MM)
S=COOLANT
R=MIN SLEEVE
P=MAX SLEEVE
O=MIN BODY
M=MAX BODY
L=MIN FUEL
J=MAX FUEL

Fig. A-8

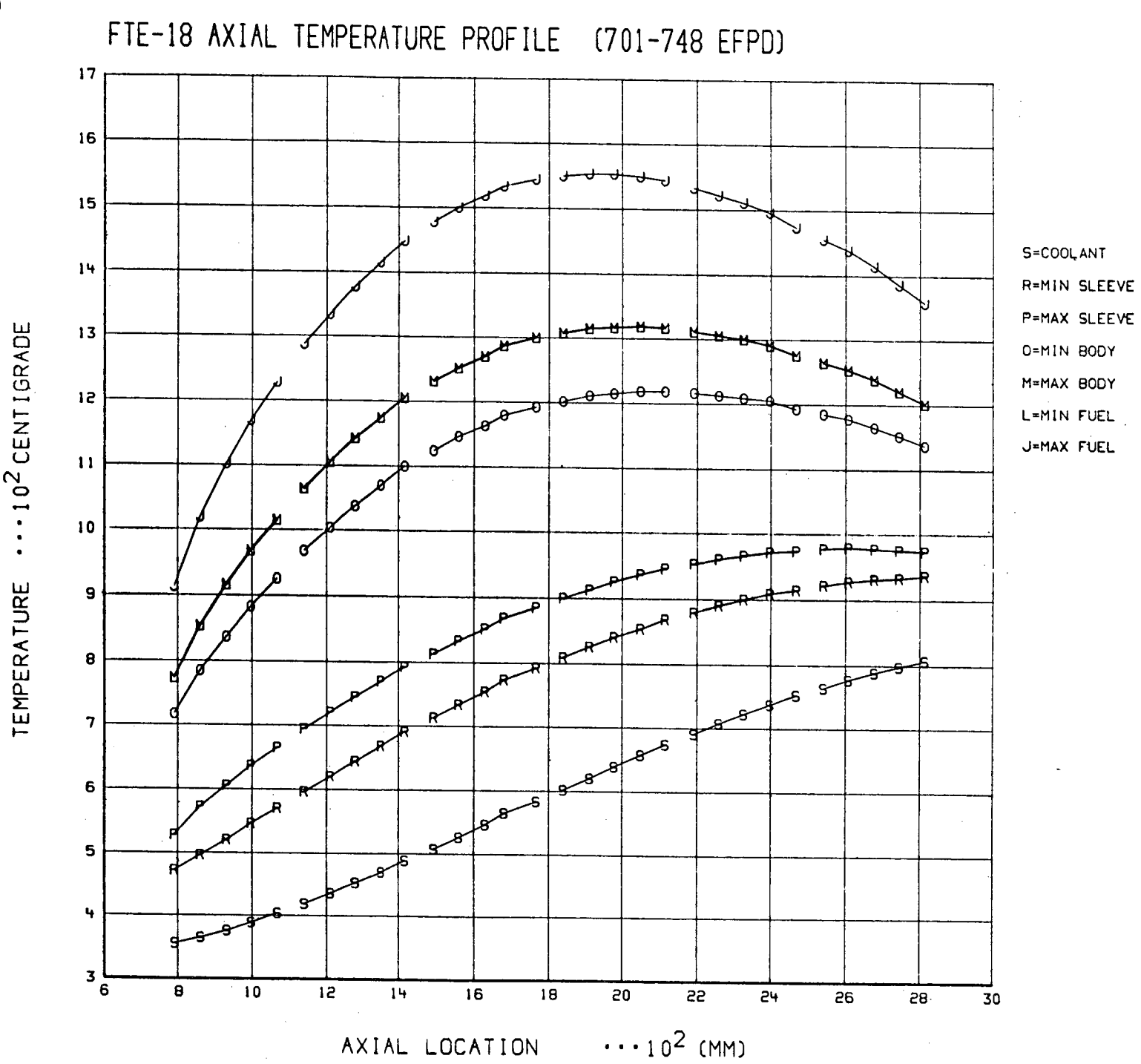
FTE-18 AXIAL TEMPERATURE PROFILE (701-748 EFPD)
TEMPERATURE ...10² CENTIGRADE
AXIAL LOCATION ...10² (MM)
S=COOLANT
R=MIN SLEEVE
P=MAX SLEEVE
O=MIN BODY
M=MAX BODY
L=MIN FUEL
J=MAX FUEL

Fig. A-9

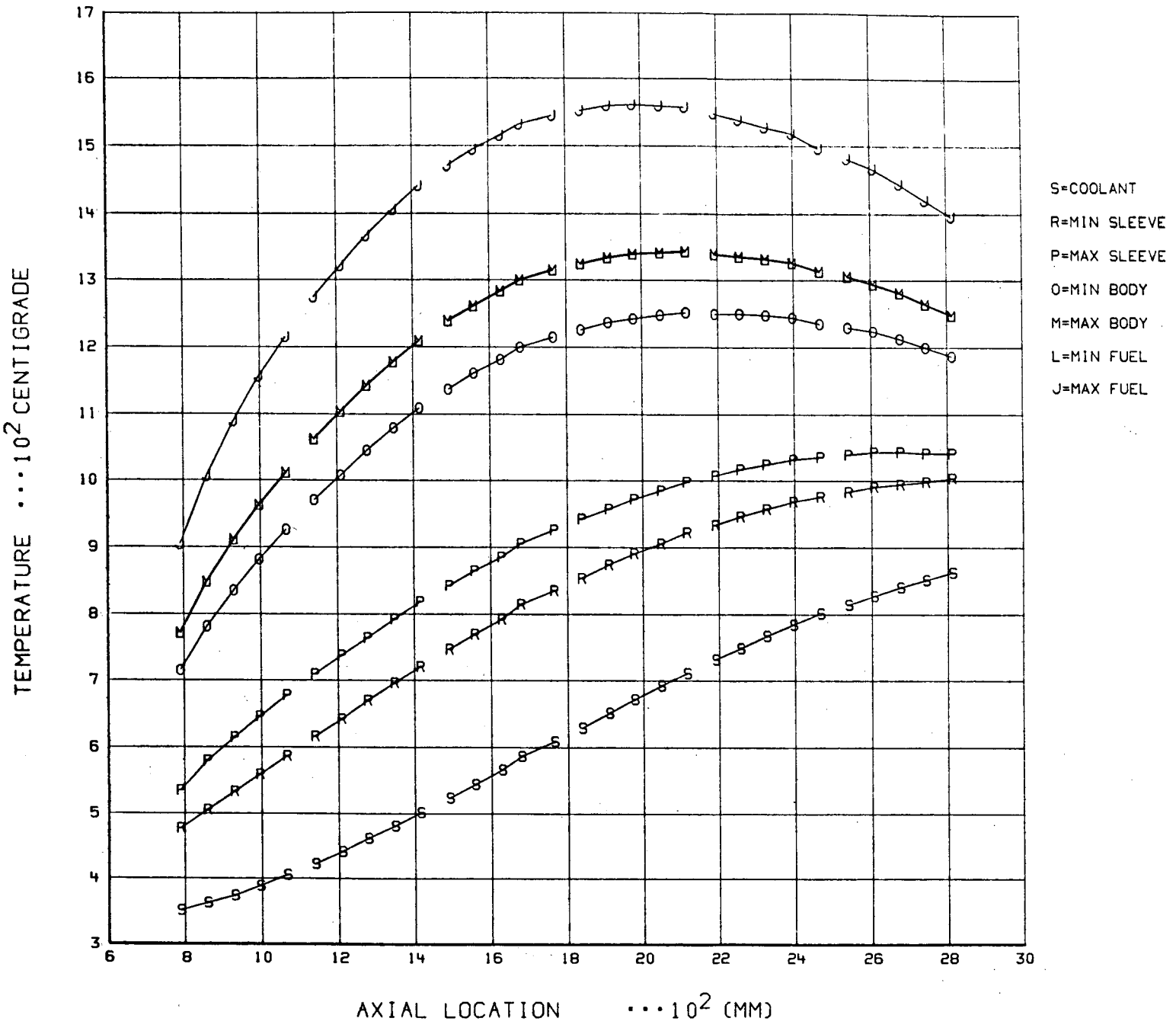
FTE-18 AXIAL TEMPERATURE PROFILE (748-788 EFPD)
TEMPERATURE ...10^2 CENTIGRADE
AXIAL LOCATION ...10^2 (MM)
S=COOLANT
R=MIN SLEEVE
P=MAX SLEEVE
O=MIN BODY
M=MAX BODY
L=MIN FUEL
J=MAX FUEL

Fig. A-10

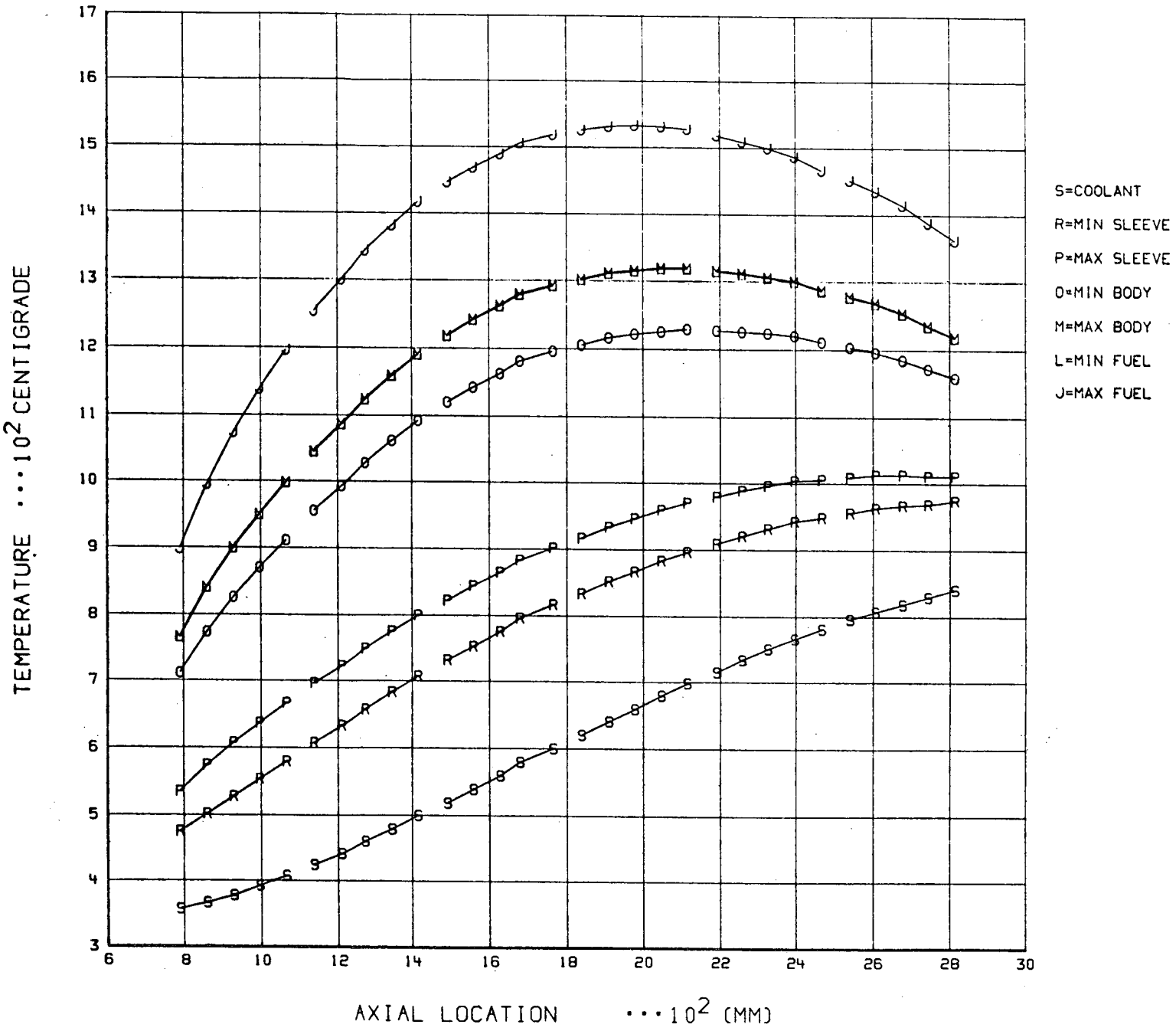
FTE-18 AXIAL TEMPERATURE PROFILE (788-818 EFPD)
TEMPERATURE ···10² CENTIGRADE
AXIAL LOCATION ···10² (MM)
S=COOLANT
R=MIN SLEEVE
P=MAX SLEEVE
O=MIN BODY
M=MAX BODY
L=MIN FUEL
J=MAX FUEL

Fig. A-11

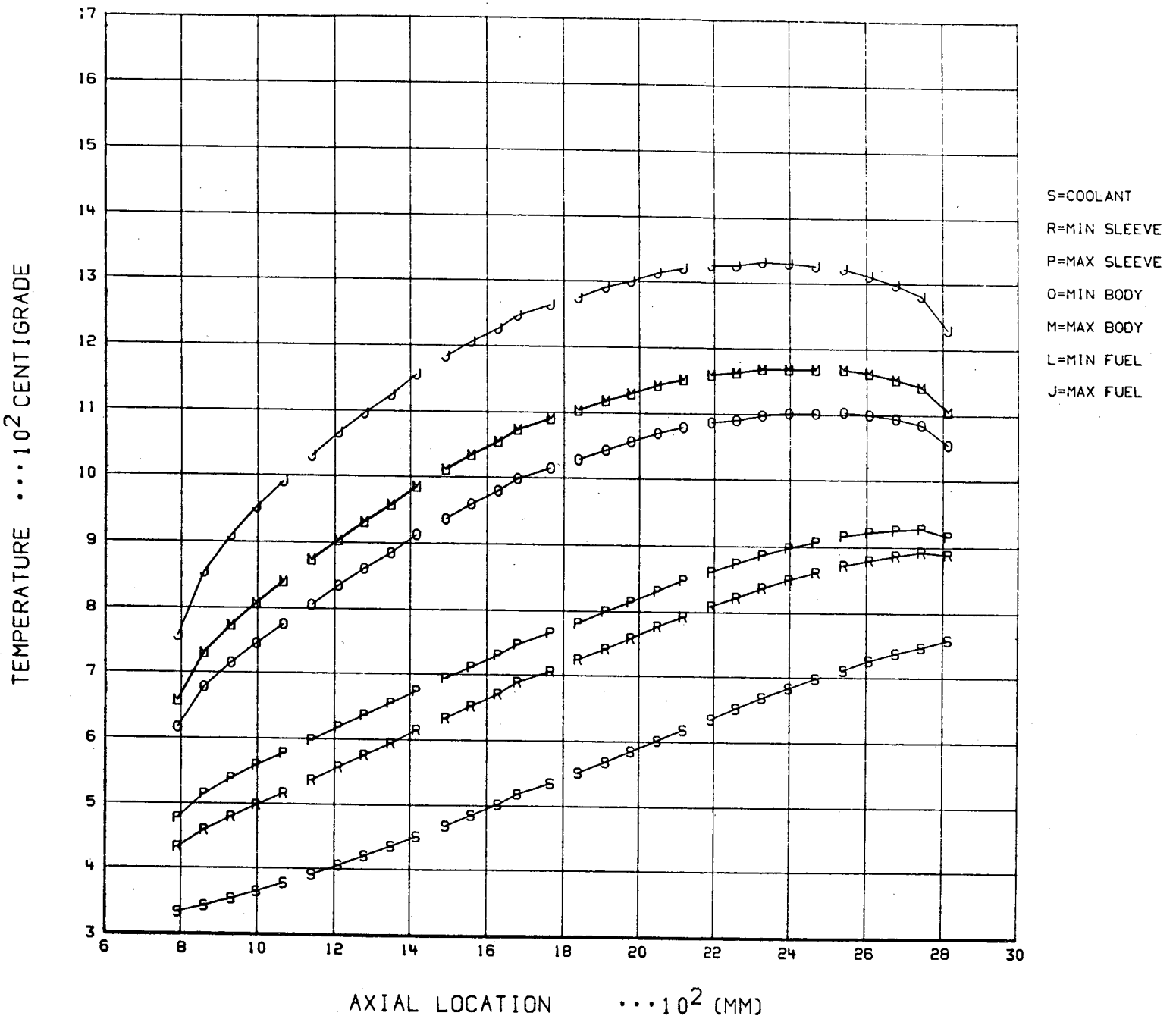
FTE-18 AXIAL TEMPERATURE PROFILE (818-835 EFPD)
TEMPERATURE ...10^2 CENTIGRADE
AXIAL LOCATION ...10^2 (MM)
S=COOLANT
R=MIN SLEEVE
P=MAX SLEEVE
O=MIN BODY
M=MAX BODY
L=MIN FUEL
J=MAX FUEL

Fig. A-12

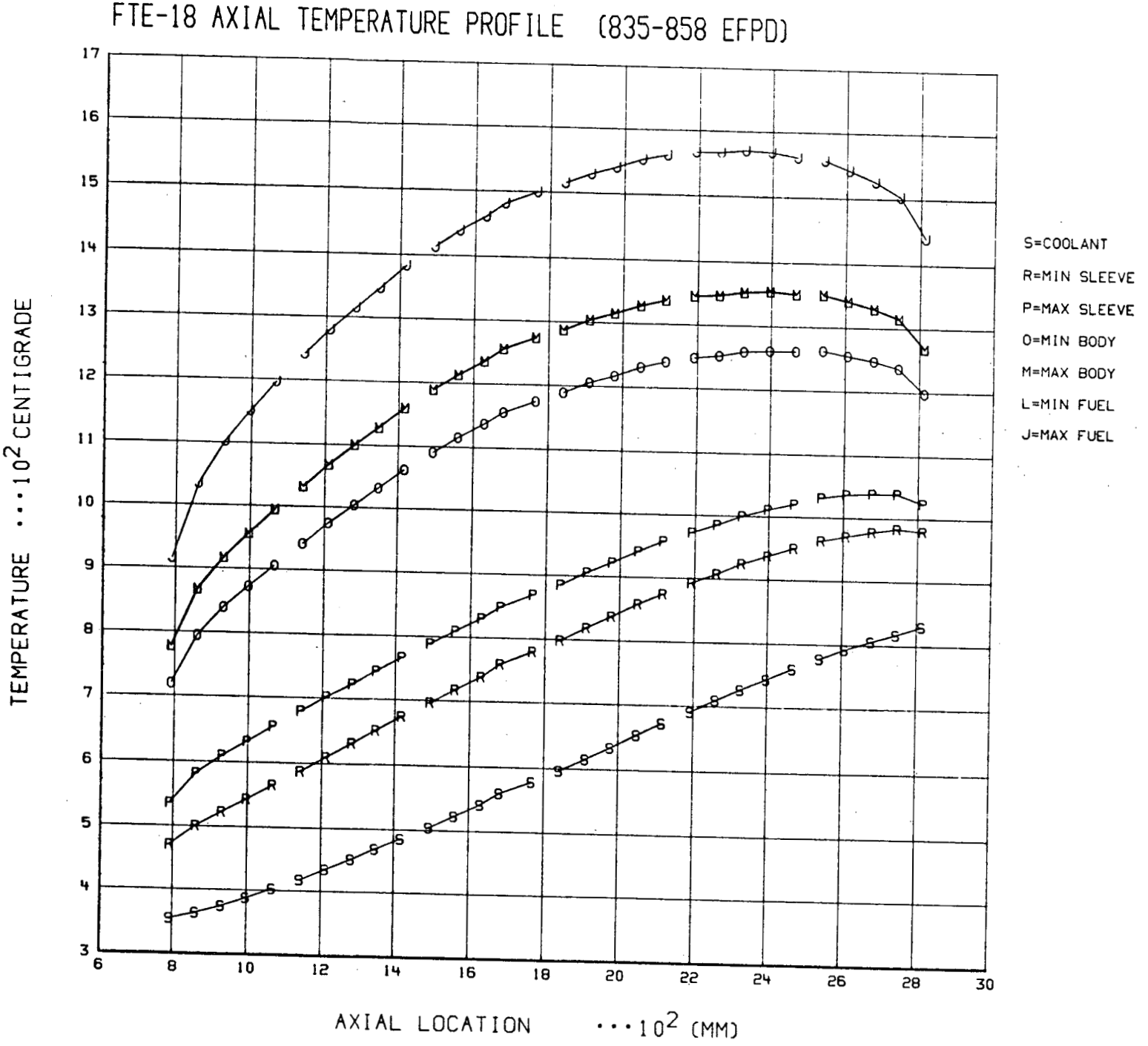
FTE-18 AXIAL TEMPERATURE PROFILE (835-858 EFPD)
TEMPERATURE ...10² CENTIGRADE
AXIAL LOCATION ...10² (MM)
S=COOLANT
R=MIN SLEEVE
P=MAX SLEEVE
O=MIN BODY
M=MAX BODY
L=MIN FUEL
J=MAX FUEL

Fig. A-13

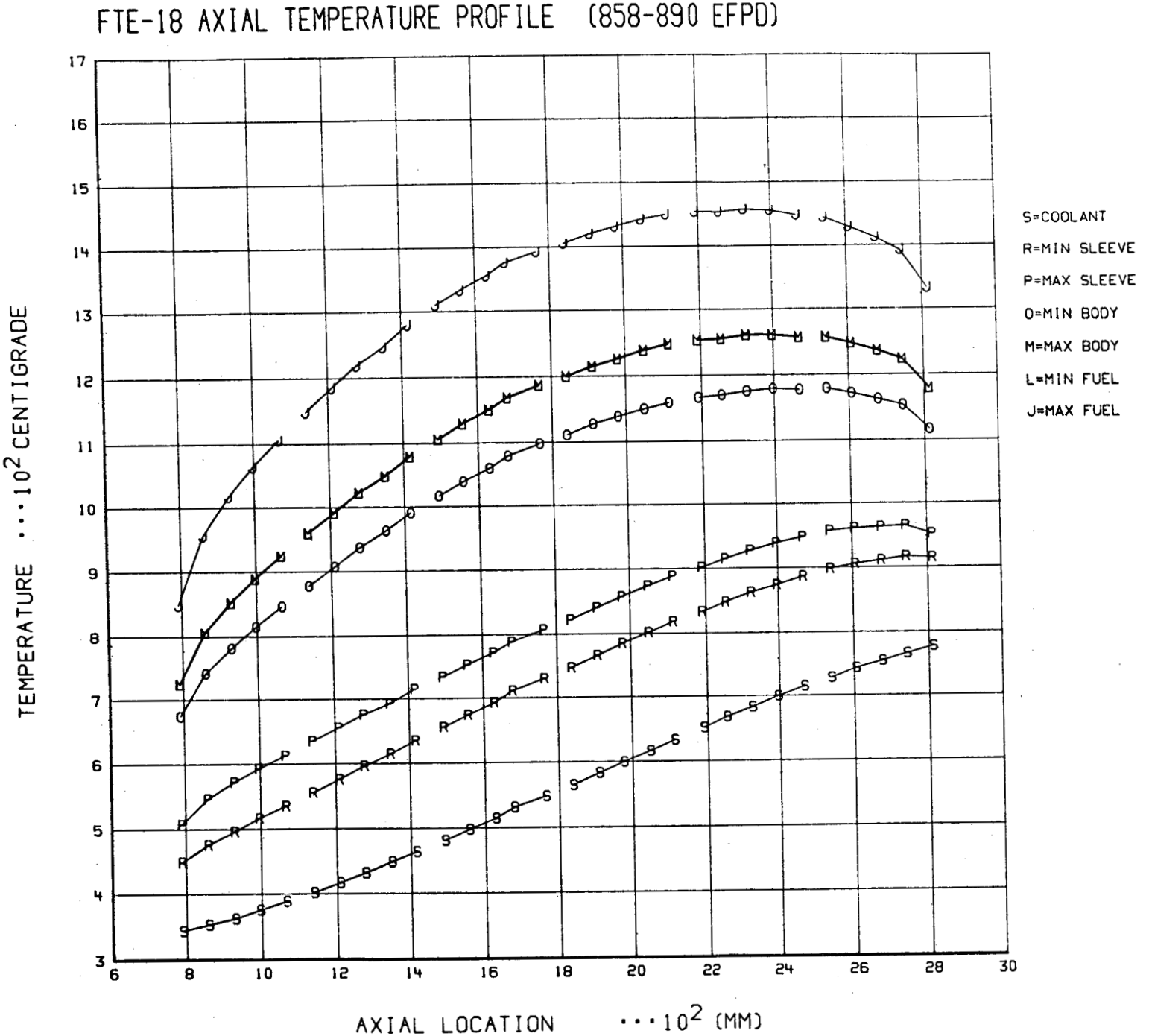
FTE-18 AXIAL TEMPERATURE PROFILE (858-890 EFPD)
TEMPERATURE ...10² CENTIGRADE
AXIAL LOCATION ...10² (MM)
S=COOLANT
R=MIN SLEEVE
P=MAX SLEEVE
O=MIN BODY
M=MAX BODY
L=MIN FUEL
J=MAX FUEL

Fig. A-14

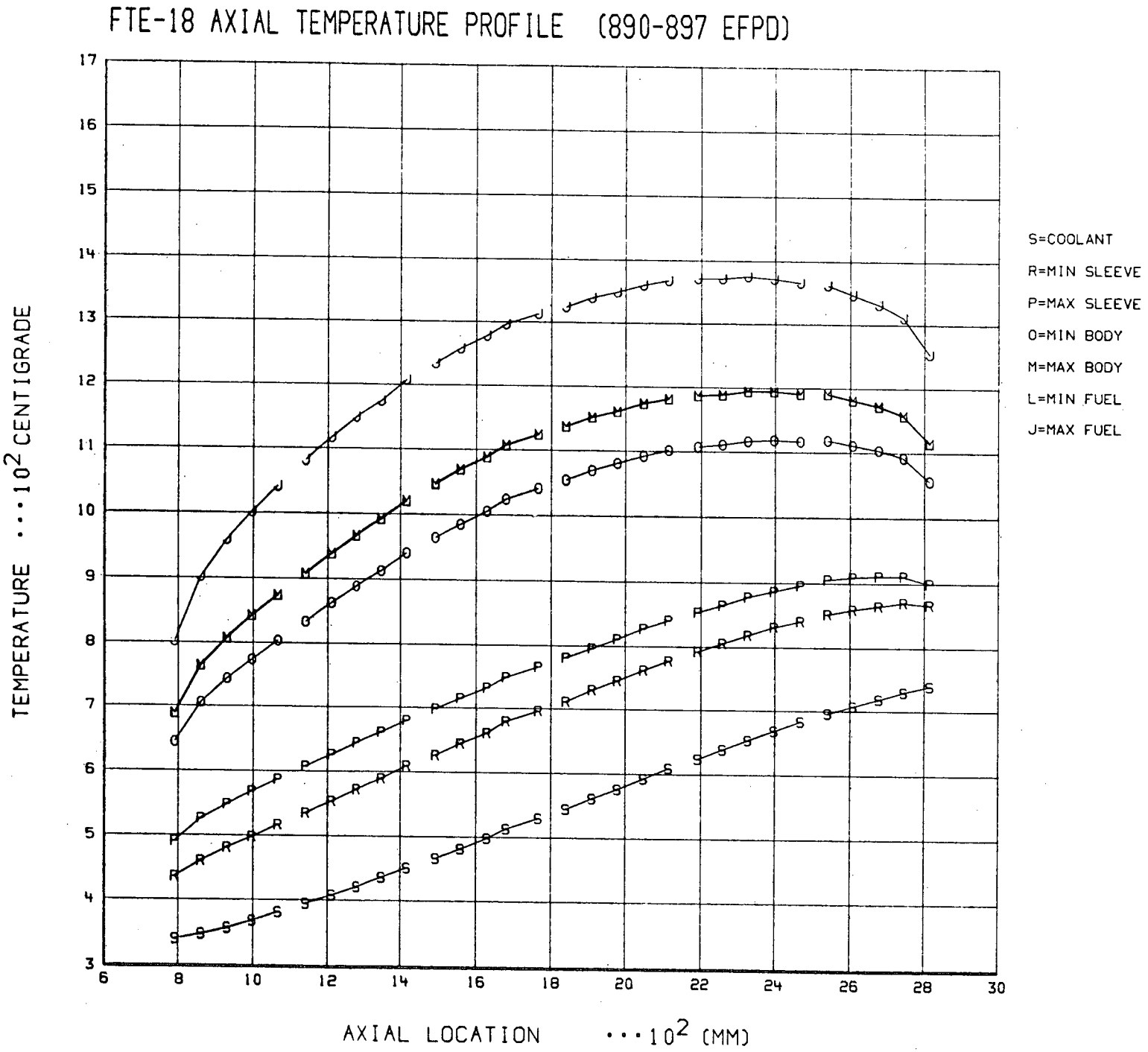
FTE-18 AXIAL TEMPERATURE PROFILE (890-897 EFPD)
TEMPERATURE ...10^2 CENTIGRADE
AXIAL LOCATION ...10^2 (MM)
S=COOLANT
R=MIN SLEEVE
P=MAX SLEEVE
O=MIN BODY
M=MAX BODY
L=MIN FUEL
J=MAX FUEL

Fig. A-15

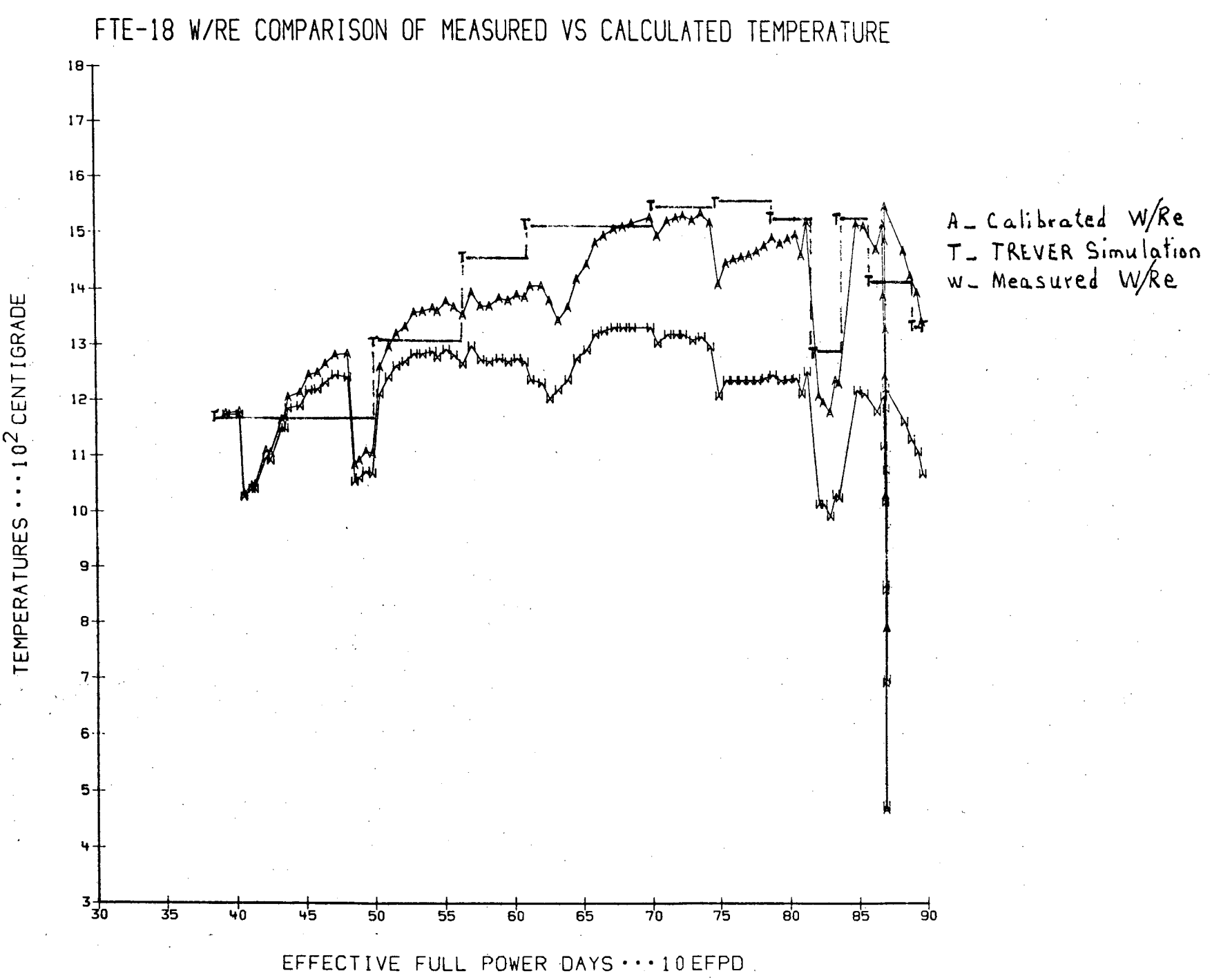
FTE-18 W/RE COMPARISON OF MEASURED VS CALCULATED TEMPERATURE
TEMPERATURES • • • 10² CENTIGRADE
EFFECTIVE FULL POWER DAYS • • • 10 EFPD
A_ Calibrated W/Re
T_ TREVER Simulation
w_ Measured W/Re
18
17
16
15
14
13
12
11
10
9
8
7
6
5
4
3
30
35
40
45
50
55
60
65
70
75
80
85
90

Fig. A-16